Theoretical and experimental study of optical coupling in optomechanical systems

Boris Taurel

▶ **To cite this version:**

Boris Taurel. Theoretical and experimental study of optical coupling in optomechanical systems. Physics [physics]. Université Grenoble Alpes, 2020. English. NNT : . tel-02499125v1

HAL Id: tel-02499125

https://cea.hal.science/tel-02499125v1

Submitted on 5 Mar 2020 (v1), last revised 23 Sep 2020 (v2)

HAL is a multi-disciplinary open access archive for the deposit and dissemination of scientific research documents, whether they are published or not. The documents may come from teaching and research institutions in France or abroad, or from public or private research centers.

L'archive ouverte pluridisciplinaire **HAL**, est destinée au dépôt et à la diffusion de documents scientifiques de niveau recherche, publiés ou non, émanant des établissements d'enseignement et de recherche français ou étrangers, des laboratoires publics ou privés.

THÈSE

Pour obtenir le grade de

DOCTEUR DE L'UNIVERSITÉ GRENOBLE ALPES

Spécialité : PHYSIQUE APPLIQUEE

Arrêté ministériel : 25 mai 2016

Présentée par

Boris TAUREL

Thèse dirigée par **Laurent DURAFFOURG**, Chef de laboratoire, Communauté Université Grenoble Alpes

et **Pierre LABEYE**

préparée au sein du **Laboratoire Laboratoire d'Electronique et de Technologie de l'Information (LETI - CEA)**
dans **l'École Doctorale Physique**

Etude théorique et expérimentale du couplage optique dans les systèmes optomécaniques

Theoretical and experimental study of optical coupling in optomechanical systems

Thèse soutenue publiquement le **9 janvier 2020**,
devant le jury composé de :

Monsieur BERNARD LEGRAND
DIRECTEUR DE RECHERCHE, CNRS DELEGATION OCCITANIE OUEST, Rapporteur, Président du jury.
Monsieur PIERRE VIKTOROVITCH
DIRECTEUR DE RECHERCHE EMERITE, CNRS DELEGATION RHONE AUVERGNE, Rapporteur
Madame ELISE GHIBAUDO
MAITRE DE CONFERENCES HDR, UNIVERSITE GRENOBLE ALPES, Examinateur
Monsieur LIONEL BUCHAILLOT
DIRECTEUR DE RECHERCHE, CNRS DELEGATION HAUTS-DE-FRANCE, Examinateur

Contents

List of abbreviations and acronyms

AS Antisymmetric

BOX Buried oxide

BPM Beam propagation method

CCW Counter clock wise

CMP Chemical mechanical polishing

CROW Coupled resonator optical waveguide

CRR Classical ring resonator

CW Clock wise

DBR Direct Bragg reflector

EIM Effective index method

FCA Free carrier absorption

FCI Free carrier index changes

FDTD Finite difference time domain

FEM Finite element method

FSR Free spectral range

FWHM Full width at half maximum

GC Grating coupler

HDP High density plasma

ICP-RIE Inductively coupled plasma reactive ion etching

LIA Lock in amplifier

LOD Limit of detection

MIR Mid infrared

MZI Mach-Zehnder interferometer

NOMS Nano optomechanical systems

PD Photodetector

PMF Polarization maintaining fiber

PML Perfectly matched layer

PSD Power spectral density

RMS Root mean square

RTOP Response theory of optical forces

S Symmetric

SMF Single mode fiber

SOI Silicon on insulator

SQL Standard quantum limit

SRR Suspended ring resonator

SWG Sub wavelength grating

TE Transverse electric

TED Thermo-elastic damping

TLS Tunable laser source

TM Transverse magnetic

TPA Two photons absorption

UV Ultraviolet

WGM Whispering gallery mode

ZPF Zero point fluctuations

Remerciements

La rédaction de ce mémoire symbolise l'aboutissement de trois années de travail que je n'aurais pas su réaliser seul. Bien qu'il soit difficile d'exprimer avec satisfaction ma gratitude envers toutes les personnes ayant participé au bon déroulement de cette thèse, je vais tout de même m'atteler à cette entreprise au fil des paragraphes suivants.

En premier lieu, je souhaite tout d'abord remercier mes encadrants et directeur de thèse Pierre Labeye et Laurent Duraffourg. Votre expertise complémentaire vis-à-vis des différents aspects du sujet, l'attention et le temps que vous m'avez consacrés, et la motivation dont vous avez fait preuve ont sans conteste fortement contribué au bon déroulement de cette thèse. Au-delà de cet aspect purement relatif à l'encadrement, j'ai également réellement apprécié le caractère humain de nos échanges journaliers.

Une importante part de cette thèse repose sur la réalisation en salle blanche. A cet égard, je remercie chaleureusement Jean-Marc Fedeli pour son aide et son implication concernant l'ensemble de ces questions. Je remercie également Maryse Fournier et Florian Fedeli, qui m'ont accompagné en salle blanche et ont répondu à mes questions à de nombreuses reprises.

Au jour le jour, j'ai été amené à évoluer au sein du laboratoire des capteurs optiques. Les efforts qui y sont faits pour intégrer tout le monde et pour ne pas créer de groupes au sein de l'équipe permettent d'y créer une ambiance et un environnement de travail que j'ai particulièrement appréciés, et je remercie l'ensemble des membres du laboratoire pour cette raison. Je ne me risquerai pas, comme le veut la coutume, à établir une liste individuelle de noms. Une telle énumération ne saurait pas nécessairement restituer avec justesse mon sentiment, et je tiens plutôt à ré-affirmer le plaisir que j'ai eu à évoluer avec chacun de vous au quotidien.

Je souhaite aussi remercier Daivid Fowler, Karim Hassan, Philippe Grosse et Karen Ribaud, pour l'aide apportée sur des questions de conception et de mesure expérimentale, et pour avoir partagé leurs bancs de mesure avec moi.

Naturellement, je tiens à remercier Bernard Legrand et Pierre Viktorovitch, rapporteurs de ce manuscrit, ainsi qu'Elise Ghibaudo et Lionel Buchaillot, pour avoir accepté de participer à mon jury de thèse et d'examiner mon travail.

Enfin, je remercie ma famille. Bien que le doctorat représente la partie finale des études, il repose sur l'ensemble du parcours précédemment effectué, au cours duquel j'ai pu bénéficier de votre soutien et de vos encouragements constants. Je souhaite saisir l'opportunité ici présente pour vous en remercier, et pour vous exprimer ma gratitude et ma reconnaissance.

Cavity optomechanics: an introduction

Cavity optomechanics explores the reciprocal interactions between an optical and a mechanical resonator. It forms a large and diversified field of Physics, whose applications include both fundamental and applied research, with motivations as varied as quantum manipulation of light, gravitational wave detection, and realization of high precision sensors.

While cavity optomechanics was originally considered in the context of large scale interferometers, the strength of most optomechanical interactions actually tends to be inversely proportional to the resonator dimensions. For this reason, the community has mainly focused its recent research efforts towards the miniaturization of optomechanical cavities, and many long-anticipated optomechanical phenomenons were demonstrated for the first time in micro and nano-optomechanical cavities.

Following this trend, integrated photonics naturally became a privileged platform for cavity optomechanics. Owing to its excellent optical and mechanical properties and to the fabrication expertise provided by the micro electronic industry, silicon is a promising candidate for cavity optomechanics, that could pave the way towards on-chip optomechanical systems. The aim of achieving optomechanical interactions in silicon integrated photonic circuits is the underlying motivation of this thesis work.

We begin this discussion with an introductory overview to cavity optomechanics. An historical introduction is given, followed by an intuitive description of important concepts, realizations, and applications of cavity optomechanics. Finally, this work is put into perspective in regard to the present state-of-the-art.

Historical introduction

In 1619, Keppler observed that the tail of comets bends away from the sun, and hypothesized that light could exert forces on mechanical bodies. In 1873, Maxwell theorized

transfer of momentum between light and matter and the existence of an optical force known as radiation pressure. A few years later in 1901, the existence of this force was verified experimentally by Lebedew [1] and Nichols and Hull [2].

In the late 1970s, Braginsky studied the effects of radiation pressure in the context of astronomical interferometers exhibiting a harmonically suspended mirror. He predicted a dynamic backaction effect of the optical force, that could be used to provide either damping or anti-damping of mechanical motion, and demonstrated this result in the case of microwaves [3]. He also derived the existence of the so-called "Standard Quantum Limit" (SQL) on the accuracy at which the position of a free test mass can be measured by interferometric means, because of the quantum fluctuations of radiation pressure [4].

Later on, the field of cavity optomechanics was extended to the quantum world. It was theoretically proposed to use the quantum properties of radiation pressure to realize quantum non-demolition measurements [5], to create non-classical states of the light field [6], and to observe non-classical entangled states of light and mechanics [7].

In parallel to the discussion about radiation pressure in optical cavities, Ashkin studied the possibility to manipulate small dielectric particles with optical forces. In 1970, he demonstrated the possibility to accelerate and trap micro particles by means of radiation pressure and optical gradient forces [8]. In 1978, he achieved laser cooling of the atomic motion of micro particles [9]. His work laid the foundations for the realization of optical tweezers, that are now widely used to control biological particles in a non-destructive way, and of laser cooling, that became one of the major subfields of atomic, molecular and optical physics [10].

In the early 2000s, these two sides of the somehow same field were brought together when it was realized that radiation pressure and optical gradient forces[1] could be used to couple mechanical and optical modes of toroid microcavities[11, 12, 13]. As its actions are more pronounced at the micro and nano-scale, cavity optomechanics was rapidly expanded to various setups such as cantilevers [14], nanomembranes [15] or photonic crystals [16]. Over the past years, the ever going progresses in micro and nano fabrications techniques have enabled to increase the optical and mechanical quality factors of resonators and to reduce the volumes down to a regime in which optical forces are routinely dominant over other phenomenons.

Today, most teams working on the field of cavity optomechanics use micro or nano-scale resonators. Although there is a large diversity of setups, they can all be compared to a miniaturized version of a Fabry-Perot cavity with a moving back-end mirror, which constitutes the paradigmatic optomechanical cavity.

[1]Often simply referred as radiation pressure in the community

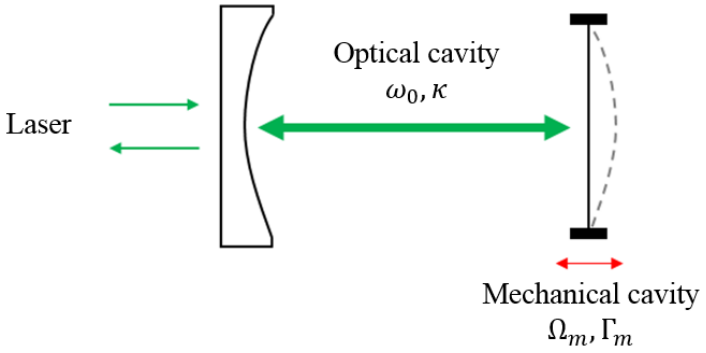

Figure 1 – Schematic of a Fabry-Perot cavity with a moving back-end mirror. An input laser is coupled into the Fabry-Perot cavity through a fixed, motionless input mirror. The back-end mirror is by some way able to vibrate and to modulate the cavity length.

Paradigmatic optomechanical setup, and important optomechanical parameters

The paradigmatic optomechanical setup is a Fabry-Perot cavity with a moving back-end mirror (see figure 1). Light is launched into the cavity by means of a laser, through a motionless input mirror. In this geometry, the optomechanical coupling between the optical and mechanical resonators is introduced by radiation pressure.

From the mechanical perspective, radiation pressure on the back-end mirror leads to mechanical motion and modulates the cavity length. From the optical perspective, when the input laser is slightly detuned from the resonance, any variation of the cavity length will strongly modulate the intra-cavity field. Now, as radiation pressure corresponds to a transfer of momentum between photons and phonons [2], its strength is proportional to the energy stored within the cavity and is therefore impacted by mechanical motion. Hence, the optical field depends on the position of the mirror, and in turn, the position of the mirror depends on the optical field ; the two resonators are effectively coupled to each other.

The Fabry-Perot setup has been extensively studied since the very beginning of the field, and led to most optomechanical development to date. It constitutes a good starting point when discussing optomechanical systems, as the majority of them can be described in analogy to the Fabry-Perot cavity with a moving back-end mirror. The description of the classical dynamics of this setup and its main implications are presented on section I.2. Remarkably, we will show that the optical field can be used to modify the mechanical properties of the mirror.

[2] A phonon is defined as the quantum of vibration of an elastic structure [17]

Prior to this theoretical discussion, we next introduce the important parameters of optomechanical resonators, give an overview of the state of the art, and present some selected optomechanical experiments and applications.

Optomechanical parameters of interest

When trying to "quantify the quality" of an optomechanical cavity, it is usual to examine the following parameters:

The mechanical frequency f, in Hz (or alternatively, the mechanical angular frequency $\Omega_m = 2\pi f$). In optomechanical systems, high resonance frequency is desirable as it allows larger bandwidth and natural isolation from acoustic waves and thermal noise [18, 19, 20].

The mass m, in kg. In mechanical resonators, the mechanical frequency is inversely proportional to the square root of the mass. Hence, an efficient way to maximize the mechanical frequency is to minimize the mass of the system. In mechanical systems supporting multiple modes of vibrations, the effective mass m_{eff} associated to a given mode is considered.

The mechanical damping rate $\Gamma_m/2\pi$, in Hz. Naturally, it is favorable to minimize the mechanical dissipation rate. Often, a somehow equivalent parameter is used, the mechanical quality factor $Q_m = \Omega_m/\Gamma_m$.

The product of mechanical quality factor and frequency $Q \times f$, in Hz. Mechanical resonators are frequently compared based on the product $Q \times f$, as these two quantities are of paramount importance for the realization of many high performance M&NEMS devices. This product is also a representation of the degree of decoupling of the mechanical resonator from its thermal bath environment, which is essential in cavity optomechanics [21]. In particular, the realization of optomechanical resonators with large $Q \times f$ products is key for the development of quantum optomechanics [22].

The optical decay rate $\kappa/2\pi$, in Hz. Similarly to the case of mechanical resonators, the optical decay rate is linked to an optical quality factor $Q_{\text{opt}} = \omega_0/\kappa$ where ω_0 is the angular resonant frequency. In optomechanical systems, a high optical quality factor confined within a small volume is desirable in order to enhance the overall performances and to magnify light-matter interaction.

The sideband suppression factor κ/Ω_m. This ratio determines the ability to realize ground-state cooling and other quantum applications. This is detailed in the following.

Single photon-phonon optomechanical coupling rate $g_0/2\pi$, in Hz (also regularly referred as "vacuum optomechanical rate", or simply "optomechanical coupling rate"). This quantity, described in section I.2, is a normalized measure of the strength of the optomechanical interaction.

In parallel to these quantitative parameters, two important qualitative factors also have to be considered: the ease of realization and the ease of operation. Indeed, many historical cavity optomechanics setups critically rely on the positioning and alignment of optical and/or mechanical elements, and have experimentally been limited by these two points. In this regard, the ability to precisely realize an optomechanical cavity with micro and nano-fabrication techniques, and to operate it by means of photonic structures with relaxed alignment constraints, is a major advantage.

Present State-of-the-art

Present optomechanical devices are really diversified, with a huge variety of optical forces and optomechanical coupling schemes at play. A brief (and not exclusive) introduction to these different geometries, and to the underlying motivation of each approach, is presented in the following. A most comprehensive state-of-the art can be found in [22].

Suspended mirrors

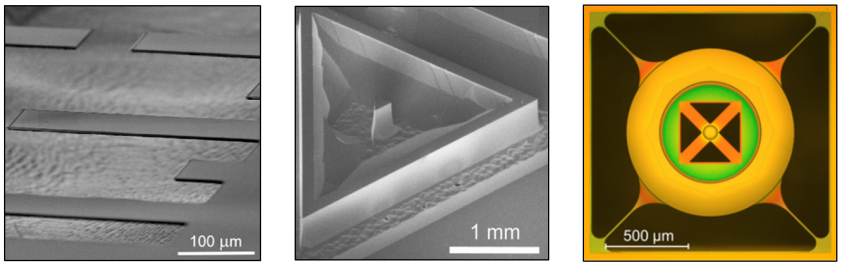

Figure 2 – Examples of suspended mirrors realized with micro-scale reflecting resonators. From left to right: cantilever [23], micropillar [24], trampoline resonator [25].

Suspended mirrors are the most straightforward way to realize a Fabry-Perot cavity with a movable back-end mirror. This coupling scheme was originally envisioned in the context of gravitational interferometers, with large-scale mirrors and optical cavities. With the development of cavity optomechanics, because the strength of optomechanical interactions is more pronounced under size reduction, this scheme is now realized at the micro-scale with highly reflecting resonators. Non-exclusively, realization with microlevers [26], micropillars [24], or trampoline resonators [25] were reported.

High optical quality factors can be achieved with suspended mirrors. However, this setup is hampered by the fact that the size of the resonator must be larger than the wavelength of light to allow efficient optomechanical coupling. It results in practical limitations of the mechanical properties (relatively low frequency - at most in the MHz range - and high mass - microgram range) in comparison to other optomechanical devices. Nevertheless, it

must be remembered that most milestones optomechanical experiments were conducted on this geometry.

Mechanical resonator in the middle of an optical cavity:

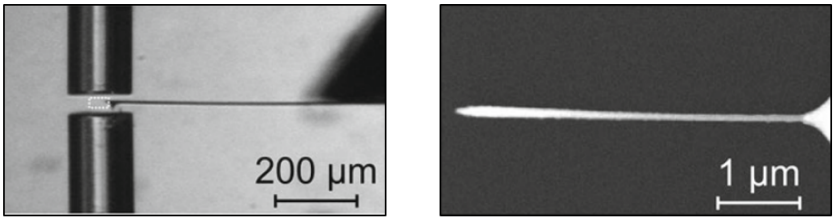

Figure 3 – Left: Fiber-based Fabry-Perot cavity with a nanoresonator in the middle (dotted box). Right: SEM image of the nanoresonator. Figures from [22].

Instead of having the back-end mirror of the Fabry-Perot cavity vibrating, it is possible to place a mechanical resonator in the middle of the cavity. Physically speaking, the effective length of the cavity is modulated by the phase shift introduced with the motion of the resonator. It also gives rise to a dissipative optomechanical interaction, in which the absorption rate of the cavity is modulated.

The major motivation behind this setup originates from the separation between the optical and mechanical degrees of freedom. As a result, most constraints imposed on the size and mass of the mechanical resonator in the case of suspended mirrors are relaxed. This way, the optical and mechanical parts can be optimized separately, without impacting each other, and high optical and mechanical quality factors can be achieved, with no limitation on the mechanical frequency and mass.

This scheme has been realized with nanorods [27] and nanomembranes of sub-wavelength thickness [15]. It however remains extremely challenging to realize and manipulate, as it critically depends on the experimental alignment and positioning of the mechanical resonator and Fabry-Perot mirrors.

Suspended optical microcavities:

The Fabry-Perot scheme can be replicated in a monolithic and integrated setup, where the structural vibration modes of a micro-sized optical cavity are excited by means of optical forces. The optomechanical interaction is enhanced by the small size of the optical cavity and by the existence of additional optical forces and coupling mechanisms, due to the optical propagation in a dielectric medium (instead of free-space).

Essentially, four kinds of optical resonators are used: microtoroids [11, 12, 13], microdisks [28], microspheres [29], and microrings [30].

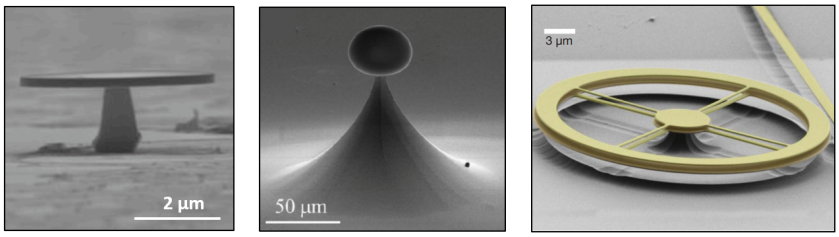

Figure 4 – Examples of suspended optical microcavities. From left to right: microdisk [28], microsphere [29], double microring [30].

Suspended optical microcavities exhibit several appealing properties in regard to cavity optomechanics: extremely small masses (down to the nanogram range), high mechanical frequencies (up to the GHz range), high mechanical quality factors, really high optical quality factors, small sizes, easy experimental operation (most constraint on optical alignment are suppressed) and compatibility with micro-fabrication techniques. Their major drawback is that they can exhibit quite large non-linear optical effects due to the high power densities confined in small volumes, which deeply complicate the behavior of the system.

In this thesis, all our cavities belong to this family of optomechanical resonators.

Near field optomechanics:

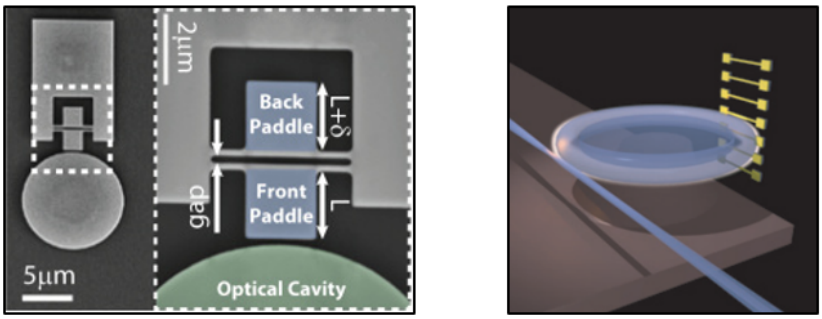

Figure 5 – Near field optomechanics with mechanical paddles [31] (left) and nanostrings [32] (right).

In this geometry, a micro or nano-resonator is placed at close proximity of an optical cavity. Similarly to the case of "in-the-middle" cavity optomechanics, the optical and mechanical resonators are distinct structures, interacting through the evanescent optical field. In the context of integrated devices, the large advantage of this setup is the ability to separately optimize the design of the optical and mechanical part, such that extremely elevated optical and mechanical quality factors can be achieved at the same time. On the other hand, the positioning of the mechanical resonator remains challenging in this setup, even with micro and nano-fabrication techniques.

Near field optomechanics can for example be realized with a disk resonator and mechanical paddles [31] or with a microtoroid and nanostrings [32].

Optomechanical crystals

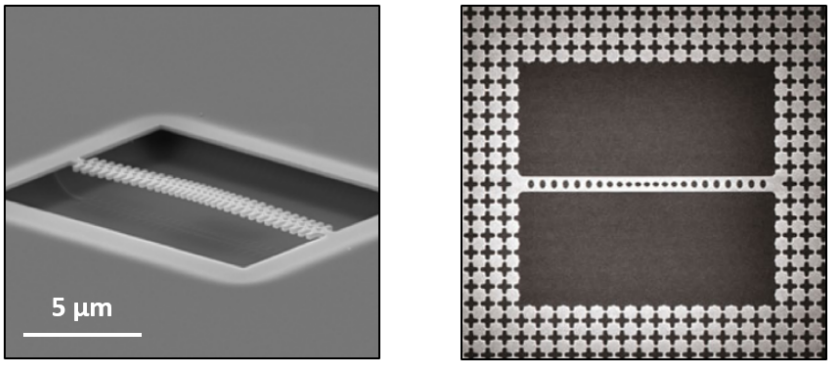

Figure 6 – Optomechanical crystals [16, 22].

In a thin dielectric medium, a photonic bandgap can be achieved by nano-patterning of a periodic structure. When a defect is introduced in the lattice, wavelength-scale localization of the optical field is achieved, which is known as photonic crystals. On the mechanical perspective, the same principle allows to create phononic crystals. In optomechanical crystals (often termed phoXonic crystals), the two approaches are combined into the same entity [16].

Optomechanical crystals offer promising perspectives for the development of cavity optomechanics, due to their high mechanical frequencies, low masses and small optical and mechanical localization volumes, and some of the best optomechanical coupling rates to date were reported with these geometries [33]. Last but not least, optomechanical crystals are compatible with classical CMOS fabrication processes and can be included on-chip, with integrated photonic architectures.

Comparison

A comparison of the previously presented optomechanical cavities is given on table 1, based on the published data.

Selected applications of cavity optomechanics

In the following, we present a qualitative description of important applications of cavity optomechanics. A more extensive presentation can be found in [22].

	f (Hz)	Mass (kg)	Q_m	Q_{opt}	$g_0/2\pi$ (Hz)
Suspended mirrors					
Complicated fabrication and operation					
Cantilever [23]	7×10^3	–	2×10^4	2.6×10^8	–
Micropillar [24]	3.2×10^6	725×10^{-6}	1.8×10^6	5.1×10^7	–
Trampoline [25]	250×10^3	100×10^{-9}	4×10^5	1.7×10^{10}	1
Nanoresonators in the middle					
Complicated fabrication and operation					
Nanorods [27]	1.9×10^6	–	1×10^4	7.25×10^6	
Nanomembranes [15]	134×10^3	4×10^{-8}	1.1×10^6	–	–
Suspended optical microcavities					
Easy fabrication and operation					
Microdisk [28]	850×10^6	20×10^{-12}	1×10^3	1×10^5	5.1×10^4
Microsphere [29]	80×10^6	–	5×10^3	8×10^7	–
Double microring [30]	600×10^3	85×10^{-12}	2	6×10^4	–
Near field optomechanics					
Complicated fabrication and easy operation					
Paddles [31]	50×10^6	3.3×10^{-12}	3.7×10^4	4×10^4	500
Nanostrings [32]	10×10^6	1×10^{-12}	1×10^5	4×10^7	50
Optomechanical crystals					
Easy fabrication and operation					
PhX. [33]	5.1×10^9	127×10^{-15}	6.8×10^5	1.2×10^6	1.1×10^6

Table 1 – Comparison between the experimental parameters of the previously presented optomechanical cavities.

Cooling of mechanical modes

One of the major goals of cavity optomechanics is to achieve ground-state cooling of the mechanical resonator and observe its quantum signature. This is approached with two schemes, relying on radiation pressure[3]: dynamical backaction cooling, and feedback cooling.

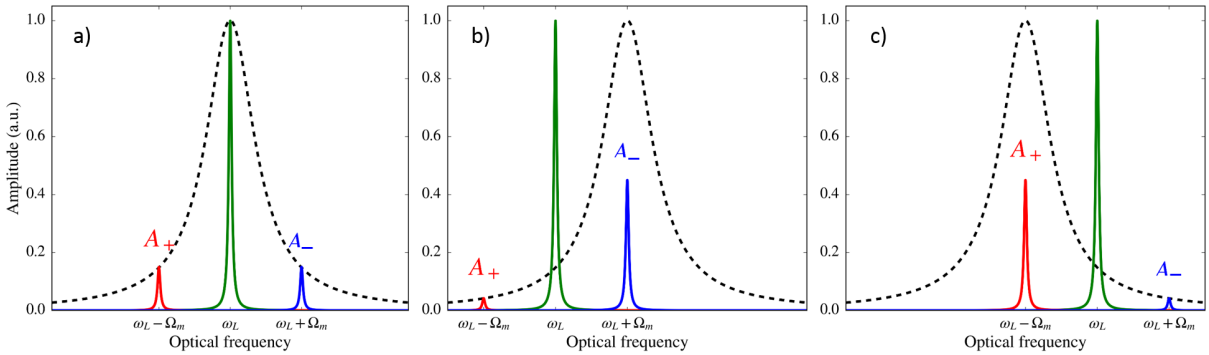

Figure 7 – (Resolved) Sideband picture. Green: laser field at ω_L. Red: sideband at $\omega_L - \Omega_m$. Blue: sideband at $\omega_L + \Omega_m$. **a)** The laser is driven at resonance, and the two sidebands are identical. **b)** The laser is red-detuned from resonance by an amount $-\Omega_m$. The imbalance between the two sidebands leads to mechanical cooling (the mechanical energy is transferred towards the optical energy, in other words, from phonons to photons). **c)** The laser is blue-detuned from resonance by an amount $+\Omega_m$. The imbalance between the two sidebands leads to mechanical amplification (optical energy is transferred towards mechanical energy).

Dynamic backaction cooling Dynamic backaction cooling can be understood in a sideband picture. Due to the exchange of energy between photons and phonons, two lateral sidebands are created at $\omega_L - \Omega_m$ (red) and $\omega_L + \Omega_m$ (blue) with a rate $A_\pm$ (ω_L is the angular laser frequency and Ω_m is the angular mechanical frequency). When the laser is detuned from the cavity resonance, it creates an imbalance between the two sidebands (see Figure 7), leading to amplification ($A_+ > A_-$) or cooling ($A_- > A_+$) of mechanical motion. This effect can be understood by analogy to Brillouin scattering in a solid crystal, in which a photon is submitted to inelastic scattering after interacting with an optical phonon. In this picture, amplification is compared to a Stokes process, and cooling to an anti-Stokes process.

From this sideband picture, one of the reason why the sideband suppression factor κ/Ω_m determines the ability to realize ground-state cooling becomes more intuitive: when $\kappa < \Omega_m$, it becomes possible to generate a blue sideband while suppressing the red sideband that falls away from resonance. This case is known as the "resolved-sideband regime".

[3]These approaches have also been conducted based on photothermal forces, with effective cooling [26]. The latter, however, can not ultimately be used for ground-state cooling, as it relies on absorption of light and heat generation.

Dynamic backaction cooling due to radiation pressure is a dynamic phenomenon, which can qualitatively be described with classical equations, as presented in section I.2, but has to be approached with a quantum description in order to get a proper estimation of the achievable low temperatures [34, 35]. With this technique, cooling from room temperature to 10K was first simultaneously observed on the 58 MHz radial breathing mode of a microtoroid cavity [36], on the 814 kHz fundamental mode of a doubly clamped beam with a coated micromirror upon its surface [14], and on a 280 kHz mode of a high reflectivity doubly clamped cantilever [37] (in this last case, radiation pressure was assisted by photothermal effects).

Feedback cooling Radiation pressure can also be used as a feedback mechanism in order to cool down a resonator. In this scheme, a first laser is used as a probe to monitor mechanical motion. The velocity of the resonator is calculated from the time derivative of the signal, and is used to modulate the intensity of a second feedback laser. This way, radiation pressure from the feedback laser counteracts mechanical motion, and effectively cools the resonator.

Optical feedback cooling was first theoretically proposed in [38], with no hint on the feedback mechanism. The first experimental demonstration was in the case of radiation pressure [39], with a reduction of the effective temperature of the 2 MHz fundamental resonance mode of a mm-sized mirror by a factor 40. Since then, cooling from room temperature to 135 mK of the 12 kHz fundamental mode of an AFM cantilever with an attached micromirror [40], and cooling from 2.2 K to 3 mK of the 3.9 kHz fundamental mode of a silicon cantilever [41] were achieved.

Comparison of the two schemes in the prospect of ground-state cooling Fundamentally, feedback cooling is different from dynamic backaction cooling. In the first case, radiation pressure is used as a way to induce a real-time viscous force counteracting the mirror motion. In the second case, it is used as a retarded backaction to modify the dynamics of the mechanical resonator and to "pump-out" its thermal energy.

The two schemes were compared in regard to their ability to reach ground-state cooling in [42]. The comparison reveals that cooling with dynamical backaction is favorable in the resolved-sideband regime $\kappa < \Omega_m$ (accordingly with the sideband picture), while feedback cooling is favorable in the unresolved-sideband regime $\kappa \gg \Omega_m$.

In this regard, a simplistic way to differentiate these two schemes is based on where it is decided (and possible) to ease the problem. A scheme based on dynamical backaction is experimentally easier to operate, but requires to reach the resolved-sideband regime. A high quality optomechanical cavity (high frequency and low optical dissipation) is necessary, or in other words, the efforts are focused towards the fabrication process. On the other hand, a scheme based on feedback cooling is less constrained by the optomechanical cavity, but is harder to experimentally operate.

On-chip Nano-OptoMechanical Systems (NOMS)

While dynamical backaction can be used to cool the resonator when the laser is red-detuned from resonance, it can alternatively be used to amplify its motion if the laser is blue-detuned. Above a certain optical power threshold, the optomechanical amplification can overcome the intrinsic mechanical damping, and self-sustained (or regenerative) mechanical oscillations are generated. This parametric instability, first proposed by Braginsky [43], can be exploited to realize on-chip optomechanical oscillators, often referred as NOMS by analogy to their electrical counterpart. On the following, we present some of their applications.

Mechanical sensing Sensitive measurement of the deflection of a micro or nano-scale cantilever is at the heart of many applications involving displacement, force and mass sensing, such as inertial detection, environmental monitoring, mass spectroscopy and biological metabolite detection and quantification [44, 45, 46]. Albeit M&NEMS devices are the privileged platform for such measurements, the upper limit of their operation bandwidth is limited by parasitic electric coupling and readout impedance mismatch [47], and their ultimate sensibility is inferior to optical transduction, that furthermore suffers from less theoretical bandwidth limitations [45, 48].

Free-space optical methods are already widely used and have demonstrated sensitivities below the attogram/$\sqrt{\text{Hz}}$ range [49], but are limited by the diffraction limit, *i.e.* by the fact that the device dimensions must remain superior to the optical wavelength.

Alternatively, optomechanical devices can offer the same advantages as free-space methods, while avoiding the diffraction limit and the difficulties of optical alignment [45, 50]. Additionally, optomechanical oscillators also benefit from their natural immunity to electromagnetic fields, low operation power and low noise level [51, 52]. This makes on-chip optomechanical devices an appealing platform for high precision mechanical sensing, and several demonstrations have already been presented, with displacement resolutions down to a few 10^{-18} m/$\sqrt{\text{Hz}}$ [47, 53] and mass sensitivities down to the zeptogram level [54], demonstrating that optomechanical architectures can be advantageously used to make small, fast and of extremely sensitive mechanical sensors.

High-quality frequency reference NOMS can be used as high-quality frequency references, as the optically induced mechanical oscillations are subsequently carried out in the transmitted optical power.

Such photonic clock presents interesting advantages in comparison to other state-of-the-art frequency reference sources [55, 52]. Notably, the optomechanical oscillator is powered by a continuous optical source, is by essence simple to operate, and has a small footprint. Additionally, optomechanical oscillators can be integrated on-chip and operate at high frequency.

By opposition, quartz crystal oscillators, the most widely used frequency reference source, can be used as a way to modulate a laser diode. Quartz crystal oscillators exhibit remarkably low phase noise performances, but suffer from their incompatibility with CMOS fabrication processes that hinder the integration of such sources on-chip.

Integrated silicon photonic clocks, based on optoelectronic oscillators, have also been reported [56]. While the replacement of the quartz crystal oscillator by a MEMS device allows on-chip integration and size reduction, this setup relies on more complex operation schemes and higher power consumption than optomechanical oscillators. More importantly, the operation bandwidth remains degraded at high frequency by parasitic and impedance mismatch effects, contrary to optical methods.

Signal processing NOMS can also be used in signal processing applications, such as optical wavelength conversion and frequency downmixing.

Optical wavelength conversion involves two optical cavity modes (between which the conversion occurs) that are coupled to the same mechanical resonator. Each mode is pumped by a laser red detuned from the optical resonance by an amount equal to the mechanical frequency [57]. The wavelength conversion is mediated by the shared resonator by a relatively complex mechanism described in [58]. Depending on the optical power of each pump, input signals can be up-converted or down-converted, with an efficiency close to unity [57, 19].

Frequency downmixing can be achieved the following way: self-sustained oscillations at Ω_m are entertained in the optomechanical oscillator (with sufficient optical power), in which a signal modulated at Ω_{RF} is injected. Natural downmixing occurs between the mechanical frequency and the signal frequency, that is converted down from Ω_{RF} to $\Omega_{\mathrm{RF}} - \Omega_m$ [59]. This kind of downmixer is quite versatile, as it is possible to change the mechanical frequency Ω_m by detuning of the optical wavelength and selecting a new mechanical mode. This way, Ω_{RF} can be downmixed by multiple frequencies (the mechanical harmonics) with the same optomechanical oscillator.

Optically induced synchronization between mechanical oscillators Synchronization between mechanical oscillators is an attractive perspective in physical micro and nano-systems, as it could provide additional control and increased performances in signal processing, microwave communication and computation techniques [60]. Arrays of many coupled optomechanical oscillators have been proposed has a way to realize collective synchronization of mechanical oscillators by an optical field [61, 62] and demonstrated [63, 64]. Practical important realizations, such as phase noise reduction by a factor N of N synchronized nanoresonators have been accomplished [65] (N = 7 in this experiment).

Note that synchronization between mechanical oscillators can also be achieved based on NEMS [66].

Optomechanically induced transparency

Optomechanically induced transparency is analogous to atomic electromagnetically induced transparency [67] ; in the presence of a strong pump laser and weak probe laser, destructive interference of the two fields, mediated by the mechanical resonator, can cancel the intracavity field and open a transparency windows in the probe transmission.

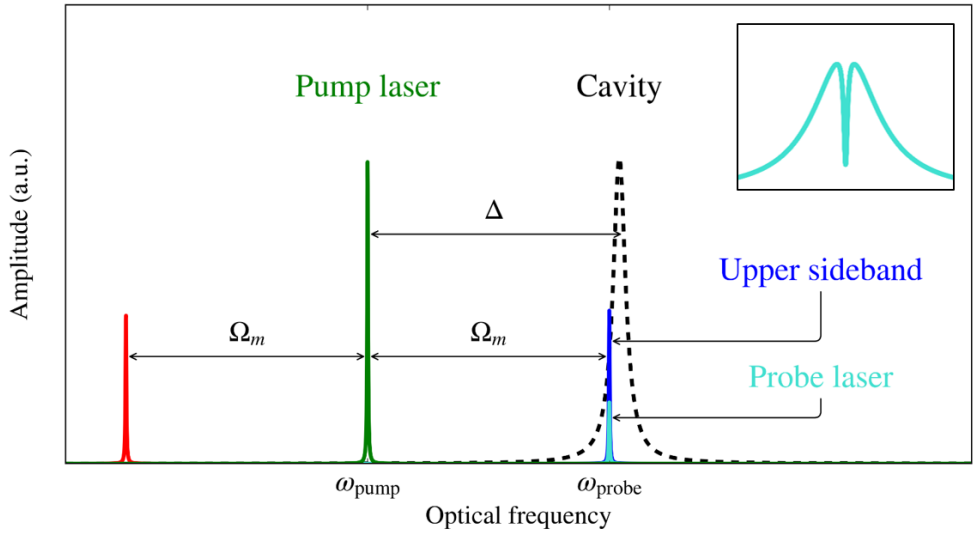

Figure 8 – Frequency configuration for optomechanically induced transparency. **Inset:** Illustration of the transparency windows in the probe transmission.

More precisely, the two lasers are launched into the cavity with a relative detuning $\Delta_{pp} = \omega_{\text{probe}} - \omega_{\text{pump}}$ and yield a time varying radiation pressure force at Δ_{pp}. The pump is launched with a detuning Δ in regard to the cavity. If the detuning Δ_{pp} matches the mechanical resonant frequency Ω_m ($\Delta_{pp} = \Omega_m$), the mechanical resonator is driven resonantly. In a resolved sideband regime ($\kappa \ll \Omega_m$), two lateral sidebands appear at $\omega_{\text{pump}} \pm \Omega_m = \Delta_{pp}$ for the pump laser (assuming that the probe is weak, its lateral sidebands are negligible). Thus, the upper sideband of the pump field appears at the same frequency that the probe field (see figure 8). Because the two fields are naturally phase-matched, they cancel each other due to destructive interference, which open-up a transparency windows in the cavity transmission. Alternatively, when the interferences are constructive, this can also lead to amplification of the intracavity field at resonance, which is known as optomechanically induced amplification.

Optomechanically induced transparency was first proposed in [68] and first observed in [69]. In the last decade, it has continuously attracted more and more attention from the optomechanical community because of its attractive promises in regard to optical manipulation. Applications of optomechanically induced transparency include a wide range of on-chip optical signal processing functions, precision measurement, Qbit manipulation, and an alternative route for ground-state cooling, as illustrated in the recent review paper [70]

Aim of this work & overview of the manuscript

This doctoral work is part of on-chip silicon cavity optomechanics. The aim is to study, theoretically and experimentally, optomechanical coupling arising within on-chip photonic suspended structures, realized over silicon wafers. The underlying motivation is to pave the way towards the realization of NOMS devices at CEA-Leti, as an alternative and complementary approach to NEMS devices. In particular, integrated optomechanical inertial sensors are targeted.

In this framework, we studied two approaches that could find practical applications as NOMS devices: suspended ring resonators and sub-wavelength patterned waveguides. Suspended ring resonators are a classical optomechanical cavity, similar to micro-toroids or micro-disks. They offer a wide range of mechanical degrees of freedom, and could, *inter alia*, find applications as optomechanical gyroscopes. On the other hand, the use of Sub-Wavelength Grating (SWG) structures as photonic waveguides is already known, but has not yet been considered in the context of cavity optomechanics. Among other applications, they allow to replicate electrical accelerometers combs, but with a purely optical operation.

The manuscript is organized around three main parts, each one being shared between several chapters.

The first part aims at providing the necessary theoretical elements for the understanding of the discussion. In a first chapter, we present the semi-classical theory of cavity optomechanics, in the generic case of a Fabry-Perot cavity harboring a moving back-end mirror. As we will see, this simple configuration already allows to introduce most important effects associated to cavity optomechanics. In a second chapter, we briefly present the theory associated to silicon photonic waveguides and introduce the notion of guided optical mode. Finally, in a third chapter, we bring these two worlds together and consider integrated silicon optomechanics. We show that due to the confined nature of light in a dielectric medium, new optomechanical schemes and optical forces arise in silicon waveguides.

In the second part, we focus on suspended ring resonators. The first chapter is centered over the theoretical description of suspended ring resonators, while the second chapter deals with practical realization, from fabrication to optical and optomechanical characterizations. In this part, we notably discuss the existence of a possible rotational (or Sagnac) optomechanical interaction, that to date and to the best of our knowledge is specific to this setup.

In the third part, we propose to co-integrate SWG waveguides and on-chip optomechanical devices, as a way to enhance the fundamental optomechanical interaction. We consider two geometries: "ladder-like" SWG waveguides, that are classical SWG waveguides suspended by means of two lateral beams, and SWG interdigitated-combs waveguides, a new kind of SWG waveguide that mimics the principle of electrical combs.

Part I

Silicon cavity optomechanics

CHAPTER I

Classical theory of cavity optomechanics

In this chapter, we present the classical (by opposition to quantum) theory of cavity optomechanics.

On the first section, we present the classical equations of motion that describe the dynamics of the coupled optical and mechanical resonators. Both dispersive and dissipative coupling are considered, respectively meaning that the optical frequency and optical decay rate are modified by mechanical motion. The exact nature of the optomechanical system is voluntarily not discussed, as the presented equations are canonical and can be applied to any optomechanical device.

We next simplify the discussion by considering a Fabry-Perot cavity with a movable back-end mirror, as most interesting properties of optomechanical systems can be derived from this configuration. In particular, we show how the properties of the mechanical resonator are modified by the optical dynamical backaction. Under linear behavior, it leads to a modification of its resonance frequency (optical spring effect) and a modification of its damping rate (optomechanical damping). Under non-linear behavior, it results in optomechanical self-sustained oscillations.

It should be noted that the classical theory of cavity optomechanics is more qualitative than quantitative, and that it notably fails to properly describe the lower limit of optomechanical cooling. A more complete and precise description of cavity optomechanics relies on the quantum theory, and can for example be found in [22]. Yet, the classical picture provides a simple and relatively intuitive description of the canonical optomechanical cavity, that is sufficient in the scope of this work.

I.1 Equations of motion

We begin the discussion from the classical equations describing the complex field amplitude and the mechanical displacement. Only one mechanical and one optical mode are considered, and it is assumed that both a large number of photons N_{ph} and a large number of phonons are present within the cavity, such that the classical picture is legitimate.

On a first section, we introduce the uncoupled equations describing separately the optical and mechanical resonators. Next, we present the coupled equations of motion, in a very general case including both dispersive and dissipative coupling. The calculation of the optical force acting on the back-end mirror is conducted, and we show that it can be separated between a dispersive contribution and a dissipative contribution.

I.1.1 Uncoupled equations of motion

Optical field: When an optical cavity is driven by a laser, the temporal evolution of the complex field amplitude $a(t)$, normalized such that $N_{\mathrm{ph}} = |a(t)|^2$, can be described by [71]:

$$\frac{\mathrm{d}a}{\mathrm{d}t} = \left[i\Delta - \left(\frac{\kappa_i + \kappa_e}{2}\right)\right] a + \sqrt{\kappa_e} s_{in} \tag{I.1}$$

where $\Delta = \omega_L - \omega_0$ represents the detuning of the laser angular frequency ω_L with respect to the cavity angular resonant frequency ω_0. κ_i represents the intrinsic cavity decay rate, and κ_e describes the power coupled to outgoing optical modes (the total cavity decay rate is $\kappa = \kappa_i + \kappa_e$). Finally, $|s_{in}|^2$ is the incident photons flux, such that $P_{in} = \hbar\omega_L |s_{in}|^2$ is the input power launched into the cavity.

Mechanical displacement: Very generally speaking, the mechanical resonator can be described as a damped harmonic oscillator [72], such that its motion $x(t)$ reads:

$$\frac{\mathrm{d}^2 x}{\mathrm{d}t^2} + \Gamma_m \frac{\mathrm{d}x}{\mathrm{d}t} + \Omega_m^2 (x - x_0) = \frac{F_{\mathrm{ext}}(t)}{m_{\mathrm{eff}}} \tag{I.2}$$

with Ω_m the frequency of harmonic oscillation, Γ_m the mechanical damping rate, and m_{eff} the effective mass. $F_{\mathrm{ext}}(t)$ represents the sum of all forces acting on the resonator, generally including a random Langevin force induced by thermal fluctuation $F_L(t)$.

We introduced an effective mass in the previous equation. Strictly speaking, this notion is only defined in the case of multiple modes of vibration of a mechanical resonator, as the mass that a given mode of vibration would have as a spring-mass system (in other words, this is a way to take into account that only a portion of the matter participates

to the vibration). In the case discussed here, the effective mass and the total mass are equal. We use this notation for consistency with the other parts of the manuscript.

I.1.2 Coupled equations of motion

When we consider an optomechanical system, equations (I.1) and (I.2) are modified due to the optomechanical interaction. In the most general case, both the detuning Δ (dispersive coupling) and the cavity decay rate κ (dissipative coupling) become functions of the mechanical displacement in equation (I.1). The forces acting on the resonator include a term $F_{\text{opt}}(a)$ representing optical forces in equation (I.2).

Under optomechanical interaction, the equations of motion form a coupled system:

$$\begin{cases} \dfrac{\mathrm{d}a}{\mathrm{d}t} = \left[i\Delta(x) - \left(\dfrac{\kappa_i(x) + \kappa_e(x)}{2} \right) \right] a + \sqrt{\kappa_e(x)} s_{in} \\ \dfrac{\mathrm{d}^2 x}{\mathrm{d}t^2} + \Gamma_m \dfrac{\mathrm{d}x}{\mathrm{d}t} + \Omega_m^2 (x - x_0) = \dfrac{F_{\text{opt}}(a)}{m_{\text{eff}}} + \dfrac{F_L(t)}{m_{\text{eff}}} \end{cases} \tag{I.3}$$

Note that here, we consider a case where both the intrinsic and extrinsic cavity decay rate are modified with mechanical motion. In many dissipative systems, as κ_i represents pure optical losses and κ_e represents coupling between the resonator and the input and output fields, only the latter is modified: $\kappa(x) = \kappa_i + \kappa_e(x)$.

Optomechanical coupling rate

We introduce the dispersive optomechanical coupling rate[1] g_{om}, and the dissipative optomechanical coupling rate κ_{om}, defined as:

$$g_{\text{om}} = \frac{\partial \omega_0}{\partial x} \quad , \quad \kappa_{\text{om}} = \frac{\partial \kappa_e}{\partial x} \tag{I.4}$$

These two quantities are a measure of the strength of the dispersive and dissipative interactions, as they represent by how much the optical frequency and decay rate are modified under mechanical motion. We point out, however, that they are not a figure of merit for optomechanical resonators, as their magnitude depends on the definition of the displacement, that is somehow arbitrary ; for example, rescaling x to αx implies to rescale g_{om} to g_{om}/α. In other words, g_{om} and κ_{om} can not be used to compare two different optomechanical systems. A true figure of merit of optomechanical resonators, derived from them, is introduced in the following.

[1] Also referred as "frequency pull-parameter" in the literature

From g_{om} and κ_{om}, $\Delta(x)$ and $\kappa(x)$ are expanded to:

$$\Delta(x) = \Delta + g_{\mathrm{om}}x + ... \quad , \quad \kappa(x) = \kappa + \kappa_{\mathrm{om}}x + ... \tag{I.5}$$

Optical force

In order to calculate the optical force, we follow the results obtained with the Response Theory of Optical Forces (RTOF) proposed in [73]. RTOF proposes to calculate analytically the optical forces acting on an *open* optomechanical system, *i.e.* an optomechanical system that exchanges electromagnetic energy with the environment through input and output ports. This is an important point, as most authors tend to lead the calculation of the optical force considering a closed system with a constant number of photons within the cavity, which has proven to be accurate in a dispersive coupling, but fails in a dissipative one [73, 74, 75].

RTOF relies on optical energy and photon-number conservation arguments. In an open optomechanical system with a unique mechanical degree of freedom x, the optical force reads [73]:

$$F_{\mathrm{opt}} = \Phi\hbar\frac{\mathrm{d}\phi(x)}{\mathrm{d}x} \tag{I.6}$$

where $\Phi = P_{in}/\hbar\omega_L$ is the incident photon flux and ϕ is the phase shift that an incident wave experiences through the system at steady-state.

From equation (I.3), the steady-state solutions are of the form $\mathrm{C} \times \Big(\kappa(x)/2 + i\Delta(x)\Big)$ with C a constant, such that $\phi(x)$ reads:

$$\phi(x) = \arctan\left(\frac{2\Delta(x)}{\kappa(x)}\right) \tag{I.7}$$

We can then calculate the optical force:

$$F_{\mathrm{opt}} = -\frac{P_{in}}{\omega_L}\frac{2}{\kappa^2(x) + 4\Delta^2(x)}\Big[g_{\mathrm{om}}\kappa(x) + \kappa_{\mathrm{om}}\Delta(x)\Big] \tag{I.8}$$

$$= -\frac{P_{in}g_{\mathrm{om}}}{\omega_L}\frac{2\kappa(x)}{\kappa^2(x) + 4\Delta^2(x)} - \frac{P_{in}\kappa_{\mathrm{om}}}{\omega_L}\frac{2\Delta(x)}{\kappa^2(x) + 4\Delta^2(x)} \tag{I.9}$$

$$= \underbrace{-\frac{1}{2}\hbar g_{\mathrm{om}}\frac{\kappa(x)}{\kappa_e(x)}|a(t)|^2}_{F_{\mathrm{disp}}}\underbrace{-\frac{1}{2}\hbar\kappa_{\mathrm{om}}\frac{\Delta(x)}{\kappa_e(x)}|a(t)|^2}_{F_{\mathrm{diss}}} \tag{I.10}$$

The total optical force is hence the sum of a contribution from the dispersive coupling, and a contribution from the dissipative coupling. As κ is the optical cavity decay rate

and Δ is the detuning from resonance, these two values will typically have the same order of magnitude. Thus, the relative strength of the dispersive and dissipative forces will be dictated by the relative strength of g_{om} and κ_{om}. Their respective magnitude strongly depends on the size and nature of the considered optomechanical device, and purely dispersive, purely dissipative or mixed schemes can be engineered [74, 75].

To date, most optomechanical systems evolve in a purely dispersive scheme[2], such that the dissipative force is null. However, the introduction of a dissipative scheme present interesting benefits for optomechanical applications [75] ; notably, ground state cooling should be possible for any value of the sideband suppression factor κ/Ω_m, while it requires $\kappa \gg \Omega_m$ with a purely dispersive scheme.

As a final remark, we note that under the critical coupling condition ($\kappa_e = \kappa/2$), the dispersive force takes the "usual" form found in the literature: $F_{\text{disp}} = -\hbar g_{\text{om}}|a(t)|^2$.

Summary

Based on equations I.3, (I.4) and I.10, we obtain the equations of motion describing a generic optomechanical system, with both dispersive and dissipative coupling:

$$\begin{cases} \dfrac{\mathrm{d}a}{\mathrm{d}t} = \left[i\left(\Delta + g_{\text{om}}x\right) - \left(\dfrac{\kappa + \kappa_{\text{om}}x}{2}\right)\right] a + \sqrt{\kappa_e + \kappa_{\text{om}}x}\, s_{in} \\ \dfrac{\mathrm{d}^2x}{\mathrm{d}t^2} + \Gamma_m \dfrac{\mathrm{d}x}{\mathrm{d}t} + \Omega_m^2(x - x_0) = -\dfrac{\hbar g_{\text{om}}}{2m_{\text{eff}}}\dfrac{\kappa(x)}{\kappa_e(x)}|a(t)|^2 - \dfrac{\hbar\kappa_{\text{om}}}{2m_{\text{eff}}}\dfrac{\Delta(x)}{\kappa_e(x)}|a(t)|^2 + \dfrac{F_L(t)}{m_{\text{eff}}} \end{cases} \tag{I.11}$$

I.1.3 "Normalization" of the optomechanical coupling rates

As already pointed out, the definition of the optomechanical coupling rates g_{om} and κ_{om} depends on the mechanical displacement x, that is not always well defined and may be arbitrary chosen (as a way to ease calculations). This is ambiguous, as different definitions of x can significantly change the magnitude of the coupling rates.

A true, unambiguous figure of merit for optomechanical resonators is the vacuum optomechanical coupling rate (or single photon-phonon optomechanical coupling rate), that is defined as the product of the optomechanical coupling rate by the magnitude x_{ZPF} of the Zero Point Fluctuations (ZPF) of the mechanical oscillator [76]:

$$g_0 = g_{\text{om}} \times x_{\text{ZPF}} \quad , \quad \kappa_0 = \kappa_{\text{om}} \times x_{\text{ZPF}} \tag{I.12}$$

[2]For many quantum applications, it is detrimental to have optical losses

As it names implies, x_{ZPF} represents the non-zero mechanical fluctuations when the point of zero energy of the oscillator is reached. In other words, this is the minimum achievable displacement for a given mechanical mode. It is defined as:

$$x_{\mathrm{ZPF}} = \sqrt{\frac{\hbar}{2m_{\mathrm{eff}}\Omega_m}} \tag{I.13}$$

I.2 Fabry-Perot cavity with a moving back-end mirror

We now restrict the discussion to the generic optomechanical setup: a Fabry-Perot cavity with a moving back-end mirror, as depicted on figure 1. The optical resonator is a Fabry-Perot cavity whose length and optical properties are modulated by the mechanical motion of the back-end mirror, that is in turn modulated by radiation pressure. The coupling is purely dispersive, so that we set $\kappa_{\mathrm{om}} = 0$, and the dynamics of the optical and mechanical resonators are described by:

$$\begin{cases} \dfrac{\mathrm{d}a}{\mathrm{d}t} = \left[i\left(\Delta - g_{\mathrm{om}}x\right) - \dfrac{\kappa}{2} \right] a + \sqrt{\kappa_e} s_{in} \\ \\ \dfrac{\mathrm{d}^2x}{\mathrm{d}t^2} + \Gamma_m \dfrac{\mathrm{d}x}{\mathrm{d}t} + \Omega_m^2(x - x_0) = -\dfrac{\hbar g_{\mathrm{om}}}{m_{\mathrm{eff}}}|a(t)|^2 + \dfrac{F_L(t)}{m_{\mathrm{eff}}} \end{cases} \tag{I.14}$$

Here, we used the form usually found in the literature for the optical force. While it relies on some assumptions (notably critical coupling, see paragraph I.1.2), it has already proven to be an extremely good approximation when comparing theoretical and experimental results.

In the case of a Fabry-Perot cavity, the mechanical displacement corresponds to the variations of the cavity length L, and one easily finds that $g_{\mathrm{om}} = \omega_0/L$. From this formula and from the definition of g_0, it is already evident that smaller cavities will lead to increased optomechanical interactions.

When solving this system in a linear regime, we will show that the properties of the mechanical oscillator are transformed as a result of the optomechanical interaction. Its resonance frequency is shifted, which is known as the optical spring effect, and its damping rate is modified, which is known as optomechanical damping or amplification.

In a non-linear regime, the system resolution reveals the appearance of optomechanical self-sustained oscillations, beyond a certain optical power threshold.

Steady state solutions and static multi-stability: Prior to the discussion, we first consider the static equilibrium position (by setting the temporal derivatives to zero).

Resolution leads to a cubic equation on the steady state mirror position $\bar{x}$, as a function of the input power:

$$-\hbar g_{\mathrm{om}} \kappa_e |s_{in}|^2 = \left(m_{\mathrm{eff}} \Omega_m^2 \bar{x} - \bar{F}_L \right) \left(\left(\frac{\kappa}{2} \right)^2 + (\Delta - g_{\mathrm{om}} \bar{x})^2 \right) \tag{I.15}$$

For a given set of input intensity $|s_{in}|^2$ and detuning Δ, this equation admits more than one unique solution. In other words, there are multiple equilibrium positions. This is known as static bistability, and was first observed under the form of bistability using harmonically suspended mirrors [77].

For a steady state solution $\bar{x}$ of the mechanical displacement, the optical field is:

$$\bar{a} = \frac{\sqrt{\kappa_e} s_{in}}{\kappa/2 - i\left(\Delta - g_{\mathrm{om}} \bar{x}\right)} \tag{I.16}$$

Steady-state behavior is hence described by a set of two coupled equations: equation (I.15) and equation (I.16).

I.2.1 Optical spring effect & optomechanical damping

When only small fluctuations of the amplitude field and mechanical motion occur, one can linearize the problem around its steady state solutions:

$$a(t) = \bar{a} + \delta a(t) \quad , \quad x(t) = \bar{x} + \delta x(t) \tag{I.17}$$

After linearization, the coupled equations of motion read:

$$\begin{cases} \dfrac{\mathrm{d}\delta a}{\mathrm{d}t} = \left[i\bar{\Delta} - \dfrac{\kappa}{2} \right] \delta a - i g_{\mathrm{om}} \bar{a} \delta x \\ \dfrac{\mathrm{d}^2 \delta x}{\mathrm{d}t^2} + \Gamma_m \dfrac{\mathrm{d}\delta x}{\mathrm{d}t} + \Omega_m^2 \delta x = -\dfrac{\hbar g_{\mathrm{om}}}{m_{\mathrm{eff}}} (\bar{a}^* \delta a + \bar{a} \delta a^*) + \dfrac{F_L(t)}{m_{\mathrm{eff}}} \end{cases} \tag{I.18}$$

where we have introduced the effective detuning $\bar{\Delta} = \Delta - g_{\mathrm{om}} \bar{x}$, representing the static modification of the detuning due to radiation pressure, and have dropped the non-linear terms.

The system (I.18) is solved in Fourier space. We choose to define the Fourier transform of $f(t)$ as:

$$f(\omega) = \int f(t) e^{-i\omega t} dt \tag{I.19}$$

All calculations considered, we obtain:

$$\begin{cases} \delta a(\omega) = \dfrac{i g_{\mathrm{om}} \bar{a}}{i\left(\bar{\Delta} + \omega\right) - \kappa/2} \delta x(\omega) \\ \\ \delta x(\omega) = \dfrac{F_L(\omega)}{m_{\mathrm{eff}}\left(\Omega_m^2 - \omega^2 - i\Gamma_m \omega\right) + \Sigma(\omega)} \end{cases} \tag{I.20}$$

$\Sigma(\omega)$ is referred as the "optomechanical self-energy" and contains all the terms related to the optomechanical interaction. It reads:

$$\Sigma(\omega) = 2 m_{\mathrm{eff}} \Omega_m g_0^2 |\bar{a}|^2 \left(\frac{1}{i\kappa/2 + \left(\bar{\Delta} + \omega\right)} - \frac{1}{i\kappa/2 - \left(\bar{\Delta} - \omega\right)} \right) \tag{I.21}$$

where g_0 is the vacuum optomechanical coupling rate.

$\Sigma(\omega)$ describes how the linear mechanical response is modified by the optomechanical interaction. More precisely, the real part of $\Sigma(\omega)$ describes a shift in mechanical frequency (optical spring effect), and its imaginary part describes a change in mechanical damping (optomechanical damping).

Optical spring effect

Observation of equation (I.20) reveals that the real part of $\Sigma(\omega)$ can be interpreted as a change in the mechanical frequency of the resonator, by an amount:

$$\delta\Omega_m(\omega) = \frac{1}{2\omega m_{\mathrm{eff}}} \mathrm{Re}\left[\Sigma(\omega)\right] \tag{I.22}$$

$$= \frac{\Omega_m}{\omega} g_0^2 |\bar{a}|^2 \left(\frac{\bar{\Delta} + \omega}{(\kappa/2)^2 + \left(\bar{\Delta} + \omega\right)^2} + \frac{\bar{\Delta} - \omega}{(\kappa/2)^2 + \left(\bar{\Delta} - \omega\right)^2} \right) \tag{I.23}$$

where we used $\delta\Omega_m^2(\omega) \approx 2\omega\delta\Omega_m(\omega)$.

This modification of the mechanical frequency due to the optical field is known as the optical spring effect. Considering experimental parameters, $\delta\Omega_m$ is a function of the optical effective detuning $\bar{\Delta}$, and of the average number of photons within the cavity $|\bar{a}|^2$. In other words, it can be changed by modifying the input laser angular frequency ω_L or power $P_{in} = \hbar\omega_L |s_{in}|^2$.

The optical spring effect, normalized by the optomechanical coupling rate and the photon number, is presented on figure I.1, on both a resolved sideband regime ($\kappa < \Omega_m$) and an

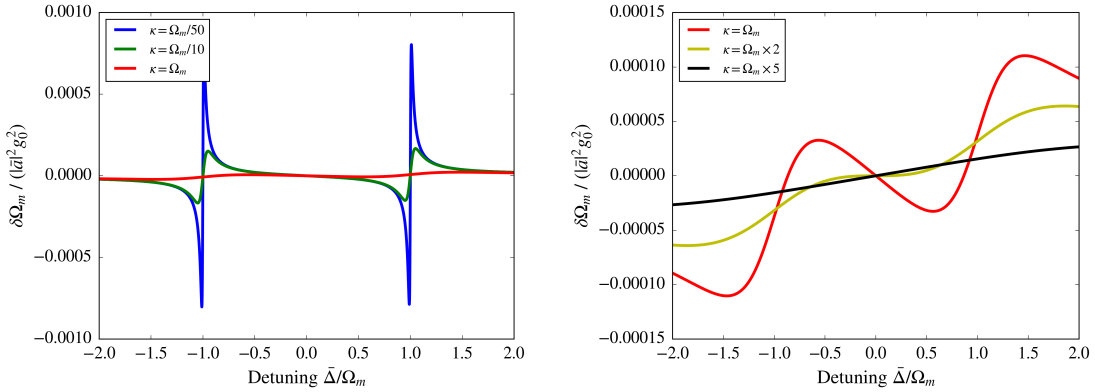

(a) Resolved sideband

(b) Unresolved sideband

Figure I.1 – Illustration of the (normalized) optical spring effect in a resolved sideband regime and in an unresolved sideband regime, at $\omega = \Omega_m$. Note that the scales differ by almost a factor 10, illustrating the fact that backaction effects are more pronounced under resolved sideband.

unresolved sideband regime ($\kappa > \Omega_m$). We arbitrarily chose $\omega = \Omega_m = 10$ kHz, which only modifies the scale of the curves.

From these curves, the first remark is that the two scales differ by almost a factor 10, indicating a more pronounced optical spring effect under resolved sideband. It is also evident that the behavior is different between each regime. In the resolved sideband regime, two opposed peaks appear around $\bar{\Delta} = \pm\Omega_m$ with an abrupt sign change, and dominate the dynamic. In the unresolved sideband, the transition is smooth and the positions of zero, maximum and minimum optical spring are no longer fixed.

Optomechanical damping

Similarly, the imaginary part of $\Sigma(\omega)$ is interpreted as a change in the mechanical damping, by an amount:

$$\Gamma_{\text{opt}} = -\frac{1}{\omega m_{\text{eff}}}\text{Im}\Big[\Sigma(\omega)\Big] \tag{I.24}$$

$$= \frac{\Omega_m}{\omega} g_0^2 |\bar{a}|^2 \left(\frac{\kappa}{(\kappa/2)^2 + \left(\bar{\Delta} + \omega\right)^2} - \frac{\kappa}{(\kappa/2)^2 + \left(\bar{\Delta} - \omega\right)^2} \right) \tag{I.25}$$

Note that the optomechanical damping rate Γ_{opt} is also a function of the optical effective detuning $\bar{\Delta}$, and of the average number of photons within the cavity $|\bar{a}|^2$. Notably,

depending on the value of the detuning, Γ_{opt} can be either positive or negative, hence respectively increasing or reducing the initial mechanical damping. This is known as optomechanical damping.

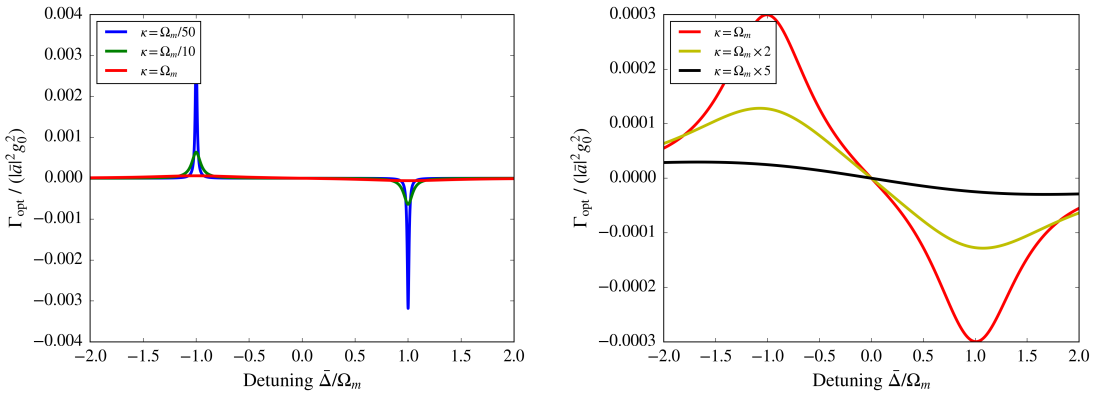

(a) Resolved sideband

(b) Unresolved sideband

Figure I.2 – Illustration of the (normalized) optomechanical damping in a resolved sideband regime and in an unresolved sideband regime, at $\omega = \Omega_m$. Here again, the scales largely differ.

The normalized optomechanical damping is illustrated on figure I.2, on both a resolved sideband regime ($\kappa < \Omega_m$) and an unresolved sideband regime ($\kappa > \Omega_m$). We arbitrarily set the scale by choosing $\omega = \Omega_m = 10$ kHz.

From the difference between the scales in the resolved sideband and unresolved sideband, one easily obtain that effective cooling or damping will only occur in the first case, around $\bar{\Delta} = \pm\Omega_m$. In accordance with the lateral sideband picture presented above (see figure 7), cooling occurs under red detuning ($\bar{\Delta} < 0$), and heating occurs under blue detuning ($\bar{\Delta} > 0$).

We point out that this semi-classical approach fails to properly describe optical cooling at really low temperature, and that a quantum description is necessary in this case. Indeed, below a certain point, the random fluctuations of radiation pressure due to photon shot noise set a lower limit to the achievable temperature [22]. This is known as quantum backaction, by opposition to the classical backaction that we consider here.

I.2.2 Optomechanical self-induced oscillations

In the blue-detuned regime, Γ_{opt} is negative and the mechanical motion is amplified by dynamical backaction. From equation (I.25), the magnitude of the heating scales with the incident laser power. If we define an effective mechanical damping $\Gamma_{\text{eff}} = \Gamma_m + \Gamma_{\text{opt}}$, there is a point where the effective mechanical damping vanishes. Beyond this threshold, any small mechanical fluctuation (*e.g.* thermal fluctuation) becomes regenerative and harbor a non-linear behavior: the fluctuation amplitude is first exponentially increased, up to

a saturation point. The intra-cavity field is then described by a set of Bessel functions, which is described in [22, 78, 79, 80]

This behavior is known as optomechanical self-oscillations, or parametric instability. Practically speaking, it enables to generate self-sustained oscillations by means of a continuous laser source, and forms the basis of on-chip NOMS devices [55, 13]. In this regard, determining the threshold value is important as it defines the functioning point of the devices.

Interestingly, while optomechanical self-oscillations induced by radiation pressure were theoretically predicted in the context of large-scale Fabry-Perot interferometers [43], they were first observed in micro-toroids optomechanical cavities [13]. As we will show in the following, this is mainly due to the strong dependence of the optical threshold power on the inverse square of the optomechanical vacuum coupling rate, that is largely enhanced in micro and nano-systems.

Threshold of optomechanically induced self-oscillations

While the previous linear picture fails to describe the non-linear dynamics of self-sustained optomechanical oscillators, it can advantageously be used to find the threshold point, simply defined by:

$$\Gamma_m + \Gamma_{\text{opt}} = 0 \tag{I.26}$$

Before reaching this point, the linear description still prevails, and we can use equation I.25 to describe Γ_{opt}. For a given effective detuning $\bar{\Delta}$, the value of the threshold in terms of optical power is:

$$P_{thr} = \hbar\omega_L \frac{\Gamma_m}{g_0^2} \left(\frac{1}{(\kappa/2)^2 + \left(\bar{\Delta} - \Omega_m\right)^2} - \frac{1}{(\kappa/2)^2 + \left(\bar{\Delta} + \Omega_m\right)^2} \right)^{-1} \tag{I.27}$$

Note that this expression corresponds to the optical power within the cavity. It can be linked to the (experimentally accessible) input optical power by:

$$P_{cav} = \frac{\kappa\kappa_e}{(\kappa/2)^2 + \bar{\Delta}^2} \times P_{in} \tag{I.28}$$

If we use $g_{\text{om}} = \omega_0/L$ and the respective definitions of g_0 and x_{ZPF}, we find that the optical threshold power scale with:

$$P_{thr} \propto L^2 \Omega_m m_{\text{eff}} \tag{I.29}$$

As most optomechanical figures, the threshold is hence strongly reduced under size reduction.

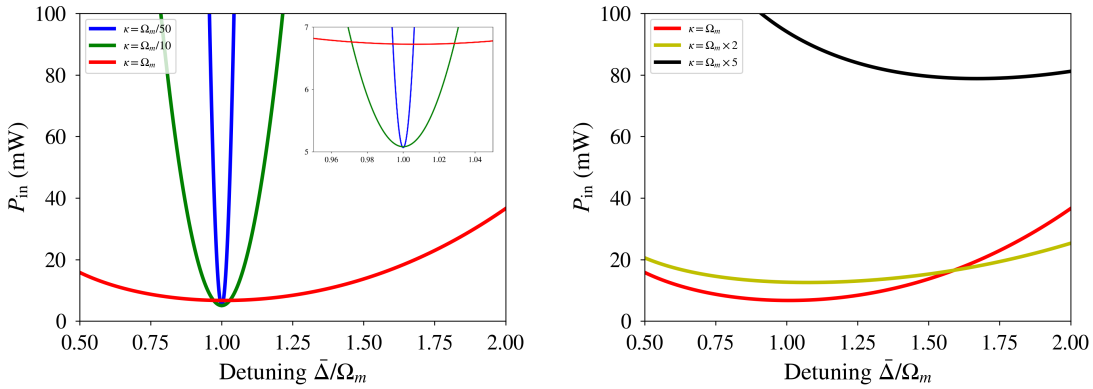

(a) Resolved sideband

(b) Unresolved sideband

Figure I.3 – Optical power threshold, on the input laser, for the observation of optomechanical self-oscillations.

The value of the optical power threshold for the observation of optomechanical self-oscillations is presented on figure I.3, on both a resolved sideband regime ($\kappa < \Omega_m$) and an unresolved sideband regime ($\kappa > \Omega_m$). We used realistic parameters based on our experimental results: $\lambda = 1550$ nm, $Q_m = 1000$, $\Omega_m = 10^6$ Hz. We considered a conservative vacuum optomechanical coupling rate of $g_0 = 1$ Hz.

Again, we observe the resolved sideband regime to be more favorable that the unresolved one. The laser power threshold is around 5 mW in the first case, but rapidly exceeds 20 mW in the second case (and even more as the ratio κ/Ω_m is deteriorated). In practical applications, our lasers are limited to a 20 mW power, such that we must aim for at least $\kappa \equiv \Omega_m$. It is not necessary, however, to be in a "really good" resolved sideband regime (*i.e.* $\kappa \ll \Omega_m$), as we observe that the minimal power does not vary much in this regime.

Conclusion

In this first chapter, we have presented the classical theory of cavity optomechanics. After introducing the general form of the equations of motion describing the coupling between one optical mode and one optical mode, we restricted the discussion to a Fabry-Perot cavity with a movable back-end mirror. From this setup, we introduced the optical spring effect, optomechanical damping, and optomechanical self-induced oscillations.

Several assumptions have been made along the analysis.

First, we only considered one optical mode and one mechanical mode. For optical modes, this is justified by the fact that only one mode is excited resonantly by the sharp laser drive. Regarding the mechanical modes, they are usually well separated in the RF spectrum, and we will generally work only around one of those resonances through filtering operations. Nevertheless, there are scenarios where this simple assumption does not stand, for example

when the spacing between two optical modes matches the mechanical frequency, or when the dynamics become non-linear.

Second, we considered only the linear terms in the optomechanical interaction. Generally speaking, the quadratic terms can no longer be "safely" omitted when $g_0 > \kappa$ [22]. In the scope of this thesis, κ is typically in the MHz range and g_0 in the kHz range, such that this approximation remains correct.

The free-space Fabry-Perot optomechanical cavity that we treated in this chapter is a canonical setup, and every optomechanical cavity can be treated by analogy to this case. The integrated silicon microcavities developed during this thesis work are no exception, and can be described by the same equations, with little adaptation. This is presented in the third chapter. Before that, we introduce theoretical elements on silicon photonics in the second chapter, that will then be used to describe the silicon optomechanical cavities.

CHAPTER II

Integrated silicon photonics

In this chapter, we introduce the notion of integrated photonics and present the general properties of silicon waveguides.

First, the principle of optical guiding is exposed through the analytical example of a symmetric planar waveguide. Important notions such as the effective index and the guided mode profile, as well as the mode polarization, are discussed. Next, the description of a directional coupler by means of coupled mode theory is given. Finally, the main sources of optical losses in photonic waveguides are introduced.

All along the chapter, the discussion is focused around silicon photonics. However, many of the results are applicable to other materials.

II.1 Introduction: from guided optics to silicon photonics

By opposition to traditional free-space optics, where light is manipulated and transmitted in free-space (air, vacuum, water), guided optics confines light in a dielectric medium surrounded by a second dielectric medium of smaller refractive index. By principle of total internal reflection, it is possible to "trap" and guide the light inside the first dielectric medium. This is the principle of optical fibers, that were developed in the seventies with the growth of telecommunication and the need for always faster information transfer rate, over long distances. Single mode optical fibers gradually replaced electrical transmission, due to really low propagation losses, insensitivity to electromagnetic noise, and high data carrying capacity.

In parallel to the development of optical fiber telecommunications, integrated optics, or

photonics, was thought as a way to realize signal processing operations at the end of optical fibers with optical circuits and components instead of electronic ones [81]. Integrated photonic circuits allow to realize many functions such as wavelength multiplexing and filtering, optical modulation, optoelectronic conversion, and signal splitting. They can also be used as a transduction platform for inertial sensors, gas sensors and bio sensors.

Numerous dielectric media are suited for the realization of integrated optical circuits, such as silica, glass, silicon, silicon nitride, III-V materials, and more [82]. Among them, silicon has proven to be a promising integration platform for photonic applications in the last decade. This success mainly resides in the double advantage of its interesting intrinsic optical properties (notably transparency at telecom wavelength and high index contrast) and its compatibility with CMOS fabrication technology, developed by the microelectronic industry for more than 20 years. Silicon photonic circuits also benefits from a footprint, enabling high density integration and reduced fabrication costs. Finally, due to its electrical properties, silicon is naturally perfectly suited for the perspective of realizing integrated active photonic devices such as modulators, photodetectors or reported/hybrid light sources.

II.2 Principle of optical guiding

II.2.1 Introduction

Generally speaking, a dielectric waveguide is constituted of a core, of refractive index n_1, and of a cladding, of refractive index $n_2 < n_1$. The dielectric waveguide is invariant along an axis (referred as z in this manuscript), named direction of propagation. In the most generic case, the core cross section is of arbitrary shape (see figure II.1). In the case of optical fibers, the cross section is circular. In the case of photonic waveguides, the cross section is often rectangular, but not exclusively.

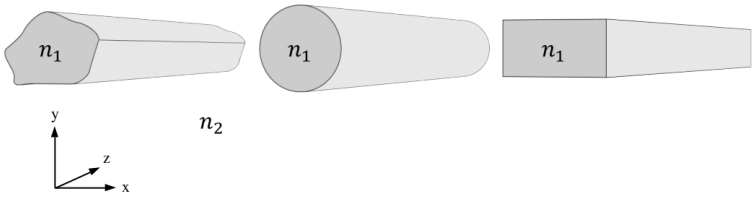

Figure II.1 – Schematic of a dielectric waveguide. From left to right: general arbitrary case, step-index circular optical fiber, and step-index strip photonic waveguide. Note that in the very general case, the core refractive index is function of the spatial coordinates: $n_1(x, y)$.

Propagation of light in a dielectric waveguide is described in a modal way ; this means that multiple waves of invariant field profile along the direction of propagation can propagate

in the waveguide, with a propagation constant β. In most waveguides, the guided mode is obtained by numerical simulation. However, an analytical resolution is possible in some particular cases, such as optical fibers and symmetric planar waveguides. This last geometry, treated in the next section, allows to introduce the main properties of dielectric waveguides.

II.2.2 Propagation along a symmetric planar waveguide

We consider the case of a symmetric planar waveguide, represented on figure II.2. A dielectric core layer of refractive index n_1 and width d is sandwiched between two infinite dielectric layers of refractive index $n_2 < n_1$. The geometry is invariant along the x and z directions.

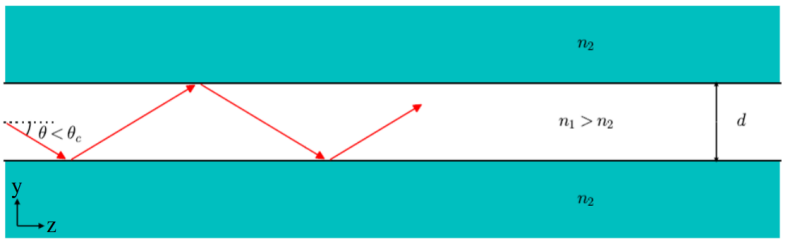

Figure II.2 – Principle of optical guiding along a symmetric planar waveguide, based on geometrical optics.

Preliminary: Geometrical optics The most intuitive way to understand and describe propagation in the symmetric planar waveguide relies on geometrical optics and Snell-Descartes law. At the entrance of the waveguide, when light is injected in the core layer with an angle[1] inferior to the critical angle $\theta_c = \arcsin n_2/n_1$, it is totally reflected at the interface between the two dielectrics and remains confined in the core (figure II.2). By successive total internal reflections, it is hence possible to guide the light along the direction of propagation of the waveguide, with theoretically no losses.

Electromagnetic theory The behavior of light in a dielectric medium is more precisely described with electromagnetic theory and Maxwell's equations [83, 71]. In the case of a monochromatic wave at pulsation ω, a guided mode can be written under the form:

$$\overrightarrow{E} = \overrightarrow{E}(x,y)\, e^{i(\beta z - \omega t)} \tag{II.1}$$

$$\overrightarrow{H} = \overrightarrow{H}(x,y)\, e^{i(\beta z - \omega t)} \tag{II.2}$$

where β is the propagation constant and z is the direction of propagation.

[1] relative to the normal

TE polarization and TM polarization Based on Maxwell's equations, it is possible to show that any guided mode can be described as a linear combination of two orthogonal sets of solutions, referred as Transverse Electric (TE) and Transverse Magnetic (TM).

In the TE case, the field reduces to only three components: E_x, H_y and H_z. The electrical field is parallel to the plane of propagation, and the magnetic field is perpendicular.

In the TM case, the field reduces to H_x, E_y and E_z, the electrical field is perpendicular to the plane of propagation, while the magnetic field is parallel.

Dispersion equation of guided modes In order to maintain light propagation, there must be constructive interference between the different optical paths followed by the wave. Based on this argument, one shows that in the case of the symmetric planar waveguide, β is solution of [83, 71]:

$$d\sqrt{k^2 n_1^2 - \beta_m^2} - 2\arctan\left(p\frac{\sqrt{\beta_m^2 - k^2 n_2^2}}{\sqrt{k^2 n_1^2 - \beta_m^2}}\right) = m\,\pi, \quad \text{with} m = 0, 1, 2, 3, ... \tag{II.3}$$

where $k = 2\pi/\lambda$ is the wavenumber, $p = 1$ for a TE polarization, and $p = (n_1/n_2)^2$ for a TM polarization.

Equation (II.3) is the characteristic equation of guided modes. It shows that optical propagation is possible only for discrete values of the propagation constant β, whose associated waves are called guided modes. Alternatively, it is usual to describe the propagation in terms of an effective guided index, instead of the propagation constant. This two quantities are linked by: $\beta = k n_{\text{eff}}$.

It is possible to show that a guided mode exists only if its effective index is included between n_1 and n_2, and the number of guided modes is hence dependent on the width d of the waveguide. When the waveguide is small enough such that only the fundamental mode exists ($m = 0$), it is said to be single mode. On figure II.3, we represented the evolution of the first effective indexes of a Si/SiO2 symmetric planar waveguide as a function of its width, in both the TE and TM cases.

Guided mode profile The guided mode profile is calculated based on Helmohtlz equation. In the case of TE polarization, it reads:

$$\left(\frac{\partial^2}{\partial y^2} + \left(k^2 - \beta_m^2\right)\right) E_x(y) = 0 \tag{II.4}$$

Helmohtlz equation is solved separately inside and outside of the waveguide, and the solutions are matched by considering electromagnetic boundary conditions.

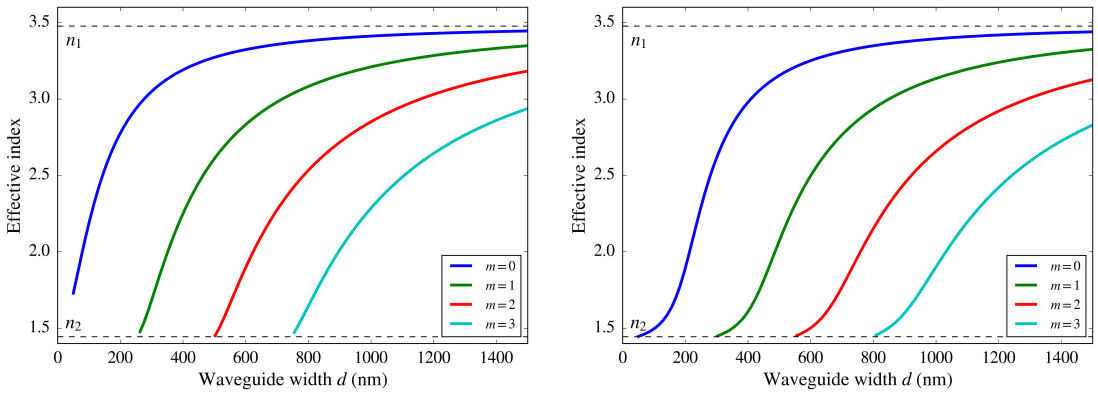

(a) TE polarization

(b) TM polarization

Figure II.3 – Effective index as a function of the width of a Si/SiO2 symmetric planar waveguide, for TE and TM polarizations.

Outside the waveguide ($|y| > d/2$), the guided mode profile has the form:

$$E_x(y) \propto \exp\left[-\frac{2\pi}{\lambda_0}\sqrt{(n_{\text{eff}}^2 - n_2^2)}\,|y| \right] \tag{II.5}$$

Inside the waveguide ($-d/2 < y < d/2$), it reads:

$$E_x(y) \propto \cos\left[\frac{2\pi}{\lambda_0}\sqrt{(n_1^2 - n_{\text{eff}}^2)}y\right] \qquad \text{if m is even} \tag{II.6}$$

$$E_x(y) \propto \sin\left[\frac{2\pi}{\lambda_0}\sqrt{(n_1^2 - n_{\text{eff}}^2)}y\right] \qquad \text{if m is odd} \tag{II.7}$$

From these equations, it appears that a part of the mode propagates outside of the core. This is the evanescent part of the field, that rapidly vanishes due to its exponential dependence.

Note that equations (II.5), (II.6) and (II.7) describe the same guided mode. Consequently, their respective associated amplitude must verify electromagnetic boundary conditions at the interfaces between the core layer and the substrate.

The first three normalized mode profiles of a symmetric planar waveguide are presented on Figure II.4, under TE and TM polarization. In the second case, due to the electromagnetic boundary conditions, we notice a strong discontinuity of the field at the interfaces between the core and the cladding.

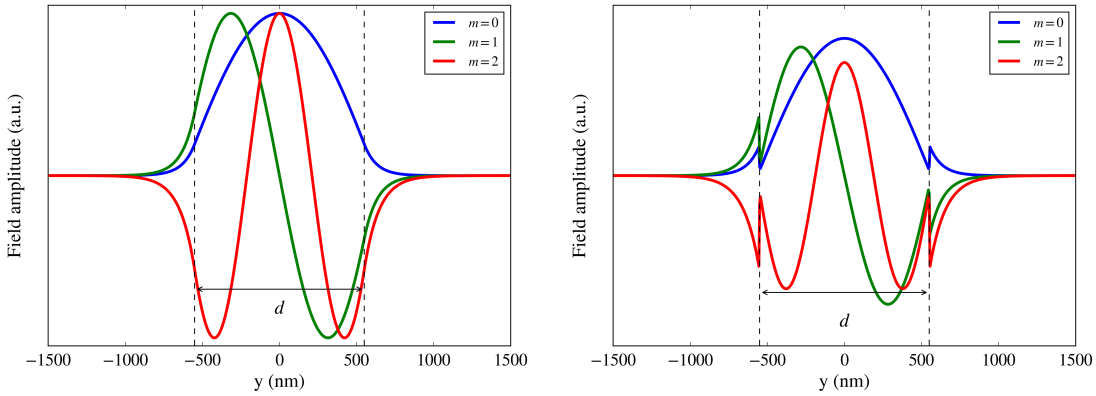

(a) TE polarization, E_x component

(b) TM polarization, E_y component

Figure II.4 – First three normalized mode profiles in a symmetric planar waveguide, for TE and TM polarizations.

II.2.3 Silicon waveguides

In this work, we use rectangular silicon waveguides, either encapsulated in silica or standing in the air. An analytical description of the guided modes in the rectangular silicon waveguides that we used during this thesis is not possible. However, some important notions derived in the case of the symmetric planar waveguide still remains.

The description of light propagation through rectangular dielectric waveguides can be studied based on approximate methods, such as the effective index method [84], or Marcatili's approach [85, 86]. Alternatively (and more generally), the study is conducted by means of numerical mode solvers [87].

Si	SiO2	Air
3.476	1.444	1.0

Table II.1 – Optical indexes at a $\lambda = 1550$ nm wavelength.

Importantly, the major difference is that the field can no longer be distinguished between TE and TM components: for each guided mode, the six components of the field are non-zero and coupled. However, by analogy to the symmetric planar waveguide, it is possible to separate "quasi-TE" and "quasi-TM" modes, where the *major* component of the field is respectively E_x and H_y. It is usual for these modes to be referred as TE and TM modes for the sake of simplicity, and we will follow this trend.

The guided effective index and mode profile of three dimensional rectangular waveguides are obtained by numerical simulations. The mode profile of the TE and TM fundamental modes of a 500 nm x 220 nm silicon waveguide are presented on figure II.6. For the TE

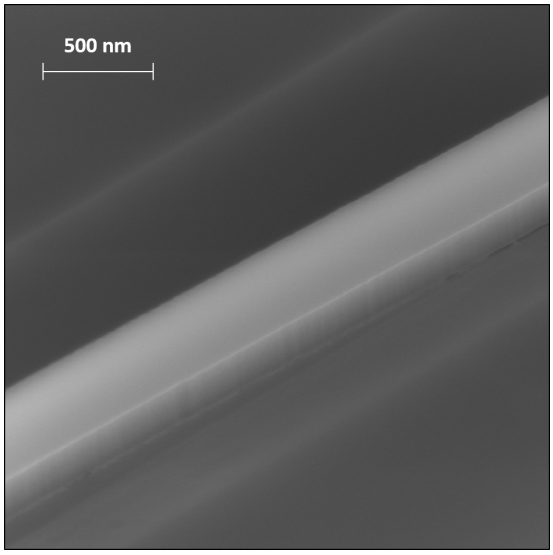

Figure II.5 – SEM image of a silicon waveguide.

polarization, we observe a discontinuity of the major component E_x along the horizontal direction. For the TM polarization, the major component E_y is discontinuous along the vertical direction. Because silicon waveguides exhibit a high index contrast between their core and cladding, there is a strong confinement of the optical field inside of the core for the TE_0 mode. This is less accurate in the case of the TM_0 mode, as a consequence of the shape ratio of the waveguide that favors TE modes.

Chromatic dispersion

A last important point regarding photonic waveguides is chromatic dispersion of light. Photonic waveguides are fundamentally dispersive, and are constituted of dielectric media that also are. As a result, because the laser pulse that are used to generate the guided mode are not purely monochromatic, each wavelength constituting the laser pulse travels at a different speed inside the waveguide. The wave packet tends to broaden and be delayed during propagation, which is taken into account with the group index, representing the velocity of the wave packet:

$$n_g = n_{\text{eff}} - \lambda_0 \frac{\mathrm{d}n_{\text{eff}}}{\mathrm{d}\lambda} \tag{II.8}$$

Locally, dispersion properties in silicon waveguides are linear with a negative slope : $\mathrm{d}n_{\text{eff}}/\mathrm{d}\lambda < 0$. The group index, around 1550 nm, is $n_g = 4.3$.

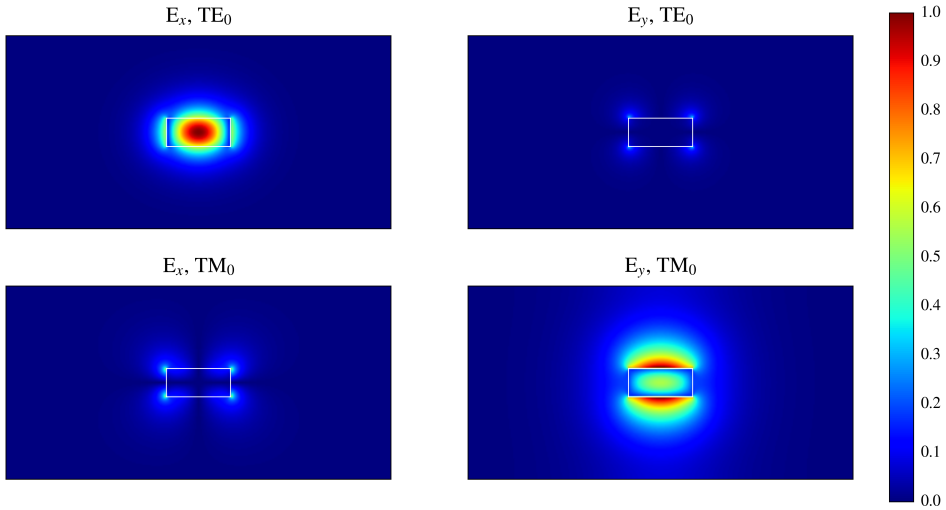

Figure II.6 – E_x and E_y mode profiles of the TE_0 and TM_0 fundamental guided modes. Waveguide cross-section is 500 nm x 220 nm.

II.3 Optical coupling

By bringing two waveguides close together, it is possible to exchange optical power between them. This phenomenon is due to the spatial expansion of the evanescent field, that excite the guided modes of the adjacent waveguide.

This exchange of light is the principle of a directional coupler, a fundamental building block of photonic circuits, that is used in optical filters, ring resonators, optical multiplexers, and others.

The coupling of light between two waveguides can be calculated with a perturbative approach [83, 71, 88]. The total field in the system formed by both waveguides is considered as the superposition of the degenerate field in each separate waveguide:

$$\overrightarrow{E}(x,y,z) = a(z)\overrightarrow{E_a}(x,y)\,e^{i\beta_a z-\omega t} + b(z)\overrightarrow{E_b}(x,y)\,e^{i\beta_b z-\omega t} + ... \tag{II.9}$$

where the additional terms include all the propagation modes of the unperturbed structure. In practice, this equation is approximated (and simplified) by not considering these additional terms.

The two amplitudes obey the following system of equations:

$$\begin{cases} \dfrac{\mathrm{d}a}{\mathrm{d}z} = i\dfrac{\beta_a - \beta_b}{2}a + \kappa_{ab}b \\ \dfrac{\mathrm{d}b}{\mathrm{d}z} = i\dfrac{\beta_b - \beta_a}{2}b + \kappa_{ba}a \end{cases} \tag{II.10}$$

where κ_{ab} and κ_{ba} represents the evanescent coupling strength from one waveguide to the other. Applying perturbation theory [83, 71, 88] (the adjacent waveguide is considered as a small permittivity perturbation of the waveguide), it is possible to show that $\kappa_{ab} = -\kappa_{ba}^*$ and that:

$$\kappa_{ab} = -i\frac{\omega}{4}\iint \Delta\varepsilon \overrightarrow{E}_a \overrightarrow{E}_b^* \mathrm{d}x\mathrm{d}y \tag{II.11}$$

where the integration is conducted over the cross section of waveguide a, $\overrightarrow{E}_a$ (resp. $\overrightarrow{E}_b$) is the normalized guided mode in waveguide a (resp. b), and $\Delta\varepsilon$ represents the relative permittivity perturbation from one guide to the other. Practically speaking, $\Delta\varepsilon$ takes the form of a mask with ε_a (resp. ε_b) on the cross-section of waveguide a (resp. b), and 0 elsewhere.

Solutions of equation (II.10) are of the form:

$$\begin{cases} a(z) = a_0 \cos\left(\sqrt{K+\delta}z\right) + a_1 \sin\left(\sqrt{K+\delta}z\right) \\ b(z) = b_0 \cos\left(\sqrt{K+\delta}z\right) + b_1 \sin\left(\sqrt{K+\delta}z\right) \end{cases} \tag{II.12}$$

where a_0, a_1, b_0 and b_1 are obtained based on initial conditions, and:

$$K = |\kappa_{ab}|^2 \quad , \quad \delta = \left(\frac{\beta_a - \beta_b}{2}\right)^2 \tag{II.13}$$

From equations (II.12), we obtain the optical power in each waveguide as a function of the propagation distance z:

$$\begin{cases} P_a(z) = 1 - F\sin^2(Sz) \\ P_b(z) = F\sin^2(Sz) \end{cases} \tag{II.14}$$

where:

$$F = \frac{K}{K+\delta} \quad , \quad S = \sqrt{K+\delta} \tag{II.15}$$

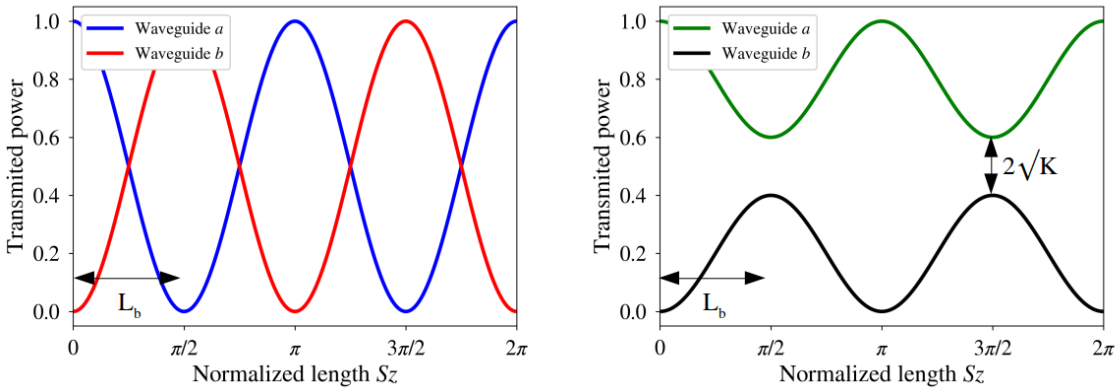

Figure II.7 – Evolution of the transmitted optical power between two waveguides, as a function of the normalized propagation distance Sz. **Left:** The two waveguides are identical. All the optical power is transferred from waveguide a to waveguide b. **Right:** The two waveguides are different. Only a portion of the optical power is transferred.

Physically speaking, F represents the amount of optical power that can be transferred from one waveguide to the other. Note that F reaches unity when the two waveguides are identical ($\beta_a = \beta_b$) ; in other words, all the optical power can be transferred from waveguide a to waveguide b.

On its part, S is related to the length L_b at which the maximal amount of optical power is transferred. L_b is called the beat length and is given by:

$$L_b = \frac{\pi}{2S} \tag{II.16}$$

Figure II.7 represents the evolution of the transmitted optical power between two waveguides, for two identical waveguides ($\delta = 0$, $F = 1$) and two different waveguides ($\delta \neq 0$, $F \neq 1$).

On the next chapters, we will see that suspended directional couplers can be exploited as a cavity-less optomechanical structure, because of the strong optical gradient forces that are generated between the two waveguides.

II.4 Optical losses in silicon waveguides

Propagation along a waveguide is limited by different loss mechanisms, that can be due to fabrication imprecision, intrinsic properties of the medium, or necessary bending of the waveguide. This losses are distinguished between absorption losses, radiation losses, and scattering losses..

II.4.1 Absorption losses

Absorption losses (*i.e.* a photon is absorbed) can occur because of deep defects in the crystal lattice, intrinsic material absorption between two energy levels, Two Photons Absorption (TPA), and Free Careers Absorption (FCA) [89, 90].

Bulk Silicon wafers are of very high purity, and silicon is transparent in a large wavelength window between 1.1 and 8 μm. The first two absorption mechanisms are negligible in silicon waveguides.

TPA and FCA are non-linear effects, that respectively scale with the second and fourth power of the intensity of the optical field. While negligible in strip waveguides, these effects can become important in optical resonators (micro-rings and micro-disks), within which high power densities are created. On our experiments, non-linear effects can become significant at a typical laser power between 2 mW and 10 mW, depending on the device. More discussion about non linear effects, TPA and FCA is provided in section IV.1.6.

II.4.2 Radiative losses

Radiative losses (*i.e.* the guided mode leaks towards the outside environment) include leakage through the substrate and bending losses.

Radiation towards the substrate is negligible for the TE_0 guided mode in our silicon waveguides, that are isolated from the substrate by a 2 μm thick buried oxide layer.

Bending losses are a fundamental loss mechanism of photonic waveguides, that are only purely lossless under straight propagation. This can be explained by the fact that there is an intrinsic increase of the phase velocity along the bending radius in a curved waveguide. To keep it up with the rest of the same wavefront, light has to travel a longer distance when it is further away from the bending origin. Hence, phase velocity increases along the radius, and passed a certain critical point, it exceeds the velocity of the wave in the medium, which induce radiation towards the external medium. Under this perspective, the use of high index contrast waveguides with a strong confinement of the field inside the core is a way to strongly limit bending losses.

In silicon waveguides, bending losses are negligible above a 3 μm bending radius [91]. For example, bending losses set a limitation around 10^{10} to the quality factor of a 3 μm radius ring resonator, while state-of-the-art values for this quantity are in the $10^4 - 10^5$ range, which clearly indicates that bending losses are not the main source of optical leak.

Additionally to "pure" bending losses(and although not radiative losses), there two other loss channels associated to bent waveguides: the mode-mismatch between guided modes at the transition between straight and bent waveguides [92], and a possible coupling between TE_0 and TM_0 guided modes [91]. For this reason, bending radii are generally kept above the 5 μm mark. We respected this criterion in this thesis.

II.4.3 Scattering losses

In photonic waveguides, any imperfection can induce scattering of the guided light. These imperfections are encountered inside of the bulk (impurities, crystalline defects, ...) and at the surface of the waveguide (roughness). Working with silicon, bulk imperfections have become negligible with the amelioration of fabrication techniques (99.9999999 % purity).

Surface roughness is thus the dominant cause of scattering losses. It mainly happens at the sidewalls, as a result of the lithography and etching patterning steps during fabrication [91]. Specific surface treatment steps aiming to improve the surface quality are often used, such as thermal oxidation and hydrogen annealing [93], sacrificial oxidation [94] or wet chemical oxidation [95]. Typical roughness amplitude of several nanometers is typically attained. In comparison, the top and bottom surfaces, which are kept intact during fabrication and benefit from well mastered polishing processes during wafer manufacturing, exhibit a roughness amplitude down to 0.1 nanometers [96].

Scattering losses can be qualitatively investigated with perturbation theory: surface roughness imperfections are considered as a small permittivity perturbation, and it possible to calculate a coupling strength coefficient towards radiative modes, that takes a form analogous to equation (II.11). Such analysis evidences that scattering losses are proportional to the square of the index contrast and to the square of the optical amplitude at the surfaces [97].

Silicon waveguides present a high index contrast and a strong overlap of the field with its lateral boundaries, due to the electromagnetic discontinuity. As a result, scattering losses at the sidewall rugosity are the major dissipation channel in silicon waveguides, with state-of-the-art propagation losses around 2 dB/cm at a 1550 nm wavelength. In contrast, low index contrast silica waveguides exhibit losses around 0.04 dB/cm at a 1550 nm wavelength, and losses in optical fibers are inferior to 0.2 dB/km [98].

Dielectric medium	Cross-section	Losses
Lithium niobate on insulator [99]	1 μm × 270 nm	0.4 dB/cm
Silicon [100] (multimode)	1.8 μm × 500 nm	0.04 dB/cm
Silicon [101]	400 nm × 230 nm	2 dB/cm
Silicon nitride [102]	4.2 μm × 65 nm	0.03 dB/cm
Aluminum gallium arsenide [103]	2 μm × 220 nm	0.4 dB/cm
Silica [104]	–	0.03 dB/cm

Table II.2 – Selected state-of-the-art propagation losses for various dielectric media and waveguides cross-section, at a $\lambda = 1550$ nm wavelength.

It is possible to reduce propagation losses in silicon waveguides by playing on the waveguide cross-section and confinement. In both cases, the mode shape is engineered such that it presents a smaller overlap of the field with its lateral boundaries. A comparison between the propagation losses of waveguides of various dielectric media and cross-section, at a $\lambda = 1550$ nm wavelength, is presented on table II.2. In this thesis, we worked with 500 nm $\times$ 220 nm silicon waveguides, such that we expect propagation losses around 2 dB/cm. The cross-section dimensions were chosen based on available wafers that fixed the silicon height to 220 nm.

Even if propagation losses in photonic waveguides can seem to be elevated in regard to optical fibers, the propagation length rarely exceeds the cm range, and actual losses remain small. Similarly, because high index contrast waveguides enable to reduce the footprint of photonic circuits, total losses in high index contrast and low index contrast waveguides remain of the same order of magnitude.

Conclusion

In this chapter, we have quickly presented the principle of optical guiding in a dielectric structure. We introduced the notions of effective index, group index and guided mode profile in the analytical case of a symmetric planar waveguide, and extended these notions to the non-analytical case of rectangular silicon waveguides. We also discussed evanescent coupling between two photonic waveguides, and optical propagation losses resulting from fabrication imperfections.

In the next chapter, we will extend the theory of cavity optomechanics to silicon waveguides. In particular, we will discuss the new optical forces and optomechanical coupling schemes that arise in such structures.

CHAPTER III

Silicon optomechanics

In this chapter, the theory of cavity optomechanics is presented in the context of optomechanical cavities constituted of silicon waveguides. To be completely correct, it must be specified that the terminology "cavity optomechanics" is a little abusive in silicon structures, because one can achieve significant optical forces without the need of an optical cavity. Examples of two typical silicon optomechanics structures are presented on figure III.1. In the left picture, two waveguides are brought close together and coupled by means of strong lateral optical gradient forces. In the right picture, a more classical disk resonator with an input waveguide is presented. The two main advantages of silicon optomechanics are already apparent in these two pictures. On the one hand, cavity-less optomechanics can lead to simpler geometries and dynamics, while totally mimicking the targeted applications of cavity optomechanics. On the other hand, even in the context of optical cavities, all the photonic tools (waveguides, grating couplers, modulators, ...) can be exploited to address the optomechanical resonator, leading to easier experimental manipulation (no longer relying one precise free-space optical alignment and less sensitive to environmental perturbations).

The basis of the discussion remains the coupled equations of motion, whose previous expression constitutes a very generic formalism and can still be used. However, the expression of the coupling strength and optical forces must be reconsidered. Due to the guided propagation of the field in a dielectric medium (by opposition to the free-space propagation in the Fabry-Perot cavity), additional optical forces and coupling schemes appear in photonic structures.

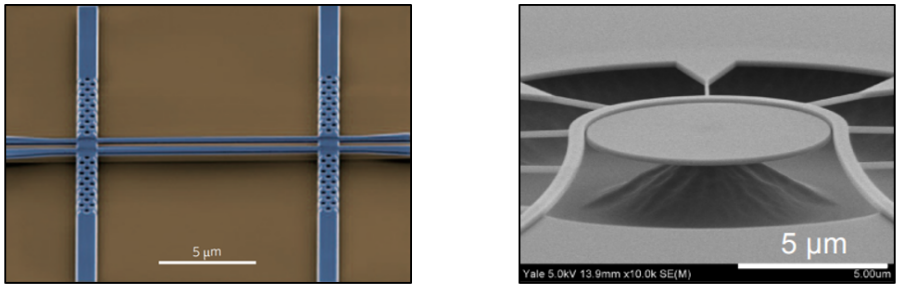

Figure III.1 – Examples of silicon optomechanics structures. **Left:** Suspended directional coupler [105]. **Right:** Suspended disk resonator and its input waveguide [106].

III.1 Equations of motion

The approach relying on the equations of motion presented in the first chapter constitute a general description of any optomechanical system, and can still be followed with photonic waveguides, under minor (yet important) modifications, when an optical cavity is considered.

The major difference in regard to the description followed in chapter I originates from the three dimensional nature of the structures. All the quantities are defined as three component vectors (for each direction), defined at any point $\overrightarrow{r}$ of the structure.

The mechanical displacement is noted $u(\overrightarrow{r},t)$. We assume separation of the spatial and temporal variables, such that the displacement is expanded to:

$$u(\overrightarrow{r},t) = \sum_{n=0}^{+\infty} \psi_n(\overrightarrow{r}) u_n(t) \tag{III.1}$$

where ψ_n is the mode shape, and the temporal oscillation $u_n(t)$ of a given mode can still be treated as a unidimensional damped oscillator. For the n-th mode:

$$\frac{\mathrm{d}^2 u_n(t)}{\mathrm{d}t^2} + \Gamma_m \frac{\mathrm{d}u_n(t)}{\mathrm{d}t} + \Omega_m^2 u_n(t) = \frac{F_n(t)}{m_{\text{eff}}} \tag{III.2}$$

The effective (or modal) mass for the n-th mode reads:

$$m_{\text{eff}} = \int \rho(\overrightarrow{r}) \left| \overrightarrow{q}_n(\overrightarrow{r}) \right|^2 dV \tag{III.3}$$

where $\rho(\overrightarrow{r})$ is the material density and $\overrightarrow{q}_n$ is the displacement vector, normalized such that $\mathrm{Max}\,\overrightarrow{q}_n = 1$.

III.2 Optical forces in silicon waveguides

We distinguish three pure optical forces in silicon waveguides, namely the radiation pressure force, the optical gradient force, and the electrostrictive force. Additionally, an (indirectly) optical force is induced by absorption of light and thermal expansion.

In the following, after giving a physical insight on the nature of each force, we will present two complementary ways of calculating optical forces in photonic waveguides, based on an analytical and a numerical approach. Later on the manuscript, we will apply these methods to our own geometries.

III.2.1 Qualitative description of optical forces in photonic waveguides

Radiation pressure and optical gradient forces are described under the same formalism, by Maxwell stress tensor. Electrostrictive forces are described by the electrostrictive tensor. Finally, photothermal forces are described by thermal expansion.

Radiation pressure and optical gradient forces

The nature of radiation pressure and optical gradient forces is more easily understood in the context of polarizable micro particles submitted to a focused laser beam (Figure III.2).

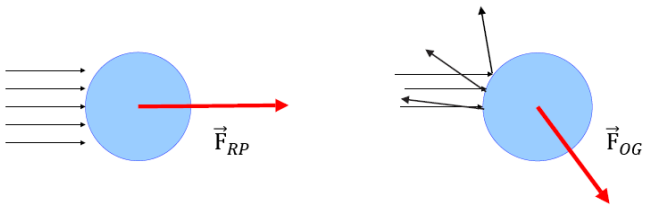

Figure III.2 – Illustration of the radiation pressure force (left) and optical gradient force (right) in the case of a polarizable micro particle, in a geometric picture.

Radiation pressure physically corresponds to the transfer of momentum between an incident photon and the particle, after absorption, reflection or scattering of the light field. When the particle is submitted to a uniform laser beam, the impulsion transfer (after absorption, reflection or scattering of light) is unidirectionally conducted along the direction of light propagation. When the laser is not uniform (in regard to the center of mass of the particle), the resulting force is off-axis and can either attract the particle towards (or repulse the particle from) the strongest fields. Radiation pressure is hence not always orientated along the direction of propagation.

In an electromagnetic picture, an additional force arise under optical gradients. When the polarizable micro particle is placed in a laterally varying optical field, a dipole is induced in the particle, whose positive and negative sides will experience slightly different forces because of the field gradient. The dielectric particle is hence naturally attracted towards the region with the stronger field.

Based on these two descriptions, the forces acting on a polarizable micro particle submitted to a focused laser beam can be separated between a longitudinal and a transverse component. These components of intertwined origin are respectively referred as the radiation pressure force and the optical gradient force (but, again, the optical gradient force include a contribution from radiation pressure and these denominations are somehow abusive). The same terminology is applied in photonic waveguides.

Electrostrictive forces

Electrostriction manifests itself as a deformation of any dielectric medium that is exposed to an electric field. Deformation and stress are equivalent in the theory of elasticity, and we can hence express electrostriction as an optical force. Contrary to radiation pressure and optical gradient induced forces, electrostrictive forces are not present in the case of the (free-space) Fabry-Perot cavity with a movable back-end mirror, and were absent of the previous discussion. As we will see, both these forces are of the same magnitude in photonic structures, and electrostrictive forces can not be neglected.

It is worth mentioning that piezoelectricity is similar to electrostriction, but does not induce optical forces. Indeed, piezoelectricity evolves linearly with the optical field, that oscillates between negative and positive value at optical frequencies. As a result, the average[1] piezoelectric deformation is nullified. By opposition, electrostriction evolves with the square of the field, and the negative and positive values add up, leading to a non zero average contribution.

Photothermal forces

When light is absorbed in a material, it generates heat that in turn induces a medium deformation. Following the same argument than with electrostrictive forces, deformation and stress are equivalent, and a photothermal force is hence generated.

The order of magnitude of photothermal forces is negligible at low optical powers, as optical absorption is negligible. However, when high power densities are created (typically in a small radius ring resonator), non-linear effects are involved and result in non-negligible optical absorption. In these cases, the photothermal force can totally surpass other contributions. Silicon exhibits pronounced non-linear effects [89], such that we expect photothermal forces to be significant.

[1]Note that while not made explicit, we actually always consider the average temporal contribution of optical forces, because optical frequencies are very high in regard to others.

We also point out that the dynamic of photothermal forces is dictated by the thermal response time and not by optical or mechanical processes. In our cases, thermal frequencies fall in the GHz range, which is superior to our mechanical frequencies (typically in the MHz range), and photothermal forces are relevant. This is not always the case, as the thermal response strongly depends on the choices of material and resonator geometry.

III.2.2 Analytical estimation

In a photonic waveguide, the RTOF theory introduced in chapter I can be used to analytically calculate the optical forces:

$$F_{\text{opt}} = \Phi\hbar\frac{\mathrm{d}\phi(x)}{\mathrm{d}x} \tag{III.4}$$

where $\Phi = P_{in}/\hbar\omega_L$ is the incident photon flux and ϕ is the phase shift that an incident wave experiences through the system at steady-state.

In a photonic waveguide, one easily finds that:

$$\phi(\lambda, x) = \frac{\omega_0}{c} n_{\text{eff}}(\lambda, x)\, L(x) \tag{III.5}$$

with L the length of the waveguide, and the optical force reads:

$$F_{\text{opt}}(\lambda, x) = \frac{P_{in}}{c}\left(n_{\text{eff}}(\lambda, x)\frac{\mathrm{d}L(x)}{\mathrm{d}x} + L(x)\frac{\mathrm{d}n_{\text{eff}}(\lambda, x)}{\mathrm{d}x}\right) \tag{III.6}$$

The optical force is hence the sum of a contribution from the waveguide length variation and a contribution from the effective index variations. Typically, radiation pressure and optical gradient forces will govern the first term, while optical gradient, photothermal and electrostrictive forces will govern the second. However, this is not always true. For example, in the case of a suspended directional coupler (discussed in chapters VI and VII), only the effective index is affected by mechanical motion and optical forces, as all mechanics rely on the variation of the gap between two waveguide submitted to attractive and repulsive forces.

This last point evidences one (if not the) of the major drawbacks of this analytical method: it requires to have a good understanding of the problem in order to properly identify the mechanical variable. This is in some way similar to the problem encountered in the first chapter when defining the optomechanical coupling rate.

From equation (III.6), the optical force is wavelength dependent, as a result of the intrinsic dispersive nature of silicon waveguides. However, the derivative must be taken at a fixed wave vector, and not at a fixed wavelength, the latter leading to a small error by a factor n_g/n_{eff}, as pointed out in [107].

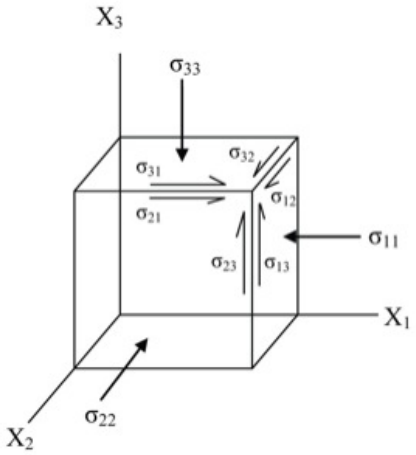

Figure III.3 – Components of the stress tensor. σ_{ij} represents the component in the direction j, acting on the surface i.

III.2.3 Numerical estimation

Preamble: On the following, we use the stress tensor formalism in order to express the density of optical forces. The link between these two quantities is:

$$f_i = -\left(\frac{\partial \sigma_{ix}}{\partial x} + \frac{\partial \sigma_{iy}}{\partial y} + \frac{\partial \sigma_{iz}}{\partial z}\right)$$

where $\overleftrightarrow{\sigma}$ is the stress tensor.

Considering notations, σ_{ij} represents the component in the direction j, acting on the surface i (figure III.3).

Regarding optical simulations, the guided modes are obtained with a commercial finite element mode solver. More information is given on appendix A.

Radiation pressure and optical gradient forces

In photonic waveguides, radiation pressure and optical gradient forces are described by Maxwell stress tensor $\overleftrightarrow{T}$, whose components are:

$$T_{ij} = \varepsilon_0 \varepsilon_r \left(E_i E_j - \frac{1}{2}\delta_{ij}\overrightarrow{E}\cdot\overrightarrow{E}\right) + \mu_0 \left(H_i H_j - \frac{1}{2}\delta_{ij}\overrightarrow{H}\cdot\overrightarrow{H}\right) \qquad \text{(III.7)}$$

with ε_0 the vacuum permittivity, μ_0 the vacuum permeability, ε_r the relative permittivity, and δ_{ij} the Kronecker's delta. Note that Maxwell stress tensor is defined with an opposite sign in regard to the "usual" stress tensor introduced in the preamble: $T_{ij} = -\sigma_{ij}$.

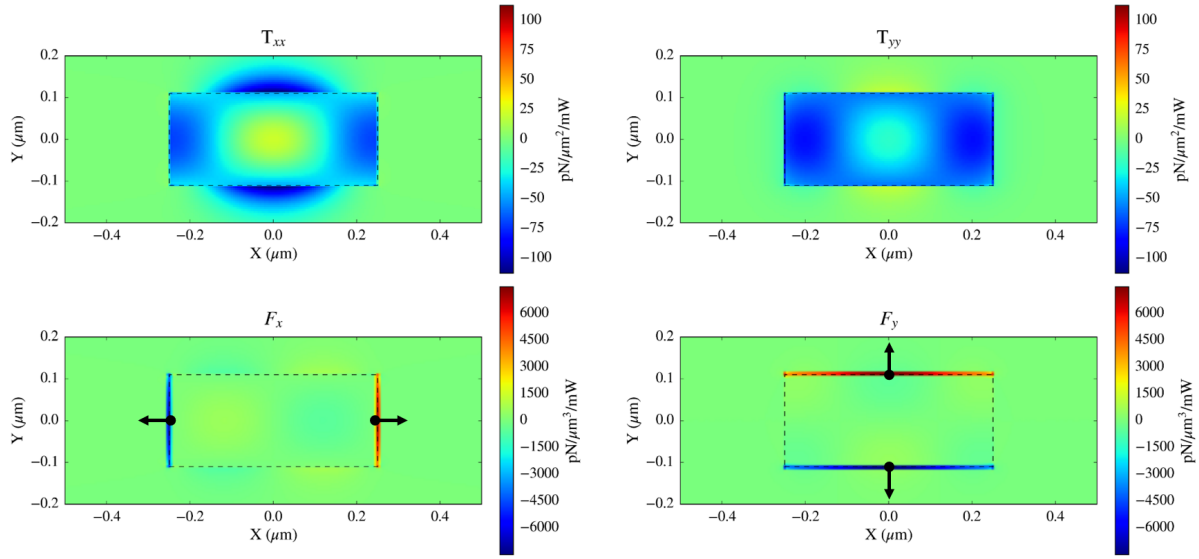

Figure III.4 – Time averaged Maxwell stress tensor components and associated force densities. Note that colorbars are truncated for easier visualization. Arrows indicate the force direction.

Based on the knowledge of the optical field and on Maxwell stress tensor, one can calculate the force induced by radiation pressure and optical gradients. Example of such calculation in a 500 nm × 220 nm silicon waveguide, surrounded by air, is presented on figure III.4. We can see that radiation pressure and optical gradient forces push outward the boundaries of the waveguide in each direction.

Electrostrictive forces

The electrostrictive stress tensor is linked to the well-known photoelastic tensor and the electrical field by [108].:

$$\sigma_{kl}^{\mathrm{EL}} = -\frac{1}{2}\varepsilon_0 n^4 p_{ijkl} E_i E_j \tag{III.8}$$

The photoelastic tensor is of rank 4, and should in principle have $3^4 = 81$ coefficients. For a material having cubic symmetry, it can however be reduced to a 6×6 matrix with only three independent coefficients p_{11}, p_{12} et p_{44}, by symmetry considerations [109]. It

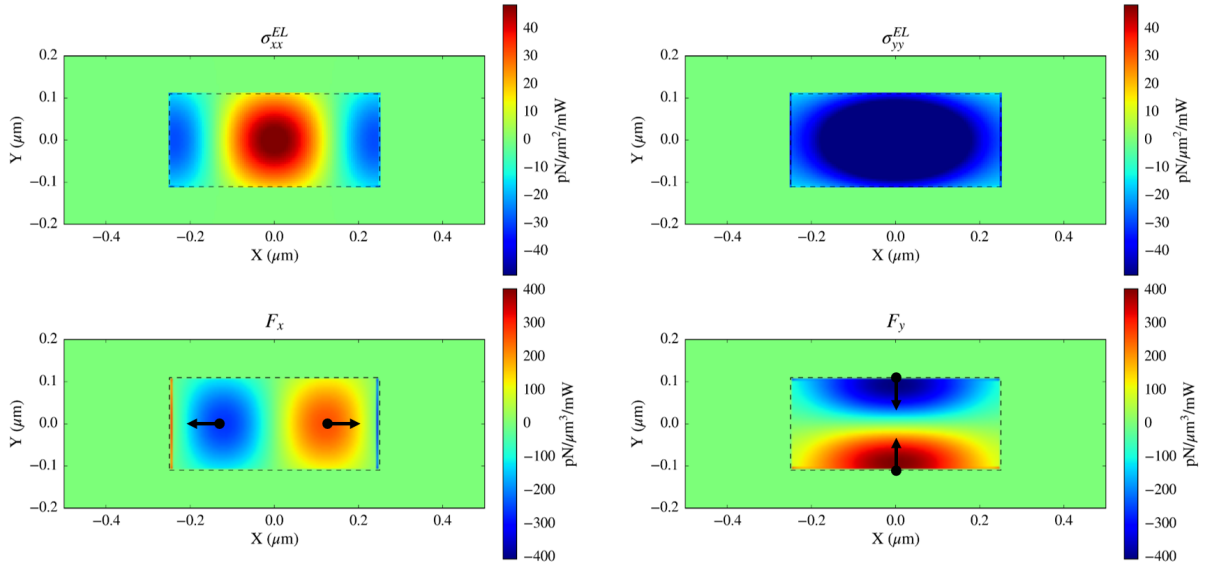

Figure III.5 – Time averaged electrostrictive stress tensor components and associated force densities. Note that colorbars are truncated for easier visualization. Arrows indicate the force direction.

relates the local material stress σ_{kl} to the electric field:

$$\begin{pmatrix} \sigma_{xx}^{\mathrm{EL}} \\ \sigma_{yy}^{\mathrm{EL}} \\ \sigma_{zz}^{\mathrm{EL}} \\ \sigma_{yz}^{\mathrm{EL}} = \sigma_{zy}^{\mathrm{EL}} \\ \sigma_{xz}^{\mathrm{EL}} = \sigma_{zx}^{\mathrm{EL}} \\ \sigma_{xy}^{\mathrm{EL}} = \sigma_{yx}^{\mathrm{EL}} \end{pmatrix} = -\frac{1}{2}\varepsilon_0 n^4 \begin{pmatrix} p_{11} & p_{12} & p_{12} & 0 & 0 & 0 \\ p_{12} & p_{11} & p_{12} & 0 & 0 & 0 \\ p_{12} & p_{12} & p_{11} & 0 & 0 & 0 \\ 0 & 0 & 0 & p_{44} & 0 & 0 \\ 0 & 0 & 0 & 0 & p_{44} & 0 \\ 0 & 0 & 0 & 0 & 0 & p_{44} \end{pmatrix} \begin{pmatrix} E_x^2 \\ E_y^2 \\ E_z^2 \\ E_y E_z \\ E_x E_z \\ E_x E_y \end{pmatrix} \tag{III.9}$$

The values of p_{11}, p_{12} et p_{44} were measured 3.39 μm in silicon [110]. They are assumed to vary only slowly with the wavelength, and we use these values at 1.55 μm: $p_{11} = -0.09$, $p_{12} = +0.017$ et $p_{44} = -0.051$.

Figure III.5 shows the calculated densities of electrostrictive forces in a 500 nm $\times$ 220 nm silicon waveguide surrounded by air. Electrostrictive forces push outward the boundaries of the waveguide in the horizontal direction, but push them inward in the vertical direction. Hence, radiation pressure / optical gradient induced forces and electrostrictive forces add up constructively in the horizontal direction, but add up destructively in the vertical direction. This is a consequence of the sign difference between the photoelastic coefficients p_{11}, p_{12} and p_{44}. Other materials (such as GaAs [111]), with no sign difference between their photoelastic coefficient, can add up constructively in every direction.

The net effects and magnitude of radiation pressure/optical gradient induced forces and

electrostrictive forces can be compared by means of the spatial averaged stress [109], defined as:

$$\bar{\sigma}_{ij} = \frac{1}{\mathrm{W} \times \mathrm{H}} \int_{\mathrm{WG}} \sigma_{ij} \mathrm{d}x\mathrm{d}y \tag{III.10}$$

The comparison between the spatial averaged stress of radiation pressure / optical gradient induced forces and electrostrictive forces is presented on table III.1 (the associated optical forces are also shown). The order of magnitude of both spatial averaged stress is equivalent. As a result, we expect cancellation of both contributions along the vertical direction.

Spatial averaged stress (mPa/mW)				
$\bar{\sigma}_{xx}^{\mathrm{M}}$	$\bar{\sigma}_{yy}^{\mathrm{M}}$	$\bar{\sigma}_{xx}^{\mathrm{EL}}$	$\bar{\sigma}_{yy}^{\mathrm{EL}}$	σ^{th}
31.96	57.59	6.59	-52.12	114.22
Optical force (nN/μm/mW)				
f_x^{M}	f_y^{M}	f_x^{EL}	f_y^{EL}	f^{th}
7.031	28.80	1.450	-26.06	57.11

Table III.1 – Comparison between the spatial averaged stress (and power normalized force per unit length, acting on the lateral boundary) associated to radiation pressure/optical gradient induced forces, electrostrictive forces and photothermal force (for the last one, only in the case of an optical cavity, and beyond the optical power threshold for non-linear and thermal effects).

Photothermal forces

Here again, we can use the tensor formalism to describe photothermal forces. The photothermal stress tensor is:

$$\sigma_{kl}^{th} = C_{ijkl} \alpha_{ij} \Delta T \tag{III.11}$$

where C_{ijkl} are the components of the stiffness tensor, α_{ij} are the components of the thermal expansion tensor, and ΔT is the change in temperature, that we suppose uniform in the waveguide.

In silicon, it is a usual approximation to consider the thermal properties to be isotropic. Under this assumption, the photothermal stress tensor reduces to a scalar:

$$\sigma^{th} = \frac{E}{2(1-\nu)}\alpha_{th}\Delta T \tag{III.12}$$

with E is the Young modulus and ν is Poisson's ratio.

Photothermal and non-linear effects (the link between these two quantities is explained in section IV.1.6) are small in silicon waveguides, such that photothermal forces usually remain negligible. However, when an optical cavity is formed, high power densities are created and these forces become significant. Typical values of ΔT can reach 1.4 mK/mW (where "/mW" refers the input laser power) during experiments (see section V.2.3). In this case, we find $\sigma^{th} = 114.2$ mPa / mW. This value is a little higher than the ones associated to other optical forces, but remains of the same order of magnitude (see table III.1).

Photothermal forces are an inherently non linear process. By working at sufficiently low optical power (typically below a laser drive at 2 mW in our experiments), non-linear processes are negligible and photothermal forces are null. On the other hand, they quadratically increase with optical power, and should surpass all other optical forces beyond a certain point (not precisely evaluated, but based on experimental knowledge, around 10 mW).

Conclusion

Stress tensors are a very powerful calculation tool, that allows to calculate the force density at any point of the waveguide, based on the knowledge of the six components of the guided mode profile. However, it comes with a computational cost and the drawback of a relative loss of physical insight regarding the general parameters of the system. On the other hand, while an approach such as the RTOF method do not give access to the force profile but only to its magnitude, it represents a simple analytical alternative that can offer supplementary information over the physical parameters of the system.

These two methods are hence complementary, and their equivalence was verified by different authors [73, 112, 113].

III.3 Coupling schemes in photonic structures

In the previous section, we presented the optical forces acting in silicon waveguides. In the following, we discuss how the optomechanical coupling rates g_{om} and κ_{om} are also modified.

III.3.1 Dispersive coupling rate $g_{\mathbf{om}}$

In a dielectric medium, dispersive coupling is separated between a geometric and a photoelastic contribution. This separation is evidenced by rewriting the definitions of the dispersive coupling rate g_{om} and the resonant frequency ω_0:

$$g_{\mathrm{om}} = \frac{\partial \omega_0}{\partial x} \quad , \quad \omega_0 = \frac{2\pi c}{n_{\mathrm{eff}} L} m \text{ with } m \in \mathbb{N} \tag{III.13}$$

Under mechanical deformation, both the cavity length L and the effective index will be modified. While the first point was already encountered in the case of the free-space Fabry-Perot cavity with a moving back-end mirror, the contribution from the effective index is particular to dielectric media. It originates from the so-called photoelastic effect: under mechanical stress, the refractive index (and equivalently, the dielectric tensor ε_{ij}) of dielectric media is modified.

Under these considerations, we can rewrite:

$$g_{\mathrm{om}} = \frac{\partial \omega_0 \left(L, n_{\mathrm{eff}}\right)}{\partial x} \tag{III.14}$$

$$= \frac{\partial \omega_0}{\partial L}\frac{\partial L}{\partial x} + \frac{\partial \omega_0}{\partial n_{\mathrm{eff}}}\frac{\partial n_{\mathrm{eff}}}{\partial x} \tag{III.15}$$

$$= \underbrace{-\frac{\omega_0}{L}\frac{\partial L}{\partial x}}_{g_{\mathrm{geom}}} \underbrace{- \frac{\omega_0}{n_{\mathrm{eff}}}\frac{\partial n_{\mathrm{eff}}}{\partial x}}_{g_{\mathrm{pe}}} \tag{III.16}$$

Note that in the case of a free-space Fabry-Perot cavity with a moving mirror, x is simply defined such that $L(x) = L + x$ and we effectively find $g_{\mathrm{om}} = -\omega_0/L$, as advanced in chapter I.

Calculation of $g_{\mathbf{geom}}$ and $g_{\mathbf{pe}}$

On the following, we assume that the total electromagnetic energy is normalized to unity:

$$N = \iiint_{\mathrm{Vol.}} \varepsilon_r \overrightarrow{E}^* \cdot \overrightarrow{E} \mathrm{d}V = 1 \tag{III.17}$$

where $\varepsilon_r = n^2$ is the relative permittivity.

Geometric contribution: The geometric contribution can be analytically calculated by applying perturbation theory to Maxwell's equation in the case of shifting material boundaries, as derived in [114]. In the limit of a small displacement of the boundaries, the optomechanical coupling strength is expressed as a surface integral relating the unperturbed optical field and the displacement of the dielectric boundaries:

$$g_{\text{geom}} = \frac{\omega_0}{4}\frac{1}{N}\iint_{\text{Bound.}} (\overrightarrow{q}\cdot\overrightarrow{n})\left[\Delta\varepsilon\left|\overrightarrow{E}_{\parallel}^{(0)}\right|^2 - \Delta\varepsilon^{-1}\left|\overrightarrow{D}_{\perp}^{(0)}\right|^2\right]\mathrm{d}A \tag{III.18}$$

where ω_0 is the unperturbed angular frequency, $\overrightarrow{q}$ is the normalized mechanical displacement vector, $\overrightarrow{n}$ is the unit vector normal to the surface, $\Delta\varepsilon = \varepsilon - 1$ is the difference in the permittivity, $\overrightarrow{E}_{\parallel}^{(0)}$ is the normalized unperturbed electric field parallel to the surface, $\Delta\varepsilon^{-1} = \varepsilon^{-1} - 1$, and $\overrightarrow{D}_{\perp}^{(0)}$ is the normalized unperturbed electric displacement field orthogonal to the surface.

Photoelastic contribution: Under strain, the dielectric tensor ε_{ij} is modified according to [108]:

$$\varepsilon_{ij}^{-1}(S_{kl}) = \varepsilon_{ij}^{-1} + \Delta\left(\varepsilon_{ij}^{-1}\right) = \varepsilon_{ij}^{-1} + p_{ijkl}S_{kl} \tag{III.19}$$

where S_{kl} is the material stress tensor and p_{ijkl} is the photoelastic tensor, already defined in the discussion of the electrostrictive force.

Similarly to the geometric contribution, the small perturbations of the dielectric tensor can be estimated formally from perturbation theory, and the photoelastic contribution to optomechanical coupling reads [33]:

$$g_{\text{pe}} = \frac{\omega_0 n^4}{2}\frac{1}{N}\iiint_{\text{Vol.}}\frac{1}{|\overrightarrow{q}|}\Big[\left|\overrightarrow{E}_x\right|^2(p_{11}S_{xx} + p_{12}(S_{yy}+S_{zz})) + \left|\overrightarrow{E}_y\right|^2(p_{11}S_{yy} + p_{12}(S_{xx}+S_{zz})) + \left|\overrightarrow{E}_z\right|^2(p_{11}S_{zz} + p_{12}(S_{xx}+S_{yy})) + 2\mathrm{Re}\left(E_x^*E_y\right)p_{44}S_{xy} + 2\mathrm{Re}\left(E_x^*E_z\right)p_{44}S_{xz} + 2\mathrm{Re}\left(E_y^*E_z\right)p_{44}S_{yz}\Big]\mathrm{d}V \tag{III.20}$$

where $\overrightarrow{E}$ is the normalized unperturbed electric field. Note that here, the integral is conducted over the volume.

Actual calculation: The calculation of g_{geom} and g_{pe} is generally conducted by means of the Finite Elements Method (FEM), from which the normalized mechanical displacement vector $\overrightarrow{q}$, the material stress tensor S_{kl} and the field components of complex geometries can easily be obtained.

FEM solvers also allow to conduct the calculation for each optical and mechanical modes supported by the optomechanical cavity. This is important, as large variations of the coupling strength can be found between each resonance.

We used FEM calculations to evaluate g_{geom} and g_{pe} on our own systems.

III.3.2 Dissipative coupling rate $\kappa_{\mathbf{om}}$

In photonic waveguides, interesting dissipative coupling[2] will occur under evanescent coupling between multiple waveguides. When two waveguides a and b are attracted towards (or repulsed from) each other, the evanescent coupling strength is modified.

In chapter II, we showed that the evanescent coupling strength from waveguide a to waveguide b is given by:

$$\kappa_{ba} = -\frac{\omega}{4}\iint_b \Delta\varepsilon \overrightarrow{E}_b \overrightarrow{E}_a^* \mathrm{d}x\mathrm{d}y \tag{III.21}$$

where the integration is conducted over the cross section of waveguide b, $\Delta\varepsilon$ represents the relative permittivity perturbation from one guide to the other, and $\overrightarrow{E}_a$ (resp. $\overrightarrow{E}_b$) is the unperturbed field in waveguide a (resp. b). Note that contrary to chapter II, the imaginary complex is omitted, which is done to be consistent with the notations of chapter I.

An equivalent formula for κ_e is obtained in the case of the coupling between a waveguide and an optical cavity (such as a ring resonator) [88], with the difference that in this case the integral is conducted over the entire volume of the cavity. From this expression, we can then directly derive:

$$\kappa_{\mathrm{om}} = -\frac{\omega_0}{4}\frac{1}{N}\iint_{\text{RR bound.}} (\overrightarrow{q}\cdot\overrightarrow{n})\,\mathrm{Re}\left[\overrightarrow{E}_{RR,\parallel}\Delta\varepsilon\overrightarrow{E}^*_{WG,\parallel} - \overrightarrow{D}_{RR,\perp}\Delta\varepsilon^{-1}\overrightarrow{D}^*_{WG,\perp}\right]\mathrm{d}A \tag{III.22}$$

with the same notations than previously.

Conclusion

In this chapter, we have presented the approach that is to be followed when theoretically considering silicon optomechanical devices.

More specifically, we have first proposed an analytical and a numerical way to calculate optical forces in silicon waveguides, that are distinguished between radiation pressure,

[2] In the sense that no optical energy is lost towards the outside environment ; the "loss" occurs from one optical element to an other.

optical gradient, electrostrictive and photothermal forces. The first three of them constructively add-up along the horizontal direction, but destructively cancel each other in the vertical direction. The fourth only occur at high optical power, when optical nonlinear effects become non-negligible, but surpass all other forces under this condition.

Second, we studied the optomechanical coupling rates in silicon optomechanics devices. In the dispersive case, there are two contributions to optical resonant shifts: a geometric one and a photoelastic one, that are respectively sensitive to the motion of surfaces and to internal motion within the device. In the dissipative case, the evanescent coupling strength is modified under motion of the motion of adjacent waveguides.

In the next chapters, we will apply these notions to two silicon optomechanics devices: suspended ring resonators, in chapters IV and V, and sub-wavelength grating suspended waveguides, in chapters VI and VII.

Part II

Suspended ring resonators

Introduction

In this part, we focus the discussion around the use of silicon-based suspended ring resonators as optomechanical cavities. It is organized in two chapters. In the first chapter, we provide the theoretical background associated to suspended ring resonators. Using the notion introduced in the first part, both the optical, mechanical, and optomechanical aspects are considered. In the second chapter, we discuss the practical realization of suspended ring resonators. We present the technological fabrication of our devices, their experimental optical characterization, and their experimental optomechanical characterization.

In the following, we introduce a general description of Suspended Ring Resonators (SRR). The geometry of SRR is presented, along with the optomechanical interactions that can occur in this device. Finally, SRR are compared to other similar optomechanical cavities, highlighting strengths and weaknesses of this optomechanical resonator.

Presentation of suspended ring resonators

A generic suspended ring resonator is presented on figure III.6. It is constituted by a thin and narrow ring attached to a central disk by means of several supporting arms. The central disk stands above a pedestal, and the ring is suspended in the plane above the substrate, standing in the air. In this work, we focus on single mode[3] SRR fabricated from a Silicon On Insulator (SOI) wafer. The wafer consists of a stack of a 220 nm silicon layer and a 2 μm buried oxide layer, over a thick silicon layer. Hence, the ring, the arms, and the central disk are made of silicon, and the pedestal is made of silica.

The SRR is at the same time an optical resonator and a mechanical resonator, and consequently, constitutes an optomechanical resonator. Optical and mechanical degrees of freedom are decoupled to a good extend (but not entirely !), which allows a separate design of each part.

[3]In the sense of the guided mode.

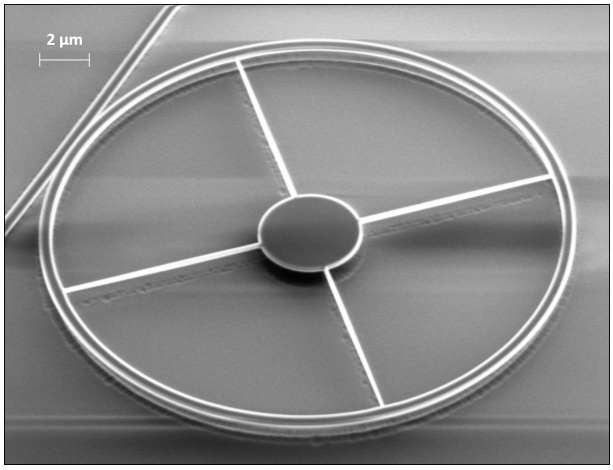

Figure III.6 – SEM image of a suspended ring resonator and of its input waveguide.

From the optical perspective, the SRR behaves like a classical ring resonator, with optical resonances similar to Whispering Gallery Modes (WGM) [115]. Light is trapped inside of a loop, and can constructively self-interfere after each lap, leading to optical resonances. Because of the high index contrast between silicon and air ($\Delta n \sim 2.476$ at $\lambda = 1.55$ μm), small bending radii can be achieved, allowing to store large quantities of light inside of a small volume at resonance. Light is injected into (and extracted from) the ring through a suspended bus waveguide.

From the mechanical perspective, the SRR is a circular ring resonator of rectangular cross-section. Being suspended in the air, it experiences in-plane and out-of-plane mechanical vibrations. Mechanical excitation is mediated by optical forces and thermal agitation. Due to its small size and effective mass, the SRR vibrates at relatively high frequency (beyond the MHz range). In addition, the SRR presents a high number of mechanical design parameters, and the shape and frequency of vibrational modes can be engineered with a good level of flexibility.

Optomechanical interactions in suspended ring resonators

Similarly to a Fabry-Perot cavity with a movable back-end mirror, the optical field and mechanical vibrations of the SRR are coupled to each other by optical forces. We identified four contributions to the optomechanical interaction.

Variation of the cavity length: Similarly to a Fabry-Perot cavity with a movable free-end mirror, the cavity length[4] and the optical path are modulated by mechanical

[4]Defined as the length of the center line of the deformed ring

motion. This is referred as the geometric contribution to optomechanical coupling..

Photoelastic effect: Under mechanical deformation, there is a modification of the optical refractive index of any dielectric media. This is known as the photoelastic effect.

Dissipative coupling: The evanescent coupling strength between the ring and the bus waveguide is modulated by mechanical motion. This leads to a variation of the optical losses with movement, and is known as dissipative (also named reactive) coupling.

Sagnac contribution: SRR present certain mode of vibration where the ring shape is not deformed, but experiences rotational motion instead. In presence of clockwise and counter-clockwise optical modes, there is a phase shift between the two waves, proportional to the angular velocity. This is known as the Sagnac effect.

The strength of these four contributions depends on the shape and frequency of the vibrational mode that is considered, and is not always significant. This will be further discussed in section IV.3.3.

Comparison between SRR and other closed-loop optomechanical cavities

In the large and diverse world of optomechanical cavities, SRR can be classified as a closed-loop optomechanical cavity, where the WGM of the resonator are perturbed by its vibrational contour modes. Inside this family, micro toroids and micro disks resonators are emblematic optomechanical cavities that have been extensively studied.

While similar to these two geometries, SRR distinguish from them in some important points, with advantages and drawbacks.

First, it is important to make a distinction between silica-based micro toroids and micro disks, and silicon-based micro disks and SRR. Silica-based micro resonators are standalone devices, with large bending radii, and can involve non conventional fabrication steps such as serial CO_2 laser reflow. On the other hand, silicon-based micro resonators are monolithic integrated devices, with small bending radii, and are compatible with silicon fabrication processes of high-yield industrial facilities. In other words, silicon-based optomechanical resonators can be seen as the photonic integrated version of their silica-based counterpart.

This comes at the cost of poorer optical performances. Typically, the optical Q factor of silicon-based micro resonators is in the $10^4 - 10^6$ range, while state-of-the-art silica-based

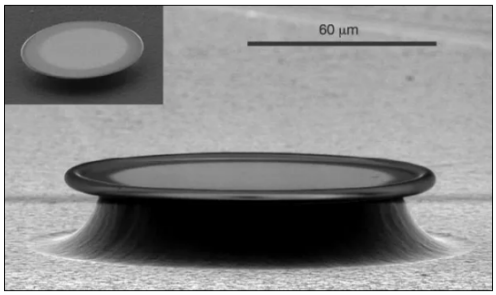

(a) Silica micro toroid [116]

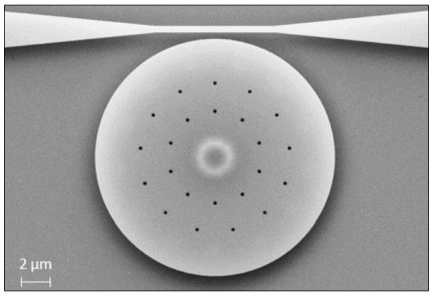

(b) Silicon micro disk [117]

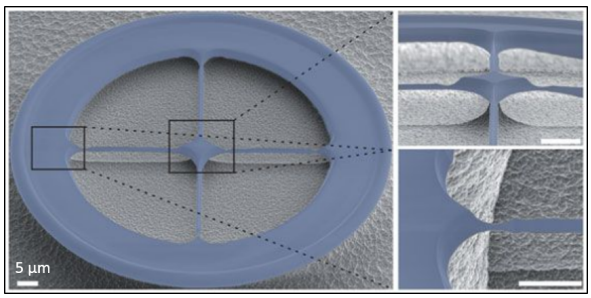

(c) Hollow disk [118]

Figure III.7 – Example of other silicon- and silica-based closed-loop optomechanical cavities.

micro resonators can attain values in the $10^8 - 10^9$ range [116, 119]. However, silicon-based micro resonators benefit from all the on-chip photonic tools. In particular, it makes it possible to use Grating Couplers (GC) and waveguides to inject and collect the light, instead of tapered optical fibers. This experimental scheme is easier to manipulate as it does not critically rely on optical alignment and is less sensitive to its environment. It also eliminates various noise sources and can lead to an increased sensitivity [120].

This distinction being made, SRR also differentiates from others closed-loop optomechanical cavities on more fundamental points.

From the mechanical perspective, SRR present interesting particular features. While mechanical frequencies and quality factors are not significantly different between each of the three geometries, SRR offer more degrees of freedom over the mechanical mode shapes and frequencies. For example, the resonance frequency can be controlled by adjusting the length of the supporting arms, which only requires simple lithographic adjustment from one ring to an other, and can be varied over the same sample. In the case of micro toroids or micro disks, the same control requires to change the pedestal radius and the etching time, which cannot be modified from one resonator to an other over the same sample. Despite not having yet attained this kind of regime in practice, SRR should also ultimately suffer from less mechanical dissipation than micro toroids or micro disks, as they exhibit smaller surfaces and volumes.

Independent control over the mechanical properties is also found to some extent in hollow

disks resonators, a particular class of micro disk resonator which are obtained by removing central quadrants while leaving intact four supporting arms and the external boundary of the disk [121, 122, 123].

An other particularity of our SRR design is that they are single mode optical resonators (the waveguide design is chosen to only allow the existence of a TE_0 guided mode). On the opposite, micro toroids and micro disks are multimodal resonators. Their optical spectrum is quite complicated, with the presence of peaks for all supported resonant modes. The correct identification of optical modes requires additional post-process operations [28], and can be difficult - if not impossible - due to a lot of uncertainties about the exact resonator geometry, refractive index, or experimental conditions (temperature, pressure, ...). The existence of numerous optical modes can also lead to optical coupling from the fundamental mode to higher order modes (either directly at the injection from the bus waveguide/fiber, or as a result of mechanical deformation). At best, this will strongly complicate the dynamics of the system. At worst, this coupling to higher order modes ends up as an additional source of optical losses, when the given optical modes are of no interest for the considered application.

At the end, the relative strength and weaknesses of each geometry will benefit certain applications while disadvantaging others. They are summed-up in table III.2. Note that we restricted the discussion to silicon and silica based optomechanical resonators, fabricated over classical SOI wafers. There is actually a larger variety of materials used in cavity optomechanics (SiN, GaAs, InP, AlN, etc...).

	SiO2 disks	SiO2 toroids	Si disks	Si hol. D.	Si SRR
Typical Radius	100 μm	100 μm	10 μm	10 μm	10 μm
Q_{opt}	up to 10^9	up to 10^8	$10^5 - 10^6$	$10^5 - 10^6$	$10^4 - 10^5$
Q_m	–	$10^4 - 10^6$	$10^4 - 10^5$	$10^5 - 10^6$	$10^4 - 10^5$
CMOS compatible	No	No	Yes	Yes	Yes
Single mode	No	No	No	No	Yes
Easy Mech. design	No	No	No	Yes	Yes

Table III.2 – Summary of the comparison between silica-based and silicon-based closed-loop optomechanical cavities. The values are extracted from the previous references and are not always chosen from the same realization.

Optomechanical coupling with the bus waveguide

In the above, we only considered the ring motion, and did not take into account the fact that the bus waveguide is suspended and is also a mechanical resonator (namely, a doubly clamped silicon beam). The waveguide displacement can lead to both dispersive and reactive optomechanical coupling, which was first proposed and observed between a suspended waveguide and a micro disk [74].

This kind of scheme can actually be ignored when considering a SRR, because the mechanical frequencies of the beam are spectrally well isolated from the ones of the mechanical ring (kHz range against MHz range). In other words, motion of the waveguide and motion of the ring do not happen under the same experimental conditions, and we chose to focus our study to the second case.

CHAPTER IV

Theoretical description of suspended ring resonators

In this chapter, we present a theoretical description of the optical and mechanical behavior of suspended ring resonators, before considering their coupled optomechanical dynamics.

IV.1 Optical description of suspended ring resonators

In this section, we discuss the optical properties of suspended ring resonators. The analytical description of the optical spectrum is provided, along with its characteristics at resonance and figures of merit. Optical losses are detailed, with an emphasize on the influence of the suspension arms. Finally, a rapid description of thermo-optic and non-linear effects is given.

A schematic of the ring resonator, of radius R, is depicted on figure IV.1. The ring resonator is coupled to a single waveguide, by means of an unidirectional evanescent coupler. This case is know as the all-pass configuration, by opposition to the add-drop configuration, where a second waveguide is present [124]. Note that we did not represent the supporting arms.

Within the ring resonator, light is circulating in a closed-loop. After one round-trip, light can constructively interfere with itself, leading to a resonance phenomenon and the storage of the optical power inside of the ring volume.

Optical resonance occurs if the light acquired an additional phase that is a multiple of 2π

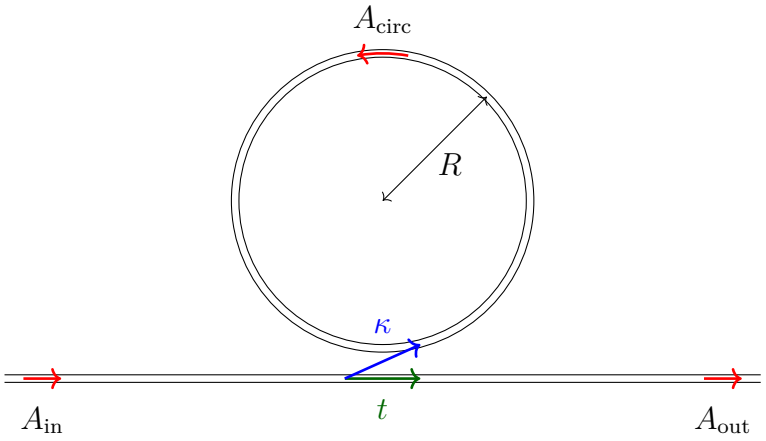

Figure IV.1 – Schematic top-view of an All-pass Optical ring resonator of radius R.

after one round trip. It reads:

$$\frac{2\pi\, n_{\text{eff}}\, \mathcal{P}}{\lambda_r} = 2\pi \times p \tag{IV.1}$$

where $p = 1, 2, ...$ is an integer, n_{eff} is the guided effective index, $\mathcal{P} = 2\pi R$ is the perimeter of the ring, and λ_r is the resonance wavelength. The guided effective index is related to the propagation constant β by: $\beta = k\, n_{\text{eff}}$, where k is the wavenumber.

IV.1.1 Optical spectrum

The coupler parameters are noted t and κ, and we restrain our discussion to the case of single mode waveguides with a lossless coupler, which brings:

$$|t|^2 + |\kappa|^2 = 1 \tag{IV.2}$$

We also only consider the $\pi/2$ radians phase shift from one arm of the coupler to another, with no additional phase effects induced by the coupler.

Under the above assumptions, the optical spectrum (circulated power or transmitted power, against wavelength) of the ring resonator can be calculated analytically. For example, see [125, 124].

The normalized transmitted power and circulating power are Airy functions, of the form:

$$\frac{P_{\text{out}}}{P_{\text{in}}} = \frac{|A_{\text{out}}|^2}{|A_{\text{in}}|^2} = \frac{\alpha^2 + |t|^2 - 2\alpha\,|t|\cos(\theta)}{1 + \alpha^2\,|t|^2 - 2\alpha\,|t|\cos(\theta)} \tag{IV.3}$$

$$\frac{P_{\text{circ}}}{P_{\text{in}}} = \frac{|A_{\text{circ}}|^2}{|A_{\text{in}}|^2} = \frac{\alpha^2\left(1-|t|^2\right)}{1+\alpha^2|t|^2-2\alpha|t|\cos(\theta)} \tag{IV.4}$$

where α is the (real) inner circulation factor representing propagation losses (for no internal losses, $\alpha = 1$), and θ is the phase mismatch after one round trip.

For a given set of parameters α and $|t|$, and for a given effective index, the Optical spectrum can be calculated based on equations (IV.3) and (IV.4) and on $\theta = 2\pi\, n_{\text{eff}}\, \mathcal{P}/\lambda$. We plotted on figure IV.2 a typical normalized transmission spectrum. On this figure, we also represented three important parameters that are experimentally measured: the Free Spectral Range (FSR), the Full Width at Half Maximum (FWHM) $\delta\lambda$, and the Contrast C_r. These parameters are closely related to the figures of merit of the ring resonator (see section IV.1.3).

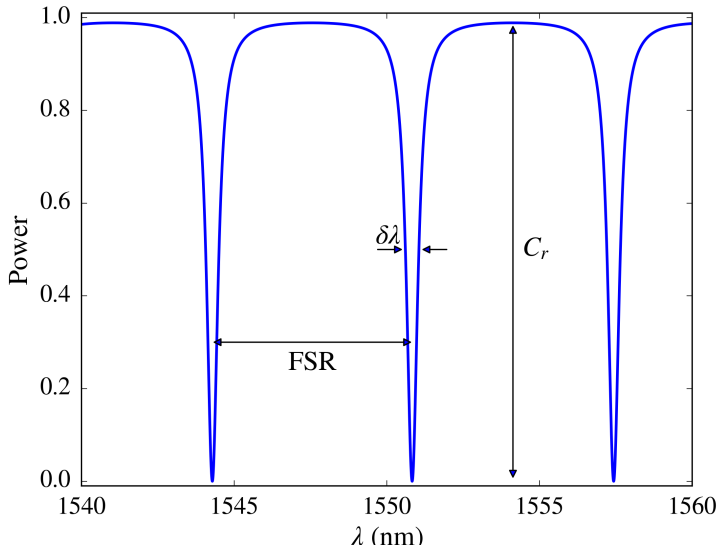

Figure IV.2 – Typical normalized transmission spectrum, with $\alpha = |t| = 0.9$.

IV.1.2 Resonance of a ring resonator

At resonance, the phase θ is a multiple of 2π and equations (IV.3) and (IV.4) become:

$$P^r_{\text{out}} = \frac{(\alpha-|t|)^2}{(1-\alpha|t|)^2} \times P_{\text{in}} \tag{IV.5}$$

$$P^r_{\text{circ}} = \frac{\alpha^2\left(1-|t|^2\right)}{(1-\alpha|t|)^2} \times P_{\text{in}} \tag{IV.6}$$

A special case happens when $\alpha = |t|$, i.e. when the internal losses are equal to the coupling losses. In this case, known as critical coupling, the optical power transmitted through the bus waveguide drops to zero, due to destructive interference between the optical field coupled from the ring resonator and the optical field transmitted through the waveguide.

Experimentally, critical coupling is favorable, because it leads to sharp & visible optical resonances, and good sensitivity. On the other hand, it is also highly beneficial to maximize the amount of Optical power stored inside of the cavity, as most optomechanical figures of merit tend to scale with it.

We represented on figure IV.3, the resonant circulating and transmitted powers, normalized by the optical power in the bus waveguide, as a function of α and $|t|$. Critical coupling is plotted as a dashed line. The choice $\alpha = |t| \longrightarrow 1$ appears to be a way to achieve critical coupling and maximum circulating power.

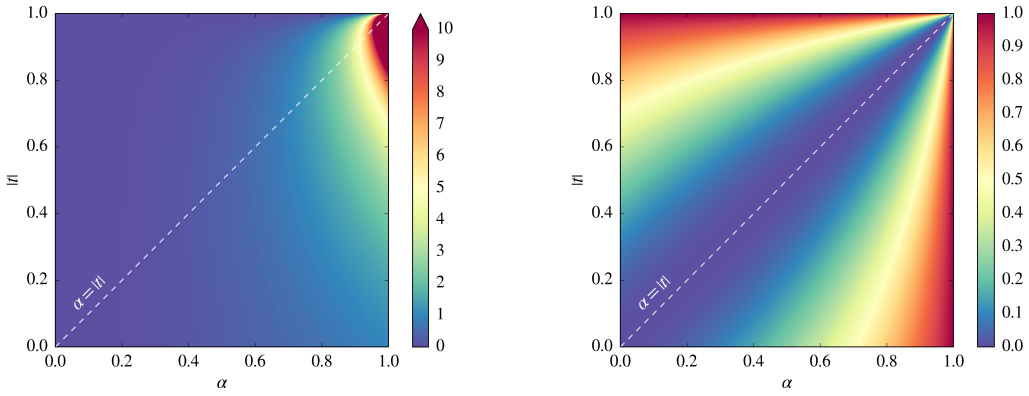

(a) Circulating power

(b) Transmitted power

Figure IV.3 – Evolution of the circulating and transmitted powers at resonance, normalized in regard to the optical power in the bus waveguide. The dashed white line represents critical coupling: $\alpha = |t|$. The colorbar scale of the circulating power is truncated.

Importantly, the scales of the colorbar are not identical. The left scale is truncated at 10, and actually takes values approaching infinity[1]. The right scale ranges from 0 to 1. This is an evidence of the storage of optical power at resonance. The intensity enhancement parameter B^r (sometimes abusively referred as field enhancement parameter), that quantifies how much the intensity is higher in the ring than in the bus waveguide, is simply extracted from equation IV.6:

$$B^r = \frac{\alpha^2\left(1-|t|^2\right)}{\left(1-\alpha\,|t|\right)^2} \underset{\text{c.c.}}{=} \frac{\alpha^2}{1-\alpha^2} \tag{IV.7}$$

where c.c. stands for critical coupling.

[1] In the ideal case $\alpha = |t| = 1$.

IV.1.3 Figures of merit of a ring resonator

The quality of a ring resonator is quantified by four figure of merits: the Free Spectral Range (FSR), the finesse $\mathcal{F}$, the quality Factor Q_{opt}, and the contrast C_r. This quantities are easily measurable from the experimental spectrum of the transmitted optical power (see Figure IV.2). They are also closely related to the propagation losses α and coupling coefficient κ, that can be calculated based on the figures of merit.

On the following, we assume $\delta\lambda \ll \lambda$ and $\kappa \ll 1$ (which is verified in practice). Based on equation (IV.3), the FWHM can be approximated to [124]:

$$\delta\lambda \approx \frac{\kappa^2\lambda^2}{\pi\mathcal{P}n_{\text{eff}}} \tag{IV.8}$$

Without directly being a figure of merit, $\delta\lambda$ is linked to $\mathcal{F}$ and Q_{opt}.

Free Spectral Range (FSR)

The free spectral range corresponds to the spacing between two consecutive resonant wavelengths (or alternatively, frequencies). By derivation of equation (IV.1):

$$\text{FSR}_\lambda = \frac{\lambda^2}{n_g\mathcal{P}} \tag{IV.9}$$

$$\text{FSR}_\nu = \frac{c}{n_g\mathcal{P}} \tag{IV.10}$$

where n_g is the group index, defined by equation (II.8), which takes into account the wavelength dispersion of the media, and c is the speed of light. The FSR is of practical importance for applications where a resonance shift is measured, as it limits the accessible dynamic range.

From the physical perspective, the FSR is related to the round-trip time T_R of a photon inside of the ring:

$$T_R = \mathcal{P}\,\frac{n_g}{c} \quad \Rightarrow \quad \text{FSR}_\nu = \frac{1}{T_R} \tag{IV.11}$$

The finesse $\mathcal{F}$

The finesse $\mathcal{F}$ is a measure of the sharpness of the successive resonances in regard to their spacing. It is analogous to the number of round trips of a photon inside the cavity, before

being lost by external coupling or internal losses. The finesse is defined by:

$$\mathcal{F} = \frac{\mathrm{FSR}}{\delta\lambda} \approx \frac{\pi}{\kappa^2} \tag{IV.12}$$

The intensity enhancement parameter B^r and the finesse are related by: $B^r \approx \mathcal{F}/\pi$. In other words, $\mathcal{F}$ is analogous to the amount of circulating light at resonance.

Quality factor Q_{opt}

The quality factor Q_{opt} is a measure of the sharpness of a resonance in regard to its position. It represents the amount of stored energy divided by the power loss after one turn, and is defined by:

$$Q_{\mathrm{opt}} = \frac{\lambda_r}{\delta\lambda} \approx \frac{n_{\mathrm{eff}}\mathcal{P}}{\lambda}\mathcal{F} \tag{IV.13}$$

Because of the analogy with mechanical and electrical resonators, the optical Q factor is often used as the main spectral characteristic in order to compare the quality of different ring resonators. It should be noted, however, that the finesse is in our case a more relevant figure. Smaller rings lead to higher finesses, but lower quality factors (see Figure IV.4). As our applications rely on storing large quantities of energy into small volumes, it is then doubly advantageous to reduce the ring radius, even if it leads to a smaller Q_{opt}.

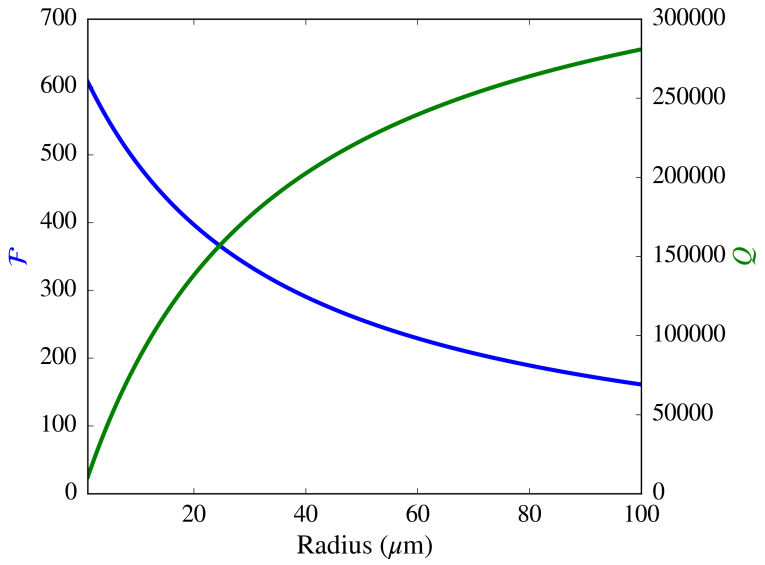

Figure IV.4 – Evolution of Q_{opt} and $\mathcal{F}$ with the radius, for linear losses of 2 dB/cm and $|\kappa|^2 = 0.01$. We can see that a smaller radius leads to an increase of $\mathcal{F}$ and a decrease of Q_{opt}.

Contrast C_r

Finally, the contrast C_r represents the relative height of the resonance peak:

$$C_r = \frac{P_{\max} - P_{\min}}{P_{\max}} = 1 - \frac{(\alpha - |t|)^2(1 + \alpha^2 |t|^2)}{(1 - \alpha |t|)^2(\alpha^2 + |t|^2)} \tag{IV.14}$$

Maximum depth is attained under critical coupling, when $C_r = 1$.

IV.1.4 Optical losses in suspended ring resonators

In a theoretical and asymptotic case $\alpha = 1$ and the amount of stored Optical power reaches infinity at resonance. In practice, however, there are optical losses that limit how much light can be stored into the ring. These losses are distinguished between intrinsic and extrinsic losses.

Intrinsic losses are "true" optical losses, with direct dissipation of optical power toward the environment. They are represented by α in our model [2].

Extrinsic losses correspond to the the amount of light that is coupled from the ring to the bus waveguide, with coupling strength κ. While it is a loss channel for light within the ring, it is not from the experimental point of view. Light is not dissipated towards the environment, but rather transferred from one element to another. The presence of κ is also a necessity: a stand-alone ring resonator without coupling to the outer world is useless.

Intrinsic losses

Intrinsic losses comprise classical losses of photonic waveguides and losses due to the curved geometry. In the case of suspended ring resonators, the presence of a mechanical anchor perturbs the guided mode and induce additional losses.

Intrinsic optical losses are hence separated between radiation losses, scattering losses, linear & non-linear absorption losses, and losses due to the mechanical anchor. This last point is discussed in section IV.1.5.

According to the previous discussion (see section II.4.3), radiation losses and linear absorption losses are negligible in silicon waveguides and ring resonators of radius superior to 3 μm. Scattering losses are the dominating loss channel in these geometries.

Actually, we expect scattering losses to be even higher in suspended ring resonators that in classical ring resonators. SRR present a larger index contrast, which naturally increases the field intensity at the sidewalls and the scattering losses. Furthermore, SRR require additional fabrication steps, which can induce a supplementary degradation of the

[2] Note that α here represents all propagation losses, including linear and non-linear contributions

waveguides facets. Due to the high energy density at resonance, we also expect non-linear optical effects to induce additional absorption of the optical power. This is discussed theoretically in Section IV.1.6 and observed experimentally in section V.2.3.

Extrinsic losses

Extrinsic losses are governed by the coupling strength κ, which represents the amount of light that is coupled from the ring to the bus waveguide. κ is formally described by equation (II.11), as a function of the overlap integral between the field on the bus waveguide and the field on the ring. The two geometries are aligned in the horizontal (xz) plan, and the evanescent field decay along the x direction is generally assumed to be exponential (by analogy to the planar waveguide), such that κ is approximated to an exponential dependence over the gap G between the ring and the bus waveguide:

$$\kappa = a \exp\left(-b \times G\right) \tag{IV.15}$$

where a and b are fitting parameters depending on the waveguide geometry, dimension, material and bending radius.

In practice, a convenient way of conception is to calculate κ for a small set of parameters (either via equation (II.11) or by direct simulations), and to extract the parameters a and b by exponential fit. The design of κ can hence be controlled by playing on the value of the gap G.

Note that experimentally, κ is entirely determined by the position, FWHM and contrast of the resonance peaks on the spectrum, and is perfectly known.

Optical losses and quality factor

The quality factor was defined in equation IV.13 in regard to the wavelength. Alternatively, it can be regarded in the frequency domain:

$$Q = \frac{\omega_0}{\delta\omega} \tag{IV.16}$$

$\delta\omega$ is the FWHM of the resonance peak in the frequency domain. From the physical perspective, $\delta\omega$ corresponds to the decay rate of a photon inside the cavity and is directly related to optical losses. For that reason, it is current in the literature to distinguish the intrinsic quality factor, the extrinsic quality factor, and the total (also called loaded) quality factor, following the same picture as optical losses:

$$1/Q_{\text{tot}} = 1/Q_{\text{int}} + 1/Q_{\text{ext}} \tag{IV.17}$$

IV.1.5 Influence of the suspension on the optical losses

On fabricated samples, the measured quality factors of SRR was always poorer than the ones of classical rings. It suggests the appearance of additional optical losses after suspension. We identified three potential channels. First, the presence of the mechanical anchor results in a local perturbation of the guided mode. This can lead to diffraction on the perturbation, or even leaking of the field through the silicon arms. Second, after suspension, there is an increased higher index contrast at the the silicon / air interface, that should increase scattering losses on the sidewall rugosity. Finally, the etching process could degrade the waveguides facets and increase the flanks rugosity or reduce the waveguide dimensions, both also leading to additional scattering losses.

The last two points are fabrication dependent, and are investigated and discussed more specifically based on experimental results, on section V.2.3.

The perturbation of the mechanical anchor is generally successfully dealt by using a waveguide wide enough to repel the local perturbation far away from the guiding outer boundary of the ring [120, 47]. A more exotic strategy relies on using particular optical supermodes. For example, a"Wiggle" mode is excited, which presents a vanishing intensity field at proximity of the ankles [126]. However, both of these approaches rely on multimodal ring resonators, and are not applicable to single mode ring resonators. We followed an alternative method, consisting on working on the geometry of the anchor itself, in order to minimize its influence on the optical behavior.

Reducing optical losses at the mechanical anchor

The mechanical anchor induces a perturbation of the guided mode, that can either diffract on or leak through the anchor.

We treated the influence of the mechanical anchor similarly to a waveguide crossing problem. At proximity of the arm, the waveguide is adiabatically widened, which increases the effective guided index, reduces its index difference with the silicon arm, and minimizes the effect of the perturbation [127]. In practice, this is done by adding a straight segment of length L_{str} in place of the inner ring boundary, at the junction with the mechanical arm (see figure IV.5). This straight segment naturally widens the waveguide locally.

In parallel to this approach, we also narrowed down the arm width at proximity of the waveguide, which reduces the size and effect of the silicon perturbation. This approach was recently shown to be effective [128], but remains limited by the minimal dimensions allowed during fabrication (notably lithographic resolution) and by the mechanical robustness of the ring. We note W_{tip} the width of the mechanical arm at the junction with the ring (see figure IV.5).

Additionally, the most efficient and straightforward way to reduce optical losses due to the mechanical arms is to simply reduce the number of mechanical arms.

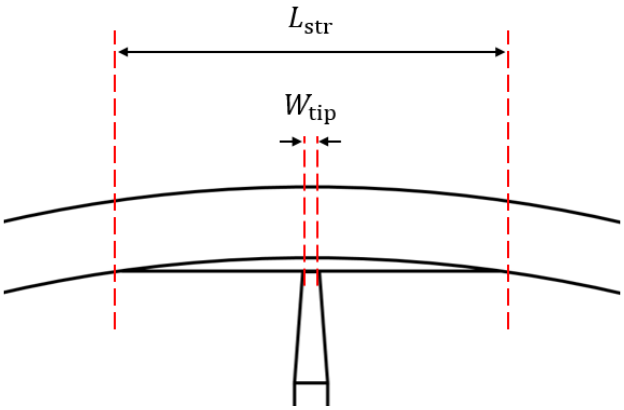

Figure IV.5 – Schematic of the junction between the ring resonator and its mechanical anchor, with a narrowed arm and a straightening of the inner ring boundary.

Simulations

In order to verify our design strategy, we conducted 2D-FDTD simulations, with an effective index method applied along the vertical direction. Typical simulation results are presented on figure IV.6, where we observe the optical field propagating across one junction. On the left picture, we simulated a wide arm with no straightening of the ring ($W_{\text{tip}} = 200$ nm and $L_{\text{str}} = 0$ μm). On the right picture, we used a narrow arm with a small straightening of the ring ($W_{\text{tip}} = 50$ nm and $L_{\text{str}} = 1.5$ μm). The ring has a 10 μm radius and a 500 nm x 220 nm cross section. We calculated a 96.26 % transmission rate in the first case, and a 99.55% transmission rate in the second case, which indicates fewer losses due to the anchor and is coherent with our design strategy[3].

The transmission after one arm for various sets of parameters ($W_{\text{tip}}, L_{\text{str}}$) is presented on Figure IV.7. Generally speaking, we observed that the influence of the mechanical arm width, W_{tip}, is a more important parameter than the straight waveguide length L_{str}. This can be explained by the fact that the resulting widening is *in fine* quite small and does not change that much the guided effective index. Nevertheless, the simulated behavior is consistent with our theoretical predictions.

It must be kept in mind that this study is really qualitative. It is based on the approximation of a 2D-FDTD simulation, and do not take into account the resonant behavior of the ring. Notably, we expect the transmission losses at proximity of the arm to be dependent on the optical azimuthal number of the resonant mode. A proper choice will place nodes of the optical intensity at proximity of the arms and reduce optical losses [128], which is a perspective for future work.

[3]While 2D-FDTD simulations are not precise enough to put an accurate number on these losses, the relative comparison between simulation results gives an accurate indication

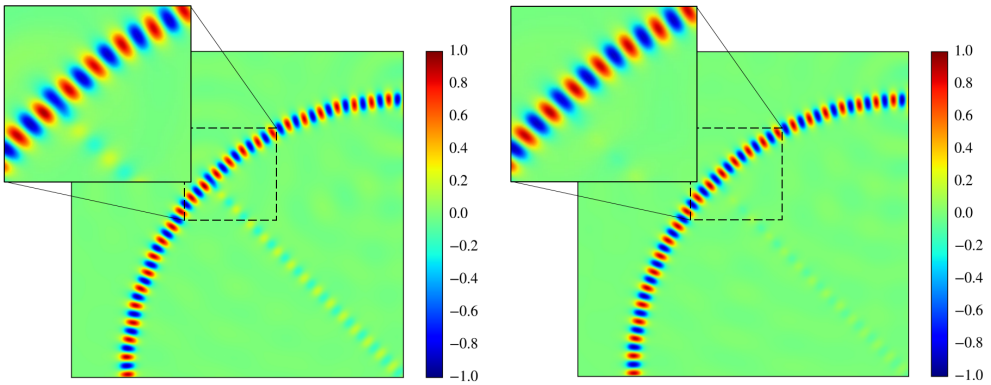

(a) Wide Arm ; T=96.26%

(b) Narrow Arm ; T=99.55%

Figure IV.6 – 2D-FDTD simulation of the propagation of the electromagnetic field at proximity of the mechanical anchor, and calculation of the transmission rate. The field leaking through the silicon arm is visible in the wide case, but almost suppressed in the narrow case. The normalized amplitude is given by the colorbar.

IV.1.6 Thermo-optic and non-linear effects in silicon ring resonators

Silicon exhibits quite large non-linear and thermo-optic coefficients (see table IV.1), and the large intensity enhancement at resonance can lead to high optical powers circulating in the ring, even with relatively small input optical powers. For example, for a 5 μm ring, the finesse is typically $\mathcal{F} > 700$, which leads to an intensity enhancement of around 220. Hence, for a 10 mW input laser power, and with inclusion of the 3 dB loss at the input grating coupler, the circulating power at resonance can reach values as high as 1 W. While this large power is desirable for strong optomechanical interactions, is also results in significant thermo-optic and non-linear effects.

The goal of this section is to give a simplistic description of the non-linear and thermo-optic effects, that helps to understand some of the phenomenons that we observed experimentally. Giving a comprehensive and exhaustive description of non-linear effects in silicon ring resonators is out of the scope of this thesis, and can be found in [89, 90].

Non-linear effects

We consider three non-linear effects: the optical Kerr effect, two-photons absorption (TPA), and free-carrier effects.

The optical Kerr effect manifests itself as a variation of the refractive index with the intensity of light. It is quantified by the non-linear Kerr coefficient n_2, that relates the

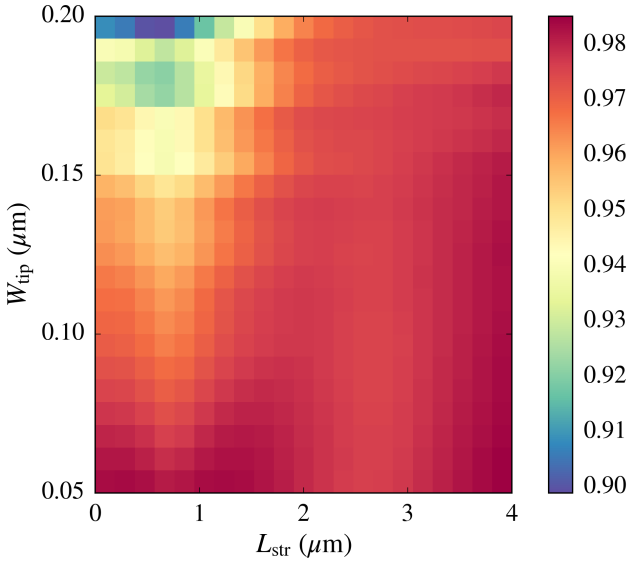

Figure IV.7 – 2D-FDTD calculation of the transmission rate after propagation of the electromagnetic field at proximity of one mechanical anchor, for various sets of parameters $(W_{\text{tip}}, L_{\text{str}})$.

variations of refractive index to the intensity:

$$n(I) = n_0 + n_2 I \tag{IV.18}$$

Two-Photons Absorption (TPA) corresponds to the non-linear simultaneous absorption of two photons, at a combined energy superior to the band gap, resulting in the absorption of both photons and in the creation of a free carrier. It is quantified by the TPA coefficient β, and is proportional to the square of the optical intensity.

Additionally to direct absorption of light, the free carriers generated by TPA (electrons and holes) also lead to two additional non-linear effects: Free Carrier Index changes (FCI) and Free Carrier Absorption (FCA). They are respectfully quantified by the parameters σ_n and σ_a. These two effects are proportional to the fourth power of the optical intensity.

When these three non-linear effects are considered, the evolution of the amplitude of the field A obeys the following equation [138, 90, 89]:

$$\frac{1}{A}\frac{\mathrm{d}A}{\mathrm{d}z} = -\frac{\alpha}{2} - \left(\frac{\beta}{2} - ikn_2\right)|A|^2 - \frac{\tau\beta}{4\hbar\omega}\left(\frac{\omega_r}{\omega}\right)^2(\sigma_a - 2ik\sigma_n)\,|A|^4 \tag{IV.19}$$

where α represents linear losses, β is the TPA coefficient, n_2 is the non-linear Kerr parameter, τ is the effective free carrier lifetime, $2\pi c/\omega_r = 1.55$ μm, $\sigma_a = 1.45 \times 10^{-17}$ cm^2, and $\sigma_n = -5.3 \times 10^{-21}$ cm^3 (in silicon).

Near and at resonance, non-linear effects and high optical power result in an increase of optical losses and in a change of refractive index.

	α_{th} (K^{-1})	κ_{th} (K^{-1})	n_2 (m^2/W)	β (cm/GW)
Si	2.57×10^{-6}	1.86×10^{-4}	4×10^{-18}	0.5
SiO2	0.5×10^{-6}	1.09×10^{-5}	2.7×10^{-20}	0.04
SiN	2.6×10^{-6}	2.44×10^{-5}	0.2×10^{-18}	–
GaAs	5.73×10^{-6}	2.3×10^{-4}	1.59×10^{-19}	10 - 15

Table IV.1 – Principle coefficients associated to thermo-optic and non-linear effects, for the main dielectric media used in photonic waveguides, at $\lambda = 1.55$ μm. β: TPA coefficient ; n_2: Nonlinear Kerr coefficient ; α_{th}: Thermal expansion coefficient ; κ_{th}: Thermo-optic coefficient. References for silicon: [129, 130, 90, 89, 131] ; for GaAs: [132, 133, 131] ; for SiO2: [134, 135, 136] ; for SiN: [135, 137]

A signature of TPA and FCA can be observed on the experimental spectrum, as the contrast becomes a function of optical power. For an over-coupled resonance, at low optical power, there is more light injected than lost at each turn ($\kappa > \alpha$). At high optical power, optical losses increase due to non-linear effects, which brings the resonance closer to the critical coupling condition and enhances the contrast. For an under-coupled resonance, by similar arguments, the resonance is brought further from critical coupling, and the contrast is degraded.

The optical Kerr effect and the FCI change are more difficult to observe. On the experimental spectrum, there is a shift of the resonant wavelength, but it is largely dominated by the thermo-optic effect. The latter is particularly important in our case, because of a poor heat outflow.

Thermo-optic effect

Additionally to non-linear effects, there is a variation of the refractive index with temperature, know as thermo-optic effect. It comes as a result of the heat generation due to linear absorption, TPA and FCA, and is hence closely related to non-linear effects.

Silicon ring resonators are known to be highly sensitive to thermal fluctuations [139, 130, 140]. Additionally, because suspended ring resonators are standing in the Air with only a small number of arms and a silica pedestal to insure thermal conduction, they present a very poor heat outflow toward the environment, which emphasizes thermal effects.

Formally, the modification of the temperature in the ring resonator actually results in two phenomenons:

1. Thermal expansion of the ring, responsible of both a photo-elastic effect and a

modulation of the cavity length.

2. Change of thermal energy, responsible of the thermo-optic effect.

However, the thermal expansion of silicon is two order of magnitude smaller than its thermo-optic coefficient[4] (see table IV.1), and we only consider the second effect. For a guided wave, it results in a modification of the effective refractive index, which in turn modifies the resonant wavelength:

$$\frac{\partial \lambda_r}{\partial T} = \frac{\lambda_r}{n_g} \frac{\partial n_{\text{eff}}}{\partial T} \tag{IV.20}$$

and the resonant wavelength temperature dependence is simplified to the first terms of its Taylor expansion:

$$\lambda_r(T) = \lambda_r(T_0) + (T - T_0) \frac{\partial \lambda_r}{\partial T}(T_0) \tag{IV.21}$$

where T_0 is the ambient laboratory temperature, and T is the temperature inside the optical cavity.

Combining equations (IV.20) and (IV.21), the temperature shift is related to the resonant wavelength shift by:

$$\Delta T = \Delta \lambda_r \frac{n_g}{\lambda_r} \left(\frac{\partial n_{\text{eff}}}{\partial T} \right)^{-1} \tag{IV.22}$$

On the following, we note κ_{th}^{eff} the thermo-optic coefficient associated to the effective index.

On the other hand, at steady state, the amount of circulating optical power that is converted to heat is equal to the heat flow towards the substrate, and the variation of temperature reads:

$$\Delta T = \frac{A}{G} P_{\text{circ}} \tag{IV.23}$$

where A is the fraction of circulating optical power that is absorbed and turned into heat within the ring, and G is the thermal conductance between the ring and the substrate, in W/K. In the previous equation, we did not consider heat outflow from the ring to the air environment. This assumption is reasonable when working in a vacuum environment (which is the case in all our optomechanical experiments), but maybe less when working in an air environment. Also, certain models consider a different temperature between the substrate and the environment [135], but we believed it was not necessary to apply in our case.

[4]The thermal expansion coefficient must actually be multiplied by the effective index (*i.e.* by $\equiv 2$) to give sense to this comparison.

Calculation of A, G, and κ_{th}^{eff} in the SRR

Optical power turned into heat: A is the fraction of optical power that is absorbed and turned into heat. It includes linear absorption, TPA, and FCA. To the best of our knowledge, A is difficult to properly calculate, and is often rather obtained experimentally, by measuring $\Delta\lambda_r$ and using equations (IV.23), (IV.22), (IV.27), and (IV.26).

Thermal conductance: We respectively note G_A, G_D and G_P the thermal conductance of the arms, of the silicon disk above the pedestal, and of the pedestal, such that:

$$1/G = 1/G_A + 1/G_D + 1/G_P \tag{IV.24}$$

The thermal conductances are functions of the thermal conductivities of silicon and silica, $\kappa_{\text{Si}} = 149$ W/(m.K) and $\kappa_{\text{SiO2}} = 1.4$ W/(m.K), and of the geometry parameters [141]:

$$\frac{1}{G} = \frac{1}{\kappa_{\text{Si}}} \frac{L_A}{\text{N}_A W_A H} + \frac{1}{\kappa_{\text{Si}}} \frac{H}{\pi (R_i - L_A)^2} + \frac{1}{\kappa_{\text{SiO2}}} \frac{H_P}{\pi R_P^2} \tag{IV.25}$$

where H is the silicon height ($H = 220$ nm in all our designs), $R_i = R - W/2$ is the inner ring radius, N_A is the number of arms, W_A is the width of the arms, L_A is the length of the arms, R_P is the pedestal radius, and H_P is the pedestal height.

In practise, because $\kappa_{th}^{\text{SiO2}} \ll \kappa_{th}^{\text{Si}}$, the contributions from the ring and the silicon disk vanish in front of the contribution of the silica pedestal. The contribution from the silicon arms is however quite significant and cannot be ignored. Under this assumption, the thermal conductance reduces to:

$$G = \frac{\kappa_{th}^{\text{SiO2}} \kappa_{th}^{\text{Si}} N_A W_A H \pi R_P^2}{\kappa_{th}^{\text{SiO2}} \pi R_P^2 L_A + \kappa_{th}^{\text{Si}} H_P N_A W_A H} \tag{IV.26}$$

Effective thermo-optic coefficient: Based on a FEM mode solver and on the thermo-optic coefficient of silicon, we calculated:

$$\frac{\partial n_{\text{eff}}}{\partial T} = 0.973 \times 10^{-4} \text{ K}^{-1} \tag{IV.27}$$

This value is almost two times smaller than the thermo-optic coefficient of silicon (see table IV.1), which is attributed to the fact that the evanescent field propagating in the air.

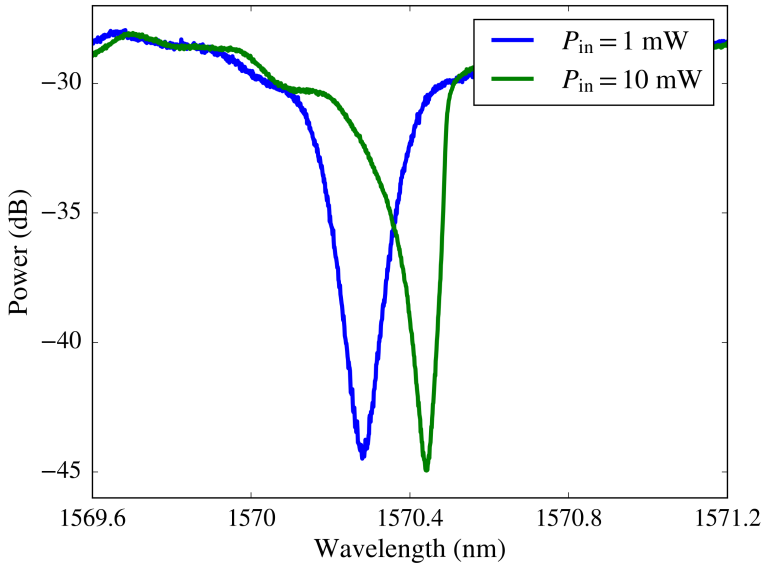

Figure IV.8 – Observation of Optical bistability.

Optical bistability

Non-linear and thermo-optic effect result in a contrast modification and a shift of the resonance wavelength. Additionally, they induce a modification of the form of the resonance peak, evolving from a Lorentzian shape to a triangular shape. This is a manifestation of optical bistability [142, 140].

IV.2 Mechanical description of suspended ring resonators

In the previous section, we described the optical properties of the suspended ring resonator. We now consider its mechanical vibrational modes.

The exact description of mechanical oscillations is a rather complicated problem, solved with numerical simulations. Yet, we begin the discussion with an analytical (and simplified) description of the vibrations of cantilevers and free circular ring. The suspended ring resonator can be seen, in a simplistic description, as a combination of these two systems, and that hence provide a "feeling" about the modes shapes and the scaling of their mechanical resonant frequencies.

We next provide numerical simulation results of the vibrations of various suspended ring resonators geometry, with discussion of the influence of the available design parameters. Finally, we investigate the origin of mechanical losses in suspended ring resonators.

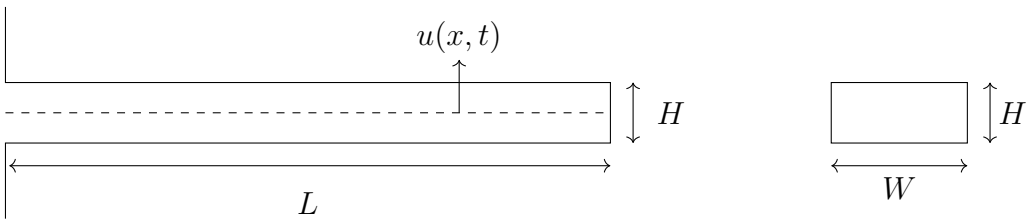

(a) Lateral view, in the (xz) plane

(b) Cross section, in the (xy) plane

Figure IV.9 – Lateral and cross section schematics of a thin and homogeneous simply clamped cantilever. L is the length of the beam, H its thickness, W its width. $u(x,t)$ is the displacement in the (xz) plane.

IV.2.1 Analytical description of mechanical vibrations

Cantilever theory

Silicon cantilevers, first proposed by Kurt Petersen [44] in the early '80s, are widely used in sensing applications such as mass sensing, chemical sensing or biological sensing [46]. The case of small deflections of thin, homogeneous cantilevers, is accurately described with Euler-Bernoulli beam theory [143]. In the following, we provide a rapid analytical description of the vibrations of such beam, based on this theory.

A schematic of the beam, with principal notations, is presented of figure IV.9. We note L the length of the beam and $S = W \times H$ its cross-section. The beam is described by the displacement of its center of line. The displacement in the (xz) plane is noted $u(x,t)$ and is associated to a momentum of inertia $I = H \times W^3/12$. It is described by Euler-Bernoulli equation [143, 46]:

$$EI \frac{\partial^4 u(x,t)}{\partial x^4} + \rho S \frac{\partial^2 u(x,t)}{\partial t^2} = 0 \tag{IV.28}$$

where E is the Young modulus, and ρ is the material density. The deflection in the (xy) plane can be obtained from the previous equation with an adapted momentum of inertia (the cross-section remains the same).

We assume separation of the spatial and temporal variables, and the solution is expanded with respect to the orthonormal basis $(\psi_n)_{n\in\mathbb{N}}$ of its mode shapes. The coefficients $(u_n)_{n\in\mathbb{N}}$ describe the temporal oscillation of the beam, at frequency $f_n = \omega_n/2\pi$.

$$u(x,t) = \sum_{n=0}^{+\infty} u_n(t)\psi_n(x) = \sum_{n=0}^{+\infty} U_n e^{-i\omega_n t}\,\psi_n(x) \tag{IV.29}$$

Equation (IV.28) becomes, for the n-th mode, an eigenvalues problem:

$$\frac{\partial^4 \psi_n(x)}{\partial x^4} - \lambda_n^4 \psi_n(x) = 0 \qquad \text{where } \lambda_n^4 = \omega_n^2 \frac{\rho S}{EI} \tag{IV.30}$$

The general form of the solutions of equation (IV.30) is:

$$\psi_n(x) = A_n \sinh \lambda_n x + B_n \cosh \lambda_n x + C_n \sin \lambda_n x + D_n \cos \lambda_n x \tag{IV.31}$$

where A_n, B_n, C_n and D_n are obtained from the boundary condition of the beam. The boundary conditions for a simply clamped cantilever and for a doubly clamped cantilever are presented on Table IV.2.

Simply clamped	Doubly clamped
$\psi_n(0) = 0$: There is no deflection at the base of the beam.	$\psi_n(0) = 0$: There is no deflection at the left-end of the beam.
$\psi_n^{'}(0) = 0$: The base of the beam is horizontal, and the derivative of the deflection is zero.	$\psi_n(L) = 0$: There is no deflection at the right-end of the beam.
$\psi_n^{''}(L) = 0$: There is no bending moment at the free-end of the beam.	$\psi_n^{'}(0) = 0$: The left-end of the beam is horizontal, and the derivative of the deflection is zero.
$\psi_n^{'''}(L) = 0$: There is no shearing force at the free-end of the beam.	$\psi_n^{'}(L) = 0$: The right-end of the beam is horizontal, and the derivative of the deflection is zero.

Table IV.2 – Boundary conditions for a simply clamped and a doubly clamped cantilever.

The eigenvalues λ_n are obtained by solving a transcendental equation on $\lambda_n L$. This equation is derived by setting to zero the determinant of the system formed by the boundary conditions. For a simply clamped cantilever and for a doubly clamped cantilever, the transcendental equation is presented on Table IV.3, along with the numerically calculated first four solutions.

Simply clamped	Doubly clamped
$\cos\lambda_n L \cosh\lambda_n L + 1 = 0$	$\cos\lambda_n L \cosh\lambda_n L - 1 = 0$
$\lambda_1 L = 1.875 \quad ; \quad \lambda_2 L = 4.694$	$\lambda_1 L = 4.730 \quad ; \quad \lambda_2 L = 7.853$
$\lambda_3 L = 7.854 \quad ; \quad \lambda_4 L = 10.995$	$\lambda_3 L = 10.996 \quad ; \quad \lambda_4 L = 14.137$

Table IV.3 – Transcendental equation for a simply clamped and a doubly clamped cantilever, and the associated first four solutions.

From the transcendental equation on $\lambda_n L$ and from the definition of λ_n, the resonant frequencies of the beam are deduced to be:

$$f_n = \frac{(\lambda_n L)^2}{4\pi L^2}\sqrt{\frac{E}{\rho}\frac{I}{S}} \tag{IV.32}$$

where the $\lambda_n L$ values are given on table IV.3.

Finally, the mode shapes $(\psi_n)_{n\in\mathbb{N}}$ only depend upon the parameter A_n, whose value is numerically calculated based on the $\lambda_n L$ values and one the fact that the mode shape is normalized to unity. For a simply clamped and for a doubly clamped cantilever, expressions of $(\psi_n)_{n\in\mathbb{N}}$ are given on table IV.4, along with the first four values of A_n. They are also plotted on figure IV.10.

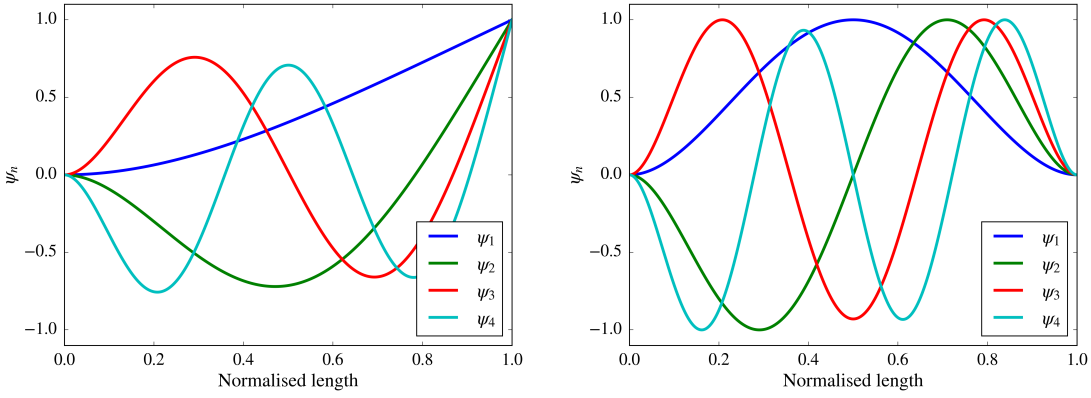

(a) Simply clamped cantilever

(b) Doubly clamped cantilever

Figure IV.10 – Mode shapes of the first four modes of vibrations of a simply clamped and a doubly clamped cantilever, against normalized length.

Simply clamped	$\psi_n(x) = A_n \left(\sinh \lambda_n x - \sin \lambda_n x - \dfrac{\sinh \lambda_n L + \sin \lambda_n L}{\cosh \lambda_n L + \cos \lambda_n L} \left(\cosh \lambda_n x - \cos \lambda_n x \right) \right)$
	$A_1 = -0.3671 \quad ; \quad A_2 = 0.5093 \quad ; \quad A_3 = -0.5000 \quad ; \quad A_4 = 0.5003$
Doubly clamped	$\psi_n(x) = A_n \left(\sinh \lambda_n x - \sin \lambda_n x - \dfrac{\sinh \lambda_n L - \sin \lambda_n L}{\cosh \lambda_n L - \cos \lambda_n L} \left(\cosh \lambda_n x - \cos \lambda_n x \right) \right)$
	$A_1 = -0.6186 \quad ; \quad A_2 = 0.6631 \quad ; \quad A_3 = -0.6611 \quad ; \quad A_4 = 0.6612$

Table IV.4 – Analytical expression of the first four mode shapes for a simply clamped and a doubly clamped cantilever.

Vibrations of a circular ring

We now consider the vibrations of a circular, thin and narrow ring, of rectangular cross-section. With an approach similar to cantilever theory, the vibrational mode shapes and frequencies can be obtained analytically. For example, see [143, 144, 72, 145]. To keep it brief, we only provide the results of such an analysis.

The vibrational modes can be distinguished between four families: extensional, inextensional (or flexural), and torsional, which are both in the plane of the ring[5], and flexural out of the plane of the ring. From axial symmetry arguments, one can show that each mode of vibration occurs in degenerate doublets.

Extensional vibrations This kind of mode is analogous to the longitudinal vibrational modes of a beam: the ring experiences longitudinal elongation and contraction along its own center line. If i denotes the number of wavelengths to the circumference, the frequencies of the modes of vibration of the ring are given by:

$$f_i = \frac{1}{2\pi R} \sqrt{\frac{E}{\rho}} \sqrt{1 + i^2} \tag{IV.33}$$

where R is the ring radius, E is the Young modulus, and ρ is the material density.

[5] In the sense that the center line of the ring remains in the same plane

In the case $i = 0$, the center line of the ring forms a circle of periodically varying radius. There is only purely radial displacement, with no rotation. This is known as the radial breathing mode.

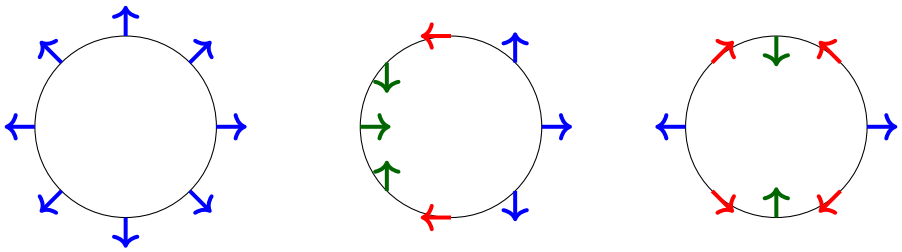

(a) $i = 0$ (b) $i = 1$ (c) $i = 2$

Figure IV.11 – Mode shape of the $i = 0, 1, 2$ extensional vibrational modes.

Inextensional vibrations Inextensional modes are flexural in-plane flexural vibrations, with little to no longitudinal elongation or contraction along the center line of the ring. Their vibration frequencies are given by:

$$f_i \underset{i\geq 2}{=} \frac{1}{2\pi R^2}\sqrt{\frac{E}{\rho}\frac{I_y}{S}}\frac{i(i^2-1)}{\sqrt{1+i^2}} \tag{IV.34}$$

where I_y is the moment of inertia of the cross section along vertical axis.

Equation (IV.34) begins at $i \geq 2$. $i = 0$ corresponds to a pure rotation of the ring, and $i = 1$ corresponds to translation of the solid ring with no deformation of its shape. There is no vibration in this two cases, and the fundamental mode of flexural vibration is therefore $i = 2$. Interestingly, however, this kind of mode appears in the case of SRR, as they couple with vibrations of the arms. This will be discussed in section IV.2.2.

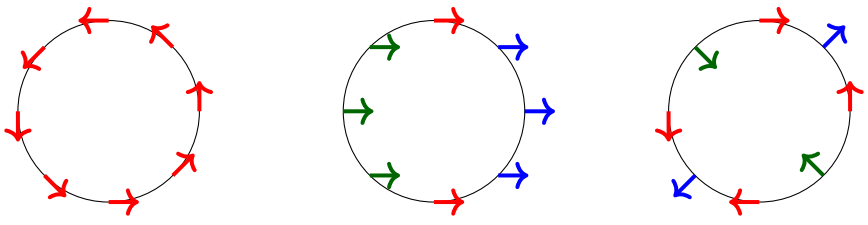

(a) $i = 0$ (b) $i = 1$ (c) $i = 2$

Figure IV.12 – Case $i = 0$ and $i = 1$, and mode shape of the $i = 2$ fundamental inextensional vibrational mode.

Torsional vibrations In this case, the cross section of the ring itself rotates around the center line of the ring. The vibration of the i-th mode occurs at frequency:

$$f_i = \frac{1}{2\pi R}\sqrt{\frac{E}{\rho}\frac{I_x}{I_p}}\sqrt{1+i^2} \tag{IV.35}$$

where I_x is the moment of inertia of the cross section along the x axis, and I_p is the polar moment of inertia of the cross section.

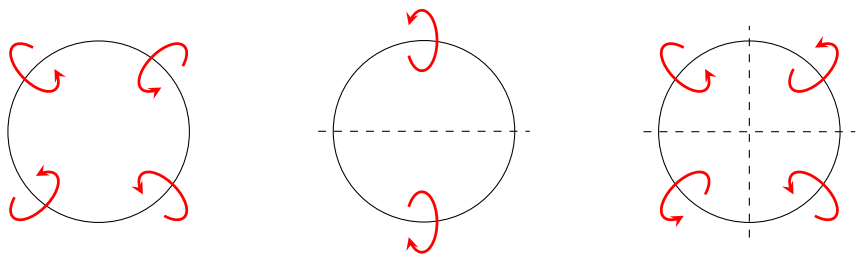

(a) $i = 0$ (b) $i = 1$ (c) $i = 2$

Figure IV.13 – Mode shape of the $i = 0, 1, 2$ torsional vibrational modes.

Out-of-plane flexural vibrations The resonance frequency of out-of-plane flexural modes is given by:

$$f_i \underset{i\geq 2}{=} \frac{1}{2\pi R^2}\sqrt{\frac{E}{\rho}\frac{I_x}{S}}\frac{i(i^2-1)}{\sqrt{(1+\nu)\beta+i^2}} \tag{IV.36}$$

where I_x is the moment of inertia along horizontal axis, ν is Poisson's ratio, and $\beta \approx 0.286/3$ is a parameter depending on the ratio between W and H, whose value is taken from [72]. Similarly to in-plane flexural vibrations, the fundamental out-of-plane flexural mode is $i = 2$.

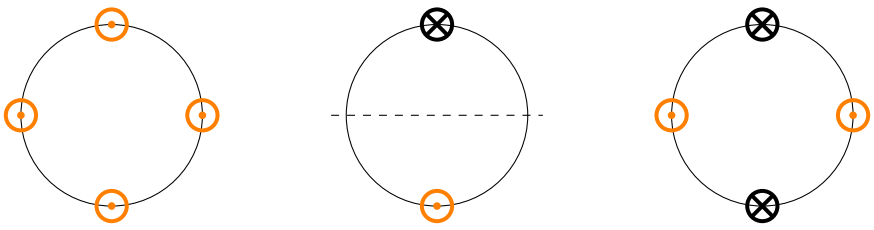

(a) $i = 0$ (b) $i = 1$ (c) $i = 2$

Figure IV.14 – Case $i = 0$ and $i = 1$, and mode shape of the $i = 2$ fundamental flexural out-of-plane mode.

Discussion

Spectrally, the in-plane and out-of-plane flexural modes have much lower frequencies than the torsional and extensional ones. This is a reminiscence of a beam behavior, whose stiffness approximately scale according to EI/L^3, $E/(1-\nu)$ and E for a flexural, torsional and extensional mode, that consequently appear at relative low, medium and high frequency.

IV.2.2 Numerical modeling of vibrational modes

Complementary (and more rigorously) to the "feeling" that we can get from the analytical models, we used 3D FEM mechanical simulations in order to study the mechanical behavior of SRR. The exact theoretical[6] design of the ring can be taken into account, as well of the fact that the pedestal and ring are not composed of the same material (respectively, silica and silicon). The eigenfrequency response can be calculated for various set of parameters in a reasonably fast time (generally less than 10 minutes, even for really small mesh elements and large number of modes). The commercial software COMSOL Multiphysics® was used to perform the simulations [146].

A sample of the large variety of mode shapes and frequencies that can be obtained is presented on figure IV.15, for the first three modes and frequencies of vibrations of SRR of various designs (higher order modes up to $n = 11$ can be found on appendix B). Between two geometries, similar mode shapes are found, but at different mechanical frequencies, and certain mode shapes are sometimes absent.

Comparison with the analytical model

The comparison between the analytical and numerical models reveals that similar mode shapes are found, but rather different resonant frequencies.

More precisely, the numerical mode shapes can be seen as a coupling between the mode shapes found with the analytical description of of a cantilever and of a circular ring. For example, figure IV.15a corresponds to the first in-plane flexural mode of vibration of the beam, coupled with the case $i = 0$ of flexural in-plane vibration of the ring. Figure IV.15b corresponds to the first out-of-plane flexural mode of vibration of the beam, coupled with the case $i = 0$ of flexural out-of-plane vibration of the ring. And so on ... Interestingly, the cases $i = 0$ and $i = 1$ encountered with flexural vibrations of the ring are now true vibrational modes.

The divergence between the analytical and numerical models in regard to the resonant frequencies is easily explained. With the analytical model, we consecutively considered the case of a free standing beam and of a free standing ring (without mechanical arms), but without coupling these two elements. It is hence expected to find erroneous resonant

[6] To be distinguished from the actually fabricated design

frequencies, as the stiffness of a suspended ring resonator is modified by the presence of the mechanical arms.

Influence of the design parameters

Between each SRR, we varied 5 mechanical parameters: the ring radius, the pedestal radius, the arms width, the number of arms, and the number of rings. Providing an exact description of the influence of each parameter is difficult. However, some tendencies can be identified from the analytical results.

First, as a result of the $1/R$ and $1/R^2$ dependency of the vibration frequency of the ring, and of the $1/L^2$ dependency of the vibration frequency of the beam, the ring and pedestal radii can be used as a way to control the vibration frequency of the SRR. Depending on the target, a wide control can be achieved. By only changing the ring radius, we mainly influence the ring oscillations. By only changing the pedestal radius, we mainly influence the beam oscillations. Finally, by changing both the ring and pedestal radii (*i.e.* by conserving the arm length), we influence both the ring and the beam oscillations.

The arms width can be used as a way to favor vibrational modes involving in-plane flexural vibration of the beam over vibrational modes involving out-of-plane flexural vibration of the beam, and vice-versa. Indeed, in-plane and out-of-plane flexural vibration frequencies of the beam only differ by the momentum of inertia that is considered (see equation IV.32). This momentum of inertia is $H \times W^3/12$ in the first case, and $H^3 \times W/12$ in the second case. Hence, by changing the arms width, we can rapidly modify the ratio of the momentums of inertia, and favor one direction over the other.

Finally, the number of arms and the number or rings is mainly a way to improve the mechanical solidity of the structure, and to reduce the risks of breaking or collapsing of the SRR during fabrication (see section V.1.3 for some examples). As a consequence, they can also result in the appearance or extinction of particular modes. For example, the addition of a supplementary ring also introduces new (and not really interesting in this case) mechanical modes, where the internal ring is put into motion.

Note that the addition of a second ring must be done far enough from the first ring, in order to avoid optical coupling between the internal and external ring, which would drastically increase optical losses. While we did not conduct such study, we also believe that the second ring could be used to isolate the outer ring from the substrate and reduce mechanical loses, in a way similar to the use of destructive interference elastic waves discussed in references [31, 147].

As a practical example of mechanical engineering, it is possible to control the resonant frequency of torsional modes (such as the ones presented on subplots (d) and (h) of figure IV.15), at a fixed ring radius, by playing on the pedestal radius. By taking a larger pedestal, it is possible to keep the arms short and to achieve a high mechanical frequency. Inversely, it can be reduced by decreasing the pedestal radius.

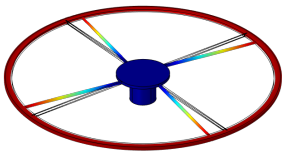

(a) $\Omega_0 = 0.0416$ MHz

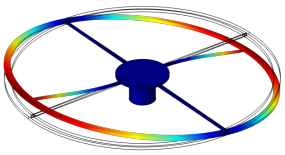

(b) $\Omega_1 = 0.91236$ MHz

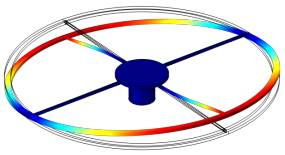

(c) $\Omega_2 = 0.91254$ MHz

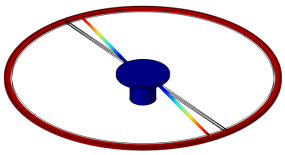

(d) $\Omega_0 = 0.029559$ MHz

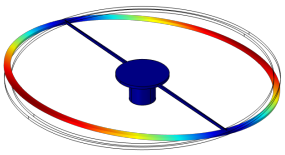

(e) $\Omega_1 = 0.14196$ MHz

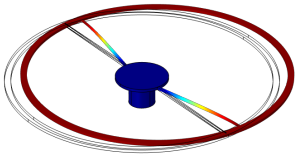

(f) $\Omega_2 = 0.14779$ MHz

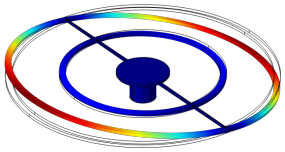

(g) $\Omega_0 = 0.14437$ MHz

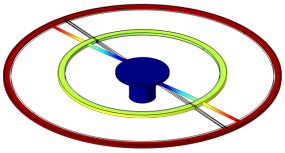

(h) $\Omega_1 = 0.15752$ MHz

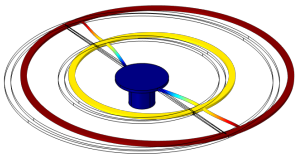

(i) $\Omega_2 = 0.6067$ MHz

Figure IV.15 – 3D-FEM simulation of the first three mechanical modes of a 10 μm radius SRR, with various design parameters.

Choice of design parameters

Typical design parameters of our suspended ring resonators are presented on table IV.5. While there is a large number of design parameters, we only explored a limited amount of designs[7]. We chose to vary the ring radius, the number of mechanical arms, and the number of rings. The pedestal and mechanical arms (in the sense of its cross section) are kept constant between each design. This (relatively) limited set of design parameters is justified by the exploratory nature of this work. Our aim was to demonstrate optomechanical interaction on suspended ring resonators integrated on a silicon chip. In this regard, a really precise engineering of the mechanical frequency and shape is not necessary. This should however be further explored in future work, when practical applications with targeted mechanical frequencies will be considered.

The design parameters choice is based on the numerical study and on the characteristics of our optomechanical test bench. Experimentally, our photodetector performances are improved below 14 MHz, and our measuring bandwidth is anyway limited to 50 MHz. Consequently, we took care to have a good number of mechanical modes falling below 14 MHz. By varying the number of arms, we also ensured to have a large variety of mechanical modes.

Ring radius (μm)	5, 15 or 25
Pedestal radius (μm)	2
Arms length (μm)	3, 13 or 23
Arms cross section	500 nm $\times$ 220 nm
Number of arms	2, 3 or 4
Number of rings	1 or 2
Waveguide width	500 nm
Waveguide height	220 nm

Table IV.5 – Typical design parameters of our suspended ring resonators.

IV.2.3 Mechanical losses in suspended ring resonators

We now briefly discuss the main sources of mechanical losses in suspended ring resonators, and some of the strategies that can be used to reduce them. Similarly to optical resonators, mechanical losses degrade the overall mechanical quality of the resonator and ultimately limit its performances, leading to a reduced sensitivity, a shorter coherence time, an increased power consumption, poorer phase noise performances, etc ... [147, 148, 149].

[7] Nevertheless, we still realized about 200 variations.

Dissipation in mechanical resonators can be separated between five distinct mechanisms, that are considered to be independent of each other [150]:

1. Radiation towards the substrate.
2. Damping and squeezed-film losses, due to the surrounding environment.
3. Surface-related losses.
4. Thermo-elastic damping.
5. Akhiezer effect.

Within this mechanisms, the last two are intrinsic to the medium and will always impose a limitation, will the others can be suppressed by proper design, fabrication and experimental choices. We expect radiation towards the substrate to be the dominant channel of mechanical dissipation in SRR.

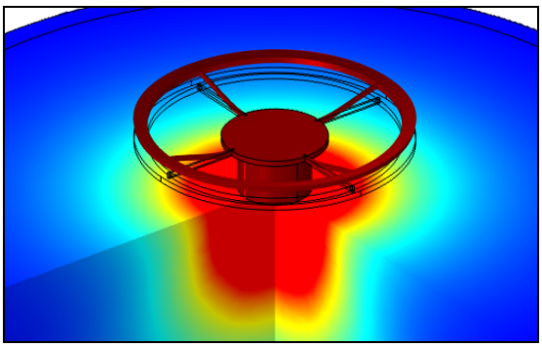

(a) Exemple of a FEM simulation. The colorbar range (not shown) have been truncated in order to emphasise the radiations.

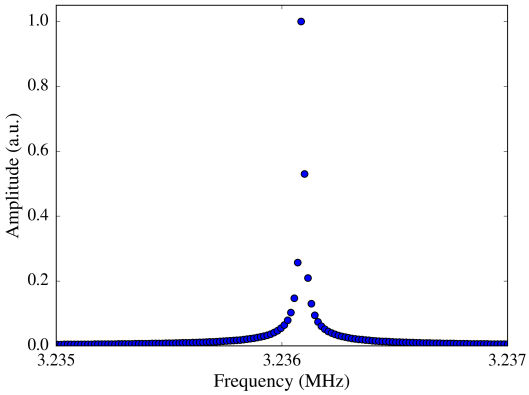

(b) Associated Lorentzian response, when including PMLs. Anchor losses are obtained from the FWHM of the peak.

Figure IV.16 – The strength of radiations losses towards the substrate can be estimated from mechanical numerical simulations including PMLs.

Radiation towards the substrate (anchor losses) One of the (if not the) major loss channel in micro- and nanomechanical resonators is the radiation of elastic waves towards the substrate, occurring at the anchor points [31, 147].

Anchor dissipation can be estimated via a FEM simulation including PML boundaries. Example of such a simulation is presented on figure IV.16. The mechanical spectrum is calculated by varying the excitation frequency of the system. Because the substrate is included on the simulation with PML boundaries, the radiation loss is effectively taken into account, and the anchor losses are extracted from the FWHM of the Lorentzian response.

These simulations provide a general idea about the order of magnitude, but can be out of touch from reality and should be considered with care. They are highly dependent on the choice of the PML parameters, that should and must be reasonably chosen, and actual radiation losses will also greatly depend on the real fabricated geometry of the supporting pedestal, which is hard to take into account in the simulations.

In the literature, several strategies have been proposed to reduce anchor dissipation. Phononic shielding was proven to be really effective [151], but it relies on sup-μm pitch lattices, that are not compatible with our μm sized resonators. Alternatively, mesa isolation [152] and "tuning fork-like" strategies [147, 118] exploit interference between several elastic waves. In the first case, the elastic wave is (partially) reflected back by the mesa onto the resonator. Depending on the distance between the two objects, constructive or destructive interference can happen, respectively decreasing or increasing radiation losses (for a given mechanical mode). This strategy is particularly efficient with out-plane modes. In the second case, the principle of a tuning fork is replicated. In a tuning fork, both arms are anti-symmetrically excited, such that the radiated elastic waves destructively interfere and cancel out at the anchor point. The same principle is used in double-disk resonators [147] and hollow-disk resonators [118]. In arm supported structures, it can be implemented by choosing a beam length equal to an odd multiple of a quarter wavelength of the selected mechanical mode [153].

We did not have time to implement this kind of solutions[8], but they should be investigated in future work in order to increase the resonator performances. In parallel, it must be pointed-out that the right selection of the mechanical mode is primordial to minimize the energy loss through the anchors. In particular, choosing a mode with an attaching point located at a nodal point will consequently mitigate this kind of losses.

Additionally, the radiation of elastic waves can occur between distinct mechanical modes vibrating at similar frequencies. This coupling between mechanical modes can be avoided by selecting mechanical modes well isolated in the mechanical spectrum, with an anti-crossing behavior [19, 118].

Viscosity of the environment (gas or liquid) The viscosity of the environment results in direct damping of the oscillator, with a (major) normal force exerted against surfaces perpendicular to the direction of propagation, and a (minor) shear force exerted against surfaces parallel to the direction of propagation. This damping is also amplified by a "squeezed-film" effect, because of the proximity of the substrate [154]. Considering that we are working under vacuum, viscous damping can safely be neglected.

We also point out the difference between ring resonators and disk resonators regarding this source of losses. It is expected that the out-of-plane modes of disk resonators will experience significantly larger damping than the in-plane modes, due to their larger area (πR^2 against $2\pi Rh$). For ring resonator, in-plane and out-of-plane modes have similar areas, and both should experience small damping, even outside vacuum.

[8] At some point, we preferred to begin the fabrication rather to focus on all the design aspects.

Surface losses The exact nature of the mechanisms behind surface-induced mechanical losses is not always well identified, and only scaling relations for beams and membranes are available, suggesting a linear increase of these losses with decreasing thickness [155]. We believe surface losses to be of small importance in our resonators, because the overall silicon surface quality is relatively good, with a roughness down to the order of the nm-scale, and because they are not considered to be a major dissipation channel in disk resonators of thickness similar to our geometries. Additionally, the surface to volume ratio of suspended ring resonators is really small, which will decrease the phenomenon even more.

In the future, it could yet be interesting to incorporate to our process flow a surface treatment step, that will benefit to both the optical and mechanical quality factors. Typically annealing at 1100^o C for an hour is included after encapsulation [156]. At the end of the thesis, we tried to incorporate thermal annealing in a different manner (800^o C for 10 seconds after the final etching step), principally in order to reduce optical losses due to the rugosity, but could not investigate its impact on mechanical surface losses.

Thermo-elastic damping (TED) and Akhiezer damping Thermo-elastic damping (TED) results from strain gradient inducing temperature gradients in the material. Under deformation, tensile stress regions cool down and compressive stress regions heats up. As a result, there is a thermal flow between these two regions, considered as a damping (the mechanical energy is converted to thermal energy). TED is an intrinsic loss mechanism: it is independent on the geometry and is only governed by the thermodynamic properties of the material [157]. For silicon, TED is expected to limit the quality factor to an upper value above the $10^4 - 10^5$ range, for μm scale thin beams [157, 158]. Because the measured quality factors on our devices are at most of 10^3, it is safe to neglect TED.

Akhiezer damping also relates to strained-induced perturbations of the thermal phonon equilibrium, but is a local process. Akhiezer damping is an intrinsic channel loss, independent on the geometry. The limitation it sets on the mechanical Q factor reads [156]:

$$Q_{Akh} = \frac{1}{f} \frac{\rho c^2 C_D^2}{2\pi \gamma_{\text{eff}}^2 \kappa T} \tag{IV.37}$$

where f is the mechanical frequency, ρ is the density, c is the velocity of the acoustic wave, C_D is the Debye velocity, γ_{eff} is the effective GrÃijneisen free parameter, κ is the thermal conductivity, and T is the temperature. From this formula, estimation of the $f \cdot Q$ products are around 10^{13} for silicon [158], which is way above our current values. It is also notable that Akhiezer damping can be reduced by working at low temperature.

IV.3 Optomechanical description of suspended ring resonators

On the previous sections, we considered separately the optical and mechanical behaviors of suspended ring resonators. In the following, we consider their coupled optomechanical behavior. The coupling between a single optical and a single mechanical modes is described by the generic optomechanical equations of motion introduced in the first chapter, with the necessity to properly define the coupling mechanisms and optical forces (that depend on the considered mechanical mode).

IV.3.1 Optical forces

Optical forces in the SRR are similar to the optical forces in straight waveguides presented in chapter III, with the exception of two differences.

First, the magnitude of optical forces is multiplied by the intensity enhancement parameter B^r, defined by equation (IV.7) (or in a analogous picture, by the finesse of the cavity). Typically, B^r can reach a value around 200, such that optical forces can reach values in to the μN / μm / mW range (compared to a few nN / μm / mW for a single waveguide).

The second minor difference resides on the slightly different field profile due to the bending of the waveguides constituting the ring, that "pushes" outward the optical field and creates a little imbalance between forces at the inner radius and forces at the outer radius.

As a result, the same general behavior is encountered: radiation pressure and optical gradient forces push the waveguides boundaries outward in the vertical and horizontal directions, while electrostrictive forces push them outward in the horizontal direction and inward in the vertical direction. These two forces are of the same order of magnitude, and they will principally excite in-plane mechanical modes, because their respective out-of-plane components consequently cancel each other.

We also expect a strong contribution from photothermal forces beyond the optical power threshold for non-linear behavior (typically beyond 10 mW at the laser input). Under this regime, photothermal forces should overcome all other forces and isotropically excite the mechanical modes. This is however difficult to access experimentally, because as we will see, the ring optical response is strongly modified under non-linear behavior, which effectively detunes the input laser far from resonance.

IV.3.2 Contributions to optomechanical coupling

Both dispersive and dissipative optomechanical coupling schemes are anticipated in a SRR.

Regarding dispersive coupling, we expect a geometric contribution and a photoeslatic contribution, which were introduced in chapter III. Additionally, we discuss the possible existence of a third contribution, arising in rotational mechanical modes from the optical Sagnac effect.

A dissipative coupling is also likely to happen in SRR. The motion of the ring regarding the bus waveguide will impact the relative overlap between the guided mode in each structure, and modify the evanescent coupling strength. In other words, the extrinsic cavity decay rate is a function of displacement, as discussed in chapter I.

There are hence four different contributions to the optomechanical coupling:

1. A geometric contribution, of coupling strength g_{geom}.
2. A photoelastic contribution, of coupling strength g_{pe}.
3. A dissipative contribution, of coupling strength κ_{om}.
4. A Sagnac contribution, of coupling strength g_{rot}.

Here, we stress again that the values of the coupling strengths depends on the mechanical mode under consideration. In particular, we only expect a Sagnac contribution in the case of a in-plane flexural mode of the circular ring (noted with $i = 0$ in the analytical model).

The first three contributions are discussed in the following. The Sagnac contribution is discussed in a separate section.

Geometric contribution

g_{geom} is calculated from equation (III.18). To do so, both the mechanical and optical mode shapes are computed. The mechanical displacement vector is calculated with a 3D-FEM simulation, and normalized such that $\mathrm{Max}\overrightarrow{q} = 1$. The electrical field is calculated with a 2D-FEM simulation assuming rotational symmetry.

Photoelastic contribution

g_{pe} is calculated from equation (III.20). Here, additionally to the optical mode, the internal strain must be computed. It is calculated during the same 3D-FEM simulation than the mechanical displacement.

Dissipative contribution

κ_{om} is calculated from equation (III.22), based on the results of the mechanical 3D-FEM simulation and on the knowledge of the guided modes in the ring and in the bus waveguide, obtained by optical 2D-FEM simulation.

Results & discussion

Typical optomechanical vacuum coupling strengths (*i.e.* after multiplication by the amplitude of mechanical zero point fluctuations) for the 8 first mechanical modes of a 10 μm ring with 3 arms and an internal mechanical ring are presented on table IV.6. This choice of illustration corresponds to a ring actually measured (in the next chapter). We find that the geometric contribution is largely dominant in comparison to the photoelastic and dissipative contributions.

$\Omega_m/2\pi$ (MHz)	x_{ZPF} (pm)	$g^0_{\mathrm{geom}}/2\pi$ (kHz)	$g^0_{\mathrm{pe}}/2\pi$ (kHz)	$\kappa^0_{\mathrm{om}}/2\pi$ (kHz)
0.199	4.860×10^{-2}	3.019×10^{-2}	-1.047×10^{-2}	-3.512×10^{-8}
0.947	3.757×10^{-2}	2.435	-3.082×10^{-2}	-1.047×10^{-5}
1.490	1.931×10^{-2}	-1.454×10^{1}	-1.048×10^{-3}	1.970×10^{-4}
2.434	2.056×10^{-2}	-0.993	-1.930×10^{-1}	-7.624×10^{-5}
2.470	1.773×10^{-2}	0.869	-1.754×10^{-2}	-2.100×10^{-7}
3.402	1.780×10^{-2}	0.192	-3.846×10^{-2}	1.693×10^{-6}
4.300	2.641×10^{-2}	-1.386	-2.846×10^{-1}	-4.625×10^{-5}
5.053	1.321×10^{-2}	1.173×10^{1}	-3.339×10^{-1}	-3.753×10^{-5}

Table IV.6 – Typical angular mechanical frequency, zero point fluctuations and optomechanical vacuum coupling strengths for a 10 μm radius SRR. The mode shapes are illustrated on figure IV.17.

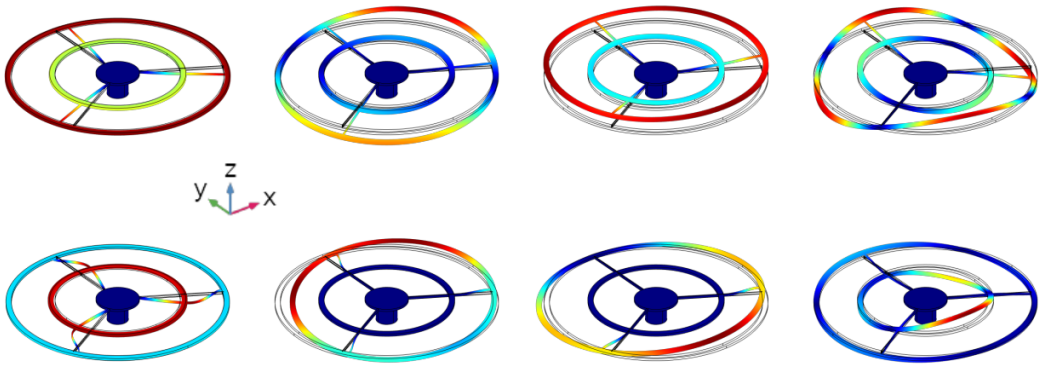

Figure IV.17 – Mode shapes of the mechanical modes presented on table IV.6 (from left to right, and from top to bottom).

Regarding the photoelastic contribution, its relatively weak value can be explained by the fact that most of the strain is contained in the supporting arms and not in the ring itself,

so that the field overlap with mechanical strain is relatively weak for most mechanical modes. Additionally, because the components of the photoelastic tensor p_{11}, p_{12} et p_{44} are of opposite signs in silicon, they tend to cancel each other out.

Regarding the dissipative contribution, a simple comparison of equations (III.18) and (III.22) explains the large difference between the orders of magnitude. In the geometric contribution, the product of the optical guided mode in the ring with itself is integrated within the ring. In contrast, in the dissipative contribution, the product is also integrated within the ring, but between the optical guided modes in the ring and in the waveguide. The latter is naturally weak within the ring, such that the integral is smaller than the previous one.

From the previous discussion and simulations, it appears that geometric contribution to optomechanical coupling is largely dominant. The obtained orders of magnitude, in the kHz range, which is consistent with state-of-the-art values on similar geometries. In particular, we observe that two mechanical modes (at 1.490 and 5.053 MHz) exhibit an optomechanical coupling rate one order of magnitude above the others. These two modes are rotationally invariant around the center of the ring and all radial displacements add up constructively, efficiently modulating the ring perimeter. In contrast, the cavity length remains almost unchanged with other modes that do not exhibit this rotational symmetry, and the coupling rate is weaker (see figure IV.18).

Note that we did not observe a radial breathing mode with our suspended ring resonators in the frequency range that we considered (below 50 MHz - chosen in line with our experimental setup). The radial breathing mode of suspended ring resonators will fall at higher mechanical frequency, as it implies in-plane elongation modes of the mechanical arms. It should exhibit a large geometric contribution to the optomechanical coupling rate, as already observed several times in suspended disk resonators. For example, in GaAs disks, the coupling strength of the first radial breathing mode is in the GHz range, while other coupling strengths are in the kHz range, similarly to our device [132]. In the future, an adaptation of the experimental setup and/or of the mechanical design, allowing higher mechanical frequency monitoring or for this mode to fall at lower mechanical frequencies, should be an axis of research.

Variation of the index profile due to the vertical movement Actually, an additional fifth effect could also occur. When the waveguide is subject to vertical movement, it gets closer and further from the substrate. Hence, the vertical index profile changes, which could lead to an optomechanical contribution. This kind of coupling have already been demonstrated with low confinement waveguides [159]. We do not expect this kind of coupling to be significant in our case, because we use highly confined TE_0 guided modes, with a substrate placed 2 μm below the ring. As a matter of fact, we verified by numerical simulations that the effective guided index is not modified when we reduce the distance between the ring and the substrate down to 1 μm. Accordingly, this effect can safely be neglected.

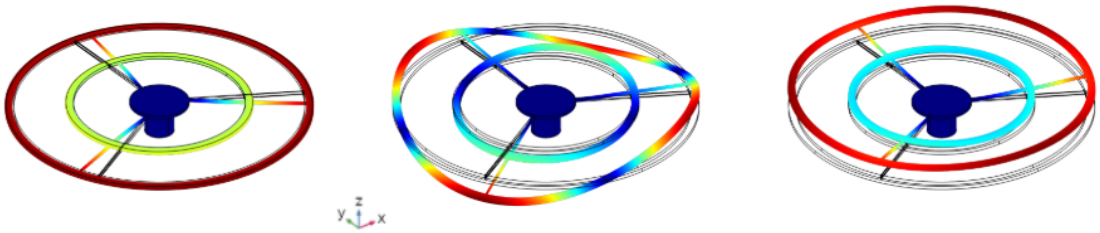

Figure IV.18 – From left to right: visualization of the mechanical modes at 0.199 MHz, 2.434 and 1.490 MHz, with exaggerated deformation. The surface color indicates normalized total displacement between -1 (blue) and +1 (red). In the first case, there is no ring deformation (pure rotation), and the cavity length remains unchanged. In the second case, the positive and negative out-of-plane deformations compensate each other and the cavity lengths is only slightly changed. In the third case, all the radial displacements add up constructively and the cavity length is more efficiently changed.

IV.3.3 Sagnac contribution

Qualitative description

The first mechanical mode at 200 kHz, presented on table IV.6 and figure IV.18, is a rotational mode. According to the perturbation approach and equation (III.18), only variations of the boundaries normal to the direction of propagation should shift the resonant frequency. By opposition, a rotation is conducted along the direction of propagation, and should not induce optomechanical coupling on its own. This is verified on table IV.6: this mode presents weak coupling rates, with g_0 around 10 Hz.

While this is true for a stand alone wave, the situation is different when we consider a situation where Clock-Wise (CW) and Counter Clock-Wise (CCW) waves are propagating in the ring. In this case, a Sagnac effect happens, leading to a phase mismatch Θ between the two opposite waves, proportional to the angular velocity Ω_{rot} [160]:

$$\Theta = \pm \frac{\mathcal{P}^2 \Omega_{\text{rot}}}{c\lambda} \tag{IV.38}$$

In the case of two CW and CCW waves, rotation of the ring could therefore induce optomechanical coupling. The presence of two opposite waves actually occurs in practice. While an ideal ring is unidirectional, actual rings present a coupling between their CW and CCW waves due to fabrication imperfections. This manifests itself on the Optical spectrum by the presence of double peaks (see Section V.2.3). Under rotation, as the phase mismatch between the CW and CCW waves is modified by the Sagnac effect, the spacing between the two resonances will be modified, as represented on figure IV.19.

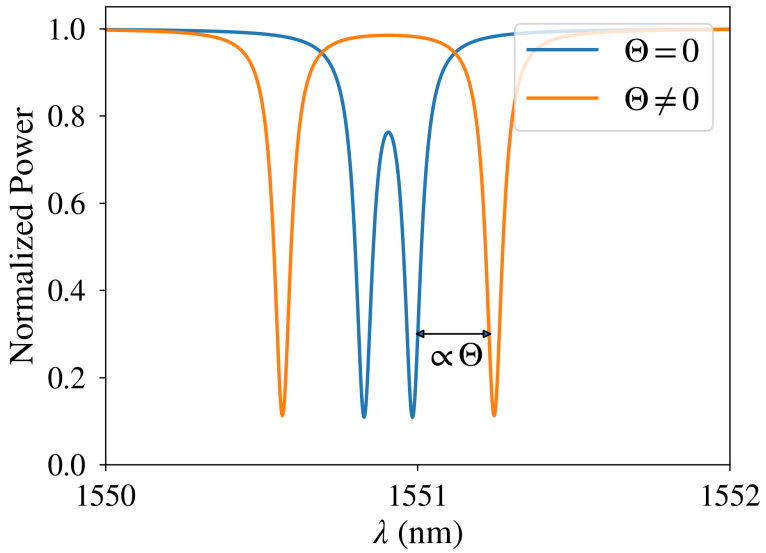

Figure IV.19 – The blue curve presents a double peak resonance, due to coupling between CV and CCW waves propagating in the SRR, with no rotation. The green curve presents the same geometry, under rotation at Ω_{rot}. The phase mismatch due to Sagnac effect is $\Theta \neq 0$, which modifies the spacing between the two peaks. For the sake of clarity, the parameters used to draw the curves are chosen in order to emphasize the phenomenon

Analytical description

We consider a purely rotational case where the ring is not deformed, so that we can ignore the "non Sagnac" contributions to optomechanical coupling. Hence, the mechanical oscillator is know described as a torsional pendulum (see below).

Here, we are interested in the effect of the angular velocity Ω_{rot} on the dynamics. As a result, we define a rotational optomechanical coupling strength parameter by:

$$g_{\text{rot}} = \frac{\partial \omega_r}{\partial \Omega_{\text{rot}}} \tag{IV.39}$$

Note that g_{rot} is here in units of Hz/(rad/s), while other optomechanical coupling strength are in units of Hz/m. In other words, these quantities are not comparable as such, as a natural result from the fact that their intrinsic origin is different. However, their associated optomechanical vacuum coupling strengths, in Hz, can be used for comparison.

In our case, the Sagnac shift of the optical frequency due to rotation is expressed by [161, 162, 160]:

$$\Delta\omega_{\text{Sag}} = \frac{\mathcal{P}}{\lambda_0 n_{\text{eff}}}\Omega_{\text{rot}} \tag{IV.40}$$

where $\mathcal{P} = 2\pi R$ is the perimeter and λ_0 is the wavelength in vacuum. It simply follows:

$$g_{\text{rot}} = \frac{\mathcal{P}}{\lambda_0 n_{\text{eff}}} \tag{IV.41}$$

This is really different from usual optomechanical contributions, where the coupling *inversely* scale with the cavity dimensions. Hence, the optomechanical coupling strength arising from a rotation will benefit from *larger* cavities, which is at first sight not favorable in our case.

Equations of motion: Using g_{rot} and describing the mechanical oscillator as a torsional pendulum, the equations of motion read:

$$\begin{cases} \dfrac{\mathrm{d}a}{\mathrm{d}t} = \left[i\left(\Delta - g_{\text{rot}}\left(\Omega_{\text{rot}} + \dfrac{\mathrm{d}\theta}{\mathrm{d}t}\right)\right) - \dfrac{\kappa}{2}\right] a + \sqrt{\kappa_e} s_{in} \\ \dfrac{\mathrm{d}^2\theta}{\mathrm{d}t^2} + \Gamma_m \dfrac{\mathrm{d}\theta}{\mathrm{d}t} + \Omega_m^2(\theta - \theta_0) = -\dfrac{\hbar g_{\text{rot}}}{J_{\text{eff}}}|a(t)|^2 + \dfrac{F_L(t)}{J_{\text{eff}}} \end{cases} \tag{IV.42}$$

where θ is the torsional angle, Ω_{rot} is an external angular velocity applied to the system, $J_{\text{eff}} \equiv m_{\text{eff}} R^2$ is the effective moment of inertia, and all the influence of Ω_{rot} on the mechanical motion is effectively included on $F_L(t)$. In the following, we note $\Delta_r = \Delta - g_{\text{rot}}\Omega_{\text{rot}}$.

Following the same linearization approach that in the first chapter, we obtain:

$$\begin{cases} \dfrac{\mathrm{d}\delta a}{\mathrm{d}t} = \left[i\Delta_r - \dfrac{\kappa}{2}\right] \delta a - i g_{\text{rot}} \bar{a} \dfrac{\mathrm{d}\delta\theta}{\mathrm{d}t} \\ \dfrac{\mathrm{d}^2\delta\theta}{\mathrm{d}t^2} + \Gamma_m \dfrac{\mathrm{d}\delta\theta}{\mathrm{d}t} + \Omega_m^2 \delta\theta = -\dfrac{\hbar g_{\text{rot}}}{J_{\text{eff}}}(\bar{a}^*\delta a + \bar{a}\delta a^*) + \dfrac{F_L(t)}{J_{\text{eff}}} \end{cases} \tag{IV.43}$$

It follows:

$$\begin{cases} \delta a(\omega) = \dfrac{\omega g_{\text{rot}} \bar{a}}{i\left(\Delta_r + \omega\right) - \kappa/2} \delta\theta(\omega) \\ \delta\theta(\omega) = \dfrac{F_L(\omega)}{J_{\text{eff}}\left(\Omega_m^2 - \omega^2 - i\Gamma_m\omega\right) + \Sigma_r(\omega)} \end{cases} \tag{IV.44}$$

where the optomechanical self-energy $\Sigma_r(\omega)$ contains all the optomechanical interaction

and reads:

$$\Sigma_r(\omega) = \frac{\hbar\omega g_{\text{rot}}^2 |\bar{a}|^2}{J_{\text{eff}}} \left(\frac{1}{i\left(\Delta_r + \omega\right) - \kappa/2} + \frac{1}{i\left(\Delta_r - \omega\right) + \kappa/2} \right) \tag{IV.45}$$

Optical spring: The optical spring effect is determined by:

$$\delta\Omega_m(\omega) = \frac{\hbar g_{\text{rot}}^2 |\bar{a}|^2}{2J_{\text{eff}}} \frac{\kappa}{2} \left(\frac{1}{\left(\Delta_r - \omega\right)^2 + \left(\kappa/2\right)^2} - \frac{1}{\left(\Delta_r + \omega\right)^2 + \left(\kappa/2\right)^2} \right) \tag{IV.46}$$

Optomechanical damping: The optomechanical damping rate is:

$$\Gamma_{\text{opt}} = \frac{\hbar g_{\text{rot}}^2 |\bar{a}|^2}{J_{\text{eff}}} \left(\frac{\Delta_r - \omega}{\left(\Delta_r - \omega\right)^2 + \left(\kappa/2\right)^2} + \frac{\Delta_r + \omega}{\left(\Delta_r + \omega\right)^2 + \left(\kappa/2\right)^2} \right) \tag{IV.47}$$

Application: an optomechanical gyroscope

Traditionally, optical gyroscopes operate by measuring the Sagnac shift $\Delta\omega_{\text{Sag}}$ (equation (IV.40)) with two CW and CCW waves propagating in an optical cavity. Because $\Delta\omega_{\text{Sag}}$ scales with R, a size reduction is unfavorable as it strongly limits the sensitivity.

Alternatively, with an optomechanical resonator, we can change the picture and decide to monitor the variations of the mechanical frequency $\delta\Omega_m$ rather than the optical Sagnac shift $\Delta\omega_{\text{Sag}}$. Indeed, because of the optomechanical interaction, the optical spring is related to the rotation by $\Delta_r = \Delta - g_{\text{rot}}\Omega_{\text{rot}}$, so that any change in the external angular velocity Ω_{rot} is reflected on the mechanical spectrum.

Optomechanical gyroscopes could be interesting because their sensitivity inversely scale with the ring radius, contrary to purely optical ones. It can be intuited from the observation of the fact that the prefactor of the optical spring does not depend on the size of the resonator, because the effective moment of inertia scales with R^2 and g_{rot} scales with R. [9]

This point is illustrated on the left subplot of figure IV.20, where we plotted the optical spring $\delta\Omega_m$ for different ring radii, in a resolved sideband regime. For each radius, we observe that the sidebands of maximal and minimal optical spring effect appear at higher intensity and angular velocity when the radius is decreased. This subplot is at zero optical detuning, *i.e.* $\omega_L = \omega_r$. On the right subplot of figure IV.20, we plotted the optical spring $\delta\Omega_m$ at a fixed 5 μm ring radius, but with various detuning. We observe that as the detuning is increased, the sideband intensity is kept constant but appears at

[9] Note that this is only a preliminary observation ; other parameters such as Δ_r, Ω_m, and κ also depend on the radius

lower angular velocity. This shows that the targeted angular velocity can be switched by means of a precise control of the optical detuning.

An obvious comment about these figures is that the observed value of $\delta\Omega_m$, in the nHz/mW range, is extremely small and is impossible to assess under these conditions. For instance, the resolution bandwidth of commercial spectrum analyzers is at best at 1 Hz, which could be attained with an optical quality factor $Q_{\text{opt}} \equiv 5 \times 10^8$. This order of magnitude is 500 times higher than state-of-the-art realizations, and is not conceivable with present fabrication techniques. While not explored during this work, an other way to enhance the sensitivity could be to realize more complex anchor geometries. For example, curved arms are a strategy already used in integrated microelectromechanical gyroscopes [163, 164], that could easily be adapted to an optomechanical design.

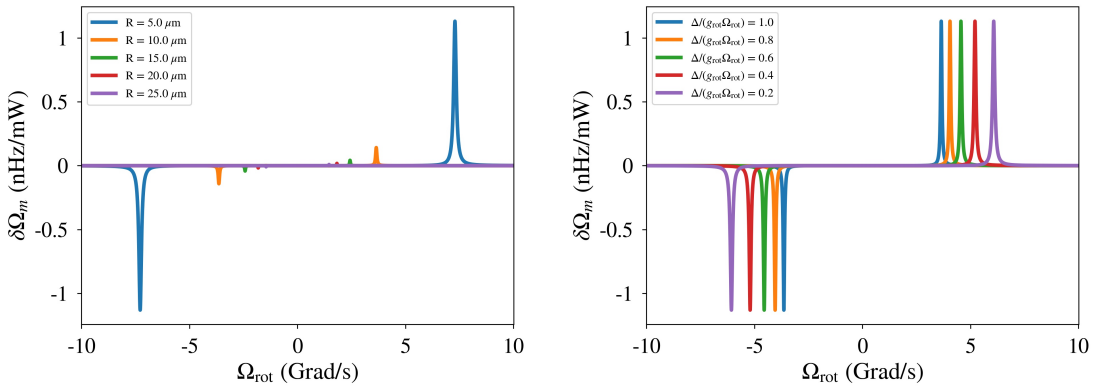

(a) The radius is varied, the detuning is zero.

(b) The detuning is varied, the radius is 5 μm.

Figure IV.20 – Evolution of the optical spring effect. We chose state-of-the-art (yet realistic) values $\Omega_m = 1$ GHz, $m_{\text{eff}} = 5$ fg, $Q_{\text{opt}} = 10^6$, for the 5 μm radius, and considered a R^3 and R dependence of the effective mass and optical quality factor with increasing radii. We suppose that the mechanical frequency is kept constant by playing on the arm length between two radii..

Despite the previous propositions, it seems difficult to efficiently increase the theoretical value of $\delta\Omega_m$ with stand-alone silicon suspended ring resonators at time of writing. Among other ways to improve their performances, the use of arrays of optomechanical gyroscope has been shown to increase the Sagnac shift in optical gyroscopes [165, 166] and could also be advantageous in optomechanical gyroscope. An other way could be to select an other photonic platform (such as SiN or GaAs), allowing further size reduction and/or better photonic performances. This is however highly hypothetical and more precise work needs to be done in order to validate or refute these options. Yet, the fact that the sensitivity of the optomechanical gyroscope inversely scales with its size appears interesting enough to be worth mentioning.

Aside from the gyroscopic application, one can also notice that the expression for the optical spring and optomechanical damping rate of a rotational optomechanical resonator

are very similar to what we found in chapter I in the case of a vibrational optomechanical resonator (equations (I.23) and (I.25))[10], with the difference that the dependence of the fractions numerators towards the parameters $\Delta - \omega$ and κ are switched. In chapter I, optical spring was governed by $\Delta - \omega$ and optomechanical damping was governed by κ. Here, it is the opposite. While we are not sure how this could be used, it is interesting enough to be worth mentioning.

Conclusion

In this chapter, we have studied the optical, mechanical, and optomechanical behavior of suspended ring resonators, from a theoretical point of view.

On the optical part, we have presented the general properties of suspended ring resonators, before discussing the influence of the mechanical suspension arms on optical losses, and of thermal and non-linear effects, that affect the optical lineshape at high optical power.

On the mechanical part, we have presented the large variety of mechanical modes that can be engineered with suspended ring resonators, based on analytical and numerical modeling. We also briefly discussed mechanical losses.

Finally, on the optomechanical part, we showed that the optomechanical interactions are mainly dominated by cavity length variations, and discussed a possible optomechanical interaction due to the Sagnac effect that arises between two opposite traveling waves. The latter could find applications as an integrated on-chip optomechanical gyroscope, with the advantage of not suffering from size reduction.

In the next chapter, we will discuss the realization of suspended ring resonators, along with optical and optomechanical measurements.

[10] Where we had used $\hbar g_{\mathrm{om}}^2 / m_{\mathrm{eff}} = 2\Omega_m g_0^2$

CHAPTER V

Realization of suspended ring resonators

In this chapter, we report on the realization of suspended ring resonators, from fabrication to characterization. At the beginning of this work, while there was a heavy baggage of photonic knowledge and tools in the team, we had no experience with cavity optomechanics. As a consequence, multiple fabrication runs, conducted all along the thesis, were necessary in order to properly achieve the suspension step. This is discussed in the first section of this chapter.

Photonic experiments are presented on the second section. While they are supposed to only be a preliminary experimental step to select the best devices, they also allowed us to investigate optical losses, thermo-optic effects and non-linear effects in SRR, and to achieve a better knowledge about their general optical behavior.

In parallel to fabrication and photonic experiments, a dedicated test bench was built in order to perform optomechanical characterization under vacuum. Unfortunately, due to fabrication difficulties and the novelty of the experiment in regard to the team, we had not enough time to conduct in-depth optomechanical experiments on SRR. In the third section, we present preliminary optomechanical results, that will be further investigated in the future.

V.1 Fabrication of suspended ring resonators

V.1.1 Introduction

In this section, we present the technological fabrication of SRR. It was conducted at the CEA-Leti cleanroom, a silicon-oriented facility with almost industrial fabrication processes. This last point comes at both a profit and a cost. On the one hand, it allows to rely on well-mastered, reproducible & state-of-the-art processes and recipes. On the other hand, there is slow inertia associated to the development of new processes and recipes, which turns unfavorable when dealing with exotic geometries.

The fabrication is conducted over a 200 mm SOI wafer. The general idea underlying the fabrication process is quite straightforward. General steps to be followed are:

1. Patterning of the Grating Couplers (GC).
2. Patterning of the photonic and optomechanical structures.
3. Encapsulation of the photonic structures.
4. Release of the optomechanical structures.

For SRR, most of the work was focused on the fourth step. The main problem that we faced was collapsing and/or sticking of the free standing waveguides and rings after the release.

It should be noted that we realized suspended ring resonators and sub-wavelength grating optomechanical cavities (discussed in part III) over the same wafers. Because the latter exhibit really small dimensions (down to 50 nm) some of the choices that were made here are a result of a compromise between these two families of devices. In particular, we used shape e-beam lithography in order to pattern the waveguide level, instead of classical UV photo-lithography.

The mask layout that we drew is presented on appendix C.

V.1.2 Process flow

The detailed fabrication steps are:

1. Partial etching of the Grating Couplers (figure V.1):
   (a) Resist deposition.
   (b) Resist insulation & development (UV photo-lithography).
   (c) 70 nm partial etching of the Si layer.
   (d) Resist removal.

2. Waveguide etching (figure V.2):
   (a) Resist deposition, insulation & development (e-beam lithography).
   (b) Complete etching of the Si layer.
   (c) Resist removal.
3. Waveguide encapsulation (figure V.3):
   (a) Deposition of a 1100 nm thick SiO_2 layer, by HDP (High Density Plasma).
   (b) CMP (Chemical Mechanical Polishing) of the SiO_2 layer, down to 700 nm above the waveguide level.
4. Waveguide release (figure V.4):
   (a) Deposition of a 1800 nm thick SiO_2 layer, by HDP.
   (b) Resist deposition, insulation & development.
   (c) 2300 nm dry etching of the SiO_2 layer, down to 200 nm above the waveguide level.
   (d) Resist removal.
   (e) Wet etching of the BOX and SiO_2 layers.

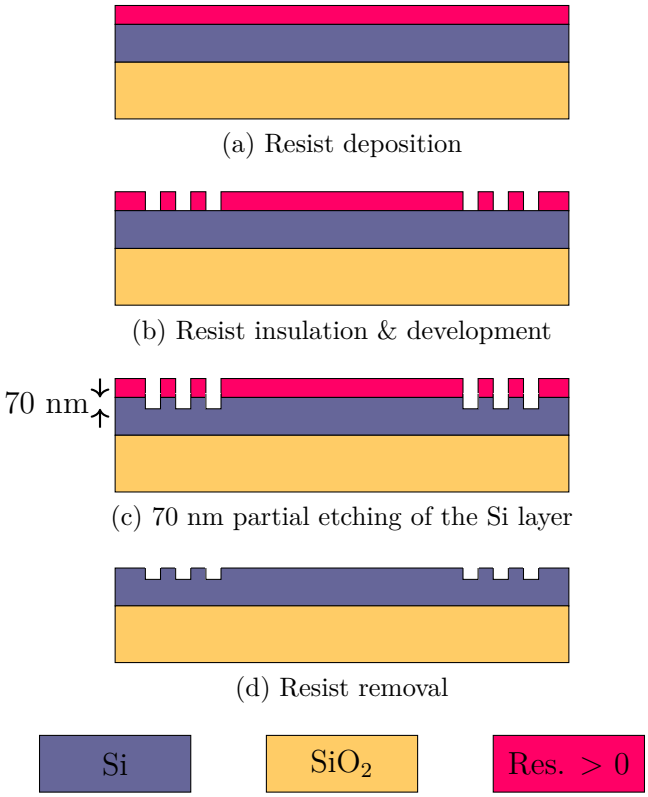

Figure V.1 – Partial etching of the Grating Couplers. Here and in the following, we do not represent the whole SOI wafer, but only the two top silicon and silicon dioxide layers.

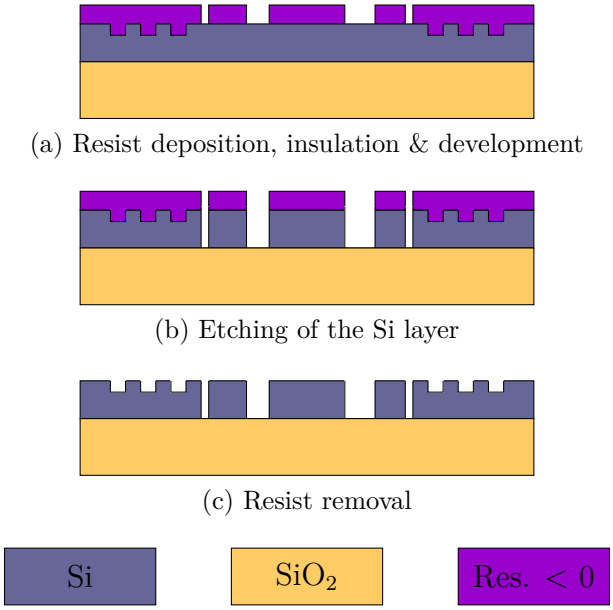

Figure V.2 – Waveguide etching.

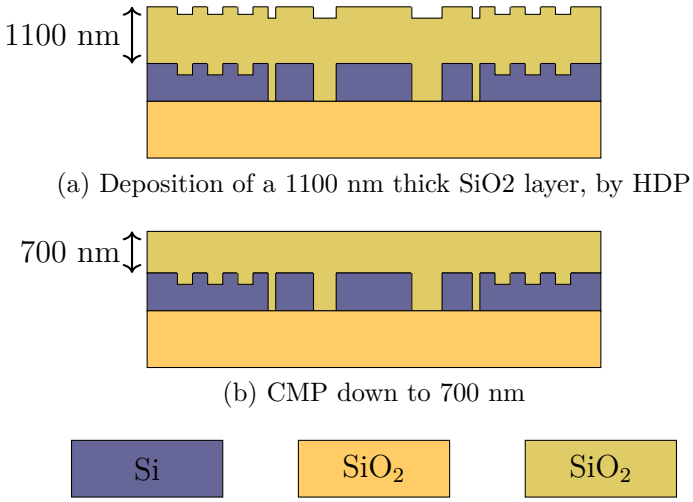

(a) Deposition of a 1100 nm thick SiO2 layer, by HDP

(b) CMP down to 700 nm

Figure V.3 – Waveguide encapsulation. Note that we used different colors in order to differentiate the thermal SiO_2 from the substrate, and the SiO_2 deposited by HDP.

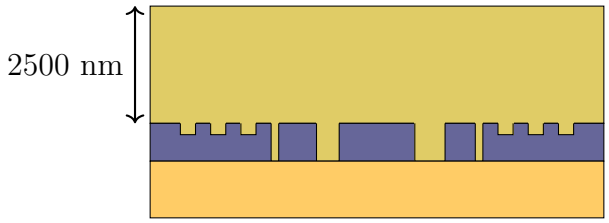

(a) Deposition of a 1800 nm thick SiO2 layer, by HDP

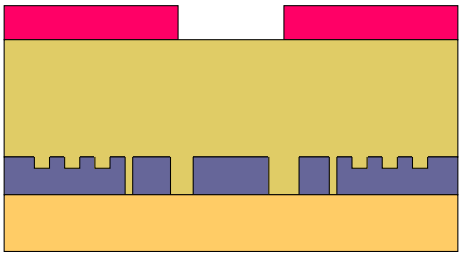

(b) Resist deposition, insulation & development

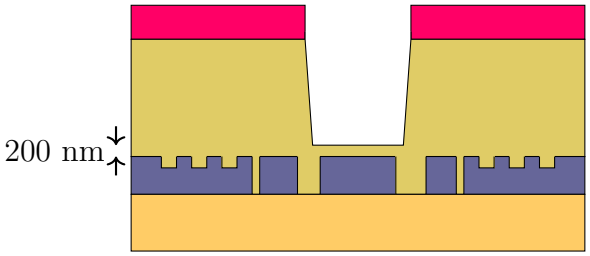

(c) Dry etching of the SiO2 layer, down to 200 nm above the waveguide level

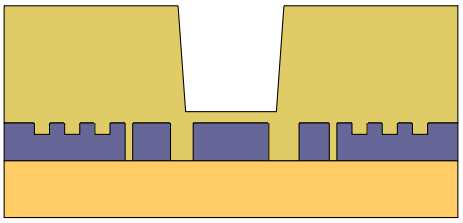

(d) Resist removal

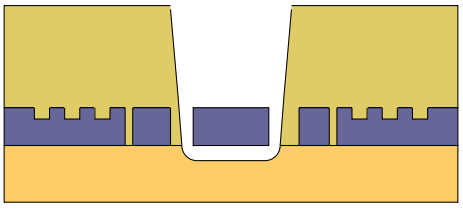

(e) Wet etching of the BOX and SiO2 layers

Figure V.4 – Waveguide release.

V.1.3 Discussion on the process flow

Initial wafer: Fabrication is realized over a 200 mm Silicon-On-Insulator (SOI) wafer consisting of a 220 nm layer of Si, a 2 μm layer of Burried OXide (BOX) SiO2, a 725 μm Si substrate, and a 1.5 μm BOX layer. Note that we only represented the Si layer and the upper BOX layer on the previous Figures.

Patterning of the grating couplers: The first fabrication step is the realization of the Grating Couplers (GC) (figure V.1), that are used to inject light into the photonic waveguides, and to collect it out of them (see paragraph V.2.1). The design of the GC relies on 150 nm thick silicon trenches, and hence implies partial etching of the 220 nm thick silicon layer. The thickness of the trenches is related to their width, and was calculated taking into account the minimal dimensions allowed by the UV lithography equipment. Because we use e-beam lithography latter in the fabrication (patterning of the waveguide level), which allows smaller minimal dimensions, we could have used a design with fully etched trenches, and merged the patterning of the GC and of the waveguide level into a single step. However, we had no experience with the design and fabrication of fully etched GC, and could not be certain that their performances would be good. As this is a critical component, without which experimental characterization is impossible, we chose to rely on the partially etched design, that was already well-mastered by the team.

Patterning of the waveguide level: Next, the waveguide level is realized (figure V.2). Due to the presence of SWG structures with dimensions down to 50 nm, shape e-beam lithography is used. The developments associated to this part of the process are presented on section VII.1.

Encapsulation of the photonic structures: Thirdly, the wafer is encapsulated by a silica superstrate (figure V.3). This step was not mandatory, and could have been merged with the final step. It was introduced as an intermediate step, from which we could investigate variations of the final release step. It also enables to end the fabrication of some wafers at this step, in order to investigate the impact of the release on the SRR optical performances (see section V.2.3).

Release of the optomechanical structures: During the final step, the optomechanical structures are released (figure V.4). The structures that are to be suspended are 500 nm wide. At the end of the process, they are either supposed to be doubly clamped between silica walls or standing on a silica pedestal. In the second case, the pedestal is protected by a 2 μm wide silicon disk. The idea is to use an anisotropic etching process, that will equally attack silica in all directions, but leave intact silicon. With a proper choice of the etching time, all the silica below the silicon waveguides and mechanical arms can be removed, while keeping a silica foot below the silicon disks.

During release, it is necessary to protect the other structures. We used a hard mask strategy in order to do so, because appropriate resists are not allowed inside of the equipment that we initially intended to use for the final liberation step. This is the first step of the release process. We tried to use a thin HfO2 layer, a thin AlN layer, and a thick silica layer as hard masks. While the first two approaches are commonly used as protective layers, we encountered difficulties with their adherence to the silica superstrate and their protective efficiency was somehow poor. The last approach revealed to be the more effective in practice. We deposited a 2.5 μm thick silica layer over the whole wafer, that was etched above the structures to be released. This first etching was an isotropic dry process, stopped 200 nm above optomechanical structures. During this first etching, the structures that would not be released were protected by a resist layer (which is possible in this case). After etching, photonic structures are hence protected by the 2.5 μm thick silica layer, acting as a hard mask, while optomechanical structures are only topped by a thin 200 nm silica layer, that will be rapidly consumed during the final etching.

Apart from the right choice of the duration, the right choice of the etching attack type was also critical during the final anisotropic liberation step. We first tried to use a classical HF vapor etching, with mitigated results. The majority of the structures ended bonded to the substrate or broken, which we think is a consequence of strong forces exerted by the HF vapor process. After a few tries, we finally opted for a chemical HF etching, that proved to be more efficient.

Problems encountered during fabrication

We faced two main difficulties during fabrication, at the waveguide patterning step and at the release step. Difficulties encountered during the patterning of the waveguide level are consequence of the presence of really small SWG structures, and are discussed in part III. The second difficulty, as mentioned above, was the release step. Note that because a process flow is sequential, it was necessary to solve the patterning problem first, before even acknowledging the release problem, which took a subsequent time.

Some of the most frequent failures that we encountered after release are presented on Figure V.5: bonding of the SRR or of the bus waveguide to the substrate, breaking of the SRR at the junction between the arms and the ring, and breaking of the bus waveguide. Generally speaking, we observed that the rings with smaller radii and the highest number of arms were easier to suspend. Adding a second mechanical ring was also verified to be effective in order to avoid breaking and or collapsing. This is easily explained due to the resulting higher rigidity of the structure.

It must be noted that some of these failures are a consequence of the design itself, and not of the fabrication process. Most notably, it was retrospectively an obvious mistake to try to suspend the bus waveguide over a 100 μm length, as it dangerously favors bonding to the substrate. On our new designs (unfortunately not fabricated at time of finishing this work), we used a modified version of the mask, that reduces the length of the waveguide (see figure V.6).

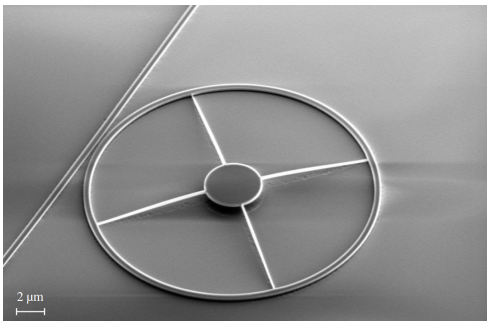

(a) Bonding of the ring and of the bus waveguide to the substrate

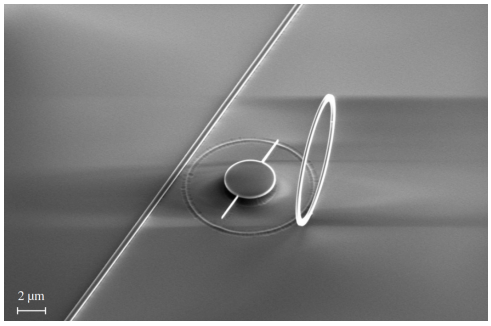

(b) Collapsing of the ring after breaking at the junction with the arms

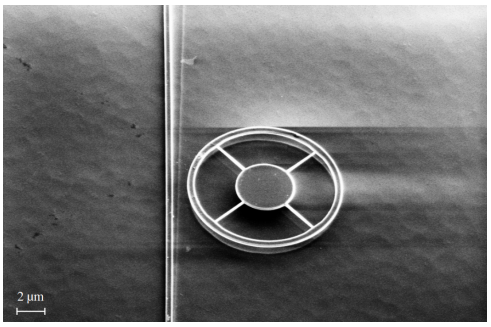

(c) Breaking of the bus waveguide (view at proximity of the ring)

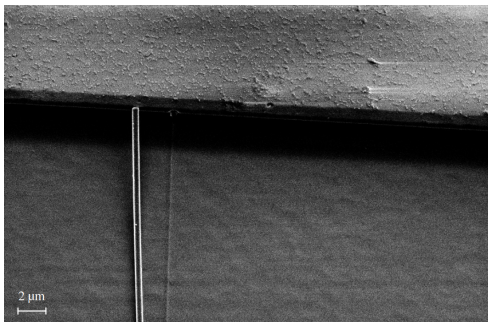

(d) Breaking of the bus waveguide (view at the silica wall)

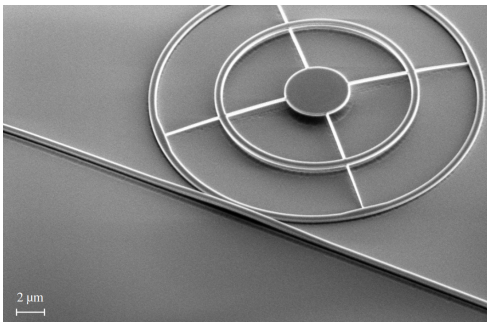

(e) Bonding of the ring to the substrate, and bonding of the bus waveguide to the ring

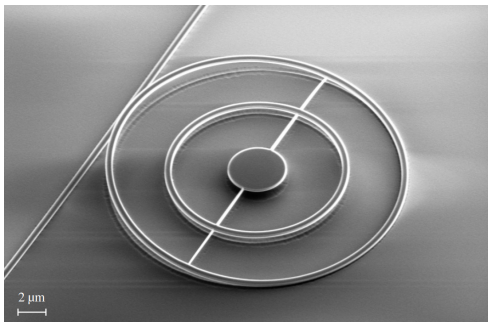

(f) Bonding of the bus waveguide to the substrate, and partial bonding of the ring

Figure V.5 – Non-exhaustive selection of the most frequent failures encountered after attempting to suspend the optomechanical structures.

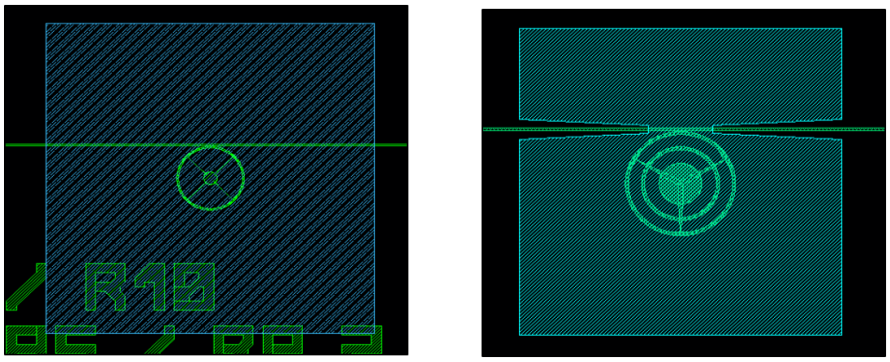

(a) Old design (b) New design

Figure V.6 – New version of the mask, that reduces the risks of bonding of the bus waveguide to the substrate. The green patterns correspond to the waveguide level. The blue patterns correspond to the opening window during release.

V.2 Integrated optics measurements

In this section, we present photonic experiments on classical ring resonators and suspended ring resonators. By using Grating Couplers (GC) and an optical probing station mounted with optical fibers, full-scale wafers can be tested during a relatively short time.

During a preliminary step, the efficiency of the GC and the propagation losses in photonic waveguides are measured, which gives a good estimation of the overall quality of the wafer. Based on these measurements, the best dies are selected.

More precise optical characterization was conducted on these dies. By comparison between classical and suspended ring resonators, and by confronting the results from different fabrication recipes, the influence of the suspension on optical losses was investigated. We also studied the doublet splitting phenomenon between clock-wise and counter-clockwise propagating waves, and the non-linear & thermo-optic effects.

V.2.1 Experimental setup

We use a probe station to perform the photonic measurements. Grating Couplers (GC) are used to couple light in and out of the wafer. A tunable fiber laser centered around 1550 nm is used to measure optical spectra.

Grating couplers: The injection and collection of light into the photonic waveguides is realized by means of a grating coupler. It consists of a periodic pattern of partially-etched trenches, above which an optical fiber is aligned (see figure V.7a). For a given angle of the fiber with respect to the normal (8^o with a silica superstrate to 12^o when the GC is in the air), the incident light coming from the optical fiber is “forced” to enter a planar

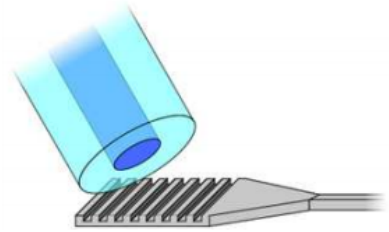

(a) Optical fiber aligned above a Grating Coupler.

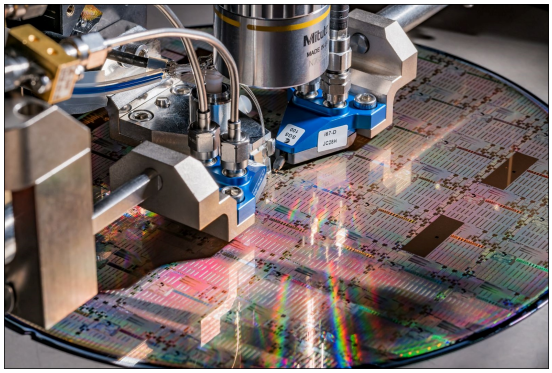

(b) Optical probing station.

Figure V.7 – On the probing station, the optical fiber are aligned above the grating couplers by means of two multi-axis piezo-controllers, and the wafer is mounted on a movable chuck.

waveguide by constructive interference, and is slowly transferred into the strip waveguides through an adiabatic taper.

Contrary to edge coupling, GC technology does not require to cleave the wafer, and the alignment of the fiber above the GC is less hazardous and time-consuming. However, the coupling efficiency is a little poorer and is bandwidth limited, usually over a 100 nm range around the target wavelength. It is also polarization dependent (TE in our case).

Additionally to easier manipulation, the main advantage of the GC resides in the resulting possibility to conduct automatized optical experiments over full-scale wafers, by using an optical probing station.

Probing station: Optical characterization is conducted with an automatized optical probing station, analogous to an electrical probing station, with the difference that electrical probes are replaced with optical fibers (see figure V.7b). The wafer is mounted on a movable chuck. Between two successive measurements, the selected dies and subdies are coarsely aligned under the optical fibers by moving the chuck. The optical fibers are then precisely aligned above the GC by means of a three-axis piezo-controller. The whole process is controlled by means of a LabVIEW® routine [167].

The use of a probing station allows to make easy and fast measurement of multiple devices over full-scale wafers. Cleaving is not necessary, and optical alignment is not critical. The measurement of a full spectrum takes less than one minute, and statistical data over numerous dies can be provided. The use of Polarization Maintaining Fibers (PMF) insures that polarization is not modified over time (as the GC are polarization-dependent).

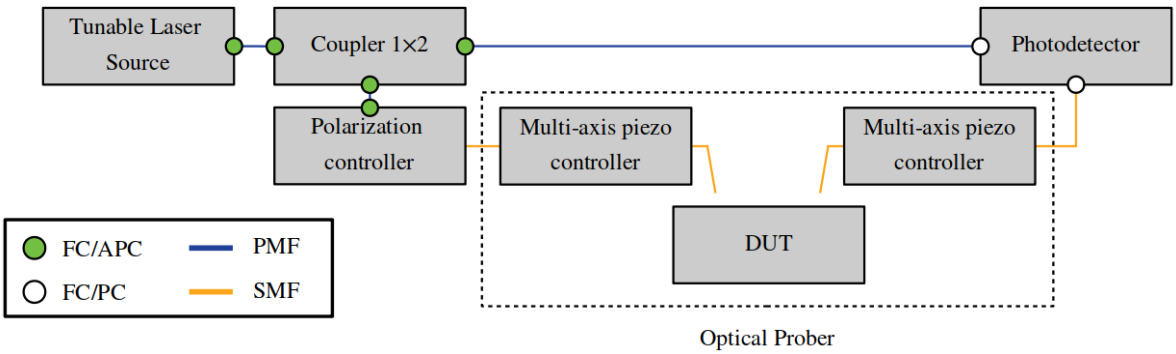

Figure V.8 – Optical test bench. DUT: Device Under Test. SMF: Single Mode Fibre. PMF: Polarization Maintaining Fiber.

Experimental setup: The complete experimental setup is presented on figure V.8. The light source is a polarized Tunable Laser Source (TLS), centered around 1550 nm, mounted with a polarization maintaining fiber. Light is first sent to a polarization maintaining 50/50 optical coupler, from which half the light is sent as a reference wavelength and power signal to the PhotoDetector (PD), and half the light is sent to the wafer. Light is coupled in and out of the photonic structures by means of GC. Once extracted, it is sent to the PD. By comparison to the reference signal, we directly obtain the value of the optical power lost at the DUT, in decibels. The wavelength is scanned step by step, with increasing wavelength, at a speed of 10 nm/s. A full spectrum can be measured in less than 10 seconds[1].

V.2.2 Preliminary measurements: efficiency of the grating couplers and linear propagation losses

We first measure the GC efficiency (at the point of maximum transmission), based on the optical spectrum of the simplest device: a 1 mm long waveguide with GC facing each other at its ends. We consider the waveguide to be short enough to add only negligible losses[2], and after subtraction of the reference spectrum that accounts for the losses due to the setup, the GC efficiency is simply obtained by dividing by the number of GC. Appart from the estimation of the GC efficiency, these spectra are also used as normalization spectra when measuring other devices.

We next calculate the linear propagation losses. The optical spectra of spiral-shaped waveguides of various lengths (1 to 6 cm) are realized. The linear propagation losses at a given wavelength are then calculated by linear regression between the spirals lengths and their output powers.

[1] In comparison, the complete alignment of the optical fibers takes between 1 to 2 minutes, and is the limiting step.

[2] This is actually quite reasonable considering the measured linear propagation losses.

	GC efficiency (dB)	GC $\lambda_{\text{Max.}}$ (nm)	Prop. losses (dB/cm)
Median	-5.60	1556.43	-4.05
Average	-5.43	1556.28	-4.08
Standard deviation	0.38	2.13	0.71
Best result	-4.55	–	-3.09

Table V.1 – Statistical results over 25 identical dies of the same wafer: unitary GC efficiency, wavelength of maximal transmission, & linear propagation losses at $\lambda = 1550$ nm. This data corresponds to typical results with an optimized process flow, at the end of the thesis. Multiple runs aiming to improve these values have been conducted.

Typical results calculated over the 25 identical dies of one wafer are presented on table V.1 and figure V.9. The losses associated to the GC are a little high in comparison to other results in the team (we expect $\equiv -4$ dB), but remain totally acceptable. We believe that the unusual thickness of the silica superstrate (the design is adapted to a thinner layer) and the possible degradation of the surface after the chemical HF vapor (in comparison to a "clean" CMP) are responsible for the small additional losses.

In contrast, linear propagation losses are quite high compared to state-of-the-art silicon photonic waveguides (by almost 2 dB/cm). We believe that this is due to the use of non-classical e-beam lithography, which is further discussed in Section VII.1.2. This is a detrimental point for ring resonators, as the quality factor is limited by propagation losses.

The systematic statistical measurement of this two figures gives a good estimation of the overall quality of a wafer, and allows to establish a comparison basis between different fabrication runs. It also allows to establish a cartography of the dies and to investigate fabrication variations over a wafer. For example, on Figure V.9d, we can see that linear propagation losses are decreasing between each successive rows, which is a signature of the fact that we used an increasing insulation dose between rows during e-beam lithography.

Note that at the end of this thesis, the part of the process related to GC and photonic waveguides is well-mastered, and the results from one wafer to an other (or from one die to an other) are reproducible.

V.2.3 Experiments on suspended ring resonators

We now present our experimental results on suspended ring resonators. Based on the optical spectrum, our first focus was on the calculation of the figures of merit of SRR, and on comparison to classical ring resonators. The calculation of these values revealed the presence of doublet splitting at resonance, thermo-optic effects, and non-linear effects.

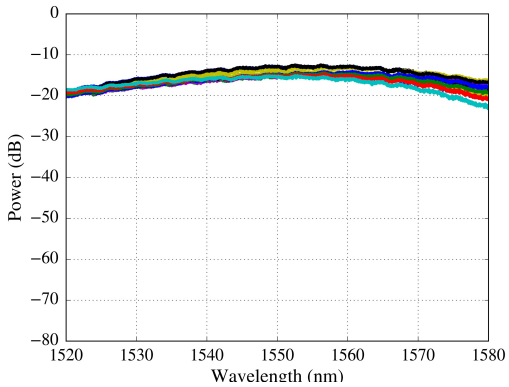

(a) Experimental spectra of the transmission of a straight waveguide with input and output GC (all dies)

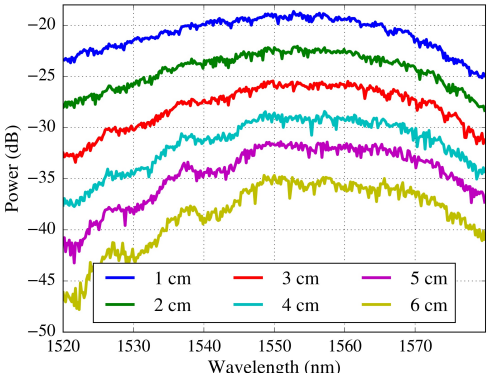

(b) Experimental transmission spectra of spirals with increasing length (one die)

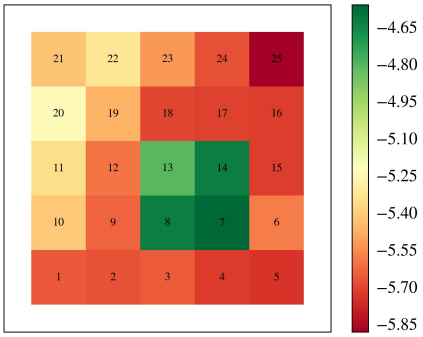

(c) Wafer cartography of the GC, in dB

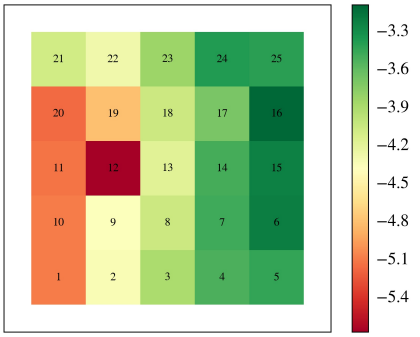

(d) Wafer cartography of the linear loses, in dB/cm

Figure V.9 – Typical results of the GC and Spirals characterization.

Figures of merit: statistical data, and comparison with classical rings

We first measured the four figures of merit of ring resonators (defined in section IV.1.3): the Free Spectral Range (FSR), the finesse $\mathcal{F}$, the quality factor Q_{opt}, and the contrast C_r.

Establishment of statistical data Calculation of the FSR, $\mathcal{F}$, Q_{opt} and C_r requires to extract, for each peak, the FWHM, the position, and the upper and lower values. While this can be easily done by hand for a few spectra, it is not an option to realize this task by hand for all the spectra. For a single wafer, there are 25 dies, each dies contains 94 rings, and each ring harbors 11 resonance peaks in average, which represents almost 26 000 resonance peaks.

Given the large numbers, we developed a routine that automatically fits each reso-

nance peak with a Lorentzian shaped function, using Levenberg-Marquadt method. The Lorentzian function is really convenient, as its fitting parameters naturally are the FWHM, the position, and the upper and lower values. Alternatively, we also developed a version of the algorithm in which the whole spectrum is fitted all at once with an Airy function (equation (IV.3)), rather than locally fitting each peak. While this approach is theoretically more rigorous, it is harder to implement and fails more often (due to a larger number of fitting parameters), and the final results differ from less than 1% between the two approaches.

In practice, the accuracy of the statistical data obtained by this method is highly limited. This is mainly due to the presence of double peaks on the spectra, and to the modification of the shape of the peaks because of non linear effects and optical bistability, which are difficult to account for in an automatized routine. Additionally, the ability of the algorithm to correctly detect the presence of each peak can be undermined if the envelope of the signal is poor (which happens when the alignment of the optic fibers above the GC is not precise enough), and even in the best case scenario, the accuracy of the Lorentzian fit itself will induce some error. For this reason, we eliminate poor fits based on their coefficient of determination R^2 and consider a set of statistical data created after removing outliers in the 30th percentile. While this treatment is classical when removing outliers from a set of statistical data, it remains an arbitrary choice that will falsify the results to some extent. The statistical results must be considered with care, and need to be hand proofed when considering a given spectrum. In other words, we consider the whole set of statistical data as a global indicator, with results becoming inaccurate when we consider a spectrum in particular.

Classical ring resonators We first consider classical ring resonators, i.e. without mechanical arms and encapsulated in silica. If we anticipate that SRR will present additional losses due to the release process and the mechanical anchors, classical ring resonators can be seen as their ideal case, and constitute a basis of reference. Typical results of statistical data established over a complete wafer are presented on table V.2.

Over the 25 dies of the same wafer, a given resonant wavelength occurs in a 10 nm window (see figure V.10). This is just a little more than half the FSR of 5 μm radius rings, which allows to properly differentiate each order of resonance (in the sense of the integer p in equation (IV.1)). For larger rings, the FSR is smaller than 10 nm, and the resonance orders can not be accurately distinguished.

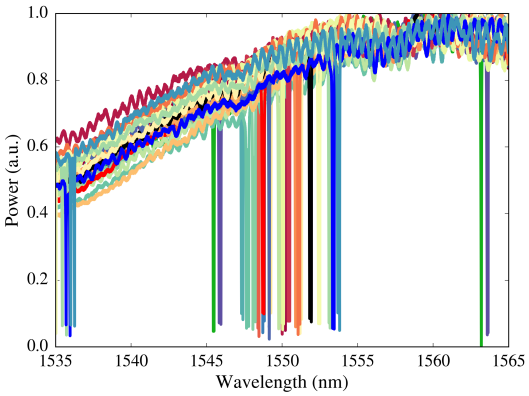

(a) Superposition of the 25 spectra of a ring resonator of radius 5 μm and gap 240 nm.

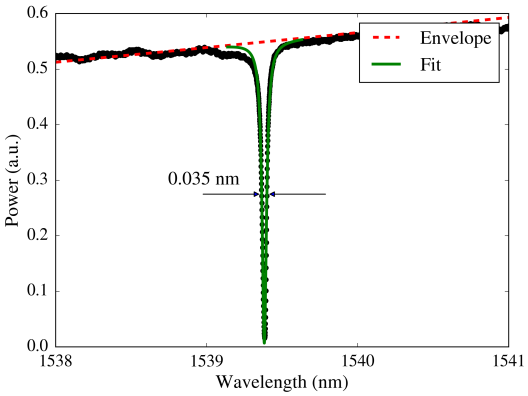

(b) High quality factor resonance with critical coupling. The ring radius is 15 μm and the gap is 240 nm.

Figure V.10 – Wavelength reproducibility and high quality factor resonance for classical ring resonators.

Radius	5 μm	15 μm	25 μm
Gap	230 nm	240 nm	250 nm
Q_{opt}			
Median	20 600	44 400	65 400
Average	24 800	43 700	61 800
Std	12 600	8 400	13 300
Best	57 600	65 300	89 400
C_r			
Median	0.938	0.980	0.989
Average	0.937	0.978	0.970
Std	0.021	0.017	0.033
Best	0.993	0.999	0.999
$\mathcal{F}$			
Median	254	169	150
Average	307	166	141
Std	157	32	30
Best	717	249	203
FSR (nm)			
Median	–	5.893	3.546
Average	–	5.891	3.539
Std	–	0.061	0.037

Table V.2 – Typical figures of merit of classical ring resonators of various radii. Quality factor and finesse values are at the state-of-the-art level [168], despite elevated liner propagation losses. The increase of optical quality factor and decrease of finesse with a radius increase is respected. Large fluctuations in the statistical data for the 5 μm radius rings are due to enhanced non-linear and thermal effects for smaller radii. Critical coupling is achieved.

Radius	10 μm	10 μm	10 μm	10 μm	10 μm	10 μm
Gap	300 nm	300 nm	300 nm	300 nm	300 nm	300 nm
Nb. Arms	2	3	4	2	3	4
Materials	Si/SiO2	Si/SiO2	Si/SiO2	Si/Air	Si/Air	Si/Air
Q_{opt}						
Median	37 300	17 900	17 800	17 300	10 600	21 900
Average	33 600	18 700	17 300	18 900	12 500	24 100
Std	15 600	12 700	11 100	3 200	4 500	9 500
Best	53 500	47 700	39 900	31 600	19 600	38 000
C_r						
Median	0.577	0.513	0.444	0.877	0.868	0.292
Average	0.592	0.476	0.443	0.732	0.893	0.273
Std	0.130	0.089	0.123	0.317	0.069	0.037
Best	0.808	0.581	0.676	0.986	0.998	0.308
$\mathcal{F}$						
Median	226	108	105	93	55	110
Average	204	113	107	98	67	122
Std	95	77	67	56	16	52
Best	333	287	244	163	106	202

Table V.3 – Typical figures of merit of encapsulated and released SRR of various number of arms. Large fluctuations make the statistical data irrelevant, and the best value is a better figure of comparison.

Suspended ring resonators Results for encapsulated (Si/SiO2) and released (Si/Air) SRR are presented on table V.3. The ring radius is 10 μm, the gap is 300 nm, and the number of arms is varied between 2, 3 and 4. From observation of the standard deviation, which is of the same order of magnitude than the median and average values, it is obvious that statistics are not really relevant here. As mentioned above, this is due to difficulties encountered during the automatic fitting of the spectra because of peaks with significant deviation from the ideal Lorentzian shape.

In this case, a more relevant figure of comparison is the best value. This quantity is more likely to be correct, as the algorithm mainly tends to return underestimated values[3], and it can easily be hand-proofed during a post-processing step.

[3]Corresponding to a fit conducted on a flat portion of the spectrum.

From observation of the optical quality factor and finesse of encapsulated SRR, we denote a strong correlation between the number of arms and the optical performances. Q_{opt} (resp. $\mathcal{F}$) is degraded by almost 6 000 (resp. 50) with each additional arm. From the theoretical model of section IV.1.1, by incorporating a parameter corresponding to the losses associated to one arm, we obtain that this degradation corresponds to a transmission rate $T = 0.998$ at each arm. This value is in the upper range of the results obtained by 2D simulation in section IV.1.5. Note that the design of each arm in regard to the design parameters $(W_{\text{tip}}, L_{\text{str}})$ is always the same in this set of data, respectively 50 nm and 1.5 μm.

Proper experimental investigation of the respective influence of L_{str} and W_{tip} should be the focus of future work aiming to improve the quality factors of SRR. In this regard, it is not necessary to make the measurements on SRR. An experimental strategy based on cascaded bends with an arm junction can be followed.

The behavior of released SRR is even more contrasted. A clear tendency based on the number of arms is difficult to extract. However, the results are clearly poorer than encapsulated SRR. Higher losses after release can have two origins. First, because of the higher index contrast, we naturally expect a higher influence of the rugosity and higher propagation losses. Second, it is also possible that the rugosity was increased during the release process. This last point actually tends to be verified by indirect measurements of the rugosity from observation of doublet splitting, presented on the next Section. However, it is difficult to determine the relative importance of each origin.

Observation of doublet splitting of resonance peaks

On the optical spectrum, we often observe two closely spaced peaks at resonance (for example, see Figure V.11). This is a manifestation of contradirectional coupling between the clockwise (CW) and counter-clockwise (CCW) waves and of the breaking in rotational symmetry due to surface-roughness and to the presence of the bus waveguide.

By opposition to the ideal unidirectional case, there are in practical cases two CW and CCW waves propagating in the ring. The existence of the CCW wave comes from back-scattering on the surface-roughness [169], back-scattering on the mechanical anchors, and back-scattering at the coupling region [170]. Additionally, these effects also result in a lifting of degeneracy of the two resonant wavelength, as they degrade the rotational symmetry of the structure.

In silicon ring resonators, it is generally assumed that surface-roughness is the main source of contradirectional coupling [168]. Under this assumption, the spacing $\Delta\lambda$ between two resonances can be linked to surface scattering by [171]:

$$\Delta\lambda = \lambda_0 \mathrm{K}(n) \frac{V_s}{V_r} \tag{V.1}$$

where λ_0 is the degenerate resonant wavelength, $\mathrm{K}(n)$ is a function of the refractive

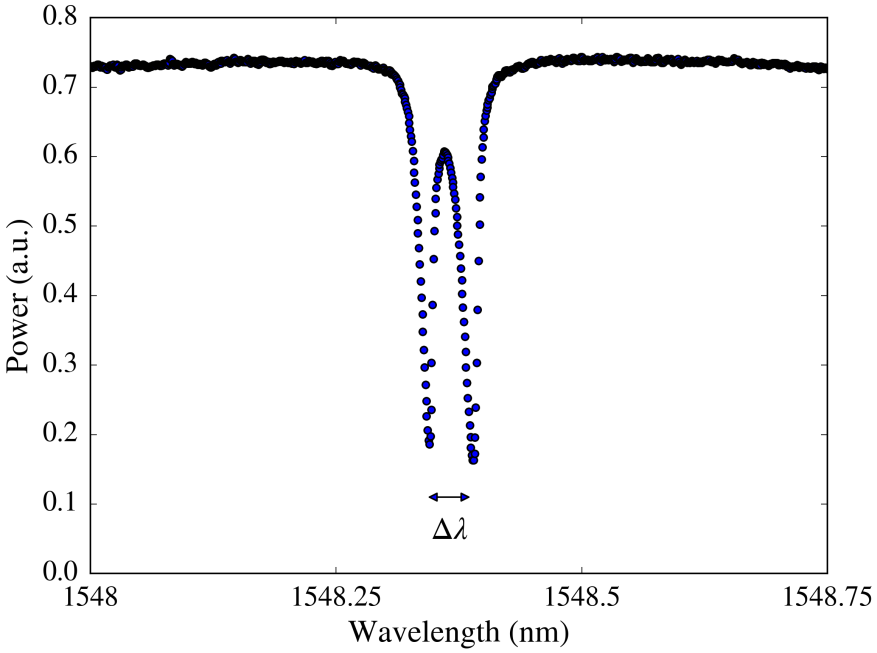

Figure V.11 – Observation of a two closely spaced peaks due to contradirectional coupling and a lifting of degeneracy. This typical doublet splitting was observed on a 5 μm ring resonator.

indexes, $V_r = \pi(R_o^2 - R_i^2)\mathrm{H}$ is the physical volume of the ring, and $V_s = \sqrt{RL_c}\mathrm{H}\sigma_r$ is a parameter that appears in the calculation of scattering losses, has the dimension of a volume, and is often regarded as the effective volume of a typical scatterer [171].

L_c and σ_r are the statistical roughness parameters, respectively the correlation length and the standard deviation. An informal and simplistic description of these parameters is that L_c corresponds to the length of the roughness, and σ_r corresponds to its "height", i.e. by how much it varies from the ideal value.

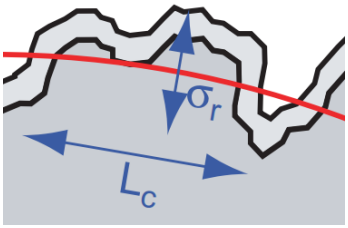

Figure V.12 – Correlation length L_c and standard deviation σ_r. Reproduced from [171].

Experimentally, we observe that the magnitude of the doublet splitting varies among the same spectrum. It can be explained by the fact that each resonance order has a slightly different field profile along the ring, and due to the randomness of the rugosity distribution, some modes will "feel" it more than others, depending on where the nodes and antinodes of the field are positioned in regard to defects. This argument is developed in [172], where a theoretical analysis based on the statistical properties of the sidewall roughness shows that mode splitting between resonant modes of different orders are uncorrelated.

On table V.4, we present the value of the product of the rugosity parameters, obtained

from experimental values of doublet splitting and equation (V.1). We consider encapsulated classical ring resonators (CRR), encapsulated SRR, and released SRR.

	CRR, encaps.	SRR, encaps.	SRR, released
$\Delta\lambda$ (nm)	0.01 – 0.05	0.03 – 0.10	0.05 – 0.12
$\sqrt{L_c}\sigma_r$ (nm$^{3/2}$)	27.27 – 136.3	51.73 – 172.4	91.46 – 219.5

Table V.4 – Rugosity values measured from the doublet splitting.

For classical ring resonators, the product is a little more elevated than previous measurements on waveguides fabricated at our cleanroom facility [93], but remains at the same order of magnitude, indicating that (or at least, not refuting that) surface-roughness is probably the main source of contradirectional coupling. This is expected given the high linear propagation losses that we measured.

We obtain higher values for encapsulated SRR than for encapsulated CRR, and higher values for released SRR than for encapsulated SRR. This suggests that the rugosity is at the same time increased by a degradation of the quality of the surfaces after the release step, and by an additional back-scattering at the mechanical anchors. Note that the latter is conveniently counted as an increase of rugosity here, but should be formally described separately, as it is not a random process.

Summary on the optical losses due to the mechanical anchor and the release step

From the discussion of the previous sections, it appears that:

1. Mechanical anchors degrade the optical quality factor and the finesse of the SRR, with a linear dependence on the number of arms.
2. The sidewall rugosity of the SRR is increased after the release.
3. The optical quality factor and the finesse are strongly undermined after the release. It is not possible to say yet how much the higher rugosity and the higher index contrast contribute to the deterioration.

Observation of thermo-optic and non-linear effects

Figures V.13 and V.14 represent the optical spectra of a classical ring resonator and a suspended ring resonator, of 5 μm radius, for various optical powers. Also represented is the evolution of the resonance position and of the extinction ratio (that is, the contrast, but expressed in dB). Note that similar yet less pronounced results are obtained with 10 μm radius ring resonators, due to the finesse reduction (and hence power density within the ring) with increasing radii (see figure IV.4).

The first straightforward observation is that there are thermo-optic and non-linear effects in both cases: we observe the typical resonance shift and triangular optical instability due to thermo-optic effects, and in the case of the classical ring resonator, we observe a strong variation of the contrast with optical power, a signature of TPA and FCA.

These effects, introduced in section IV.1.6, are more pronounced in the classical ring resonator, because of their larger finesse compared to those of suspended ring resonators ; with superior losses in the second case, less power builds up within the cavity.

Heat generation and the resulting thermo-optic effects are a consequence of optical absorption within the ring, that is mainly governed by TPA and FCA. These two phenomenons respectively square with the power 2 and 4 of the optical power, and one could expect the resonance wavelength shift to be at least quadratic (because TPA is predominant over FCA). Yet, we observe a linear shift. When more optical power is stored in the cavity, total optical absorption naturally increases, and so does the heat generation. As a result of the thermo-optic effect, the resonance is shifted to higher wavelengths, and the ring is slightly detunned, which counterbalances and slows down the increase of optical power and optical absorption, leading to an almost linear thermo-optic shift.

As we already argued in section IV.1.6, modification of the contrast with increasing laser powers is a signature of TPA and FCA and of an increase of intrinsic losses in the ring. We observe that the contrast of the classical ring resonator quadratically drops from 95% at 1 mW to 50% at 15 mW, which suggests that optical losses in the ring effectively evolve quadratically, in accordance with theory.

From the variation $\Delta\lambda_r$ of the resonance wavelength, we can calculate the raise of temperature in the ring, based on equation (IV.22). We find $\Delta T = 20$ mK/mW in the classical ring, and $\Delta T = 1.4$ mK/mW in the suspended ring. As already pointed out in chapter I, this heat generation could lead to important photothermal forces.

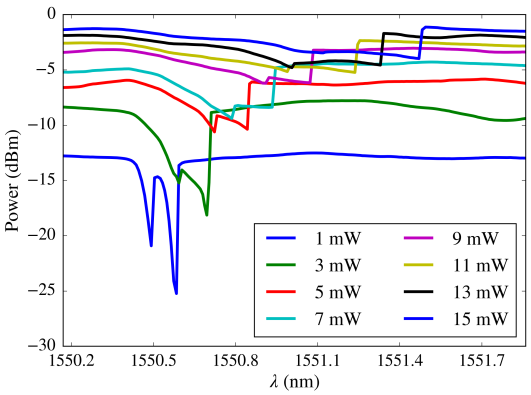

(a) Optical spectra for increasing laser powers.

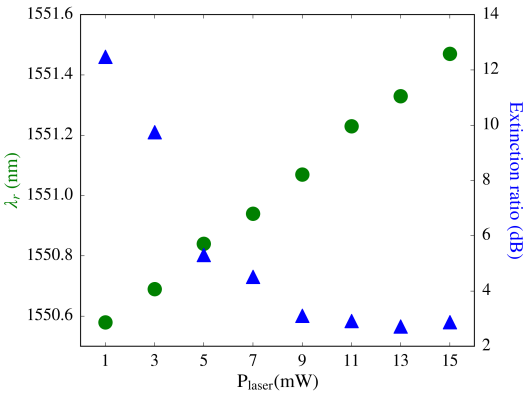

(b) Observation of the shift of the resonant wavelength (green) and decrease in extinction ratio (blue) with increasing laser powers.

Figure V.13 – Observation of thermo-optic and non-linear effects on a 5 μm radius ring resonator.

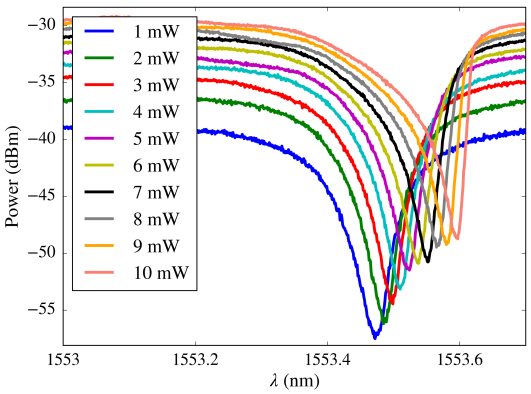

(a) Optical spectra for increasing laser powers.

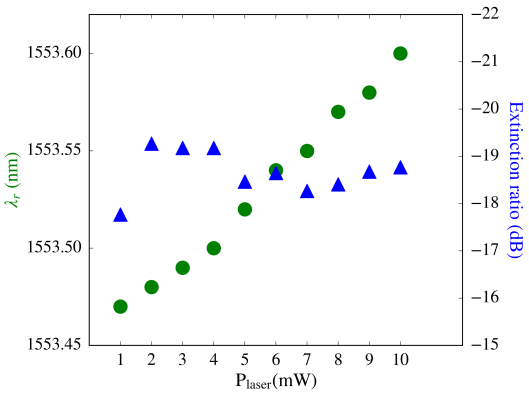

(b) Observation of the shift of the resonant wavelength (green) and decrease in extinction ratio (blue) with increasing laser powers.

Figure V.14 – Observation of thermo-optic and non-linear effects on a 5 μm radius suspended ring resonator.

V.3 Cavity optomechanics measurements

Based on the results of optical characterization, the best dies and rings are selected and undergo optomechanical measurement. Experiments are conducted on a custom optomechanical bench, operating under vacuum.

V.3.1 Optomechanical test bench and principle of measure

Test bench presentation

Optomechanical experiments are conducted under vacuum, on a custom dedicated test bench, developed during the thesis. Under vacuum experiments allow to reduce damping of the mechanical oscillations due to the viscosity of the environment, and to exacerbate the optomechanical effects. Typically, the mechanical quality factor of cantilevers remains limited by air damping while the pressure exceeds 10^{-3} mbar.

The optomechanical test bench is separated between two parts: the vacuum chamber, where the samples are characterized, and an experimental table, where the optical experimental equipments are placed.

Presentation of the vacuum chamber: The vacuum chamber is presented on figure V.15. The basic concept is to fix an optical fiber to a motorized stage, and to displace the fiber between each GC, such that the principle of the optical prober is reproduced.

Inside the vacuum chamber, there are two three-axis miniature linear stages (x, y, z), on which single mode optical fibers are mounted. The angle of the optical fibers is fixed at 11.5^o in order to correspond to the design of the GC, but can easily be replaced. The range of motion of the linear stages is large enough to cover a complete die (2.2 cm $\times$ 2.2 cm), with a displacement precision down to 2 nm. This resolution precision is smaller that the one we use on optical probers (1 μm), such that the the optical fibers can finely be aligned above the grating couplers.

During alignment, the position of the optical fibers is verified through a glass viewport and an extra-long distance work camera positioned above the vacuum chamber. The latter is fixed on a three-axis manual linear stage, such that the whole sample can be observed.

The vacuum chamber and the pump are designed to attain a pressure of 10^{-5} mbar. The pump system is composed of a primary diaphragm pump and a secondary turbomolecular pump. Typically, the chamber is pumped down to 1 mbar with the primary pump, and the secondary pump is switched on beyond this point. Depending on the level of impurity in the chamber (in other words, on how long the chamber had been set off vacuum), the pumping time down to the 10^{-5} mbar range can take between one hour and half a day.

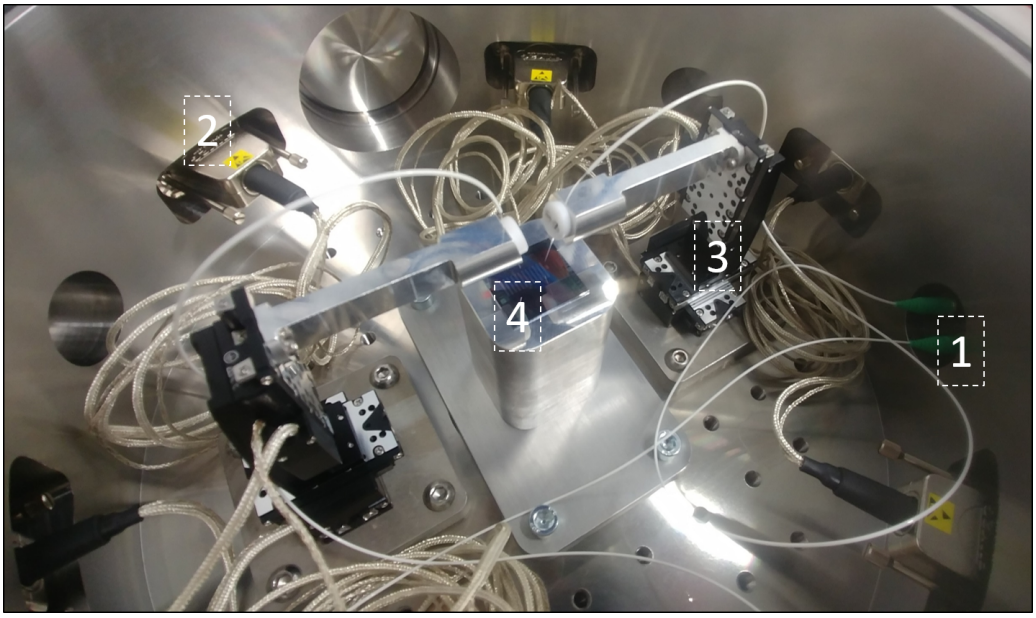

(a) View of the inside of the chamber. 1: Optical fiber feedthrough. 2: Sub-D15 feedthrough. 3: Three-axis miniature linear stage. 4: Die, placed under two optical fibers.

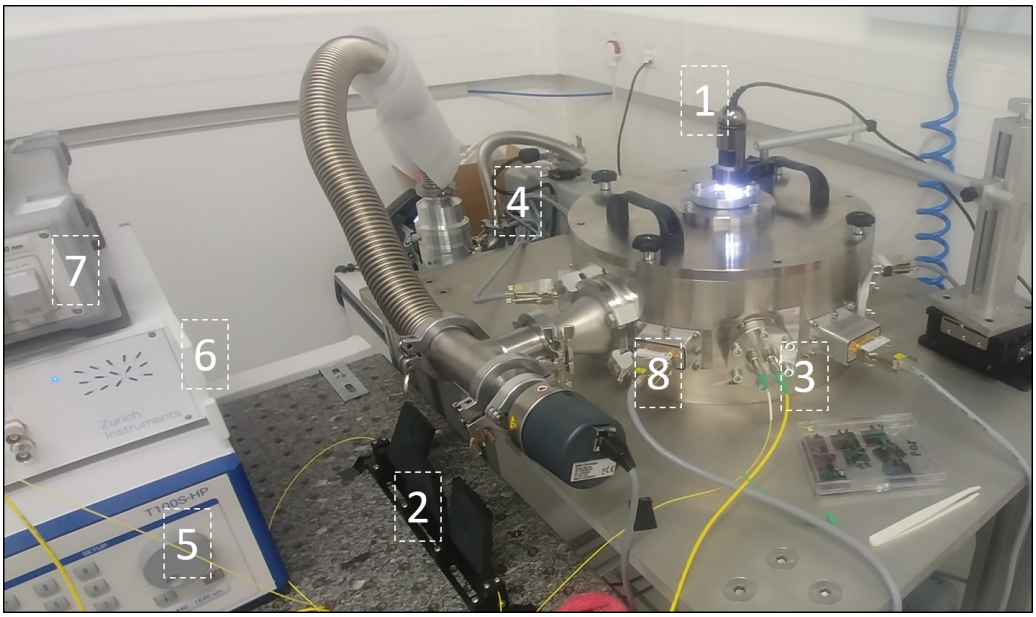

(b) View of the outside of the chamber. 1: Extra-long distance working camera. 2: Polarization controller. 3: Optical fiber feedthrough. 4: Pump. 5: Laser source. 6: Lock-in amplifier. 7: Optical spectrum analyzer. 8: Sub-D15 feedthrough.

Figure V.15 – View of the vacuum chamber and of the test bench.

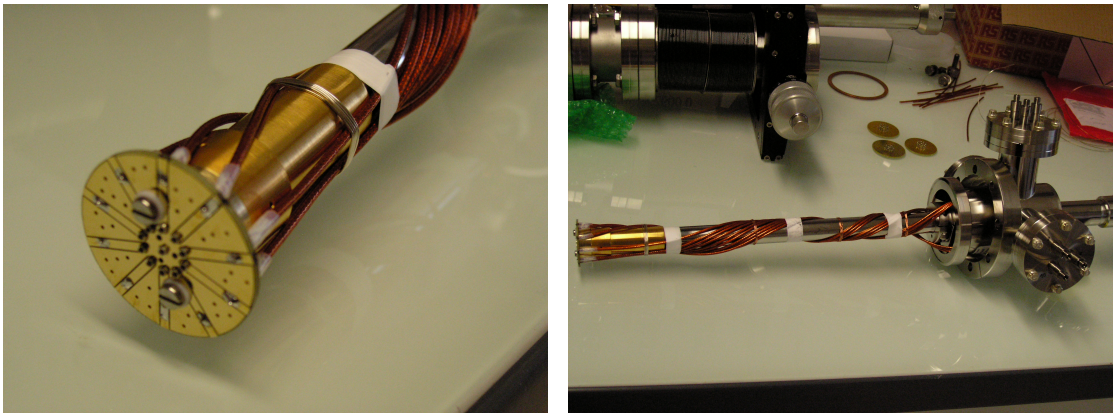

(a) Cold finger, with an adaptation piece allowing wire bonding with the die under test

(b) Cryogenic cane

Figure V.16 – A planned upgrade is to add a cryogenic cane and the cold finger of a cryostat.

At time of writing, the die is placed on a metallic support. A planned upgrade is to replace this support by the cold finger of a cryostat, with the added possibility to realize an electrical activation based on wire bonding between the tested sample and an adapted support. This upgrade is adapted from the cryogenic cane presented on figure V.16. The chamber is realized in a way that allows the addition of a cane either vertically or horizontally.

One of the advantages of low-temperature operation is that it allows to eliminate thermo-elastic damping and Akhiezer damping that limit the mechanical quality factor. As a matter of fact, an increase of the mechanical quality factor from 7 600 at room temperature to 37 000 at 22K was reported on [31]. Another advantage is that it should also reduce thermo-optic effects and improve the stability at high optical powers.

In order to limit external, which are detrimental for the alignment of the optical fibers above the grating couplers, the chamber stands on an anti-vibration table.

Optical fibers are brought inside and outside the chamber by mean of a low-loss single mode feedthrough, mounted with FC/APC connectors. There are six sub-D15 feedthroughs, used to control the linear stages, and three remaining passages that could allow additional inputs or outputs (for example, electrical connections).

Rapid presentation of the measurement equipments: Multiple measurement equipments can be installed alongside the vacuum chamber. The link between these equipments and the vacuum chamber is assured by means of two feedthrough for single mode optical fibers. The simplest experimental arrangement is described in the following section, and schematically presented on figure V.17.

Generally speaking, a tunable laser source, a polarization controller, a photodetector and

a lock-in amplifier are used. Besides these fundamental elements, the optical setup can easily be modified, as all optical components are fibered. For example, an additional laser source, electro-optic modulators, or wavelength filters can easily be added when performing more complex measurements.

Setup for thermomechanical noise measurement

Because all components are fibered, the experimental setup outside of the chamber can easily be modified between two measurements. On the following, we present the setup used for the measurement of the thermo-mechanical noise of SRR.

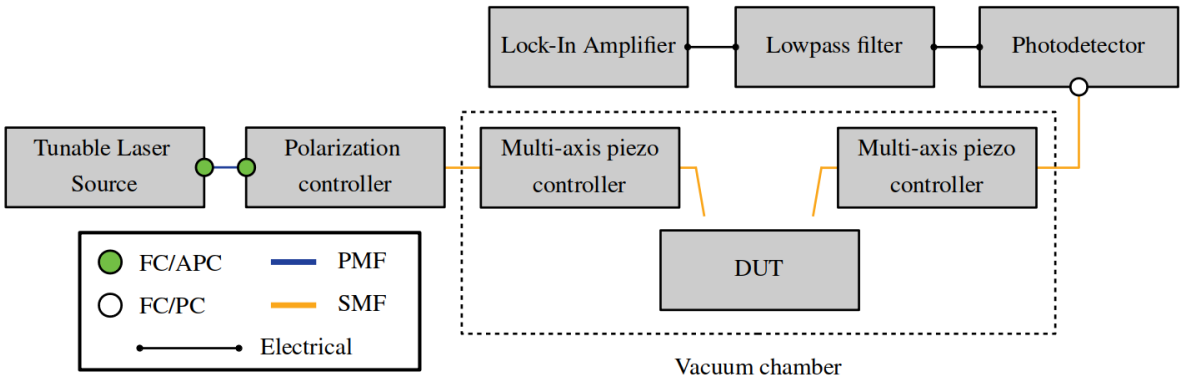

Figure V.17 – (Slightly) simplified schematic of the experimental setup used for thermomechanical noise measurement. DUT: Device Under Test. SMF: Single Mode Fibre. PMF: Polarization Maintaining Fiber.

The schematic of the setup is presented on figure V.17. This is the simplest version of the optomechanical setup. In order to measure the thermomechanical noise, we use a Tunable Laser Source (TLS), a low noise PhotoDetector (PD) with integrated transimpedance amplifier, and a Lock-In Amplifier (LIA).

The mechanical modes are probed by setting the input laser at the point of maximum slope of an optical resonance (on the blue side), and recording the noise spectrum of the optical transmission. The optical resonant wavelength is shifted with mechanical fluctuations, resulting in an amplitude modulation of the optical transmission at the mechanical frequency. The signature of mechanical motion is hence present on the noise spectrum of the optical transmission.

In this configuration, the optical power is kept low enough to induce only negligible optomechanical gain and optical forces (which are proportional to optical power), such that the measured motion is assumed to be entirely due to thermomechanical noise. This hypothesis is verified by doing the measurement at two distinct wavelength. According to the general theory presented in the first part of this manuscript (in particular equations (I.23) and (I.25)), optomechanical effects are a function of the detuning between the laser wavelength and the cavity resonance wavelength. In this regard, by doing the

measurements at two distinct wavelengths, we can assume that optomechanical effects are negligible if the results are comparable.

Additionally, keeping a low enough optical power (typically in the milliwatt range at the input laser) is a way to avoid non-linear effects. As pointed out in photonic experiments, we observe significant thermomechanical and non-linear effects in silicon suspended ring resonators, which modify the shape and position of the resonance peaks. In the context of cavity optomechanics, where all effects are a function of the laser detuning in regard to the cavity, this is a real experimental complication, as this means that the detuning is not kept constant under non-linear effects.

On the other hand, we can not either work at a too low optical power, to which the efficiency of the transduction scheme is proportional. Below a certain optical power (depending on experimental conditions), the optomechanical transduction is weaker than the background noise, and mechanical motion can not be resolved.

The exact compromise between an optical power strong enough to surpass the background noise and low enough to limit optomechanical gain and non-linear effects is not directly quantifiable, as it depends on the experimental setup, the experimental conditions, and the quality of the device under test. As a general and phenomenological rule, powers between 0.5 mW and 1 mW at the tunable laser source were used.

V.3.2 Thermomechanical noise measurement

Theory

In this configuration, we aim to measure the mechanical spectrum of the mechanical ring by monitoring its thermomechanical noise. We expect to observe several peaks on the spectrum, corresponding to the vibrational modes identified in the previous chapter. Thermomechanical noise originates from thermally driven random motion of the mechanical resonator, that can be seen as a stochastic force acting in every direction, such as the force noted F_L in equation (I.3). From the fluctuation-dissipation theorem, the Power Spectral Density (PSD) associated to this force is:

$$S_F(\omega) = \frac{4k_B T}{\omega} \mathrm{Im}\left[\frac{1}{\chi(\omega)}\right] \tag{V.2}$$

where $S_F(\omega)$ is in units of N^2/Hz, k_B is the Boltzmann constant, T is the temperature of the heat bath, χ is the mechanical susceptibility, and there is a factor 4 instead of 2 because we consider one-sided spectral densities.

The mechanical susceptibility is defined by $\delta x(\omega) = \chi(\omega) F_L(\omega)$, such that using the results

from chapter I:

$$\chi(\omega) = \frac{1}{m_{\text{eff}}\left(\Omega_m^2 - \omega^2 - i\Gamma_m\omega\right) + \Sigma(\omega)} \tag{V.3}$$

The link with the PSD of the thermally driven oscillations is $S_{th}(\omega) = S_F(\omega) \times |\chi(\omega)|^2$. On the following, we will consider very weak optomechanical interaction such that $\Sigma(\omega) \equiv 0$ and:

$$S_{th}(\omega) = \frac{4k_B T\Omega_m}{m_{\text{eff}}Q_m} \frac{1}{\left(\omega^2 - \Omega_m^2\right)^2 + \left(\frac{\omega\Omega_m}{Q_m}\right)^2} \tag{V.4}$$

where $S_{th}(\omega)$ is in units of m^2/Hz, k_B is the Boltzmann constant, T is the temperature of the heat bath, Ω_m is the angular mechanical resonant frequency, m_{eff} is the effective mass of a given mode, and Q_m is its mechanical quality factor.

At resonance, $\omega = \Omega_m$, and the PSD of thermomechanical noise is:

$$S_{th}^r = \frac{4k_B T Q_m}{m_{\text{eff}}\Omega_m^3} \tag{V.5}$$

Torsional modes: The previous derivation was (implicitly) conducted for vibrational mechanical modes. It can easily be adapted to torsional mechanical modes, which leads to the PSD for rotational thermal fluctuations:

$$S_{th,\theta}^r = \frac{4k_B T Q_m}{J_{\text{eff}}\Omega_m^3} \tag{V.6}$$

Note that S_{th}^r is in units of m^2/Hz, while $S_{th,\theta}^r$ is in units of rad^2/Hz. The PSD for angular velocity is $S_{th,\text{rot}}(\omega) = \omega^2 S_{th,\theta}(\omega)$, such that:

$$S_{th,\text{rot}}^r = \frac{4k_B T Q_m}{J_{\text{eff}}\Omega_m} \tag{V.7}$$

that is in units of $(\text{rad/s})^2/\text{Hz}$, consistently with the unit of angular velocity.

Optomechanical transduction:

The mechanical motion results in resonance wavelength variations, which are in turn converted to optical power variation. The PSD of the transmitted optical signal is hence linked to the PSD of thermomechanical noise, as we derive on the following.

Beneath Lorentzian approximation, the optical power transmitted by the optomechanical chain reads:

$$P_{\text{out}} = \left(1 - \frac{C_r \gamma^2}{(\lambda - \lambda_r)^2 + \gamma^2}\right) P_{\text{in}} \tag{V.8}$$

where P_{in} and P_{out} are the optical power at the entrance and exit of the bus waveguide (hence not the optical powers at the laser source and on the photodetector).

Under small fluctuations ($\Delta\lambda \ll \gamma$), we can write:

$$P_{\text{out}}\left(\lambda + \Delta\lambda\right) = P_{\text{out}}\left(\lambda\right) + \Delta\lambda \frac{\partial P_{\text{out}}}{\partial \lambda} + ... \tag{V.9}$$

which leads to:

$$\Delta P_{\text{out}} = \Delta\lambda \times 2 P_{\text{in}} C_r \frac{\gamma^2(\lambda - \lambda_r)}{\left[(\lambda - \lambda_r)^2 + \gamma^2\right]^2} \tag{V.10}$$

Experimentally, C_r, λ_r and γ are known from optical characterization. λ is fixed by the laser, and the only unknown is $\Delta\lambda$. We are interested in the mechanical fluctuations, so that we rewrite:

$$\Delta\lambda \approx \frac{\partial \lambda}{\partial x} \times \Delta x = -\frac{\lambda^2}{2\pi c} g_{\text{om}} \times \Delta x \tag{V.11}$$

where the $-\lambda^2/2\pi c$ term comes from the fact that g_{om} is defined in terms of angular frequency $\omega = 2\pi c/\lambda$.

Combining equations (V.10) and (V.11), we obtain:

$$\Delta P_{\text{out}} = -\frac{P_{\text{in}} C_r \lambda^2}{\pi c} \frac{\gamma^2(\lambda - \lambda_r)}{\left[(\lambda - \lambda_r)^2 + \gamma^2\right]^2} \times g_{\text{om}} \times \Delta x \tag{V.12}$$

Alternatively, in terms of spectral densities, we can write:

$$S_{\text{out}}(\omega) = \left| \frac{P_{\text{in}} C_r \lambda^2}{\pi c} \frac{\gamma^2(\lambda - \lambda_r)}{\left[(\lambda - \lambda_r)^2 + \gamma^2\right]^2} \times g_{\text{om}} \right|^2 \times S_{th}(\omega) \tag{V.13}$$

And we have effectively linked the PSD of the transmitted optical signal to the PSD of thermomechanical noise $S_{th}(\omega)$. In particular, based on the amplitude $\sqrt{S_{\text{out}}(\Omega_m)}$ of the

peak at mechanical resonance, we will be able to extract $g_{\rm om}$:

$$g_{\rm om} = \left(\frac{P_{\rm in} C_r \lambda^2}{\pi c} \frac{\gamma^2 |\lambda - \lambda_r|}{\left[(\lambda - \lambda_r)^2 + \gamma^2 \right]^2} \right)^{-1} \times \frac{\sqrt{S_{\rm out}(\Omega_m)}}{\sqrt{S_{th}^r}} \tag{V.14}$$

where S_{th}^r is given by equation (V.5).

Torsional modes: The same procedure can be derived for torsional modes, by replacing $g_{\rm om}$ and S_{th}^r by $g_{\rm rot}$ and $S_{th,{\rm rot}}^r$

Measurements:

We work on a SRR of radius 10 μm, with 2 rings and 3 arms. The first step consists of measuring the optical spectrum and extract the optical parameters of interest. The optical spectrum is presented on the inset of Figure V.18. We observe double peaked resonances, due to CW and CCW waves co-propagating within the ring. The associated optical parameters are summed-up on Table V.5.

$P_{\rm laser}$ (mW)	C_r	λ_{rs} (nm)	λ_{bs} (nm)	λ_r (nm)	γ (nm)	$Q_{\rm opt}$
0.8	0.87	1549.555	1549.523	1549.540	0.05	30 000

Table V.5 – Optical parameters of interest. λ_r refers to the position of the first peak, along which we conducted the optomechanical transduction. λ_{bs} and λ_{rs} respectively correspond to the laser wavelength during blue side and red side experiments (in other words, at the left and right side of the resonance peak). Note that $P_{\rm laser}$ is linked to $P_{\rm in}$ by $P_{\rm laser} = \alpha_{input} P_{\rm in}$ where α_{input} represents the losses due to the 50/50 coupler and the GC: $\alpha_{input} \equiv -7$ dB.

We next process to measure the power spectral density of thermomechanical noise. On the LIA, the signal magnitude is:

$$V_{\rm LIA}(f) = {\rm R} G_{pd} \times \sqrt{S_{\rm pd}(f)} \quad \left[{\rm V}/\sqrt{\rm Hz} \right] \tag{V.15}$$

where R is the sensitivity of the photodetector (R = 0.95 A/W @ 1550 nm), G_{pd} is the (variable) gain of the photodetector ($G_{pd} = 10^7$ V/A in the following measurements), $S_{\rm pd}(f) = \alpha_{\rm out}^2 S_{\rm out}(f)$ is the PSD on the photodetector, with $\alpha_{\rm out}$ the optical losses between the exit of the bus waveguide and the photodetector, including contributions from the GC and a 50/50 coupler. The DC component of the signal is filtered out by the photodetector.

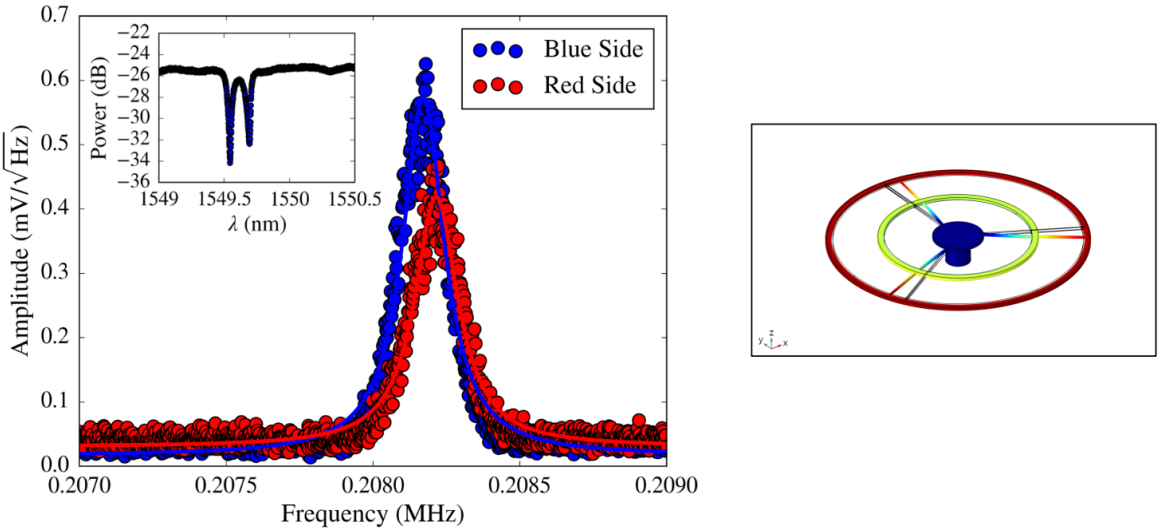

Figure V.18 – **Right:** Optomechanical transduction of the first mechanical mode, by monitoring of the thermomechanical noise. Dots: experimental data. Lines: analytical fit. **Inset:** Associated optical spectrum. **Left:** Shape of the mechanical fundamental mode, obtained by FEM simulation.

Fundamental mode: We begin by acquiring a mechanical spectrum around the first mechanical mode, which corresponds to a torsional mode. The recorded spectrum is presented on figure V.18.

Measurement were conducted on both the red and blue sides of the optical resonance (shown as an inset), with little to no variations between the measured mechanical frequencies and quality factor, as shown in table V.6. Because there is little variation, we can safely assume that the optomechanical actuation is negligible in comparison to the thermomechanical noise (*i.e.* $\Sigma(\omega) \equiv 0$). The amplitude of the peak, however, is different between the two measurement. This is because the laser detuning was different during the measurements. As we will see, the measured amplitudes lead to the same g_{rot} which is also consistent with the hypothesis of a negligible optomechanical gain.

	Blue side	Red side	Deviation
f_m (kHz)	208.1718	208.2153	99.98 %
Γ_m (kHz)	2.0820	2.0839	99.91 %
Q_m	993	999	99.60 %
Ampl. ($\text{mV}/\sqrt{\text{Hz}}$)	0.573	0.418	–

Table V.6 – Comparison of the mechanical parameters obtained by blue side and red side optomechanical transduction.

We find the mechanical frequency at 208 kHz, which considering fabrications uncertainties

is in reasonable agreement with the value 199 kHz found with FEM simulation.

While we qualify the mechanical mode as torsional, we must also consider that there is a little deformation of the ring. As the ring rotates, the length of the support arms is slightly modified, and the ring shape is mildly deformed. In this regard, we consider the optomechanical interaction to be the sum of a torsional and a vibrational contributions, of respective coupling strengths $g_{\rm rot}$ and $g_{\rm om}$.

From the theoretical model introduced in section IV.3.3, the torsional contribution is governed by a Sagnac effect, while the vibrational mode is (mainly) governed by a geometric contribution (*i.e.* by the variation of the cavity length).

Based on f_m and Q_m, the values at mechanical resonance of the angular velocity and mechanical motion PSD are:

$$\begin{cases} S^r_{th,\rm rot} = 1.08 \times 10^{1}\ (\rm rad/s)^2/Hz \\ S^r_{th}\ =\ 4.03 \times 10^{-22}\ \ \rm m^2/Hz \end{cases} \tag{V.16}$$

where we used $J_{\rm eff} = 1.17 \times 10^{-24}$ kg .m^2 and $m_{\rm eff} = 1.83 \times 10^{-14}$ kg, obtained by FEM simulation.

We next calculate $g_{\rm rot}$ and $g_{\rm om}$. We use:

$$g_{\rm rot} = \left(\frac{P_{\rm in} C_r \lambda^2}{\pi c} \frac{\gamma^2 |\lambda - \lambda_r|}{\left[(\lambda - \lambda_r)^2 + \gamma^2 \right]^2} \right)^{-1} \times \frac{\sqrt{S_{\rm out}(\Omega_m)}}{\sqrt{S^r_{th,\rm rot}}} = \mathcal{R} \times \frac{\sqrt{S_{\rm out}(\Omega_m)}}{\sqrt{S^r_{th,\rm rot}}} \tag{V.17}$$

and the equivalent formula for $g_{\rm om}$.

The value measured on the LIA is linked to $S_{\rm out}(\Omega_m)$ by equation (V.15) and $S_{\rm pd}(f) = \alpha^2_{\rm out} S_{\rm out}(f)$, such that we find:

$$\begin{cases} \sqrt{S_{\rm out}(\Omega_m)} = 8.80 \times 10^{-11}\ \rm W/\sqrt{Hz}, & \text{On the red side} \\ \sqrt{S_{\rm out}(\Omega_m)} = 1.21 \times 10^{-10}\ \rm W/\sqrt{Hz}, & \text{On the blue side} \end{cases} \tag{V.18}$$

From table V.5, we calculate:

$$\begin{cases} \mathcal{R} = 2.23 \times 10^{14}\ \rm Hz/W, & \text{On the red side} \\ \mathcal{R} = 2.06 \times 10^{14}\ \rm Hz/W, & \text{On the blue side} \end{cases} \tag{V.19}$$

From which we finally find:

$$\begin{cases} g_{\text{rot}} = 5.99 \times 10^3 \ \text{Hz/(rad/s)}, & \text{On the red side} \\ g_{\text{rot}} = 7.59 \times 10^3 \ \text{Hz/(rad/s)}, & \text{On the blue side} \\ g_{\text{om}} = 0.98 \ \text{kHz/nm}, & \text{On the red side} \\ g_{\text{om}} = 1.24 \ \text{kHz/nm}, & \text{On the blue side} \end{cases} \tag{V.20}$$

Discussion: The values of g_{rot} and g_{om} that we find experimentally are respectively a factor 100 and 5 more elevated than the values that we find with theoretical and numerical modeling.

We can make two hypothesis to explain this (large) discrepancy. What we believe to be the most likely explanation is that due to the reality of fabrication and its associated imperfections, the mechanical mode deviates from its simulated behavior and presents an increased deformation of its shape, which increases the magnitude of the geometric contribution[4] to g_{om}.

An other straightforward explanation could be that we in fact do not observe a mechanical mode. We have a number of clues that tend to refute this theory. First, we observed similar results with other suspended ring resonators of different design and hence different mechanical resonant frequencies. Second, the peak disappears when not operating under vacuum (which strongly degrades the mechanical quality factor), suggesting that this is indeed a mechanical mode. Example of these two points are presented on figure V.19).

Nevertheless, we can not conclude on these measurements. Both additional measurements on new samples and additional theoretical modeling considering the possibility of a coupling between the geometric and rotational contributions need to be done to validate or refute these results.

Higher order modes: The higher order modes are more "classical" vibrational modes, with pure deformation of the ring. We were not able to address them with our present experimental setup. This can be explained based on the noise evaluation of the experiment. Because the thermomechanical noise scale with Ω_m^{-3}, it rapidly decreases at high frequencies, and the optical output after optomechanical transduction is at the same level than the background floor noise due to instrumentation (laser, PD and LIA).

The voltage noise density background value is the sum of the decorrelated laser shot noise and instrumental noise due to the LIA and photodetector. It reads:

$$S_{\text{floor}} = \text{R}^2 G_{pd}^2 \times \left(\alpha^2 S_{\text{shot}} + \text{NEP}^2\right) + S_{\text{LIA}} \qquad \left[\text{V}^2/\text{Hz}\right] \tag{V.21}$$

[4]Note that we still do not consider the photo-elastic and dissipative contributions, which according to table IV.6 are systematically at least two orders of magnitude smaller than the geometric contribution.

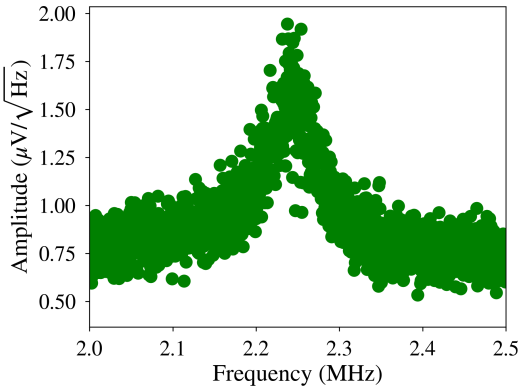

(a) Observation of the torsional mode of a 5 μm ring

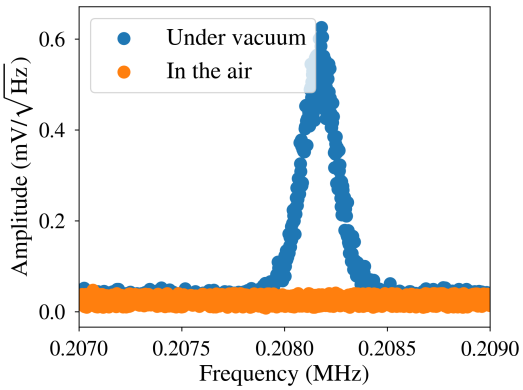

(b) Superposition of the measurements under and off vacuum

Figure V.19 – **Left:** Observation of the torsional mode of a 5 μm radius suspended ring resonator, with 2 rings and 3 arms. We find: $Q_{\text{opt}} = 9\,000$, $Q_m = 100$ and $f_m = 2.24$ MHz. **Right:** Superposition of measurements under and off vacuum on the previously presented 10 μm radius suspended ring resonator. In the air, the resonance peak disappears.

Gain setting (low noise) (V/A)	10^2	10^3	10^4	10^5	10^6	10^7
Upper cut-off frequency (–3 dB)	200 MHz	80 MHz	14 MHz	3.5 MHz	1.8 MHz	220 kHz
NEP (/√Hz, @ 1550 nm)	180 pW	22 pW	1.9 pW	390 fW	140 fW	50 fW
Measured at	20 MHz	8 MHz	1.4 MHz	350 kHz	180 kHz	22 kHz
Integrated input noise (RMS)*	4.9 µW	380 nW	23 nW	3.3 nW	0.84 nW	71 pW
CW sat. power (@ 1550 nm)	10 mW	1.0 mW	100 µW	10 µW	1.0 µW	100 nW

Gain setting (high speed) (V/A)	10^3	10^4	10^5	10^6	10^7	10^8
Upper cut-off frequency (–3 dB)	175 MHz	80 MHz	14 MHz	3.5 MHz	1.8 MHz	220 kHz
NEP (/√Hz, @ 1550 nm)	132 pW	6.3 pW	1.4 pW	350 fW	113 fW	47 fW
Measured at	18 MHz	8 MHz	1.4 MHz	350 kHz	180 kHz	22 kHz
Integrated input noise (RMS)*	3.0 µW	285 nW	21 nW	3.2 nW	0.84 nW	71 pW
CW sat. power (@ 1550 nm)	1.0 mW	100 µW	10 µW	1.0 µW	100 nW	10 nW

Figure V.20 – Noise performances of our photodetector (Femto OE300).

where R, G_{pd} and NEP are the responsitivity, transimpedance gain and Noise Equivalent Power of the photodetector. α represents optical losses along the circuit due to optical couplers and GC, S_{shot} is the laser shot noise, and S_{LIA} is the LIA noise.

The noise performances of the photodetector are dependent on the experimental bandwidth and transimpedance gain. They are presented on figure V.20.

The PSD associated to the laser shot noise, S_{shot}, is given by [173]:

$$S_{\text{shot}} = P_{laser}\frac{2hc}{\lambda} \qquad \left[\text{W}^2/\text{Hz}\right] \tag{V.22}$$

where P_{laser} is the laser power, h is Planck constant, c is the speed of light, and λ is the vacuum wavelength.

The voltage noise density for the LIA is also dependent on experiment parameters. Typically, $\sqrt{S_{\text{LIA}}} = 10$ nV/Hz, which is negligible in front of other noise contributions.

Based on the LIA and PD datasheet, we calculated the expected voltage noise density background value S_{floor} for various bandwidths. The results are presented on table V.7.

Cut-off	S_{floor}, high PD gain	S_{floor}, low PD gain
220 kHz	3.80×10^{-1} mV / $\sqrt{\text{Hz}}$	3.80×10^{-2} mV / $\sqrt{\text{Hz}}$
1.8 MHz	3.81×10^{-2} mV / $\sqrt{\text{Hz}}$	3.81×10^{-3} mV / $\sqrt{\text{Hz}}$
3.5 MHz	3.82×10^{-3} mV / $\sqrt{\text{Hz}}$	3.82×10^{-4} mV / $\sqrt{\text{Hz}}$
14 MHz	4.03×10^{-4} mV / $\sqrt{\text{Hz}}$	4.33×10^{-5} mV / $\sqrt{\text{Hz}}$
80 MHz	7.16×10^{-5} mV / $\sqrt{\text{Hz}}$	2.35×10^{-5} mV / $\sqrt{\text{Hz}}$

Table V.7 – Voltage noise density background with $P_{laser} = 1$ mW

Cut-off	S_{out}, high PD gain	S_{out}, low PD gain
220 kHz	5.80×10^{-1} mV / $\sqrt{\text{Hz}}$	5.80×10^{-2} mV / $\sqrt{\text{Hz}}$
1.8 MHz	2.80×10^{-2} mV / $\sqrt{\text{Hz}}$	2.80×10^{-3} mV / $\sqrt{\text{Hz}}$
3.5 MHz	6.31×10^{-4} mV / $\sqrt{\text{Hz}}$	6.31×10^{-5} mV / $\sqrt{\text{Hz}}$
14 MHz	5.35×10^{-6} mV / $\sqrt{\text{Hz}}$	5.35×10^{-7} mV / $\sqrt{\text{Hz}}$
80 MHz	5.65×10^{-8} mV / $\sqrt{\text{Hz}}$	5.65×10^{-9} mV / $\sqrt{\text{Hz}}$

Table V.8 – Output voltage noise density after optomechanical transduction with $P_{laser} = 1$ mW

The voltage noise density background must be compared to the optical voltage noise density after optomechanical transduction S_{out} (converted in units of $\mu\text{V}^2/\text{Hz}$). For the calculation of S_{out}, we used the values simulated in section IV.3.3 for g_{om}, m_{eff}, Ω_m and S_{th}^r, and typical experimental values for $\mathcal{R}$. The results are presented on table V.8

From comparison of the two tables, we observe that S_{floor} and S_{out} are of similar magnitude until 1.8 MHz, and that beyond this bandwidth the noise floor exceeds the transduced thermomechanical noise. As already pointed out, this is a consequence of the fact that thermomechanical noise scales with Ω_m^{-3}. Based on this observation, the fact that we could not assess mechanical modes around and below 1 MHz is more understandable.

There are three ways around which future work could be conducted in order to enhance the noise performances (other than selecting experimental instruments with better noise performances).

First, we can work on the optical chain, which will increase $\mathcal{R}^{-1}$ and the efficiency of the optomechanical transduction. The main objective here should be to reduce optical losses

due to sidewall rugosity and the suspension arms, and to achieve critical coupling such that the contrast is maximal. The product of the contrast and the optical quality factor is a good quantity to maximize.

Second, we can work on the mechanical part. Generally speaking, we want to reduce mechanical losses to increase the mechanical quality factor. In particular, the strategies presented on the theoretical section aiming to reduce radiation towards the substrate could be followed.

Third, we could select a mechanical mode with a larger optomechanical coupling strength. In particular, aiming for the radial breathing mode seems to be a prospective lead, as already discussed.

A note on optomechanical self-oscillations: Based on the measured experimental parameters, we can calculate the power threshold for optomechanical self-oscillations, defined by equation (I.27). We use: $Q_{\text{opt}} = 30\,000$, $g_{\text{om}} = 1$ kHz/nm, $Q_m = 1\,000$, $f_m = 200$ kHz, $P_{\text{laser}} = 0.8$ mW, $\lambda = 1550$ nm. The value $x_{\text{ZPF}} = 4.860 \times 10^{-14}$ m, used to calculate g_0, is extracted from numerical simulations.

Based on this set of parameters, we find $P_{\text{thre}} \approx 10^{15}$ W, at the laser source. This extremely elevated value is, among other, a consequence of the unresolved sideband regime of our optomechanical oscillator: using notations from part I, we have $\kappa \approx 40$ GHz $\gg \Omega_m \approx 1.25$ MHz (where κ is hence the cavity decay rate).

Realistically, we can expect to improve the optical quality factor and mechanical quality factor to $Q_{\text{opt}} = 100\,000$ and $Q_m = 10\,000$ in future fabrication runs, and obtain an optomechanical coupling rate in the hundred of kHz/nm range. Yet, the power threshold would still be in the MW range, which remain totally unrealistic for practical applications (as a reminder, our laser sources are limited to a 25 mW input power). It highlights the necessity to work in a resolved sideband regime, which should be pursued by working at higher mechanical frequency.

Practically speaking, it again leads to targeting the radial breathing mode in the mechanical spectrum. As already discussed, this mode should present a coupling rate in the MHz/nm range, and a mechanical frequency in the GHz range (based on the comparison to similar published geometries [174, 128, 132]). With this set of parameters, we find a power threshold in the mW range, which is now realistic.

Conclusion

In this chapter, we have discussed the technological realization of suspended ring resonators, as well as our photonic and optomechanic experiments.

Regarding technological realization, we have presented the process flow realized in our

clean-room, and its associated critical steps ; in particular, the release of the optomechanical resonator was a complicated yet crucial part of the process.

The optical characterization was realized on probing stations mounted with optical fibers. We showed a strong correlation between the number of supporting arms and the optical losses within the suspended ring resonator. We also evidenced that the latter are increased after the release step, because of higher rugosity and index contrast. In parallel, we evidenced thermo-optic and non-linear effects in classical and suspended ring resonators, that can strongly perturb the shape of the optical resonance at high optical power.

Finally, we conducted preliminary optomechanical measurements on a dedicated test bench, under vacuum, that was developed during the thesis. We could observe the thermomechanical noise of the fundamental mechanical mode of a suspended ring resonator. This mode is mainly rotational, which is an exotic configuration for optomechanical oscillators, and that has not been extensively studied yet. These experimental results remain preliminary. Notably, improving the test bench, devices performances and the theoretical understanding of the optomechanical interaction in torsional modes are still a work in progress in the team.

Among other solutions to upgrade the optomechanical transduction, the test bench could be modified to realize optomechanical downmixing of the mechanical frequency, which is presented on the perspective part at the end of the manuscript. Without giving details about the procedure, this could be a way to realize the optomechanical transduction of high order modes at an arbitrary low frequency. This way, we could in particular target the radial breathing mode, from which we expect the best optomechanical coupling strength.

Part III

Sub-wavelength grating cavity optomechanics

Introduction

In this part, we focus the discussion on a new approach to cavity optomechanics, centered around Sub-Wavelength Grating (SWG) waveguides. In particular, we point out how the use of SWG waveguides, by introducing a new form of optomechanical coupling, could be beneficial to the field of cavity optomechanics. The discussion is organized around two chapters. In the first chapter, we present the modeling and design of the two different approaches that we studied during this thesis: interdigitated combs SWG waveguides and optomechanical "ladder-like" SWG waveguides. In the second chapter, we discuss the realization and characterization of these structures.

In the following, we introduce the underlying concept of SWG waveguides, and briefly introduce how they could benefit the field of cavity optomechanics.

Introduction to SWG photonic waveguides

A dielectric sub-wavelength grating medium is a periodic material of alternative dielectric layers n_1 and n_2, with a pitch Λ way smaller than the optical wavelength:

$$\Lambda \ll \frac{\lambda}{2n_{\text{eff}}} \tag{V.23}$$

where n_{eff} is the guided effective index. Under this condition, the pitch is small enough to suppress any diffraction or interference effect arising from the periodicity of the medium, that can be considered as a uniform and lossless one, with an anisotropic averaging effect over the refractive index.

SWG medium were initially used in free-space non-linear optics due to their birefringent behavior [175]. More recently, with the progresses of e-beam lithography, SWG medium started to be used as constituting parts of photonic waveguides. The core (and/or cladding) of the waveguide is patterned into periodic segments small enough to respect the SWG condition (V.23), as shown on figure V.21. The resulting SWG structure is lossless, supports quasi-guided optical modes, and can be considered as a wire waveguide

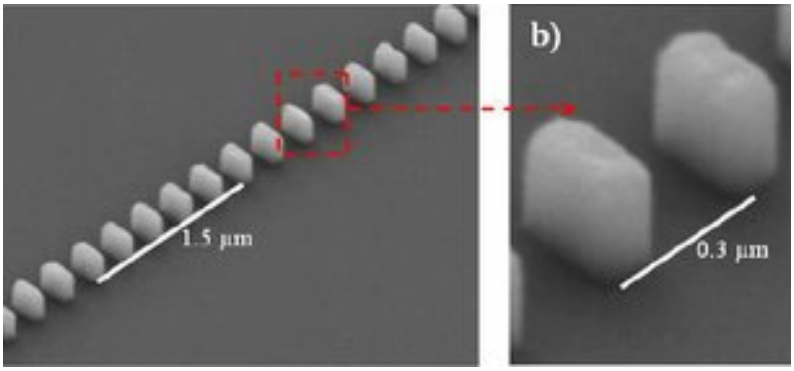

Figure V.21 – SEM image of a SWG waveguide [176].

with an equivalent core refractive index $\bar{n}$ (this is explained in section VI.1.1). It is hence referred as a SWG waveguide.

SWG waveguides were first proposed and demonstrated in 2010 [177, 178], as a new way to both easily engineer the effective guided index through a simple lithographic process, and to reduce linear propagation losses. Since then, they have been exploited to improve the performances of many photonic components, such as filters [179], waveguide crossing [180], optical true delay lines [181], and fiber to chip grating couplers [182]. Recently, it was also realized that SWG waveguides can be used to manipulate the dispersion profile of light, notably to provide a flat profile with zero dispersion [183, 184].

In parallel, SWG waveguides have found applications in the field of Mid InfraRed (MIR) photonic [185]. With a proper design of the SWG media, it is possible to avoid the use of silicon dioxide, that absorbs light beyond the 4 μm wavelength, and to fully exploit the silicon transparency window up to 8 μm [186, 187].

SWG waveguides are also used in photonic bio-sensors [188], where the interaction of a molecule with the evanescent field of an optical cavity is tracked down through interferometric detection. Because the field of SWG waveguides presents a better overlap with its surrounding environment than classical waveguides, the sensor sensitivity and performances are improved. Additionally, in a fully-etched SWG waveguide, this (already) higher sensitivity is even further improved by the fact that the analyte can directly interact with the field at the gap between two consecutive pads.

Cavity optomechanics with SWG photonic waveguides

During this thesis, we studied the application of SWG waveguides to the field of cavity optomechanics. Our interest came from the realization that the equivalent refractive index $\bar{n}$ of a SWG waveguide is modified under displacement (see section VI.1.1). As a result, strong optomechanical interactions should naturally appear in suspended SWG waveguides.

Formally speaking, the displacement dependence of the refractive index of SWG waveguides is similar to the photo-elastic effect, such that we can describe the optomechanical interaction as the sum of three contributions: the geometric and photo-elastic contributions, already presented on the previous parts, and the additional SWG contribution, that adds-up with the others. We tried to exploit the SWG ability to enhance the optomechanical coupling strength with what we call optomechanical "ladder-like" SWG waveguides, presented on section VI.3.

In parallel to this approach, we also studied optomechanical structures where the SWG properties allow to replicate interdigitated combs MEMS inertial sensors. Contrary to classical optomechanical schemes, neither the refractive index nor length of SWG interdigitated combs photonic waveguides are modified with mechanical displacement. However, the width of an equivalent waveguide is. This is presented on section VI.2.

CHAPTER VI

Optomechanical "ladder-like" & interdigitated combs SWG photonic waveguides

In this chapter, we present the two geometries that we studied during this thesis: SWG interdigitated combs waveguides and "ladder-like" SWG waveguides.

Prior to the discussion, we introduce a general description of SWG photonic waveguides. An analytical model is proposed, whose description is verified with rigorous numerical simulations. This model is then used to describe our optomechanical SWG waveguides.

SWG interdigitated combs waveguides are described on section VI.2. They rely on classical interdigitated combs structures, but with sub-wavelength dimensions. Apart from optomechanical applications, this waveguide could also be also find applications in MIR photonics or as a bio-sensing platform.

"Ladder-like" SWG waveguides are described on section VI.3. The pads constituting this suspended SWG waveguide are supported by two thin lateral beams. The waveguide can either be integrated inside a directional coupler, a Fabry-Perot cavity, or both at the same time. The resulting optomechanical coupling will be, respectively, either dissipative, dispersive, or both.

VI.1 Modeling of SWG waveguides

VI.1.1 Analytical description of SWG waveguides

We consider a periodic medium of alternative dielectric layers n_1 and n_2, with a pitch Λ that satisfies the SWG condition:

$$\Lambda \ll \frac{\lambda}{2n_{\text{eff}}} \tag{VI.1}$$

As already mentioned above, the SWG medium can be considered as a uniform and lossless one, with an anisotropic averaging effect over the refractive index. The equivalent refractive indexes can be expressed by Rytov's formula [189]:

$$\bar{n}_{\parallel}^2 = n_2^2 + \text{FF}\left(n_1^2 - n_2^2\right) \tag{VI.2}$$

$$\frac{1}{\bar{n}_{\perp}^2} = \frac{1}{n_2^2} + \text{FF}\left(\frac{1}{n_1^2} - \frac{1}{n_2^2}\right) \tag{VI.3}$$

for a polarization parallel or perpendicular to the layers interfaces, where $\text{FF} = a/\Lambda$ is the Filling Factor (FF) ; a is the first layer length, and $\Lambda - a$ is the second layer length.

From formulas (VI.2) and (VI.3), the refractive indexes $\bar{n}_{\parallel}$ and $\bar{n}_{\perp}$ are a function of the filling factor. This is the reason why the refractive index of SWG waveguides is sensitive to mechanical motion and particularly suited to cavity optomechanics ; under elongation or shrinkage of the waveguide, the two layers will respond differently to the mechanical stress, and the filling factor is modified.

Following Rytov's equivalent picture, a waveguide whose core is made of SWG material can be treated as a strip waveguide with an adapted refractive index $\bar{n}_{\parallel}$, which is depicted on figure VI.1, with the main notations that we use. In the following, we will always be in the case of a parallel polarization, and we simply write $\bar{n}_{\parallel} = \bar{n}$.

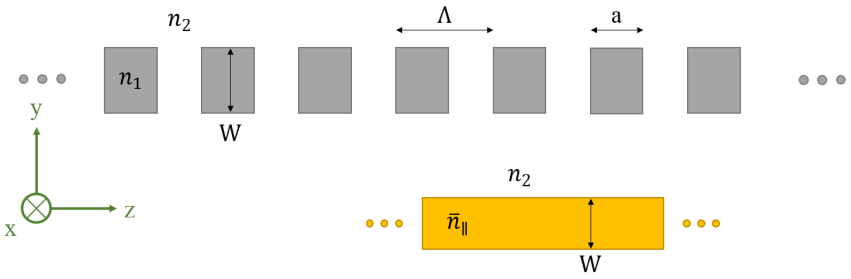

Figure VI.1 – Schematic of a SWG waveguide and its equivalent strip waveguide.

Side comment - Influence of the pitch Λ and comparison to photonic crystals

At first sight, SWG waveguides are very similar to a classical photonic crystal. If we consider a segmented waveguide such as the one of figure VI.1, based on the pitch Λ, we can identify three regimens:

SWG regimen: $\Lambda \ll \lambda/2n_{\mathbf{eff}}$**.** This is the case we discuss all along. The pitch is small enough to suppress diffraction and interference effects arising from the periodicity of the medium, and lossless propagation of light occurs.

Bragg regimen: $\Lambda \approx \lambda/2n_{\mathbf{eff}}$**.** In this case, destructive interference of light occurs, preventing propagation of light. This is the regimen of photonic crystals.

Dissipative regimen: $\Lambda \gg \lambda/2n_{\mathbf{eff}}$**.** In this last case, the pitch is large enough to avoid the Bragg zone, but at the cost of large diffraction losses between each segment.

These three regimens are illustrated on figure VI.2.

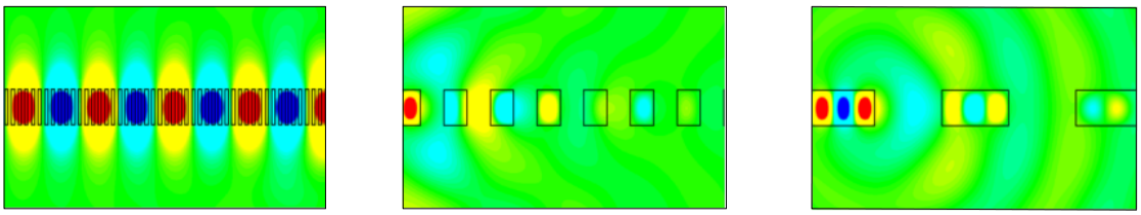

Figure VI.2 – From left to right: SWG regimen, Bragg regimen, and dissipative regimen.

VI.1.2 Modeling and simulation of SWG waveguides

The modeling and design of a SWG waveguide can conveniently be conducted with the analytical model based on Rytov's formulas. From the calculated equivalent refractive index $\bar{n}$, the Effective Index Method (EIM) [84] or a numerical mode solver is used in order to calculate the optical properties of the waveguide and chose a set of design parameters. Example of such approach can for example be found on [83, 71].

While this analytical approach is easy to implement and almost instantaneous, it is not highly accurate. As a matter of fact, Rytov's formulas are only valid for infinite structures with a wavelength to pitch ratio $\lambda/\Lambda \longrightarrow \infty$. In a more rigorous approach, we can rely on numerical simulations. However, mode solving in SWG waveguides is not a straightforward problem ; because a SWG waveguide is not invariant along the direction of propagation (z axis), we can not use classical Finite Element Method (FEM) or Beam Propagation Method (BPM) mode solvers. To overcome this problem, we tried to develop a method based on 3D FDTD simulations, which is accurate, but at the expense of heavy computational time.

The driving idea of this method is to let a wave propagate far enough in the SWG waveguide such that only the guided mode remains. In order to do so, the simulated structure is excited along the z-direction, with an arbitrary launch field. The field profile in the (xy) plane is periodically recorded, and the overlap integral between two successive profiles is calculated. Once this integral attains unity and remains constant, we assume to have reach steady state behavior and that only the guided mode profile remains. From this stationary state, the guided mode field profile is extracted from a cut in the (xy) plane, and the guided mode effective index is extracted from the field oscillations along the z direction.

The drawback of this approach is that it requires large simulation domains (because of the "far enough" condition on the propagation length) with small meshes (because SWG waveguides are by essence small), which resulted in very time and material demanding simulations. They were typically conducted over a $7 \times 3 \times 40$ μm^3 domain, with a grid size of $10 \times 10 \times 10$ nm^3, PML boundaries, and a time step satisfying the Courant-Friedrichs-Lewy condition, and one full simulation could take up to one week, even with cluster calculations.

As a result, we chose to conduct the design of SWG waveguides with the analytical model, and to only use 3D simulations as a way to verify our results. As a matter of fact, we actually obtained good agreement between the two schemes. Typically, we found an 85% overlap between the calculated guided modes and a 10% error between the effective indexes, in good agreement with previous results from the literature [177].

Despite its somewhat poorer accuracy, we again stress out that the analytical model is almost instantaneous to solve. This way, it provides a good starting point for the general understanding and design of SWG structures, as it allows to rapidly investigate the behavior of the waveguide for large sets of parameters.

VI.2 SWG interdigitated combs as photonic and optomechanical waveguides

VI.2.1 Presentation

A SWG interdigitated combs photonic waveguide is presented on figure VI.3. Two rows of teeth are facing each other, out of phase. They overlap at the middle of the device. Each row of individual combs bears a pitch small enough to form a SWG material, such that so does the interlocking region, and light can be guided in the middle overlap, perpendicularly to the beams.

Along the direction of propagation, each comb is periodic with a pitch Λ_{cl} chosen to respect the SWG condition ($\Lambda_{\mathrm{cl}} \ll \lambda/(2n_{\mathrm{eff}})$). Following Rytov's picture, the comb can be considered as a homogeneous medium of equivalent refractive index $\bar{n}_{\mathrm{co}}$. At the combs overlap, the pitch is reduced to half is value $\Lambda_{\mathrm{co}} = \Lambda_{\mathrm{cl}}/2$, which automatically respects the

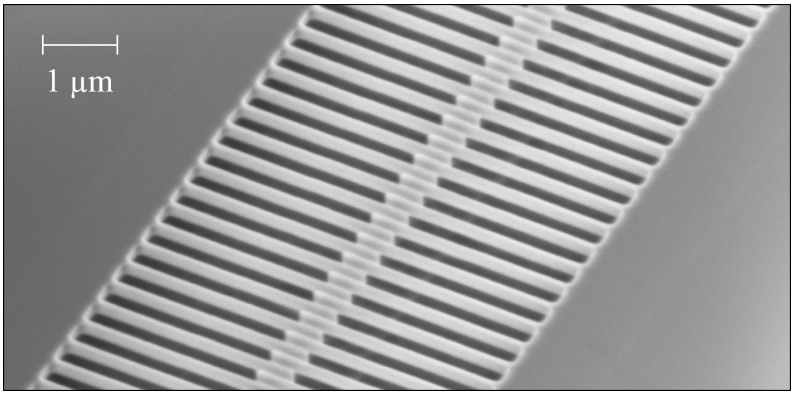

Figure VI.3 – SEM image of a released SWG interdigitated combs waveguide.

SWG condition, and has an associated equivalent refractive index $\bar{n}_{\mathrm{cl}}$. The filling factor is by essence higher at the combs overlap, which assures $\bar{n}_{\mathrm{co}} > \bar{n}_{\mathrm{cl}}$. Hence, the overlap region behaves as the core of a waveguide, and the external regions behave as a lateral cladding for this waveguide. The width of the core, denoted W, corresponds to the width of the combs overlap. The equivalent waveguide is presented on figure VI.4.

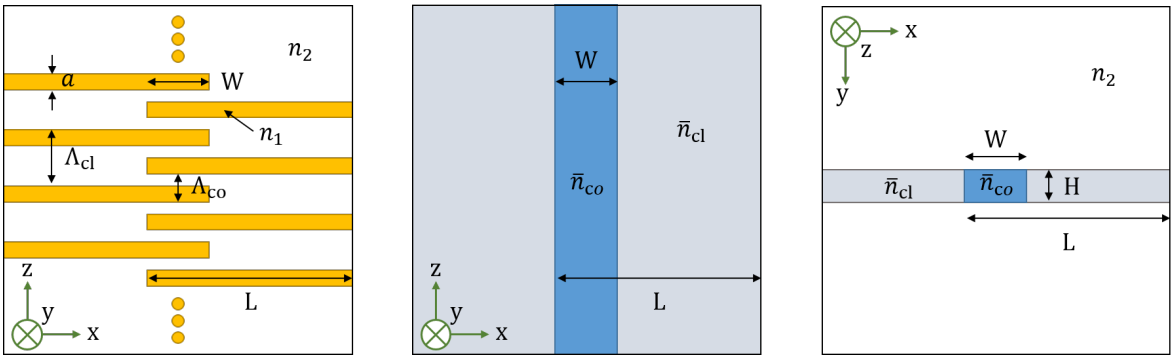

(a) Schematic top view of the SWG interdigitated combs waveguide.

(b) Schematic top view of the associated equivalent waveguide.

(c) Schematic cross view of the associated equivalent waveguide.

Figure VI.4 – Schematics of the equivalent waveguide associated to SWG interdigitated combs. Typically: $W = 500$ nm, $H = 220$ nm, $L = 3$ μm, $\Lambda_{\mathrm{co}} = \Lambda_{\mathrm{cl}}/2 = 150$ nm, $a = 75$ nm, $n_1 = 3.476$ and $n_2 = 1$.

A drawback of the SWG interdigitated combs waveguide can already be pointed out from the previous description. Because we want the lateral regions to be SWG materials, and because $\Lambda_{\mathrm{co}} = \Lambda_{\mathrm{cl}}/2$, the pitch at the middle of the structure has to respect half the SWG criterion: $\Lambda_{\mathrm{co}} \ll \lambda/(4n_{\mathrm{eff}})$. We can thus expect really small pitches at the middle of the structure, that could be difficult to fabricate.

Although not necessary, SWG interdigitated combs waveguides can easily be suspended into an air media, after complete etching of the substrate (in the following, we actually only

consider the case of suspended SWG interdigitated combs waveguides). With a proper opening window, a released SWG interdigitated combs waveguide remains anchored to the substrate at the back-end of the beams. There is no risk of collapsing of the SWG pads constituting the waveguide, and there is no need for additional anchoring mechanism, which function is fundamentally included in the design of the waveguide, and will by essence not perturb the optical behavior.

Easy suspension makes SWG interdigitated combs waveguides particularly suited for MIR photonic applications, bio-sensing applications, and optomechanical applications, in which the release of the SWG structure is particularly beneficial (if not necessary), but can be challenging when not intrinsically included in the design of the waveguide.

It is noteworthy that SWG interdigitated combs waveguides are in principle easily integrable into already existing photonic circuits, and can be fabricated with (almost) classical CMOS fabrication processes.

VI.2.2 Modeling & design

Guided mode

We are first interested by the guided mode effective index and field profile. Ideally, we want a single mode waveguide with a TE polarization, in order to match the other strip waveguides on the wafer. Additionally, single mode behavior has also been shown to strongly limit losses due to jitter effects on fabricated SWG waveguides [190], and the confinement of the TE_0 mode in the (yz) plan makes substrate leakage losses negligible, as already investigated in [191]. There are 4 parameters that can be engineered: the core filling factor FF_{co}, the core pitch Λ_{co}, the overlap width W, the beam length L. The last 4 parameters are fixed: the height H is 220 nm, the cladding filling factor and pitch are linked to the values in the core: $FF_{cl} = 2\,FF_{co}$ and $\Lambda_{cl} = \Lambda_{co}/2$, and the beam width is $a = FF_{co} \times \Lambda_{co}$. Regarding the materials, we consider silicon beams standing in the air.

We conducted the design based on Rytov's formulas and a FEM mode solver. The SWG waveguide varying along z is simplified into its equivalent waveguide invariant along z of refractive indexes $\bar{n}_{co}$ and $\bar{n}_{cl}$:

$$\bar{n}_{co} = \sqrt{n_2^2 + FF_{co}\,(n_1^2 - n_2^2)} \tag{VI.4}$$

$$\bar{n}_{cl} = \sqrt{n_2^2 + FF_{cl}\,(n_1^2 - n_2^2)} \tag{VI.5}$$

The only design parameter on this formulas is $FF_{co} = 2\,FF_{cl}$. Typically, we chose $FF_{co} = 0.5$, which sets $\bar{n}_{co} = 2.5576$ and $\bar{n}_{cl} = 1.9418$. This choice was made with fabrication in mind, as a compromise between the ease of lithography patterning and etching.

The choice of the filling factor sets the values of the equivalent refractive indexes, and the design of the equivalent waveguide can be conducted following the same principles that

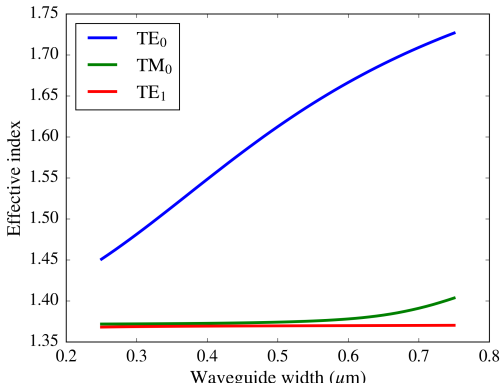

(a) Effective index of the three first modes, against width. We set $FF_{co} = 0.5$. Note that given the fixed FF, the behaviour does not depend on a.

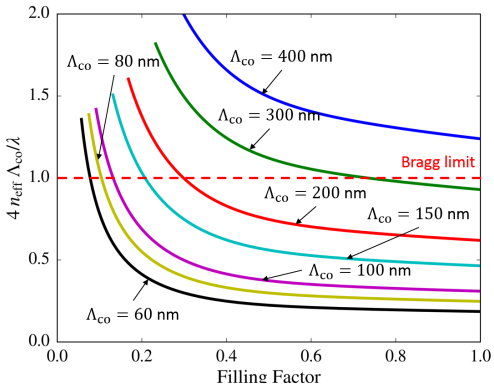

(b) SWG criterion for various comb widths (in regard to the z direction) and filling factors. Comb width values are, from top curve to bottom curve: 200 nm, 150 nm, 100 nm, 75 nm, 50 nm, 40 nm & 30 nm.

Figure VI.5 – Evolution of the guided effective index for various sets of parameters

for a classical strip waveguide. In order to ensure TE single mode behavior, we chose a conservative width $W = 500$ nm, based on the results presented on figure VI.5a. This value is slightly lower than the cut-off (around 600 nm), but presents the advantage to match the width of our strip waveguides and to ease the realization of the taper between the two waveguides (see section VI.2.2).

At this point, having chosen the filling factor and the width, if the condition $\Lambda_{co} \ll \lambda/(4n_{eff})$ is respected, the entire behavior of the waveguide is determined. The simulated field profile is presented on figure VI.6, and is as expected a TE_0 mode. The effective index is $n_{eff} = 1.6197$, which gives an estimate of the maximum pitch that we can use while still respecting the SWG criterion: $\Lambda_{co} \ll 240$ nm. Accordingly, we take an upper limit $\Lambda_{co} < 200$ nm for the pitch.

The lower limit for the pitch is set by the limitations of fabrication technology. Minimal reachable dimensions are dictated by the lithography equipment and the etching process, the later being highly dependent on the etching ratio between horizontal and vertical directions and on the filling factor. After discussions with the lithography and etching teams, we chose to use e-beam lithography and a (challenging) lower limit $\Lambda_{co} > 100$ nm for the pitch.

The last design parameter is the beam length. On the one hand, because the beams will be anchored to large silicon pads with high refractive index, they must be long enough to prevent any field leakage towards the silicon pads at the boundaries. On the other hand, it is also favorable to keep the beams as short as possible, to avoid collapsing or sticking during fabrication, and insure mechanical solidity in general. As a compromise between these two contradictory requirements, we chose the point from which more than

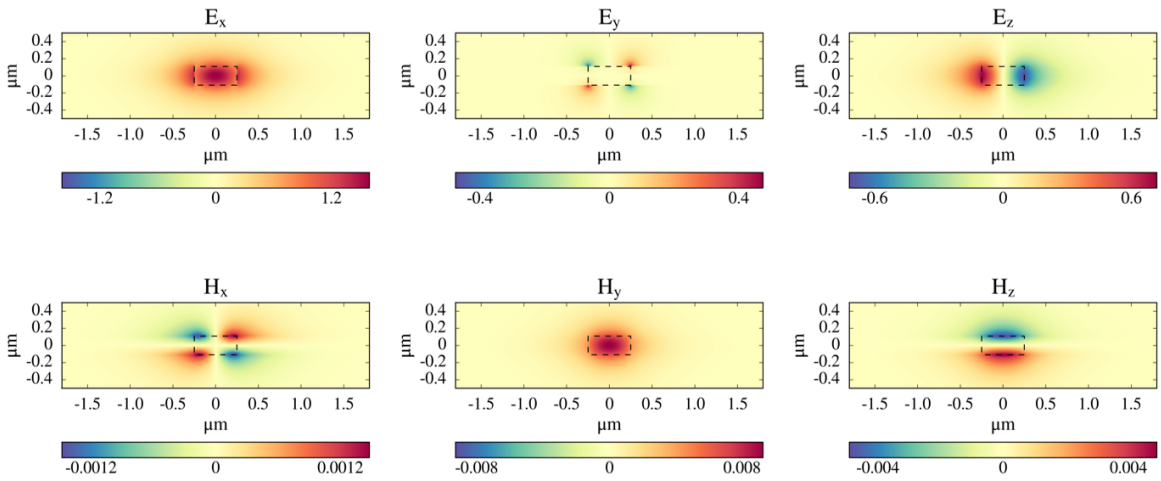

Figure VI.6 – Guided mode profile of the equivalent waveguide, obtained by FEM simulations and an equivalent media approach. The simulated domain corresponds to the schematic cross-view of figure VI.4c

99.99% of the field energy is localized as the minimum beam length. This corresponds to a $L = 3$ μm beam length. Note that the calculation was conducted on the field obtained by 3D-FDTD simulations (see next section), as it is more accurate.

The whole set of design parameters is presented in table VI.1.

Core filling factor	FF_{co}	0.5
Cladding filling factor	FF_{cl}	0.25
Core pitch	Λ_{co}	100 - 200 nm
Cladding pitch	Λ_{cl}	200 - 400 nm
Overlap width	W	0.5 μm
Height	H	0.22 μm
Beam length	L	3 μm
Beam width	a	50 - 100 nm
Beam material		Silicon
Beam cladding		Air

Table VI.1 – Design parameters of a single mode TE_0 SWG interdigitated combs waveguide.

3D simulation of the guided mode

We verified the previous design with 3D FDTD simulations of the guided mode, following the procedure described in section VI.1.2. In the case of SWG interdigitated combs, these simulations are of particular importance, as they take into account the alternating symmetry of the combs, which totally disappears when we apply Rytov's formula. In particular, within a comb, the field profile is transferred towards the beam boundary, as illustrated on figure VI.7 for a right comb.

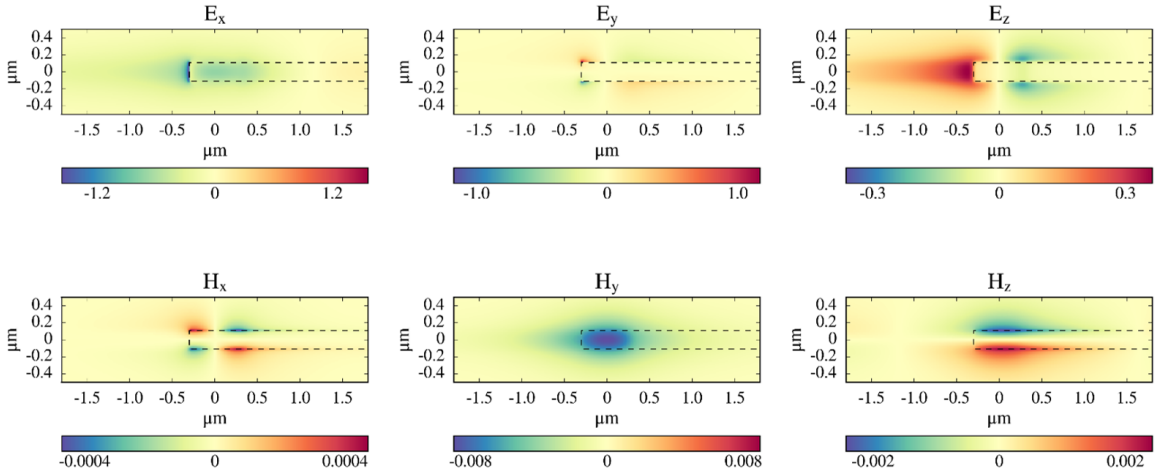

Figure VI.7 – Typical guided mode profile of a SWG interdigitated combs waveguide, in a right comb, obtained by 3D FDTD simulation. Note that the field profile within a left comb is axially symmetric to this picture, with respect to the vertical direction.

The three main components E_x, H_y and H_z are transverse to the wafer plane, and consistently with the previous model, this mode can be identified as the first transverse electric guided mode. Similarly to a strip waveguide, we observe a discontinuity and enhancement of the field at the boundary of the comb. This is evidenced in figure VI.8a, that represents the Poynting vector of such field.

Due to the alternating axial symmetry, the field profile quickly evolves from right to left between each left and right successive comb (this is visible on figure VI.8b). Such axially symmetric variation of the field with a sub-wavelength period is an interesting particularity of SWG interdigitated combs waveguides.

The field profile amid two combs (at) the gap between two beams), is presented on figure VI.9. It is reasonably similar to what is obtained with Rytov's formula and FEM simulations, but less confined inside the core of the waveguide, as already observed with other SWG waveguides. Interestingly, while this field is standing in the air, there is a field enhancement at each "virtual" boundary, as a reminiscence of the silicon beams.

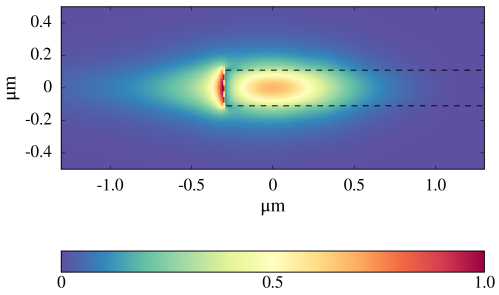

(a) Normalised Poynting vector associated to the field of figure VI.7

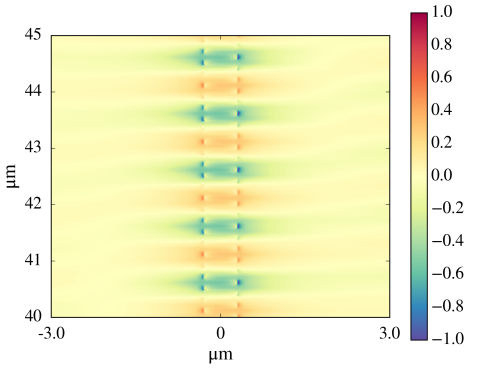

(b) Top view of the amplitude of the E_x component of a guided mode propagating in a SWG interdigitated combs waveguides, obtained by 3D FDTD simulation.

Figure VI.8 – There is a large enhancement of the field at the boundary, that quickly evolves from left to rigth between successive combs.

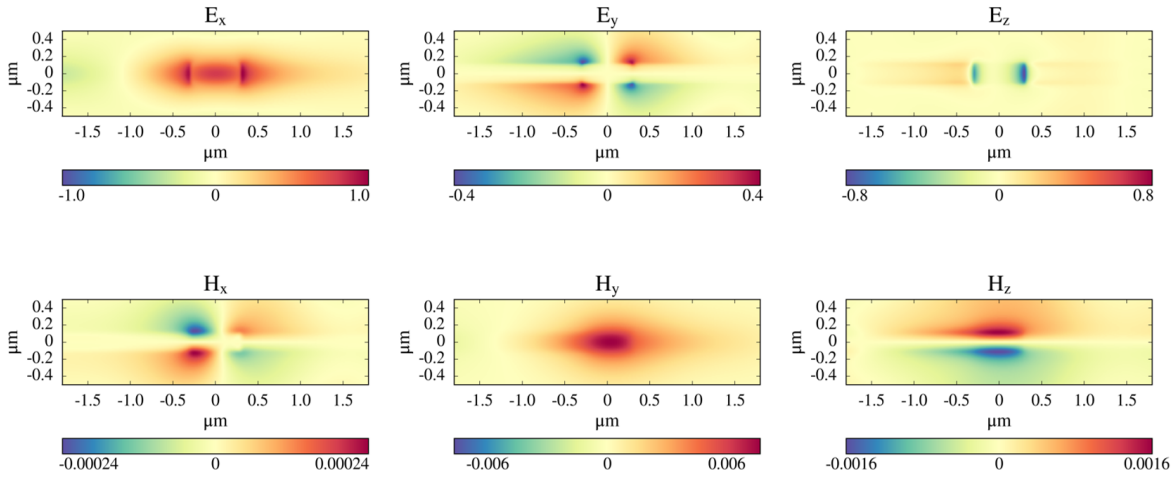

Figure VI.9 – Typical guided mode profile of a SWG interdigitated combs waveguide, at the gap between two combs, obtained by 3D FDTD simulation.

Taper

For practical integration of SWG interdigitated combs waveguides inside photonic circuits, it is mandatory to insure minimum losses at the junction with classical waveguides.

When trying to directly inject the guided mode of a strip waveguide into a SWG interdigitated combs waveguide, the difference between the mode profile and effective index in the two structures results in transition losses. In particular, the difference in symmetry[1] tends to induce additional losses if not taken into account.

In order to reduce the transition losses, we designed an adiabatic taper within which the field smoothly evolves from the symmetric mode profile of a strip waveguide to the asymmetric and quickly oscillating mode profile of a SWG interdigitated combs waveguide.

An example of a fabricated taper is presented on figure VI.10. At the middle of the structure (see figure VI.10b), the classical waveguide gradually tightens into a very narrow tip (50 nm width at the end ; see figure VI.10c), while left and right alternative combs of increasing length are progressively added along the direction of propagation.

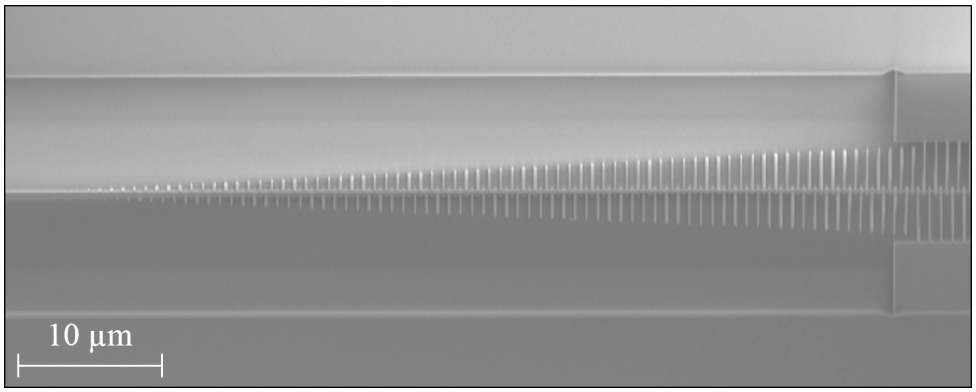

(a) Full View.

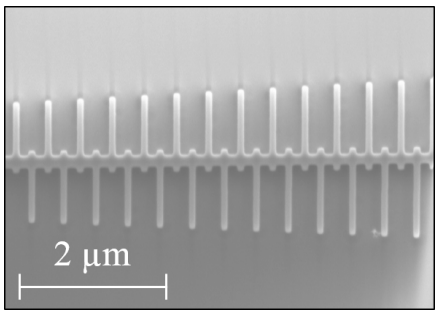

(b) Zoom at the middle.

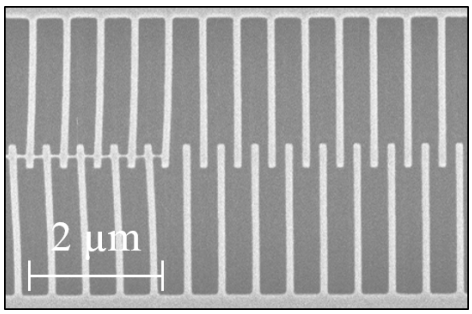

(c) Zoom at the right extremity.

Figure VI.10 – SEM image of the suspended asymmetric taper.

[1]The mode profile in a strip waveguide is symmetric in regard to the vertical direction. It is not in a SWG waveguide. See figures II.6 and VI.7.

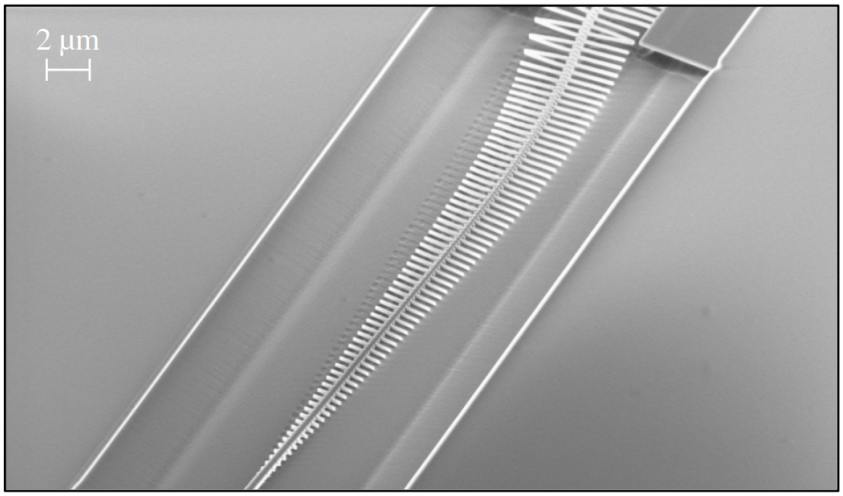

Figure VI.11 – Collapsing of the taper between the strip waveguides and SWG interdigitated combs waveguides.

A constraining problematic associated to this structure is to maintain the mechanical solidity after release (*i.e.* to avoid collapsing). At the waveguide extremity, the beam is clamped to the silica substrate. At the SWG extremity, the structure is supported by the silicon beams linked to the middle narrow tip (see figure VI.10c). Due to the increasing length of the beams, it is necessary to wait till the end of the taper to fix them, so that they are long enough (> 3 μm) to not perturb the optical field. In this end, while this condition is not attained, the middle tip is also used as a mechanical support all along the taper. Even with these precautions, collapsing could still occur, as shown in figure VI.11).

The taper design was verified with FDTD simulations, reduced to a 2D geometry by application of the effective index method along the vertical direction. We simulated an entire geometry, with input and output strip waveguides, input and output taper, and a 10 μm long SWG interdigitated combs waveguide. Varying length of the taper were tested, with always a linear evolution profile. Based on these simulations, we chose the generic taper to be 20 μm long. The taper could probably be shorter, notably by using non-linear evolution profiles [192], but we preferred to keep a simple & safe design, as the footprint was not our first concern.

SWG taper	Classical taper	Abrupt
0.99	0.7	0.3

Table VI.2 – Comparison of the transmission at the junction among the strip and SWG waveguides, between a SWG taper, a classical taper, and an abrupt transition (orders of magnitude).

The taper was also compared to an abrupt junction (directly passing from the strip waveguide to the SWG waveguide), and to a "classical" adiabatic taper: the input waveguide is

gradually tightened to a targeted width that was designed in order to match the effective index of both guided modes. These two designs resulted in higher transition losses, as presented in table VI.2. The three transition schemes are schematically represented on figure VI.12.

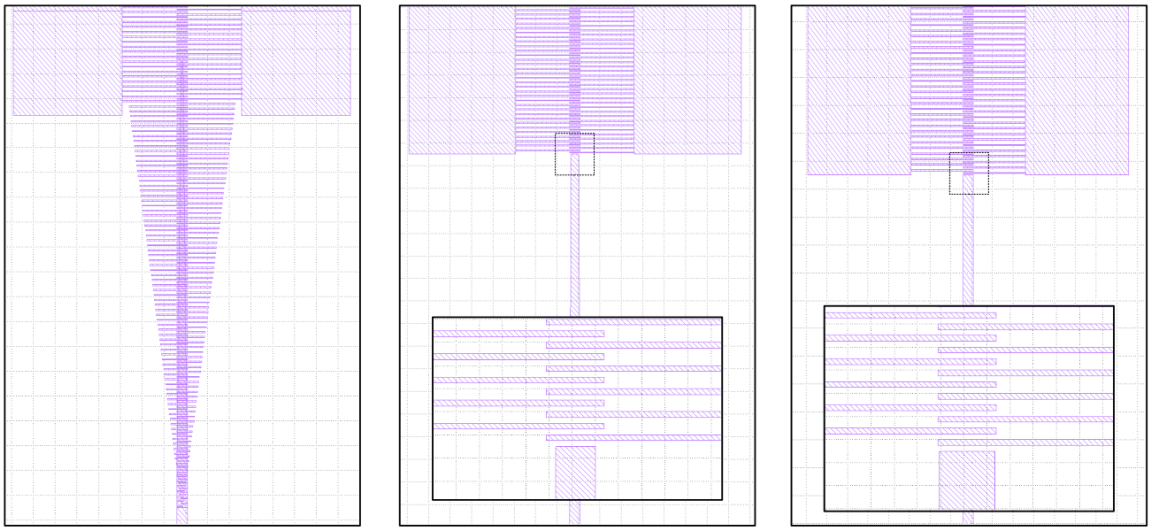

Figure VI.12 – From left to right: schematic of an asymmetric taper, a classical adiabatic taper, and an abrupt junction, at the transition between SWG and strip waveguides.

SWG interdigitated combs waveguides and optical cavities

Like most photonic waveguides, applications of SWG interdigitated combs waveguides often rely on optical cavities. More specifically, the co-integration of a SWG interdigitated combs waveguide and a ring resonator is a way to increase the effective length of the SWG waveguide ("multi-passage" behavior) and to realize an interferometric measurement (which is used when the measurand modifies the effective index ; for example in biosensors or inertial sensors).

In order to realize such co-integration, we followed two schemes: the integration of the SWG interdigitated combs waveguide within a racetrack resonator, and the realization of ring-shaped SWG interdigitated combs waveguides. These two structures are schematically presented on figure VI.13.

In the first scheme, a SWG structure comprised of an input SWG taper, a SWG waveguide, and an output SWG taper is included at the middle of a racetrack resonator. The racetrack resonator is assessed by evanescent coupling through a straight waveguide.

In the second scheme, a SWG interdigitated combs waveguide is looped back into itself in order to form a ring structure. The major problematic associated to this geometry is to couple light into the SWG ring resonator. Because of the lateral footprint of SWG

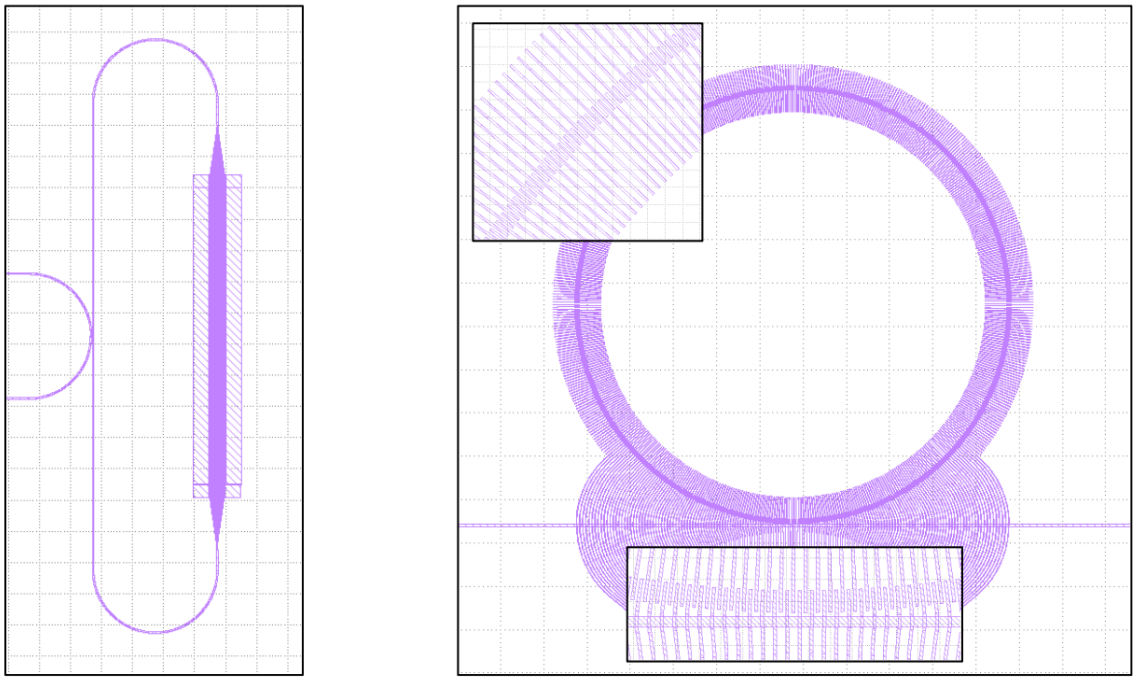

Figure VI.13 – Co-integration of a SWG interdigitated combs waveguide and a ring resonator. **Left:** SWG interdigitated combs waveguide within a racetrack resonator. **Right:** Ring-shaped SWG interdigitated combs waveguide, with a zoom on the coupling region.

interdigitated combs waveguides, it is not possible to realize the evanescent coupling by bringing a second SWG interdigitated combs waveguide at direct proximity of the ring. The coupling region is shown on figure VI.13. A narrow wire waveguide surrounded on each side by a SWG media (identical to the combs) is brought at close proximity of the ring. The narrow waveguide is designed such that its effective index matches the effective index within the ring resonator. The efficiency of the coupling function was verified by means of 2D FDTD simulations with the effective index method.

VI.2.3 Applications of SWG interdigitated combs waveguides

Released SWG interdigitated combs waveguides find applications in cavity optomechanics, MIR photonics and bio-sensing. In a nutshell, the last two points benefit from the usual advantages of suspended SWG waveguides ; respectfully the use of silicon dioxide is avoided, and sensitivity towards the analyte is increased.

Regarding applications in the field of cavity optomechanics, three schemes can be realized, either by exploiting the collective lateral motion of multiple beams, or by exploiting the flexural motion of individual or multiple beams.

In the first case, the overlap between the interlocking teeth is varied, which modifies the equivalent waveguide width and the effective index of the guided mode. This is the configuration that we mainly considered in this work, and it is further discussed in the following paragraph. The two other schemes are briefly discussed in the conclusion of this section.

Exploiting the lateral motion as an optomechanical mechanism

We consider a configuration in which multiple successive combs are laterally moving, as shown in figure VI.14a. This situation can for example be realized by anchoring part of the combs to a movable proof mass, as shown on figure VI.15.

We note x the amplitude of the lateral displacement (along the x direction). After displacement, the new overlap (and waveguide width) is $\mathrm{W} \pm x$. Because the guided effective index is a function of the waveguide width, the optical phase at the end of the waveguide is modified by lateral motion, by an amount:

$$\Delta\varphi = \frac{2\pi}{\lambda}\Delta n_{\mathrm{eff}}\mathcal{L} \tag{VI.6}$$

where $\mathcal{L} = \mathrm{N}_b\Lambda_{\mathrm{cl}}$ is the length of the movable portion, constituted of N_b beams. Under the limit of small displacement, we consider a linear variation[2] of the effective index with the waveguide width: $\Delta n_{\mathrm{eff}} \equiv \alpha\Delta\mathrm{W} = \alpha\Delta x$, where α is a free parameter, obtained by simulations or experimentally.

[2]Which is verified by numerical simulations.

On figure VI.14b, we plotted the effective index of SWG interdigitated combs waveguides for diverse filling factors, against the width of the equivalent waveguide (as the local variation are quite small, we used a large range of width values to emphasize the phenomenon). α corresponds to the slope of each curve, which we observe to be increasing with higher filling factors. We chose $\mathrm{FF_{co}} = 0.5$ when designing the waveguides, favoring easy fabrication. We can see that this is not the best choice in terms of sensibility, and remains a compromise.

From the previous formulas, the measurement of the variations of the optical phase gives access to the displacement x. This can be done by co-integrating the SWG interdigitated comb waveguide with an optical interferometer, such as a Mach-Zehnder Interferometer (MZI) or a ring resonator. This second solution is particularly appealing, because the optical phase is also proportional to the length $\mathcal{L}$, which will be magnified by the multi-passage behavior of the cavity.

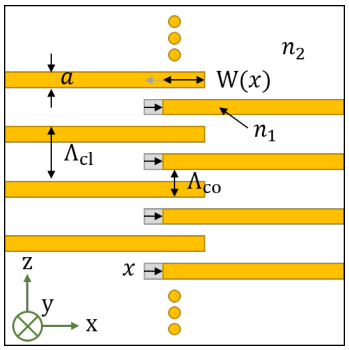

(a) Schematic of the effect of lateral motion x. The amplitude of the displacement is amplified for visualisation purposes.

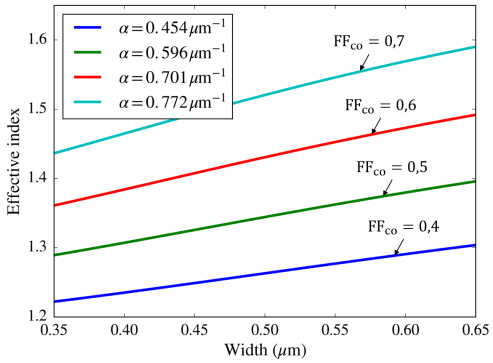

(b) Effective index against width, using Rytov's formula, for various values of the Filling Factor $\mathrm{FF_{co}}$.

Figure VI.14 – The lateral motion on an assembly of successive combs modifies the waveguide width and the effective index.

Integration within a ring resonator When the SWG interdigitated combs waveguide is integrated within a ring resonator, the variations of the optical phase φ with mechanical motion will modify the optical angular resonant frequency ω_0, in a manner completely analogous to any optomechanical cavity. We can therefore use the optomechanical coupling strength to describe the optomechanical interaction:

$$g_{\mathrm{om}} = \frac{\partial \omega_0}{\partial x} = -\frac{c}{n_{\mathrm{eff}}\mathcal{P}}\frac{\partial \varphi}{\partial x} = -\frac{c}{n_{\mathrm{eff}}\mathcal{P}}\frac{2\pi}{\lambda}\mathcal{L} \times \alpha \tag{VI.7}$$

where we used equation (VI.6), $\mathcal{P}$ is the total length of the optical cavity, and $\mathcal{L}$ is the length of the SWG waveguide.

For $FF_{co} = 0.5$, we calculated $\alpha = 0.596\ \mu m^{-1}$ with our numerical model. Typical values for other parameters are $n_{eff} = 2.35$, $\mathcal{P} = 300\ \mu m$ and $\mathcal{L} = 50\ \mu m$, such that we can estimate:

$$g_{om} \approx 10\ \text{GHz/nm} \tag{VI.8}$$

As it stands, this value of g_{om} is in the upper range of state-of-the-art cavity optomechanics devices. However, one must consider that the anchoring mechanism for such structure is also relatively large.

Typically, an anchor such as the one described in the next paragraph, has a zero point fluctuations amplitude around $x_{ZPF} \approx 0.1$ fm, such that the vacuum optomechanical coupling strength is $g_0 \approx 1$ MHz, which in the end is in a relatively low range among optomechanical cavities.

Example: SWG interdigitated combs waveguide-based accelerometer

We continue the discussion by considering the example of an accelerometer based on SWG interdigitated combs waveguides. The latter is linked to a proof mass, as shown on figure VI.15, and is used as a transduction scheme of the mechanical motion of the proof mass.

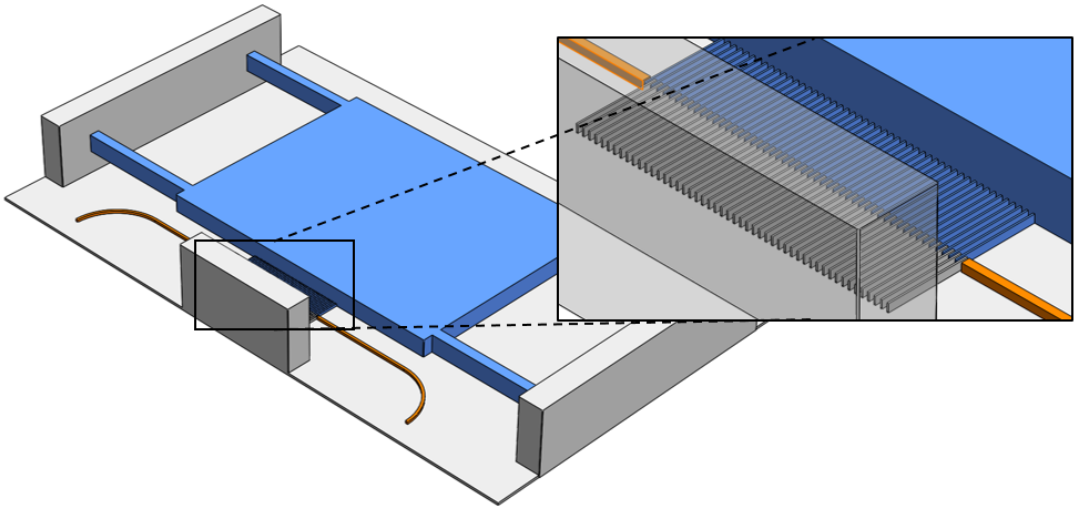

Figure VI.15 – Schematic of a SWG interdigitated combs waveguide-based accelerometer. Grey parts are fixed to the substrate and unable to move. Blue parts are released and sensitive to mechanical motion. Orange parts denote input and output waveguides. Transition tapers are not represented and scales are not respected.

More precisely, any inertial force applied on the released device induces a variation of the combs overlap and of the equivalent waveguide width. This will alter the optical phase of the propagating wave, along with its effective index. Hence, the mechanical motion can be assessed with an interferometric method, such as a ring geometry (in this case, the waveguide on figure VI.15 is simply lopped back on itself).

We follow a typical MOEMS approach [193], in which the mechanical part is a thick layer that is grown upon the photonic thin layer. We consider a proof mass supported by four springs, with mass $m \equiv 0.1$ μg and mechanical resonance angular frequency of $\Omega_m \equiv 20$ kHz.

We use an approach similar to what we used with suspended ring resonators (section V.3) in order to calculate the Limit Of Detection (LOD) at three-sigma, which reads:

$$\mathrm{LOD} = 3P_n g_{\mathrm{om}}/\mathcal{R} \tag{VI.9}$$

where P_n and $\mathcal{R}$ are the overall noise and optical response of the system. Specifically, P_n is the quadratic sum of uncorrelated noise power spectral densities:

$$P_n = \sqrt{\left(S_{\mathrm{pd}}^2 + S_{\mathrm{el}}^2 + S_\gamma^2 + S_{th}^2\right)\mathrm{BW}} \tag{VI.10}$$

where S_{pd}, S_{el}, S_γ and S_{th} are respectively the photodetector noise, the electronic noise, the photonic noise and the thermomechanical noise, and BW is the integration bandwidth.

When the SWG waveguide is included inside a ring resonator cavity, $\mathcal{R}$ is given by:

$$\mathcal{R} = \left(\frac{P_{\mathrm{in}} C_r \lambda^2}{\pi c} \frac{\gamma^2 |\lambda - \lambda_r|}{\left[(\lambda - \lambda_r)^2 + \gamma^2\right]^2} \right)^{-1} \tag{VI.11}$$

We use $g_{\mathrm{om}} = 10$ GHz/nm which we found with our model. For our typical experimental parameters on $\mathcal{R}$, the calculation leads to:

$$\mathrm{LOD} = 20\ \mu\mathrm{g}/\sqrt{\mathrm{Hz}} \tag{VI.12}$$

Even if we considered one of the simplest mechanical design, this value is at the range of other state-of-the-art accelerometers based on MEMS or MOEMS technology. Although very basic, this calculation points out the potential of SWG interdigitated combs waveguides as optomechanical transducers.

Conclusion

On this section, we have presented the analytical and numerical modeling of a new kind of SWG waveguide comprised of interdigitated combs. Compared to other SWG geometries, SWG interdigitated combs waveguides are by design easy to release, and could find applications in MIR photonics, bio-photonic sensing and cavity optomechanics. In particular, their collective lateral motion can be used as an optomechanical transduction platform, as they allow to replicate some of the already well-known architectures used in MEMS and MOEMS capacitive sensing.

Although not discussed in this manuscript, we also believe that the flexural motion (*i.e.* in the y or z direction) of individual or multiple beams could be exploited.

For example, by letting a single beam longer than the others, it is possible to isolate the frequency of its movement from the others, and to create a configuration where only one beam is excited. This is a way to reproduce the optomechanical "in-the-middle" setup, where a sub-wavelength sized nanomechanical resonator (generally a beam or a membrane) is placed in the middle of an optical cavity [194]. While this scheme is traditionally hazardous to manipulate experimentally, the integrated nature of SWG interdigitated combs waveguides should ease its realization, as it allows to release the constraints on optical alignment and resonator positioning.

In another approach, the individual flexural motion of multiple beams could be excited by the optical forces lying in the waveguide, giving raise to a complicated yet interesting dynamic of large arrays of beams coupled by an optical spring. In particular, this could be a way to realize optomechanically induced synchronization between multiple mechanical resonators.

We did not have time to investigate these last options neither experimentally nor theoretically during the thesis, and focused our work on the lateral collective scheme. It is difficult to state whether or not it is actually possible to go beyond their concept, but we believe they emphasize some interesting perspectives about the applications of SWG interdigitated comb waveguides and SWG waveguides in general to the field of cavity optomechanics.

Next, we turn the discussion around an other SWG optomechanical geometry, that we call "ladder-like" SWG waveguides.

VI.3 Optomechanical "ladder-like" SWG waveguides

VI.3.1 Presentation

On section VI.1.1, we introduced the fact that the refractive index of a SWG waveguide is a function of its filling factor:

$$\bar{n}^2 = n_2^2 + \mathrm{FF}\,\left(n_1^2 - n_2^2\right) \tag{VI.13}$$

Based on this observation, it appears that if we are able to suspend a SWG waveguide, optomechanical coupling should naturally appear, as the filling factor will be modified under displacement. We propose to do so on the following. We realize the suspension of the SWG waveguide by adding two thin lateral beams along the waveguide, as depicted on figure VI.16. We call this king of geometry a "ladder-like" SWG waveguide.

More precisely, the core of the waveguide is constituted of periodically spaced small rectangular silicon pads, supported by two lateral beams. The pitch Λ is chosen in order

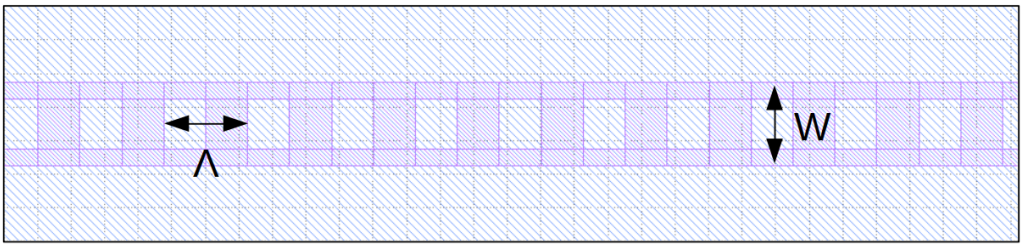

Figure VI.16 – Schematic of a "ladder-like" SWG waveguides: two thin lateral beams are added in order to support the SWG segments.

to respect the SWG criterion, and each beam width is chosen really small in regard to the waveguide width, so that they can be neglected in an analytical model. This way, the "ladder-like" SWG waveguide behaves like an equivalent waveguide whose refractive index $\bar{n}$ is calculated based on Rytov's formula. Apart from the two lateral beams, this is a classical silicon SWG waveguide, for which we expect the SWG cut-off to fall around 400 nm [177].

The "ladder-like" SWG waveguide is suspended and stands in the air. This way, it is also a mechanical oscillator. On a first simplistic description, it is possible to consider the released geometry as a perforated doubly clamped cantilever, whose mechanical mode shapes and vibration frequencies can be described with an analytical approach.

The "ladder-like" SWG structure is hence both a photonic waveguide and a mechanical oscillator. In order to exert optomechanical interactions, it can either be integrated inside a directional coupler, a Fabry-Perot cavity, or both at the same time. This is depicted on figure VI.17.

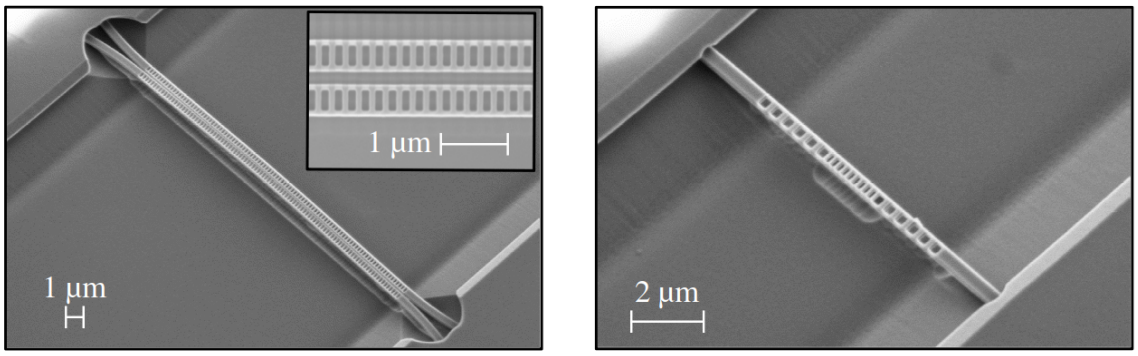

Figure VI.17 – "Ladder-like" SWG waveguides. **Left:** Two "ladder-like" SWG waveguides are brought at close proximity of each other in order to form a directional coupler. **Right:** The SWG waveguide is placed between two Direct Bragg Reflectors, such that is stands at the middle of a Fabry-Perot cavity.

In the first case, two "ladder-like" SWG waveguides are brought close enough from each other to exchange light by mean of evanescent coupling. This setup is analogous to the one studied by Povinelly *et al.*[113] in their work on the optical gradient force: the two

waveguides are attracted or repelled by an optical force that depends on their separation distance. The situation is somewhat similar to a dissipative coupling scheme, with the difference that there is no optical cavity here.

In the second case, a "ladder-like" SWG waveguide is clamped between two Direct Bragg Reflectors (DBR). This way, a Fabry-Perot cavity is created, and a dispersive optomechanical coupling scheme emerges. The classical configuration of cavity optomechanics is hence reproduced, with an additional contribution to optomechanical coupling due to the SWG nature of the medium constituting the cavity.

Finally, both cases can be associated: two "ladder-like" SWG Fabry-Perot cavities are brought close enough from each other to exchange light by mean of evanescent coupling. This way, both dissipative and dispersive coupling are exploited.

VI.3.2 Modeling & Design

Optical design

We conducted the design following the same approach as for SWG interdigitated combs waveguide. The design parameters were obtained using Rytov's formulas and a FEM mode solver, and were latter verified with 3D FDTD simulations. For this reason, we only present the general results of this study. There again, we aimed for a single mode waveguide with a TE polarization.

We chose the waveguide cross section dimensions to be 500×220 nm^2, identical to the ones of strip waveguides. This choice does not exactly correspond to the higher limit for the existence of a unique TE_0 mode, but was made to ease the transition between the classical waveguides and the SWG waveguide. Similarly to SWG interdigitated combs waveguides, the filling factor is chosen at $FF = 0.5$, in order to facilitate the fabrication. The width of each lateral beam is 100 nm. A typical mode profile (obtained with the analytical model) is presented on figure VI.18, presenting a strong similarity to the TE_0 mode of a strip waveguide. The associated effective index is $n_{\text{eff}} = 1.615$, which brings $\Lambda \ll 480$ nm in order to verify the SWG criterion. Accordingly, we chose an upper limit $\Lambda < 400$ nm for the pitch. The lower limit, set by fabrication, remains $\Lambda > 100$ nm.

The whole set of design parameters is presented in table VI.3.

Finally, we point out that we did not design (nor used) a transition taper between the SWG and strip waveguides. We were initially mainly interested in the second and third optomechanical configurations, where a DBR stands between the two waveguides. The physical phenomenon of interest occurs inside of the Fabry Perot cavity, where light is stored and progressively builds up, with no regard for the fact that some losses occur at the junction with classical waveguides. For that reason, it appeared not necessary to insure a lossless transition. Retrospectively, given the fact that we only obtained optomechanical results with the first configuration (directional coupler geometry), where there is no DBR, it appears that the presence of a taper would have been beneficial to reduce transition

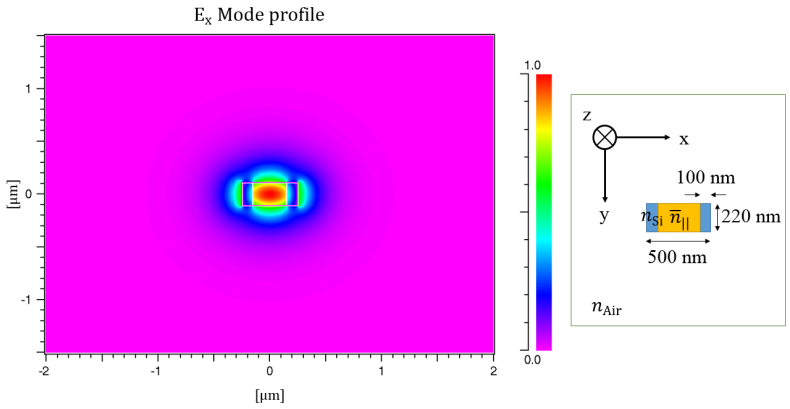

Figure VI.18 – Optical mode profile of a "ladder-like" SWG waveguide, obtained using Rytov's formula and a FEM mode solver. **Left:** E_x field component. **Right:** Schematic of the equivalent waveguide that was simulated.

Filling factor	FF	0.5
Pitch	Λ	100 - 400 nm
Waveguide width	W	500 nm
Height	H	220 nm
Lateral beams width		100 nm
Lateral beams height		220 nm
Beam material		Silicon
Beam cladding		Air

Table VI.3 – Design parameters of a single mode TE_0 "ladder-like" SWG waveguide.

losses (which fortunately remained acceptable even without a taper). On future designs, it is planned to add a transition taper between the "ladder-like" SWG waveguides and the strip waveguides.

Mechanical design

We now focus the discussion around the mechanical behavior and modeling.

The released "ladder-like" SWG waveguide is considered as a perforated doubly clamped cantilever. An analytical model for the vibrations of such cantilever can be found on [195]. We use the results of such study.

The resonant frequencies of the beam are given by:

$$f_n = \frac{1}{2\pi}\sqrt{\frac{E\, I_{\text{eq}}\, Z_n(\gamma)^4}{m_{\text{eq}} L^4}} \tag{VI.14}$$

where E is the Young modulus, I_{eq} is the equivalent moment of inertia, $Z_n(\gamma)$ are solutions of a transcendent equation, γ is a free-parameter dependent on the geometry, m_{eq} is the equivalent mass, and L is the beam length.

The precise expressions for these parameters can be found in [195] (equations 16, 20, 23 and 30, and table 1). They are functions of the number of holes N along the section ($N = 1$ in our case) and of the filling factor α along the section ($\alpha = 0.6$ in our case).

The equivalent mass per unit length of the perforated beam is:

$$m_{\text{equiv}} = \rho \text{WH} \frac{(1 - N(\alpha - 2))\,\alpha}{N + \alpha} \tag{VI.15}$$

which is calculated by integration over a beam segment [195]. The effective mass of a given mode is calculated by multiplying the equivalent mass by the factor presented on table VI.4.

Mode number	1	2	3	4	5	6
$m^n_{\text{eff}}/m_{\text{equiv}}$	0.3959	0.4381	0.4358	0.4353	0.4357	0.4339

Table VI.4 – Values of $m^n_{\text{eff}}/m_{\text{equiv}}$ for the first five modes of a doubly clamped beam with uniform rectangular cross section. n refers to the mode number. Table reproduced from [196].

In parallel to the analytical approach, we also conducted 3D mechanical FEM simulations of released "ladder-like" SWG waveguides. Typical results are presented on figure VI.19.

From observation of figure VI.19, it appears that the first mechanical modes mainly are flexural in-plane and out-of-plane modes. The fifth mode, however, is a torsional mode. This kind of mode is not taken into account by the analytical model.

The frequencies of the analytical and numerical model are compared on table VI.5. Generally speaking, we observe that the analytical model provides relatively satisfactory orders of magnitude, but remains distant from the FEM simulation.

VI.3.3 Optomechanics with "ladder-like" SWG waveguides

Integration within a directional coupler

We first consider two released "ladder-like" SWG waveguides that are brought at close proximity of each other and form a directional coupler, as depicted on the left panel of

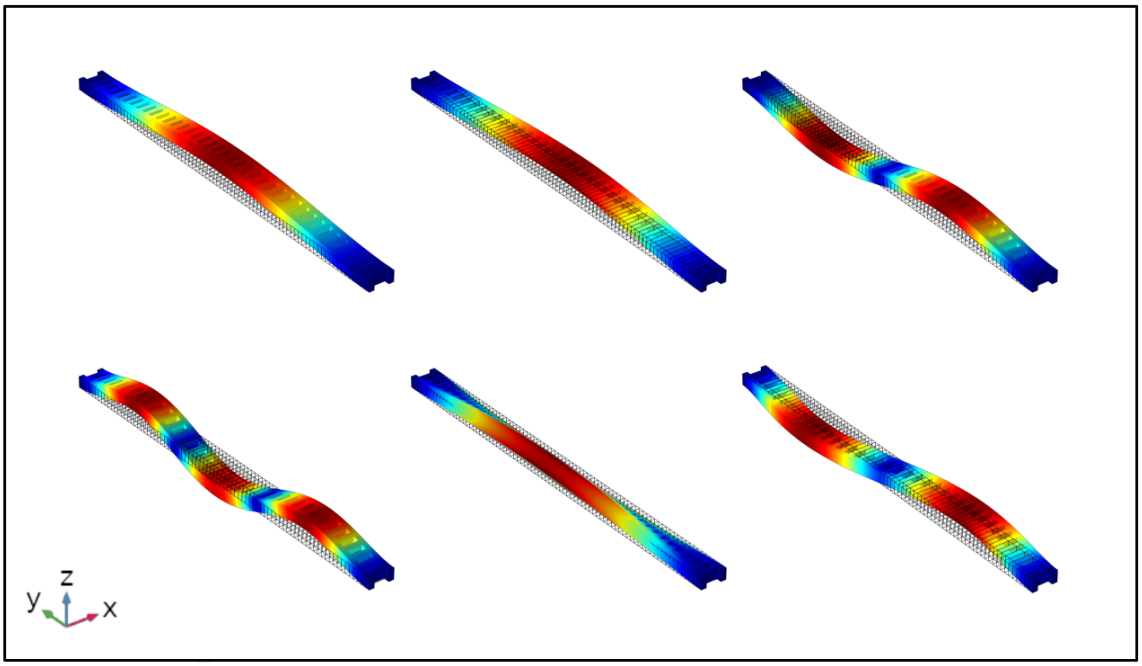

Figure VI.19 – Typical shape of the first six mechanical modes of a released "ladder-like" SWG waveguide. The first, third and fourth modes are flexural in plane, the second and sixth modes are flexural out of plane, and the fifth mode is torsional.

FEM (MHz)	22.87 – Ip	61.03 – Op	62.64 – Ip	121.80 – Ip	133.96 – T
Analytical (MHz)	25.54 – Ip	54.93 – Op	69.83 – Ip	133.45 – Ip	141.90 – Op

Table VI.5 – Comparison of the resonant mechanical frequencies obtained by FEM simulation and with the analytical model. Ip: In plane. Op: Out of plane. T: Torsional.

figure VI.17.

When the two SWG waveguides are getting closer, their respective degenerate guided modes will couple and form symmetric (S) and antisymmetric (AS) modes, whose effective guided indexes is a function of the gap x between the two waveguides. In this configuration, an optical gradient force, function of the gap, arises between the two waveguides [197, 113, 198, 30, 199].

Two springs model Mechanically speaking, the system can be modeled by two coupled springs, where the coupling is assured by the optical gradient force. We note m_1, m_2, k_1 and k_2 the masses and elastic constant of each spring. In this picture, the optical gradient force is assumed to be a third spring of elastic constant k_c: $F_{\text{grad}}(x) = k_c \times x$ (see figure

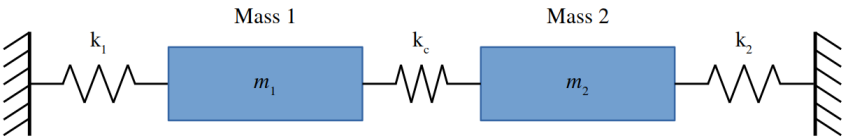

Figure VI.20 – The directional coupler is mechanically modeled by two spring coupled by the optical gradient force $F_{\text{grad}}(x) = -k_c \times x$.

VI.20). The dynamic of the system reads [200, 201]:

$$\begin{cases} m_1\ddot{x}_1 + (k_1 + k_c)\, x_1 - k_c x_2 = F_1 \\ m_2\ddot{x}_2 + (k_2 + k_c)\, x_2 - k_c x_1 = F_2 \end{cases} \tag{VI.16}$$

where we neglected mechanical damping (*i.e.* a $m\Gamma_m\dot{x}$ term), and F_1 and F_2 represent external forces applied on the system (typically, the thermal Langevin force).

If we consider two identical springs ($k_1 = k_2 = k$ and $m_1 = m_2 = m$), the coupling between the two springs breaks the degeneracy of the uncoupled springs, and we find two eigenfrequencies [200, 201]:

$$f_{\text{S}} = \frac{1}{2\pi}\sqrt{\frac{k}{m}} \quad , \quad f_{\text{AS}} = \frac{1}{2\pi}\sqrt{\frac{k + 2k_c}{m}} \tag{VI.17}$$

In the symmetric (S) case, the two springs are oscillating in phase. In the antisymmetric (AS) case, they oscillate out-of-phase. From the previous equations, we calculate:

$$k_c = \frac{k}{2}\left[\left(\frac{f_{\text{AS}}}{f_{\text{S}}}\right)^2 - 1\right] \tag{VI.18}$$

Calculation of the optical gradient force Leaving aside the two spring model, the optical gradient force can be derived from RTOF theory (see sections I.1.2 and III.2.2). It reads:

$$F_{\text{grad}}(\lambda, x) = \frac{P_{in} L}{c}\frac{\partial n_{\text{eff}}(\lambda, x)}{\partial x} \tag{VI.19}$$

where L is the length of the coupling zone. The term $\partial n_{\text{eff}}/\partial x$ is calculated using first order perturbation theory [71]. Note that this force can be either attractive (if negative) or repulsive (if positive).

A comparison between the optical gradient force (per unit length and power), between two SWG waveguides and two strip waveguides, is presented on figure VI.21. Provided that the gap is not too small (which is the case in practice), the optical force is stronger

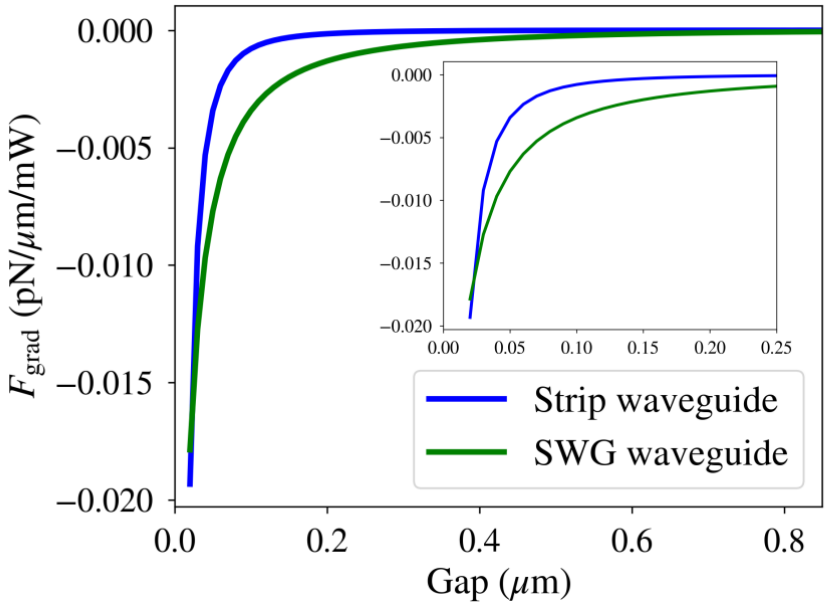

Figure VI.21 – Optical gradient force per unit length and power, between two SWG waveguides and two strip waveguides.

between the two SWG waveguides, and spawns over a larger range of gaps. This is a direct consequence of the increased optomechanical interaction due to the SWG nature of the waveguide. Here, we considered a very basic geometry for the SWG waveguides. We believe that the magnitude of the optical gradient forces could be further increased by proper engineering of the geometrical parameters of the SWG waveguides (notably the filling factor and waveguide cross-section). It can also be enhanced by an optical cavity (the field in enhanced by the finesse), which is explored in the next sections.

Following the previous remark, we point out that this geometry does not strictly fall within cavity optomechanics, as there is no optical cavity. It remains however really close to the field, and find the same kind of applications than on-chip nano-optomechanical systems. In fact, the absence of an optical cavity can be seen as a promising alternative, because it allows to avoid the requirement of finding a resonance peak to work on, and to follow its variation along time (mainly due to temperature changes).

Integration inside of a Fabry-Perot cavity

We now consider a "ladder-like" SWG waveguide integrated within a Fabry-Perot cavity, as depicted on the right panel of figure VI.17. At the input and output ends of the cavity, two Direct Bragg Reflectors (DBR) are directly encapsulating the SWG waveguide. The whole cavity is suspended by etching of the substrate, and is free to mechanically oscillate. In order to avoid collapsing, both the DBR and the SWG waveguide are supported by a left and a right doubly clamped cantilever.

This optomechanical cavity is totally analogous to the Fabry-Perot cavity with a movable

back-end mirror studied in the first chapter: the mechanical oscillation modulates the cavity length and the optical power stored in the cavity, which in turn modifies the optical forces and their action on mechanical motion. Hence, the geometry can be described with the same equations of motion:

$$\begin{cases} \dfrac{\mathrm{d}a}{\mathrm{d}t} = \left[i\Delta(x) - \left(\dfrac{\kappa_i + \kappa_e}{2} \right) \right] a + \sqrt{\kappa_e} s_{in} \\ \dfrac{\mathrm{d}^2 x}{\mathrm{d}t^2} + \Gamma_m \dfrac{\mathrm{d}x}{\mathrm{d}t} + \Omega_m^2 (x - x_0) = -\dfrac{\hbar g_{\mathrm{om}}}{m_{\mathrm{eff}}} |a(t)|^2 + \dfrac{F_L(t)}{m_{\mathrm{eff}}} \end{cases} \tag{VI.20}$$

Here, the optomechanical coupling strength takes the form:

$$g_{\mathrm{om}} = \frac{\partial \omega_0 \left(L, n_{\mathrm{eff}} \right)}{\partial x} \tag{VI.21}$$

$$= \frac{\partial \omega_0}{\partial L} \frac{\partial L}{\partial x} + \frac{\partial \omega_0}{\partial n_{\mathrm{eff}}} \frac{\partial n_{\mathrm{eff}}}{\partial x} \tag{VI.22}$$

which is the sum of a contribution from the cavity length variations (the so-called geometric contribution), and of a contribution from the variations of the effective index. Accordingly to the discussion in part I, this last contribution is separated between the classical photo-elastic contribution and a contribution from the SWG nature of the waveguide. We can rewrite:

$$g_{\mathrm{om}} = g_{\mathrm{geom}} + g_{\mathrm{pe}} + g_{\mathrm{SWG}} \tag{VI.23}$$

The first two contributions are formally calculated with equations (III.18) and (III.20), based on the precise knowledge of the optical, mechanical and strain fields. Although not explored during the thesis, the same perturbation approach that was used to formally calculate these two quantities should be applicable to the calculation of a formal expression for the SWG contribution to optomechanical coupling.

Alternatively, the variations of the effective index can be approximated to $\partial n_{\mathrm{eff}} / \partial x \equiv n_{\mathrm{eff}} / n \times \partial n / \partial x$, such that:

$$g_{\mathrm{SWG}} \equiv \frac{\omega_0}{\bar{n}} \frac{\partial \bar{n}}{\partial x} \tag{VI.24}$$

where $\bar{n}$ is the equivalent refractive index given by:

$$\bar{n} = \sqrt{n_2^2 + \mathrm{FF} \ (n_1^2 - n_2^2)} \tag{VI.25}$$

where only the filling factor is function of x:

$$\frac{\partial \bar{n}}{\partial x} = \frac{1}{2\bar{n}} \frac{\partial \mathrm{FF}}{\partial x} \tag{VI.26}$$

We make the assumption that the displacement is equally distributed between the N pads constituting the SWG waveguide, which leads to:

$$\frac{\partial \bar{n}}{\partial x} \equiv \frac{1}{2\bar{n}} \frac{1}{L} \frac{1 - \mathrm{FF}_0}{1 + x/L} \tag{VI.27}$$

where FF_0 is the unperturbed filling factor and we used $\mathrm{N} \times \Lambda = L$. Provided that $1 \gg x/L$, the approximated SWG contribution to optomechanical coupling finally reads:

$$g_{\mathrm{SWG}} \equiv \frac{\omega_0}{L} \frac{(1 - \mathrm{FF}_0)}{2\bar{n}^2} \tag{VI.28}$$

For comparison, the geometric coupling strength is approximated to $g_{\mathrm{geom}} \equiv \omega_0/L$ in a Fabry-Perot cavity. We can hence realistically expect a factor of $\chi = 25$ between the magnitude of the two contributions with our current design parameters, the SWG contribution being weaker than the geometric one. Note that the factor χ can be reduced to 5 under reduction of the filling factor.

From the previous calculation, the additional SWG contribution to optomechanical coupling seems relatively small in the Fabry-Perot configuration. However, one must consider that the mass of the SWG waveguide (and hence its effective mass) is reduced in comparison to a similar strip waveguide. This is evidenced by our analytical model and equation (VI.15). Roughly speaking, the mass of the SWG waveguide is 80% the mass of a strip waveguide of identical footprint. Consequently, the zero point fluctuations x_{ZPF}, defined by equation (I.13), and the vacuum coupling strength g_0, defined by equation (I.12), are enhanced by a 12% factor because of the SWG nature of the photonic waveguide.

Last, we point out that we considered a purely dissipative coupling scheme here. In practice, the pitch of the two DBR constituting the cavity will also be modified, which will modulate their transmission and reflection rates, and give rise to a dispersive coupling.

Two closely spaced Fabry-Perot cavities

We now briefly discuss the case of two "ladder-like" FP cavities closely spaced, as depicted on figure VI.22. This geometry is a combination of the two previous approaches.

We did not derive the full resolution of this problem, that is quite complicated. We can however make some qualitative observations. In this kind of configuration, even if the dispersive optomechanical coupling strength is not much enhanced by the new SWG contribution, the dissipative contribution (*i.e.* evanescent coupling between the

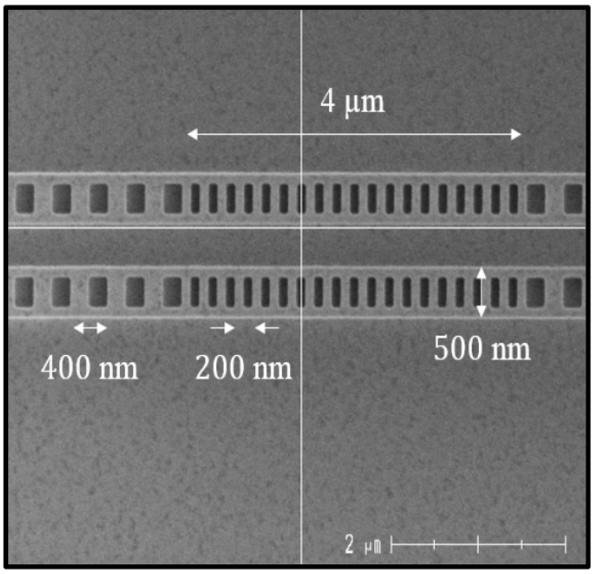

Figure VI.22 – SEM image of two closely spaced Fabry-Perot cavities with SWG "ladder-like" waveguides.

two waveguides) should be, as a consequence of the weaker field confinement of SWG waveguides in comparison to strip waveguides. Additionally, because we are here in a cavity configuration, the optical gradient force will be enhanced proportionally to the cavity finesse, which should also benefit optomechanical interactions.

Conclusion

On this section, we have presented the analytical and numerical modeling of released SWG waveguides, suspended by means of two thin lateral beams, that we call "ladder like" SWG waveguides.

Initially, we were interested in this geometry because we expected an additional contribution to optomechanical coupling in such waveguides, arising from the dependence of the effective index on mechanical motion. While this additional contribution seems to be relatively small, the effective mass of SWG waveguides is reduced in comparison to classical waveguides of the same footprint. Hence, the amplitude of the mechanical zero point fluctuation and the vacuum optomechanical coupling strength g_0 are naturally enhanced in SWG waveguides.

Additionally, we demonstrated that the optical gradient force between two SWG "ladder-like" waveguides is larger than the one between two strip waveguides. This last point could be exploited in optically tunable microphotonic devices and nanomechanical systems.

CHAPTER VII

Realization of SWG cavity optomechanics

In this chapter, we report on the realization of SWG waveguides. We first present the specificities of the process flow that were specifically developed for the fabrication of SWG waveguides. We next present photonic experiments on SWG interdigitated combs waveguides, and photonic and optomechanics experiments on SWG "ladder-like" waveguides.

VII.1 Fabrication of SWG waveguides

The fabrication of SWG waveguides is conducted following the same process flow that suspended ring resonators. Briefly:

1. Patterning of the Grating Couplers (GC).
2. Patterning of the photonic and optomechanical structures.
3. Encapsulation of the photonic structures.
4. Release of the optomechanical structures.

A general presentation of the process flow is given on section V.1. On the following, we limit the discussion to the second step, namely the patterning of photonic and optomechanic devices.

VII.1.1 Patterning of the photonic and optomechanical structures

As already mentioned, our SWG structures involve the realization of periodic patterns with small pitches, below the 100 nm mark. As a consequence, we could not use our standard DUV photolithography equipment, and instead worked with a shape e-beam lithography equipment, which implied adaptations of our regular photonic flow.

Our objective is to pattern lines of width $\Lambda/2$ spaced by $\Lambda/2$, with Λ in the 100 – 400 nm range. In the more challenging case, we are hence trying to etch lines of 50 nm width and 220 nm height, spaced by 50 nm. There are two critical steps: the lithographic definition of the lines, and the etching. At the end of the thesis, while we were able to properly define pitches down to $\Lambda = 120$ nm (see figure VII.1), there is still work that could be done on the process. In particular, the photonic performances (*i.e.* the propagation losses) remain quite elevated, and could benefit from new developments.

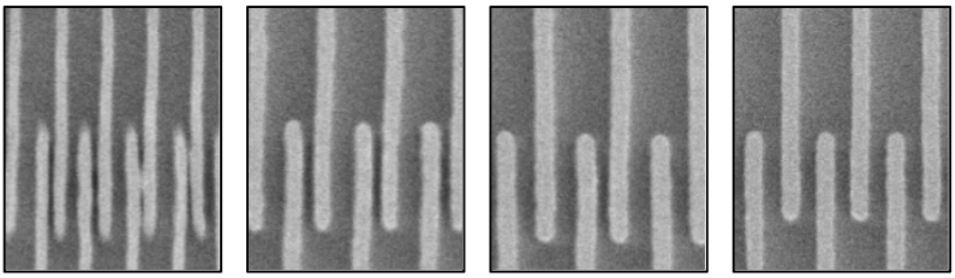

Figure VII.1 – SEM image of SWG interdigitated combs waveguides, for increasing pitches. From left to right: $\Lambda = 100$, 120, 140, 160 nm. The 100 nm pitch suffers from lithographic edge effects (the combs tend to curve towards each other) and poorer etching quality (degraded beam definition and homogeneity). As the pitch is increased, these effects are diminished. The picture is taken after etching of the waveguide level.

The lithographic patterning is first realized. The choice of the right resist and insulation dose is important at this step, to insure a proper patterning of the resist (by limiting edge effects and respecting the targeted design) and efficiently protect the lines during the etching step (even when we were able to properly pattern the resist, it could still fail to protect the silicon layer during etching). We tried several approaches, with different resist types and thicknesses, with and without a hard mask, and with different insulation doses.

Once the lithography step is conducted, the etching can be realized. We used Inductively Coupled Plasma Reactive Ion Etching (ICP-RIE) with HBr chemistry. While this step was less critical that the lithography, as it is already part of our regular photonic flow, it remained challenging to properly etch structures with an almost 5:1 aspect ratio.

In the end, while we were able to tolerably pattern and etch most of our structures, we had to find a compromise between nano-realization and photonic performances. This is

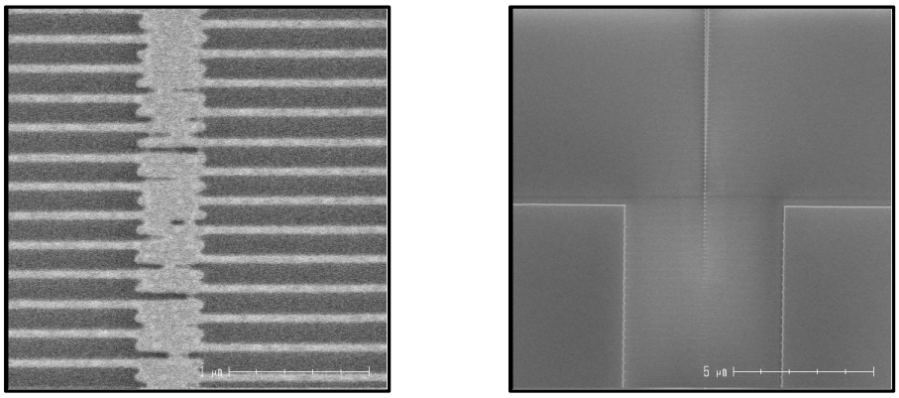

Figure VII.2 – Under (left picture) and over (right picture) etching of the SWG interdigitated combs waveguide (the right picture is taken at the taper level ; see figure VI.10 for comparison).

discussed in the following.

VII.1.2 Effect on photonic performances

The patterning of the SWG waveguides degrades photonic performances in two ways.

First, the resist that we use during e-beam lithography is different from our standard resist on DUV photolithography equipments. As already stated, propagation losses are mainly impaired to the waveguides sidewall rugosity. The latter may originate from the line edge corrugations of the resist, that are afterwards transferred to the waveguides, or from the etching process itself. Minimizing sidewall rugosity is done by choosing the right combination and optimization of lithography, resist and etching process. Consequently, when we use a new lithography equipment and a new resist, we naturally expect higher sidewall rugosity and propagation losses.

Second, we must consider the fact that propagation losses rapidly increase with decreasing waveguides width [202]. During the etching process, in order to achieve the desired pitches on the SWG waveguides, we had to over-etch a little our classical waveguides. Typically, even after trying to optimize the process, a 500 nm width waveguide would still be fabricated with a 470–490 nm width (depending on the fabrication parameters). This effect is evidenced on figure V.9d, which depicts a cartography of propagation losses over a full wafer on which we used variable resist insulation dose between each rows. As the insulation dose is increased (from left to right), the waveguide is wider and the propagation losses are reduced.

At the beginning of the process runs, the first fabricated waveguides presented propagation losses as high as 20 dB/cm (against 2 dB/cm with our standard photonic flow), because of the absence of process optimization. At the end of the thesis, propagation losses are reduced to 3–4 dB / cm. We believe that it is possible to improve the photonic

performances following three guidelines.

First and straightforwardly, the process flow can still be generally optimized by working conjointly on the lithographic and etching parameters. For example, as already stated, it seems that increasing our insulation dose is an efficient way to reduce propagation losses. Following the same idea, we also started a fabrication run on a 300 mm immersion photolithography equipment (that was not part of our cleanroom facility when we realized the first designs). Results are not available yet, but we expect an improvement in comparison to e-beam lithography, as this equipment is more specifically adapted to our designs.

Second, a new drawing of the lithographic mask, with application of a bias on the SWG pitch, could be realized. For example, this means drawing 70 nm lines spaced by 30 nm, that we know will be fabricated as 50 nm lines spaced by 50 nm. When the bias is applied with several dilatation factors over the same mask, this is a way to focus the fabrication process developments towards the realization of the targeted waveguide width ; as different SWG pitches will naturally be realized, the targeted one can be selected afterwards.

Finally, post-etch processes aiming to reduce the sidewall rugosity can be developed. Regarding this last point, we already started exploring the use hydrogen annealing and thermal oxidation as a post-etch smoothing step. While results are not satisfactory yet (in our opinion mainly because we had not enough time to properly optimize each strategy), the efficiency ot these two approaches have already been demonstrated [203, 204].

VII.2 Experiments on SWG interdigitated combs waveguides

We now discuss photonic experiments that were conducted on SWG interdigitated combs waveguides. We begin by verifying the waveguide behavior of the SWG interdigitated combs ; in order to do so, the experimental cut-off pitch and propagation losses are measured and confronted to theory. Next, the SWG taper efficiency is compared to other taper structures. Finally, we investigate the integration of SWG interdigitated combs waveguides inside closed-loop optical cavities, which is the first step towards practical application of SWG interdigitated combs waveguides.

All measurements on SWG interdigitated combs waveguides were conducted over full scale wafers, on the optical probing station that was described in section V.2.1. When not specified, the given measured value correspond to the best value obtained over the dies of the wafer ; most results presented on this section are obtained on wafers with a variable insulation dose between dies, such that statistical data is not particularly relevant.

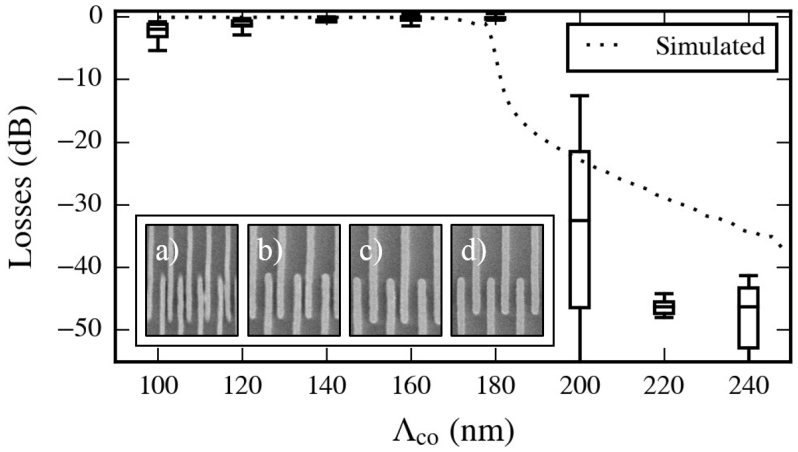

Figure VII.3 – Simulated (dashed) and experimental (boxplot) transmission rate of the SWG interdigitated comb waveguides, for increasing pitches. The boxes extend from lower to upper quartile, with a black line at the median. The whiskers show the full range of the data (measured on 25 identical dies over the same wafer). **Inset:** SEM images for increasing pitches. a) $\Lambda_{co} = 100$ nm. b) $\Lambda_{co} = 120$ nm. c) $\Lambda_{co} = 140$ nm. d) $\Lambda_{co} = 160$ nm.

VII.2.1 Guided mode behavior

Cut-off pitch

In order to identify the cut-off pitch of the SWG regime, we first measured the optical transmission of SWG interdigitated combs waveguides of increasing pitches Λ_{co}. By comparison to a reference structure, the losses due to the SWG structure are calculated at $\lambda = 1550$ nm. The results are presented on figure VII.3, along with the 2D-FDTD simulated behavior of the same structure (dashed line).

For pitches smaller than 200 nm, almost no transmission losses are measured after the SWG interdigitated combs structure. According to theory, this is the SWG regime, where $\Lambda_{co} \ll \lambda/(4n_{eff})$ and no diffraction nor interference effects arise from the periodicity of the medium, hence resulting in lossless light propagation.

On the SWG regime, we observe that transmission losses are kept constant for pitches between 120 nm and 180 nm, but drop again at 100 nm and below. This is a direct result of our difficulty to pattern such small pitches (as discussed in section VII.1) ; for pitches smaller than 100 nm, the lithographic and etching quality are poorer and the beam definition is degraded, which naturally impairs the guided mode behavior. While this is a limitation of our process flow, the SWG regime is already reached with a 180 nm pitch, and it is not necessary to go below this resolution for most targeted applications.

From and above $\Lambda_{co} = 200$ nm, we observe a high transmission drop of more than 40 dB, that rapidly out-passes the dynamic-range of the photodetector. It reveals transition towards the Bragg regime, where destructive interferences prevent the propagation of

light.

We observe a large dispersion of experimental data around $\Lambda_{co} = 200$ nm. It can be attributed to fabrication inhomogeneity over the wafer, slightly changing the cut-off pitch from one die to another. A cut-off around 200 nm is in reasonably well agreement with the condition $\Lambda_{co} \ll 250$ nm found with our 3D semi-analytical model, but a few nanometers higher than the 2D-FDTD simulation displayed on figure VII.3. This can be explained by a general tendency of 2D simulations to over-estimate guided mode indexes, resulting on an under-estimation of the pitch at which optical destructive interferences begin to occur.

Propagation losses in SWG interdigitated combs waveguides

Next, we further investigate the guided mode behavior by measuring the (theoretically nil) propagation losses along SWG interdigitated combs waveguides. Measurements of the optical transmitted power of spiral-shaped SWG waveguides of variable lengths (up to a few centimeters) are realized, and propagation losses are calculated by mean of a linear regression between the spiral length and the experimental transmission.

On the best dies, losses of -5 dB/cm were measured at $\lambda = 1550$ nm. While this is extremely elevated in comparison to a theoretical lossless propagation, two points must be considered. First, there are propagation losses in any real waveguide (because of fabrication uncertainties), and we do not expect the SWG interdigitated combs waveguide to be an exception to the rule. Second, the classical 500 x 220 nm silicon waveguides propagation losses on the same photonic circuits were measured to be around -3 dB/cm. It can thus be considered that the additional propagation losses induced by the SWG interdigitated combs waveguides are around -2 dB/cm. This last value is small enough (considering the total length) to ensure that we are not in a radiative regime and that no diffraction effects are occurring. Additional propagation losses in the SWG waveguides in regard to strip waveguides are a consequence of fabrication impressions such as facets rugosity, but do not question the guided mode behavior.

VII.2.2 Tapper efficiency

As already mentioned, the realization of an efficient taper, insuring as few losses as possible between SWG and strip waveguides, is mandatory to allow practical integration of SWG structures inside already existing photonic circuits. As we will discuss in the next section, this is also important when SWG interdigitated combs waveguide are integrated inside racetrack resonators.

The taper losses are calculated by cascading numerous tapers (0, 10, 15, 20 and 25) and realizing a linear regression between the number of tapers and the experimental transmission. The pitch is constant for all structures: $\Lambda_{co} = 150$ nm.

We first compared the losses of the SWG taper to a classical adiabatic taper, and to an abrupt junction (following the same principle that in the design section, when the

comparison was conducted by means of numerical simulations - see section VI.2.2 and figure VI.12). Here, the taper length is 10 μm. Experimental losses were of -0.22 dB / taper, which corresponds to a transmission rate of 95%. By comparison, the losses were of -2 dB / taper with the classical adiabatic taper, and of -5 dB / junction in the abrupt junction case. Considering fabrication uncertainties, these results are in well agreement with the simulated orders of magnitude obtained by numerical simulation (see table VI.2).

Second, we investigated the influence of the taper length on the transmission rate. We observe that the total losses by taper tend to increase with the taper length (see table VII.1), which is somehow contradictory ; (really) qualitatively speaking, longer tapers are smoother and should induce less transition losses. However, the losses normalized to the length of the taper tend to be reduced when the taper length is increased. This is an indication of (undesired) propagation losses occurring within the taper.

Length	10 μm	20 μm	30 μm	40 μm	50 μm
Median	-0.35	-0.43	-0.70	-0.99	-1.08
Best result (in dB / taper)	-0.22	-0.32	-0.55	-0.65	-0.78
Median	-0.035	-0.0215	-0.0233	-0.0248	-0.0216
Best result (in dB / μm)	-0.022	-0.016	-0.0183	-0.0163	-0.0156

Table VII.1 – Losses of SWG tapers of various length.

We have hence evidenced the efficiency of our transition taper, that efficaciously reduces transition losses between SWG structures and classical waveguides. At time of writing, the taper losses are still strongly correlated with the taper length, which can be associated to propagation losses in SWG interdigitated combs. With future runs aiming to reduce the propagation losses in SWG interdigitated combs waveguides, the taper efficiency should be further increased.

VII.2.3 Integration of SWG interdigitated combs waveguides within optical cavities

Many of the targeted applications of SWG interdigitated combs waveguides imply their integration within an optical cavity. Among other advantages, the optical cavity is a multi-passage interferometric detector, allowing to monitor changes in the close environment of the cavity (bio-photonic sensing applications) or in the shape of the cavity (optomechanical applications). We explored two approaches: the integration of the SWG interdigitated combs waveguide within a racetrack resonator, and the realization of ring-shaped SWG interdigitated combs waveguides.

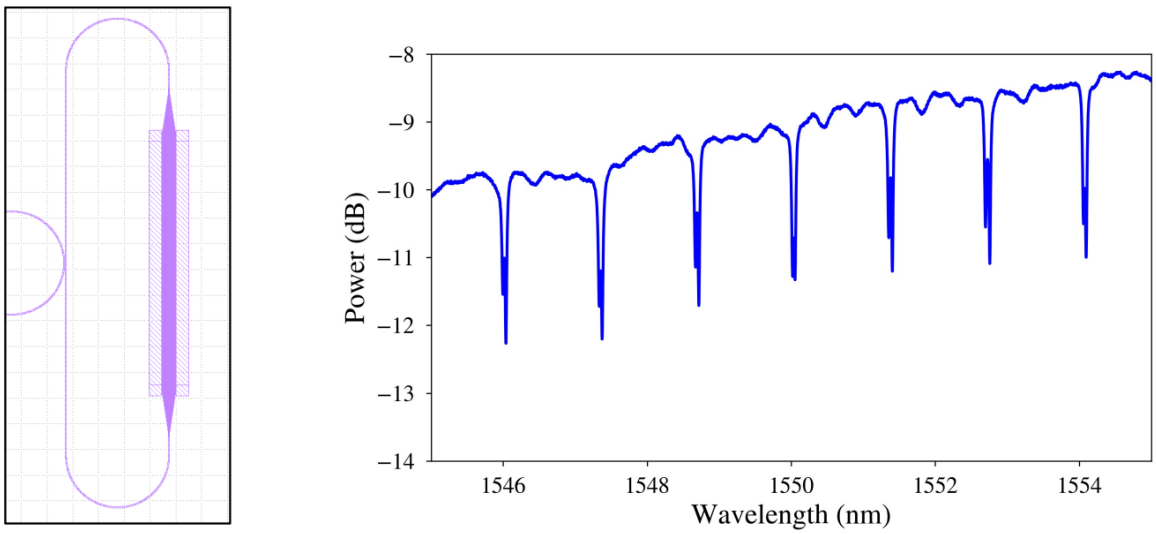

Figure VII.4 – Integration of SWG interdigitated combs waveguides within a racetrack resonator. **Left:** Setup schematic. **Right:** Typical experimental spectrum, for a setup of gap 240 nm, taper length 20 μm, SWG waveguide length 50 μm, with $\Lambda_{co} = 100$ nm.

Integration within a racetrack resonator

We first discuss the integration of SWG interdigitated combs waveguides within a racetrack resonator, as schematically represented on figure VII.4.

Typical dimensions are the following ; the straight part of the racetrack resonator is 100 μm long, its curvature radius is 20 μm. The SWG interdigitated combs waveguide is 50 μm long, and the input and output SWG taper are 20 μm long. The pitch is $\Lambda_{co} = 100$ nm. The gap between the bus waveguide and the racetrack resonator is 240 nm.

At best, we measured quality factors up to 30 000, with an extinction ratio around 2 dB. While such quality factor value remains acceptable, we measured quality factors up to 100 000 on simple racetrack resonators (without the SWG waveguide). This is an indication of the intrinsic limitation of this design. Even if the input and output tapers limit transition losses between strip and SWG waveguides, these limited losses are still suffered multiple times within the optical cavity (at each turn), and rapidly build-up.

Ring-shaped SWG interdigitated combs waveguides

The integration of SWG interdigitated combs waveguides within a racetrack resonator is relatively straightforward, but present the double drawback of poor footprint and inherent losses because of the presence of transition tapers within the cavity. Alternatively, one can design ring resonator-shaped SWG interdigitated combs waveguides, where the whole cavity is formed with SWG waveguides, as depicted on figure VII.5.

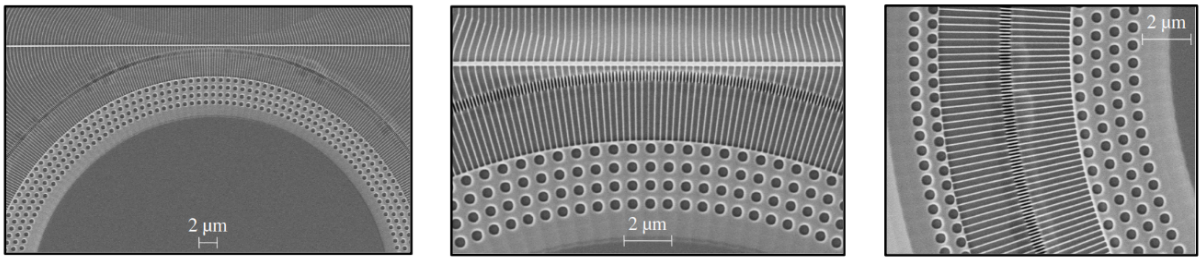

Figure VII.5 – Ring resonator-shaped SWG interdigitated combs waveguide, of radius 35 μm and pitch $\Lambda_{co} = 140$ nm. **Left:** Top view. **Middle:** Zoom over the coupling region. **Right:** Zoom on the interdigitated combs. The regularly spaced holes that can be seen on each picture are photonic crystal that were added to enhance the isolation of the optical guided mode within the SWG waveguide.

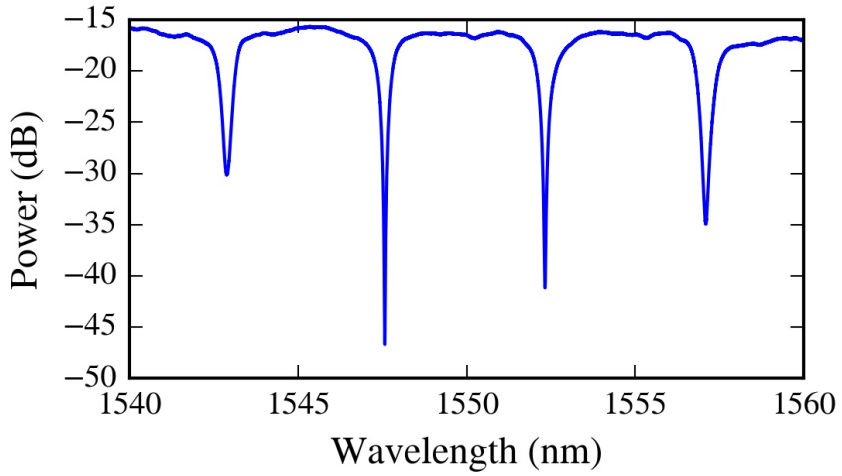

Figure VII.6 – Typical experimental spectrum of a 35 μm radius ring resonator-shaped SWG interdigitated combs waveguide, with $\Lambda_{co} = 140$ nm.

The typical experimental spectrum of a SWG ring resonator is depicted on figure VII.6. At best, quality factors up to 5 000 were measured, with extinction ratios exceeding -30 dB. Albeit the quality factor value remains quite poor, we foresee a large improvement by reducing the propagation loses of the waveguides in future work. From the measured free spectral range, we calculate a refractive group index of $n_g = 2.35$, in good agreement with our model.

An application of this geometry is to realize a bio-photonic sensor, in which the variations of the analyte surrounding the optical resonator are tracked-down by monitoring the position of the optical resonances. The expected sensitivity of the ring resonator-shaped

SWG interdigitated combs waveguides towards its environment is given by:

$$S = \frac{\partial n_{\text{eff}}}{\partial n_2} \frac{\lambda_r}{n_g} \tag{VII.1}$$

Based on our semi-analytical model and on the experimental refractive group index, we calculate $S = 350$ nm/RIU, a value in the upper range of state-of-the-art bio-photonic sensors.

A second application is to exploit the radial breathing mode of the internal disk-shaped silicon support. This way, the inner combs collectively move towards or away from the outer combs, and the middle overlap is modified in a way similar to the one described in section VI.3.3.

Conclusion

On this section, we have presented photonic experiments on SWG interdigitated combs waveguides.

First, we identified the cut-off pitch of the SWG interdigitated combs, around 200 nm, in well accordance with our theoretical predictions. We also measured propagation losses on SWG interdigitated combs waveguides. While they remain quite elevated, we believe that further fabrication developments should pave the way towards a regime where propagation losses within SWG interdigitated combs waveguides are equivalent to state-of-the-art propagation losses within silicon strip waveguides.

Second, we investigated the efficiency of the SWG taper insuring the junction between SWG waveguides and strip waveguides. We first compared the taper to a classical taper and an abrupt transition, and obtained results in agreements with our predictions. Next, we studied the influence of the taper length. At time of writing, the losses are still dominated by propagation losses within the taper, and a compromise have to be found between smoothing the transition (hence, lengthen the taper), and reducing propagation losses (hence, shortening the taper). Here again, we hope to solve this issue with next fabrication runs and reduced propagation losses.

Finally, we integrated SWG interdigitated combs waveguides inside closed-loop optical cavities. We followed two approaches, with a SWG waveguide integrated within a race-track resonator, and with a ring-shaped SWG interdigitated combs waveguide. While the second approach is most promising in terms of practical applications, it also remains limited by propagation loses.

VII.3 Experiments on SWG "ladder-like" waveguides

We now discuss photonic and optomechanic experiments that were conducted on "ladder-like" SWG waveguides.

Photonic experiments are realized on SWG directional couplers and on SWG Fabry-Perot cavities. They were conducted over full scale wafers, on the optical probing station that was described in section V.2.1.

Optomechanic measurements are only realized on SWG directional couplers. They were conducted on single dies, on the dedicated test bench described in section V.3.1.

VII.3.1 Photonic experiments

Cut-off pitch

We first investigate the cut-off pitch of SWG "ladder-like" waveguides ; the transmission of SWG "ladder-like" waveguides of increasing pitches is measured. Results are presented on figure VII.7. Depending on the wavelength, we find a cut-off pitch between 400 nm and 450 nm, which is in agreement with our theoretical prediction ($\Lambda \ll 480$ nm).

The wavelength dependence of the cut-off pitch, related to the SWG condition $\Lambda \ll \lambda/2n_{\text{eff}}$, is evidenced on the right part of figure VII.7. We plotted a typical transmission spectrum between 1520 nm and 1580 nm, for increasing pitches. For a 400 nm pitch, we observe no transmission below $\lambda = 1560$ nm, and optical transmission above this mark, which corresponds to the transition between the SWG and Bragg regime.

Finally, one can notice that the transmitted power in the SWG regime is relatively low (between -20 and -30 dB). As already explained on section VI.3.2, this is a consequence of the absence of transition taper between the segmented and strip waveguides.

Fabry-Perot cavity

We next realize the experimental characterization of a SWG "ladder-like" Fabry-Perot cavity. The experimental spectrum of a 4 μm long Fabry-Perot cavity (20 SWG pads with $\Lambda = 100$ nm) and a 5 layers DBR (with a pitch $\Lambda_{\text{DBR}} = 420$ nm) is presented on figure VII.8. The experimental spectrum is quite unusual, and we make several hypothesis to explain its shape.

We observe two unusual features on the experimental spectrum: a clear cut-off effect below the $\lambda = 1550$ nm wavelength, and a pronounced deterioration of the interference fringes (in their width and height) beyond this wavelength.

We believe that the cut-off effect is a consequence of the absence of transition taper in our design. The effective guided indexes inside and outside the cavity are different, and

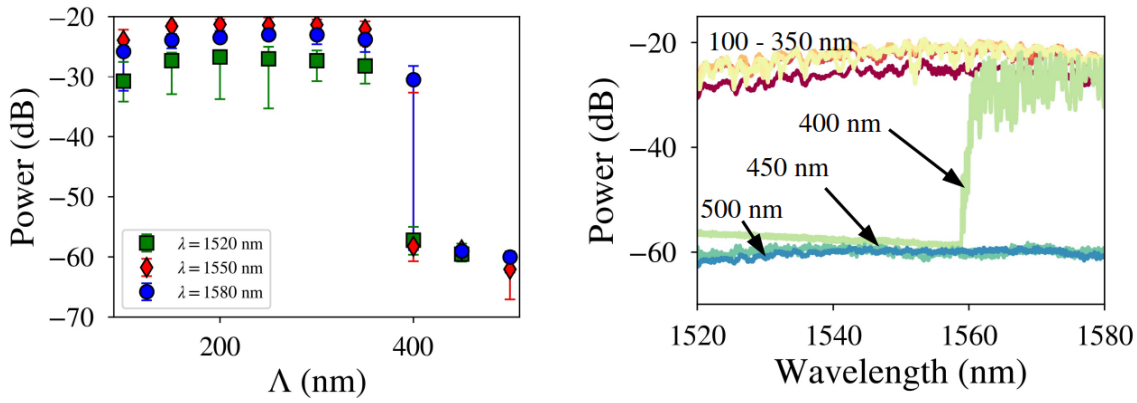

Figure VII.7 – Investigation of the cut-off pitch of SWG "ladder-like" waveguides. **Left:** Transmission against pitch, at $\lambda = 1520$, 1550 and 1580 nm. The dot indicates the median, the errorbar indicates the whole range of data, over 25 dies. **Right:** Typical transmission spectrum of one die, for pitches between 100 and 500 nm.

the two DBR are not working in the same regime for the SWG waveguide (*i.e.* inside the cavity) and the strip waveguide (*i.e.* outside the cavity). As a result, the input wave is submitted to the same cut-off effect that we evidenced in the previous section (plotted as a gray line on the experimental spectrum), and all optical wavelengths below this mark are filtered out, resulting in zero transmission.

Regarding the interference fringes, we observe a first narrow peak at $\lambda = 1550$ nm (Q-factor around 10 000), followed by a series of peak of increasing width and decreasing height. This kind of behavior is similar to what is observed in a Coupled-Resonators Optical Waveguides (CROW) configuration, *i.e.* when multiple ring resonators or Fabry-Perot cavities are coupled [205].

Qualitatively speaking, the hypothesis of coupled Fabry-Perot cavity is plausible if we consider the fact that as the wavelength is increased, the DBR reflectivity is decreased. Consequently, the wave propagates further in the layers and experiences additional reflections, hence mimicking a CROW behavior. Yet, we remain cautious with such affirmation, as we did not have time to conduct a proper study of this conjecture.

Note that we also observe small power oscillations all along the spectrum (more visible at the top and bottom parts of the interference fringes - for example at 1560 nm). These oscillations are the signature of a parasitic Fabry-Perot cavity formed between the input and output grating couplers, that is identified by means of the interfringe and cavity length, based on $\text{FSR} = \lambda^2/n_g L$.

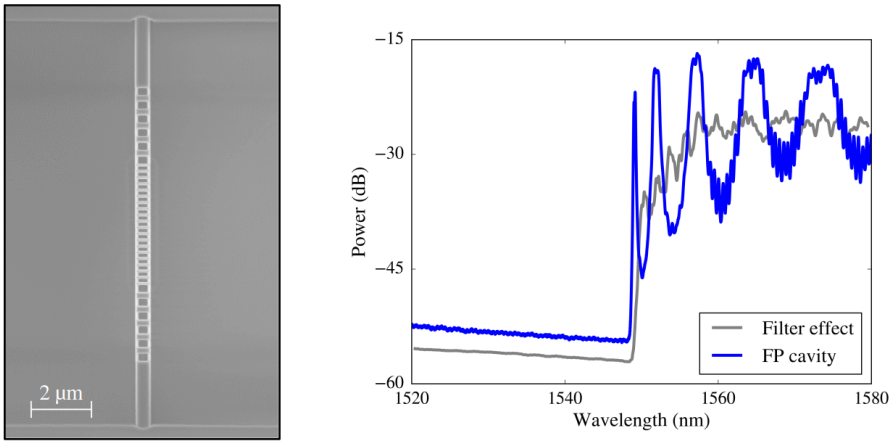

Figure VII.8 – Suspended Fabry-Perot cavity constituted of a SWG "ladder-like" waveguide placed between two DBR mirrors. **Left:** SEM image **Right:** Experimental spectrum, between 1520 and 1580 nm.

VII.3.2 Optomechanic experiments

We now consider optomechanics experiments, on a directional coupler formed with two SWG "ladder-like" waveguides, such as the ones presented on figure VI.17 (left figure).

The test bench is the one that was previously described. The experimental parameters are the following: the directional coupler is 20 μm long, with a 100 nm gap between the two SWG "ladder-like" waveguides, of pitch $\Lambda = 100$ nm. The measurement is conducted under vacuum, with a pressure in the 10^{-5} mbar range. The wavelength is set constant at $\lambda = 1550$ nm [1], and the laser optical power is varied between 1 and 25 mW. The mechanical spectrum is presented on figure VII.9. A comparison of the mechanical quality factor, maximal amplitude and mechanical frequency against optical power is presented on figure VII.10.

We observe a double resonance peak at $\Omega_m = 3.92$ MHz and $\Omega_m = 3.98$ MHz. This double resonance peak can be attributed to little fabrication inhomogeneities between the two arms and to the coupling by means of the optical spring k_c (see section VI.3.3), that lift the degeneracy of the (theoretically identical) mechanical frequencies. For comparison, we expect a mechanical frequency $\Omega_m = 4.19$ MHz with the analytical model of section VI.3.2, and $\Omega_m = 3.69$ MHz with numerical FEM simulations.

When the optical power is increased, we observe a quadratic diminution of the quality factor, a linear augmentation of the maximal amplitude, and a linear augmentation of the mechanical frequency (figure VII.10). In other words, the mechanical damping and mechanical frequency are modified with optical power, which can be compared to an optomechanical damping effect and an optical spring effect, respectfully. This is not however "true" optomechanical damping or optical spring, which are defined in the context

[1] Contrary to SRR, the wavelength position is not critical, as there is no interference peak to target.

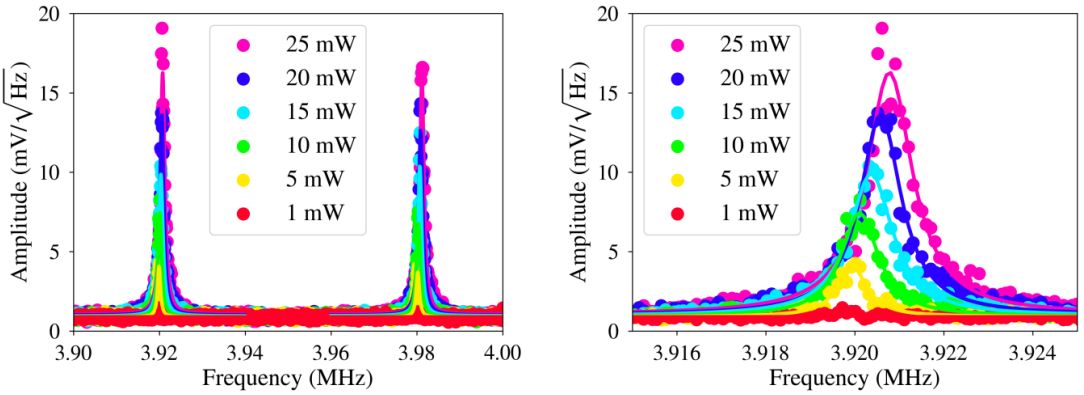

Figure VII.9 – Optomechanical transduction of the thermomechanical noise of the first mechanical doublet and zoom on the first peak. Dots: experimental data. Lines: analytical fit.

of cavity optomechanics. In contrast, there is no optical cavity here.

From the two springs model presented on section VI.3.3 and formula (VI.18), we calculate the spring constant associated to the optical gradient force:

$$k_c = 0.059 \text{ N/m} \tag{VII.2}$$

Note that in our experimental results, k_c is constant with regard to the optical power. This is not consistent with the simple hypothesis $F_{\text{grad}} = k_c \times x_{\text{opt}}$, as F_{grad} is a linear function of the optical power. We believe it is a consequence of the variations of mechanical damping with optical power, which is not taken into account in our simplified model [206, 201].

Based on the analytical approach of section VI.3.3, we calculate the value of the optical gradient force, for a 20 μm long coupling zone with a 100 nm gap:

$$F_{\text{grad}} = 0.068 \text{ pN/mW} \tag{VII.3}$$

Based on equations (VII.2) and (VII.3), and on $F_{\text{grad}} = k_c \times x_{\text{opt}}$, we estimate the value of the displacement x_{opt} induced by the optical gradient force, at increasing laser powers.

Laser power (mW)	1	5	10	15	20	25
x_{opt} (nm)	0.19	0.95	1.91	2.86	3.82	4.77
$\langle x_{\text{th}} \rangle$ (fm)	27.2	18.2	16.1	14.9	16.8	15.6

Table VII.2 – Comparison of the displacements induced by the optical gradient force, x_{opt}, and by the thermomechanical noise, x_{th}.

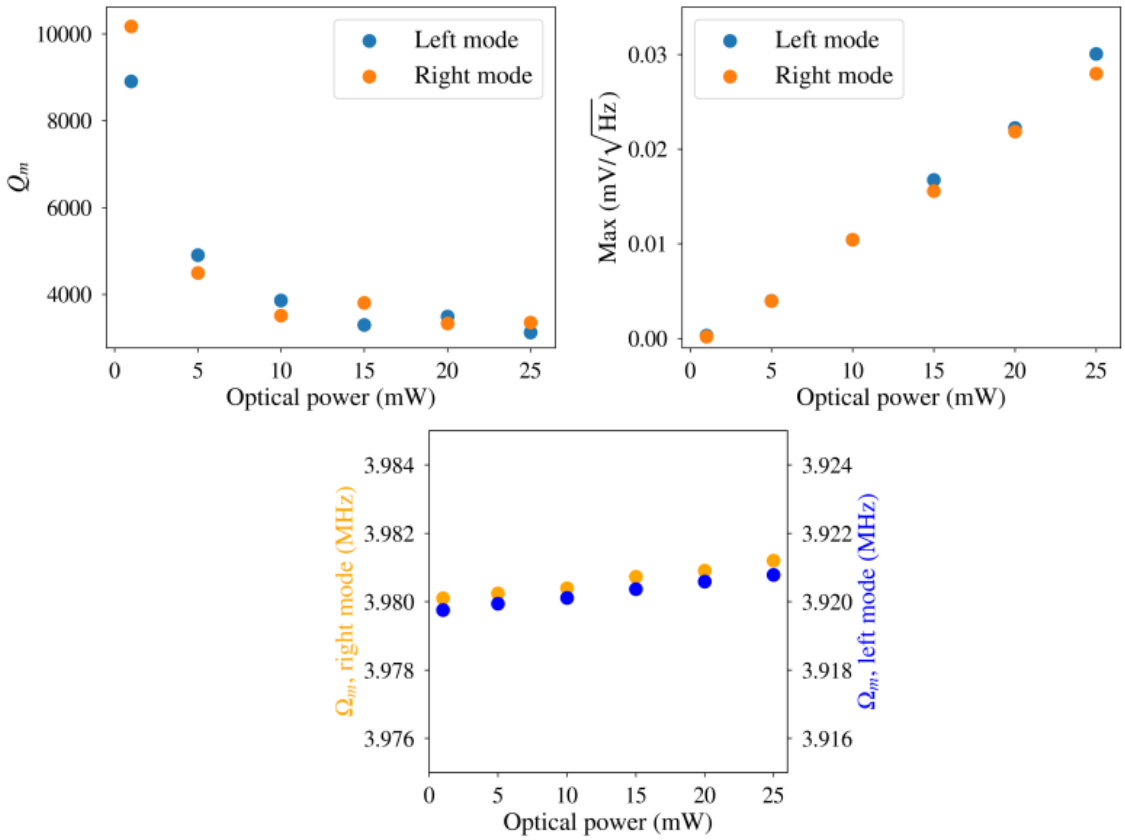

Figure VII.10 – Mechanical quality factor, maximal amplitude, and mechanical frequency, as a function of the optical power, for each mechanical mode.

Additionally to the optical gradient force, we must consider the fluctuations induced by thermomechanical noise. Based on the discussion of section V.3.2, the root mean square (RMS) of the amplitude of thermomechanical fluctuations is given by:

$$\langle x_{\text{th}} \rangle^2 = \int_{\text{BW}} S_{th}^r(\omega)\ \mathrm{d}\omega = \text{BW} \times \frac{4k_B T Q_m}{m_{\text{eff}} \Omega_m^3} \tag{VII.4}$$

where BW is the experimental bandwidth, set by the lock-in amplifier, equal to 100 Hz in this case. Q_m and Ω_m are extracted from experimental results, while $m_{\text{eff}} = 1.5 \times 10^{-15}$ kg is obtained with the analytical model of section VI.3.2.

The values of the displacements induced by the optical gradient force, x_{opt}, and by the thermomechanical noise, x_{th}, are compared on table VII.2, at increasing laser powers.

We calculate the RMS amplitude of thermomechanical noise fluctuations $\langle x_{\text{th}} \rangle$ to be around 15 fm, with the exception of the value at a 1 mW laser power that is 27 fm. From observation of formula (VII.4) and figure VII.10, we explain this slightly more elevated value by the increased mechanical quality factor at this laser power, or in other words, by the reduced mechanical losses. As already stated, the dependence of mechanical losses with the laser power is not qualitatively nor quantitatively understood yet. In

future work, it could be included in the two springs model following the approaches of [206, 201].

The displacement x_{opt} induced by the optical gradient force increases linearly with the input laser power. Even at low laser power, it is two orders of magnitude higher than $\langle x_{\text{th}} \rangle$. Although the above calculation is simplified and a more rigorous analysis needs to be conducted, this difference in magnitude suggests that the measured motion is driven by optical forces.

Conclusion

In this chapter, we have discussed the technological realization and experimental characterization of suspended SWG interdigitated combs waveguides and SWG "ladder-like" waveguides.

Regarding technological realization, we have focused the discussion around the patterning of the waveguide level. Due to small dimensions down to 50 nm, the process flow had to be adapted and the lithographic step was realized with an e-beam lithography equipment instead of our standard DUV photolithography equipment. While we achieved the realization of our SWG waveguides, the process flow can still be optimized to reduce propagation losses, which remain quite elevated at the end of the thesis.

We experimentally verified the guided behavior of SWG interdigitated combs waveguides, identified a cut-off pitch in well agreement with our theoretical predictions, and demonstrated the efficiency of the asymmetric taper at the transition between SWG and strip waveguides. We also demonstrated the realization of optical cavities based on SWG interdigitated combs waveguides, either by integrating the SWG waveguide within a racetrack resonator, or by realizing a ring-shaped SWG interdigitated combs waveguides. On both designs (taper, racetrack resonator and ring-shaped resonator), we evidenced the detrimental impact of propagation losses, and expect to improve general performances with the optimization of future fabrication runs. A second major objective will also be to realize optomechanical experiments on these geometries, that could not be conducted during the thesis.

On SWG "ladder-like" waveguides, we also identified the cut-off pitch, here again in well agreement with our modeling. We next characterized a Fabry-Perot cavity constituted of suspended SWG "ladder-like" waveguides and DBR. The experimental spectrum presents a shape similar to the one of multiple coupled optical resonator, but it lacks a proper theoretical model to validate this theory. The addition of a SWG taper, that is not included in the current design, is a perspective for future work, that should improve our theoretical understanding of the optical cavity. In parallel, we conducted optomechanic experiments on SWG "ladder-like" directional couplers. We realized optomechanical transduction of the mechanical motion and observed a doublet splitting due to fabrication inhomogeneities and the optical spring between the two arms, induced by optical gradient forces. We also observed a dependence of the damping rate and mechanical resonant frequency, in a way

somewhat similar to optomechanical damping and the optical spring effect. Finally, our calculations suggest that the mechanical motion driven by optical forces is two orders of magnitude superior than the thermomechanical motion of the system, revealing an all optical actuation and detection of mechanical motion.

Conclusion & perspectives

The aim of this doctoral work was to study theoretically and experimentally the optomechanical interactions arising in suspended silicon photonic structures. Beyond the scientific interest of this work, one of the underlying motivation of this thesis, in the context of the CEA-Leti, was to pave the way towards the realization of on-chip optomechanical inertial sensors as an alternative to electrical-based devices.

In the first part of the manuscript, we have presented a theoretical approach to on-chip silicon optomechanics, *i.e.* to cavity optomechanics applied to suspended silicon photonics structures. We have introduced the notion of dissipative and dispersive optomechanical coupling, and have discussed the nature of optical forces in photonic waveguides.

Based on this theoretical description, we have studied two optomechanical setups: suspended ring resonators, and SWG-based optomechanical waveguides.

Suspended ring resonators offer a large number of design parameters that can be used to engineer a broad variety of mechanical mode shapes and resonant frequencies. We identified the geometric contribution (*i.e.* the variations of the cavity length) to be the main optomechanical interaction in suspended ring resonators, above the photoelastic and dissipative contributions.

We studied two kinds of SWG-based optomechanical waveguides: SWG interdigitated combs waveguides, and SWG "ladder-like" waveguides. In SWG interdigitated combs waveguides, light is guided along the overlap of two interdigitated comb structures, whose pitch is small in regard to the optical wavelength. This structure is an appealing perspective for the realization of on-chip optomechanical accelerometers, as the operation principle of electrical combs is directly replicated. In SWG "ladder-like" waveguides, a SWG waveguide is suspended by means of two thin lateral beams. We realized two configurations: a Fabry-Perot cavity where a SWG "ladder-like" waveguide is placed between two DBR, and a directional coupler in which two SWG "ladder-like" waveguides are brought at close proximity of each other.

All along the thesis, the work has been balanced between theoretical, technological, and experimental developments.

On the theoretical part, we improved our understanding of suspended ring resonators by studying the influence of the suspension arms on optical losses, by introducing a simple analytical model for the modeling of mechanical modes, and by developing simulation codes allowing to estimate the optomechanical coupling rates for a given geometry. In addition, we also considered the possibility of an optomechanical coupling arising from a Sagnac effect. In parallel, we entirely designed two new kind of SWG waveguides, based on theoretical and numerical modeling. We pointed out the existence of an additional optomechanical interaction in presence of SWG waveguides, which although relatively weak, could give rise to significant optical gradient forces between photonic structures.

On the technological part, we adapted our standard photonic process flow to the specificities of SWG waveguides and optomechanical devices. In particular, the patterning of the waveguide level and the release step have been critical and required multiple trials and efforts. At the end of the thesis, while the process flow can still be improved (es-

pecially regarding propagation losses), we established a functional process flow for SWG waveguides and optomechanical devices, on an (almost) industrial fabrication line.

Finally, regarding the experimental part, we successfully verified most of our optical predictions, and a dedicated test bench for optomechanical measurement, under vacuum, have been developed. This test bench is an adapted version of our automatized optical probers: inside a vacuum chamber, two optical fibers are aligned above the grating couplers of the sample under test. The whole test bench is fibered, such that a large variety of measurement schemes can be realized. In the simplest configuration (measurement of the thermomechanical noise), a laser signal is sent through the sample and is measured by a photodetector and a lock-in-amplifier.

While we are satisfied by the theoretical and technological developments, and by the optical measurements, our experimental results are mitigated on the optomechanical part. Generally speaking, we are still at an early process stage, with a limited number of successful measurements, that sometimes lack of consistency in regard to the theory. We foresee several leads to improve optomechanical experimental results in the future.

First, we evidenced a few design misconceptions that will be corrected. Mostly, the bus waveguide of suspended ring resonators was released over a too long distance, which often resulted in the collapsing of the bus waveguide and inhibited optical coupling because of horizontal misalignment. Additionally, the absence of a transition taper between SWG "ladder-like" and strip waveguides unnecessarily complicates the optical behavior, and is retrospectively a mistake.

In parallel to these design misconceptions, we also identified the limitations of our fabrication process. The most important point is that a lot of our SWG designs were realized with an ambitious pitch of 100 nm (hence with the goal of achieving lines of 50 nm spaced by 50 nm). Based on experimental results, this pitch is at the lower edge of our fabrication capacities, while we can actually use pitches up to 180 nm and still remain in the SWG regimen. In future work, the use of a less challenging pitch should allow to relax the constraints on critical dimensions and achieve an overall better quality for our devices. As already mentioned, this will also be conducted by working on the optimization of the process flow.

An important experimental limitation is set by the photodetector and lock-in-amplifier bandwidths. Even in the best case scenario, our lock-in-amplifier is limited to a 50 MHz frequency, and higher mechanical modes can not be addressed with the simplistic setup that we used until now (not to mention that the noise performances of our photodetector are degraded with increasing frequencies). This can be solved by using an alternative (and more complex) setup, presented on figure VII.11. Without going into the specifics (see the figure caption for more details), this scheme allows to scale the mechanical frequency down to an arbitrary lower frequency. This way, it is possible to assess mechanical modes that are beyond the bandwidth of the lock-in-amplifier (that is limited to 50 MHz) and to benefit from better photodetector performances.

At the end of the thesis, I personally think that silicon is a good platform for the realization

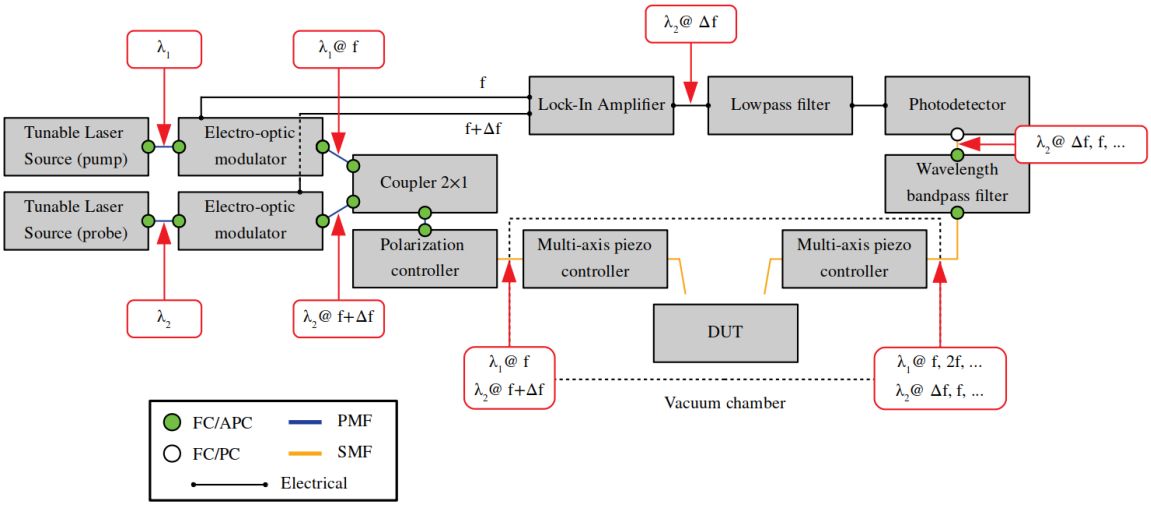

Figure VII.11 – Experimental setup for optomechanical downmixing. A high intensity laser (pump) at wavelength λ_1 is modulated at f (the targeted mechanical resonant frequency), and a low intensity laser (probe) at wavelength λ_2 is modulated at $f+\Delta f$. The pump excites the optomechanical oscillator at f by means of optical forces. The probe is weak enough to induce negligible excitation. When the probe signal passes through the excited optomechanical device, an harmonic at Δf is created, as a result of the mixing between the probe frequency and the optomechanical frequency. This way, the optomechanical signal is downmixed at the arbitrary chosen low frequency Δf. A lowpass filter is used to eliminate all frequencies above Δf, and a wavelength bandpass filter is used to eliminate the pump signal and reduce noise. High order harmonics are not represented. The lock-in amplifier is used to monitor the oscillation frequency of the two electro-optic modulators.

of suspended ring resonators, but is not necessarily the best one. The main reason is the important non-linear effects that we observed at (not so) high optical power, making it difficult to properly track the position and shape of resonance peaks. In the context of cavity optomechanics, where one wants to properly control the detuning between the input laser and the resonant frequencies, this is a major drawback. In this regard, a material such as silicon nitride, which exhibits virtually no TPA, seems to be a better alternative. Alternatively (and/or additionally), the Pound-Drever-Hall (PDH) technique [207] could be implemented, as an experimental method to stabilize the laser frequency on the resonant frequency of the cavity and to follow its variations. Regarding suspended ring resonators in general, they offer a large number of mechanical degrees of freedom and are easily integrated within photonic circuits, and I think that they are an interesting setup for cavity optomechanics.

With regard to SWG waveguides and structures, I believe that they constitute a really promising candidate for cavity optomechanics applications (and even more generally, for photonic applications). Even if their fabrication remains difficult, we evidenced strong

gradient optical forces, that can be simply engineered by controlling the filling factor. In my opinion, this is an interesting perspective for on-chip signal processing based on optomechanical devices and NOMS in general.

Cavity optomechanics is a really diversified field and is experiencing fast growth. Until now, the majority of research efforts have been motivated by fundamental considerations, such as the measurement of the quantum ground state of a macroscopic oscillator. Today, there is a growing interest for more "applied" developments with the perspective of on-chip optomechanical devices integrated alongside photonic and electric components. In this regard, this doctoral work is a first step towards such developments at CEA-Leti.

Appendixes

APPENDIX A

A note on numerical simulations

On this appendix, we give the general guidelines that we followed to conduct numerical simulations.

For optical simulations, we used finite difference time domain (FDTD) simulations and finite element method (FEM) simulations based on the commercial solver RSoft [208]. For mechanical simulations, we used FEM simulations based on the commercial solver COMSOL [146].

Optical FDTD simulations

Optical FDTD simulations are used to perform a full-vector simulation of light propagation within photonic structures. 2D or 3D simulations can be conducted. When a 2D simulation is conducted, the effective index method (EIM) is used to reduce a 3D problem to a 2D problem [209], and the polarization (TE or TM) has to be chosen accordingly to the problem.

Typically, we used a uniform rectangular 10 nm $\times$ 10 nm $\times$ 10 nm mesh, chosen such that no cell falls at the junction between two different medium (in other words, every mesh cell is homogeneous in terms of physical properties). The dielectric dispersion, nonlinear, thermal and anisotropic effects can be considered when necessary. The boundary conditions are set to perfectly matched layers (PML), *i.e.* artificial absorbing layers designed to eliminate the reflection of incident waves [210]. For a given mesh size, the time step is automatically chosen to respect the Courant-Friedrichs-Lewy condition [211]. The stop time is chosen to insure that steady-state was reached. The launch field is calculated from the associated FEM mode solver, described below. The excitation type can be either continuous or pulsed.

Optical FEM simulations

Optical FEM simulations are used as a full-vector mode solver, to calculate the complex effective guided indexes and field profiles of a given waveguide. Leaky and cavity modes can also be found.

The waveguide is assumed to be invariant along te direction of propagation, such that it is a 2D calculation. The mesh is hybrid triangular and rectangular one, with typically a 25 nm^2 footprint. First and second order elements are used, with PML boundaries. Bending modes can be computed either via a direct formulation, of via conformal transformation [212].

Mechanical FEM simulations

Mechanical FEM simulations are used as a mode solver, to calculate the resonant frequency and deformation of a mechanical structure. The commercial software COMSOL is used, with the structural mechanics module.

APPENDIX B

Selected mechanical modes of suspended ring resonators

On the following, we present a sample of the broad range of mechanical shapes and eigenfrequencies that can be engineered with suspended ring resonators.

The design parameters are selected among fabricated geometries.

The mechanical shapes are obtained by FEM numerical simulations, presented on appendix A.

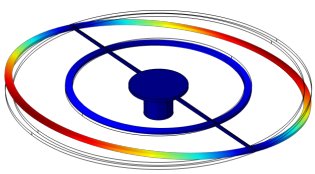

(a) $\Omega_0 = 0.14437$ MHz

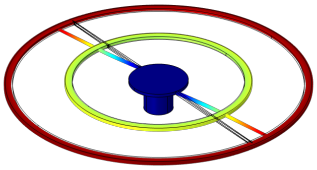

(b) $\Omega_1 = 0.15752$ MHz

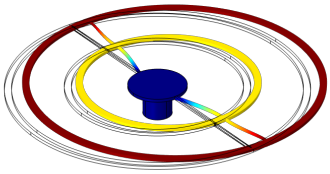

(c) $\Omega_2 = 0.6067$ MHz

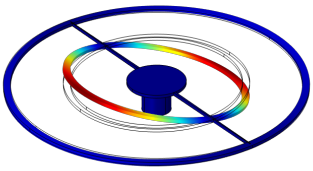

(d) $\Omega_3 = 0.77166$ MHz

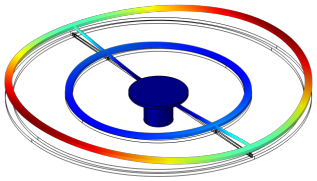

(e) $\Omega_4 = 1.1071$ MHz

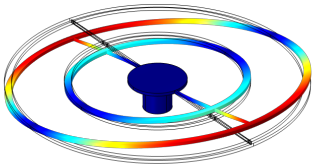

(f) $\Omega_5 = 1.1535$ MHz

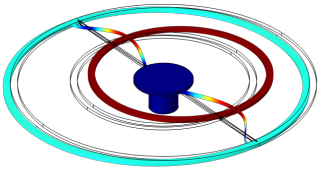

(g) $\Omega_6 = 1.935$ MHz

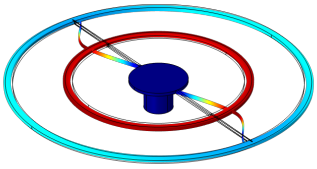

(h) $\Omega_7 = 2.073$ MHz

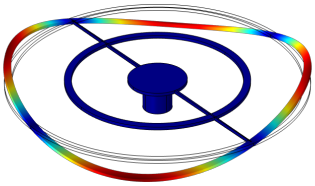

(i) $\Omega_8 = 2.3678$ MHz

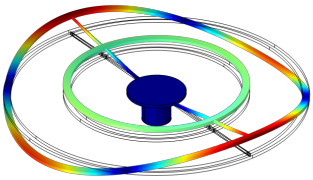

(j) $\Omega_9 = 2.581$ MHz

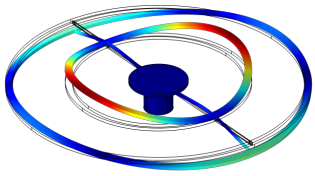

(k) $\Omega_{10} = 3.5938$ MHz

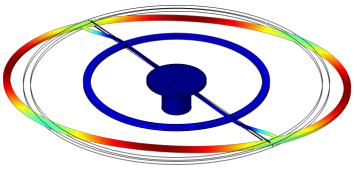

(l) $\Omega_{11} = 5.152$ MHz

Figure B.1 – First mechanical modes of a Silicon suspended ring resonator, with $R = 10\mu$m, $R_{\text{Ped}} = 2\mu$m, $\text{N}_{\text{arms}} = 2$, $\text{W}_{\text{arms}} = 0.15\mu$m, and $\text{N}_{\text{rings}} = 2$.

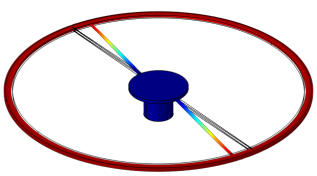

(a) $\Omega_0 = 0.029559$ MHz

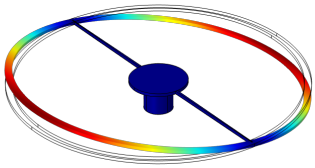

(b) $\Omega_1 = 0.14196$ MHz

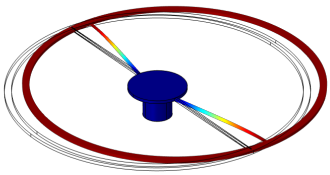

(c) $\Omega_2 = 0.14779$ MHz

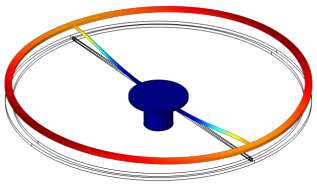

(d) $\Omega_3 = 0.84809$ MHz

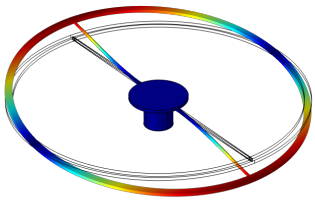

(e) $\Omega_4 = 0.90075$ MHz

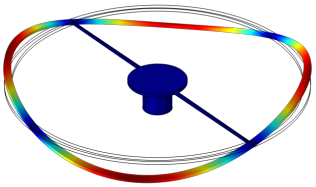

(f) $\Omega_5 = 2.363$ MHz

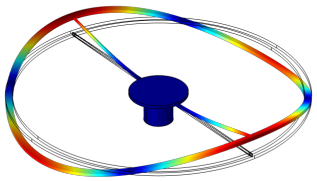

(g) $\Omega_6 = 2.468$ MHz

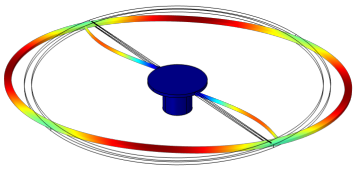

(h) $\Omega_7 = 5.0149$ MHz

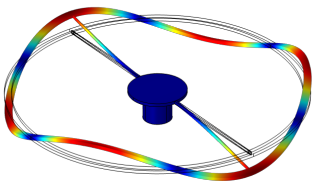

(i) $\Omega_8 = 6.5807$ MHz

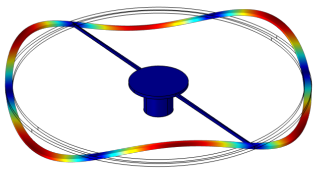

(j) $\Omega_9 = 6.6034$ MHz

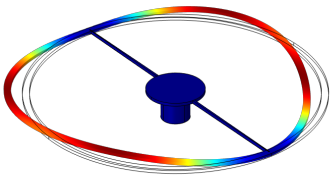

(k) $\Omega_{10} = 8.0913$ MHz

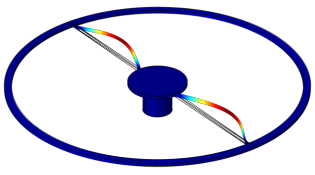

(l) $\Omega_{11} = 8.2277$ MHz

Figure B.2 – First mechanical modes of a Silicon suspended ring resonator, with $R = 10\mu$m, $R_{\text{Ped}} = 2\mu$m, $\text{N}_{\text{arms}} = 2$, $\text{W}_{\text{arms}} = 0.15\mu$m, and $\text{N}_{\text{rings}} = 1$.

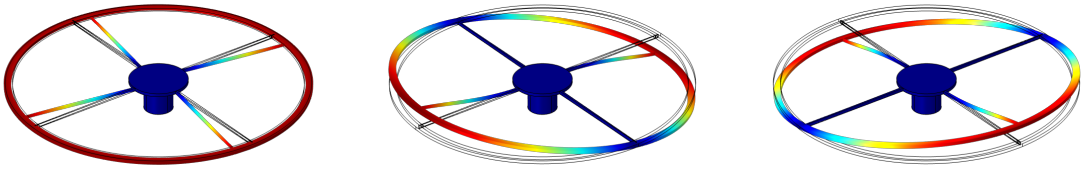

(a) $\Omega_0 = 0.0416$ MHz (b) $\Omega_1 = 0.91236$ MHz (c) $\Omega_2 = 0.91254$ MHz

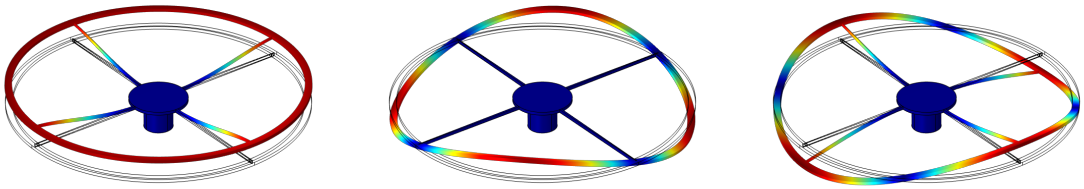

(d) $\Omega_3 = 1.1948$ MHz (e) $\Omega_4 = 2.3792$ MHz (f) $\Omega_5 = 2.5642$ MHz

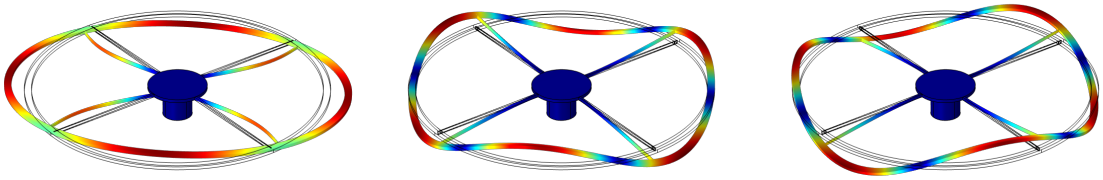

(g) $\Omega_6 = 4.9797$ MHz (h) $\Omega_7 = 6.5927$ MHz (i) $\Omega_8 = 6.5928$ MHz

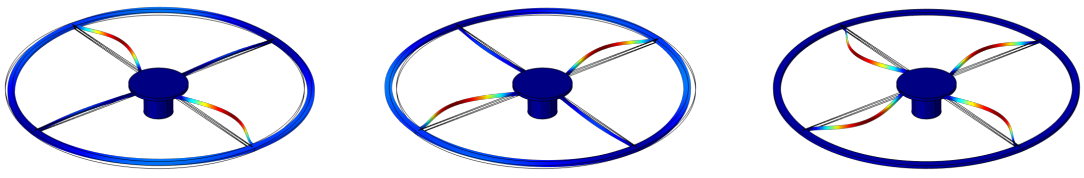

(j) $\Omega_9 = 7.5686$ MHz (k) $\Omega_{10} = 7.5687$ MHz (l) $\Omega_{11} = 8.262$ MHz

Figure B.3 – First mechanical modes of a Silicon suspended ring resonator, with $R = 10\mu$m, $R_{\text{Ped}} = 2\mu$m, $\text{N}_{\text{arms}} = 4$, $\text{W}_{\text{arms}} = 0.15\mu$m, and $\text{N}_{\text{rings}} = 1$.

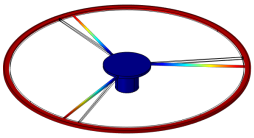

(a) $\Omega_0 = 0.035$ MHz

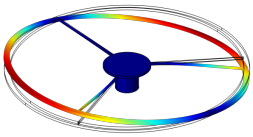

(b) $\Omega_1 = 0.779$ MHz

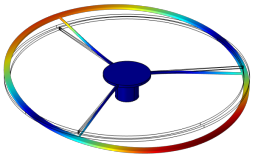

(c) $\Omega_2 = 0.780$ MHz

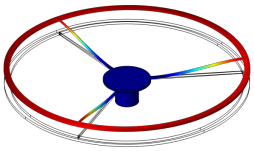

(d) $\Omega_3 = 1.065$ MHz

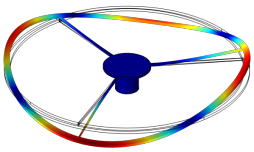

(e) $\Omega_4 = 2.465$ MHz

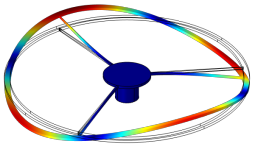

(f) $\Omega_5 = 2.466$ MHz

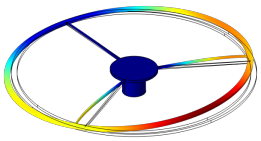

(g) $\Omega_6 = 3.058$ MHz

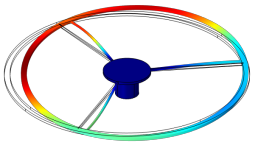

(h) $\Omega_7 = 3.058$ MHz

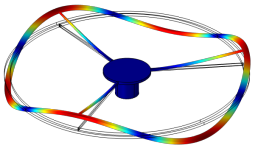

(i) $\Omega_8 = 6.569$ MHz

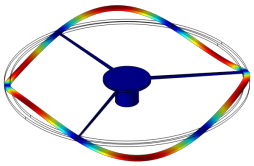

(j) $\Omega_9 = 6.626$ MHz

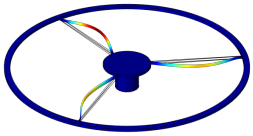

(k) $\Omega_{10} = 8.113$ MHz

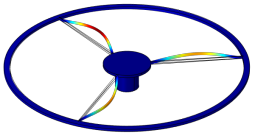

(l) $\Omega_{11} = 8.156$ MHz

Figure B.4 – First mechanical modes of a Silicon suspended ring resonator, with $R = 10\mu$m, $R_{\text{Ped}} = 2\mu$m, $\text{N}_{\text{arms}} = 3$, $\text{W}_{\text{arms}} = 0.15\mu$m, and $\text{N}_{\text{rings}} = 1$.

APPENDIX C

Description of the mask layout

The entire mask layout is displayed on figure C.1. The cell is 2.2 cm × 2.2 cm large, with 4 levels: the grating coupler level (in pink), the photonic level (in violet), the release level (in blue), and the metal level (hatched).

In a nutshell, the grating coupler level is used during the partial etching of the grating coupler, the photonic level is used during the patterning of the photonic and optomechanic devices, the release level is used during the release of optomechanical structures, and the metal level is used on some particular devices that we did not describe.

The mask is divided between several subcells (see figure C.1):

1. SWG interdigitated combs straight waveguides.
2. SWG interdigitated combs waveguides within all-pass racetrack resonators.
3. SWG interdigitated combs waveguides within Mach-Zehnder interferometers.
4. Classical ring resonators.
5. SWG interdigitated combs waveguides within add-drop racetrack resonators.
6. SWG interdigitated combs waveguides within all-pass racetrack resonators, with electrical drive.
7. Spiral-shaped SWG interdigitated combs waveguides.
8. SWG "ladder-like" waveguides.
9. Suspended ring resonators.
10. Test cell for the asymmetric taper between strip and SWG interdigitated combs waveguides.

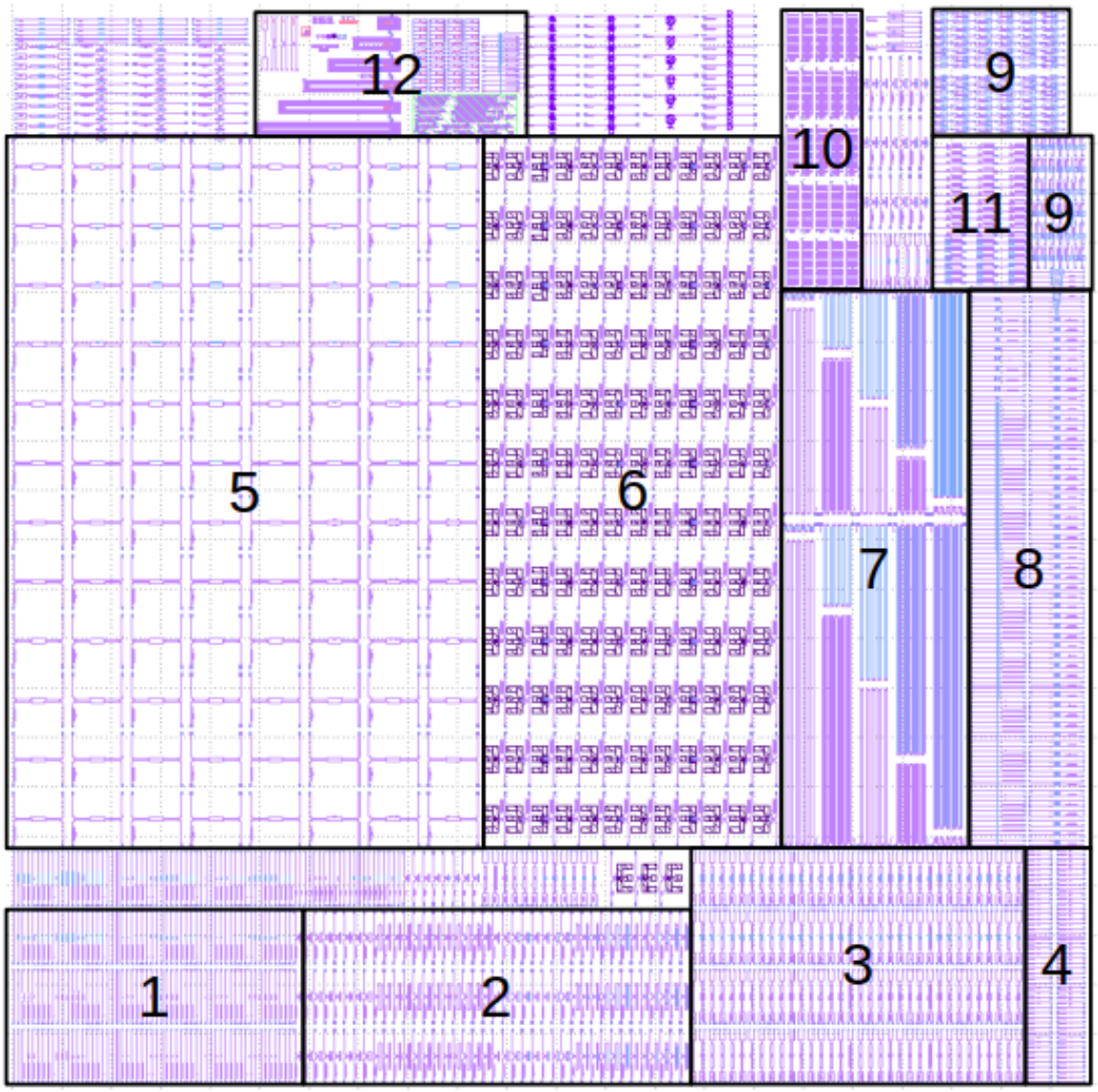

Figure C.1 – View of the entire mask layout. The cell size is 2.2 cm × 2.2 cm.

11. Ring-shaped SWG interdigitated combs waveguides.
12. Test cell for photonic devices.

SWG interdigitated combs straight waveguides

This subcell is presented on figure C.2. It is divided between:

1. SWG interdigitated combs straight waveguides with an asymmetric SWG taper between the SWG and strip waveguides.
2. SWG interdigitated combs straight waveguides with an abrupt junction between the SWG and strip waveguides.
3. SWG interdigitated combs straight waveguides with a classical, adiabatic taper between the SWG and strip waveguides.

The goal of this subcell is to explore the influence of the SWG pitch, to compare released and non-released structures, and to compare structures with an asymmetric SWG taper, with an abrupt junction, and with a classical adiabatic taper between the SWG and strip waveguides.

This subcell is exploited for the measurements presented on sections VII.2.1 and VII.2.2.

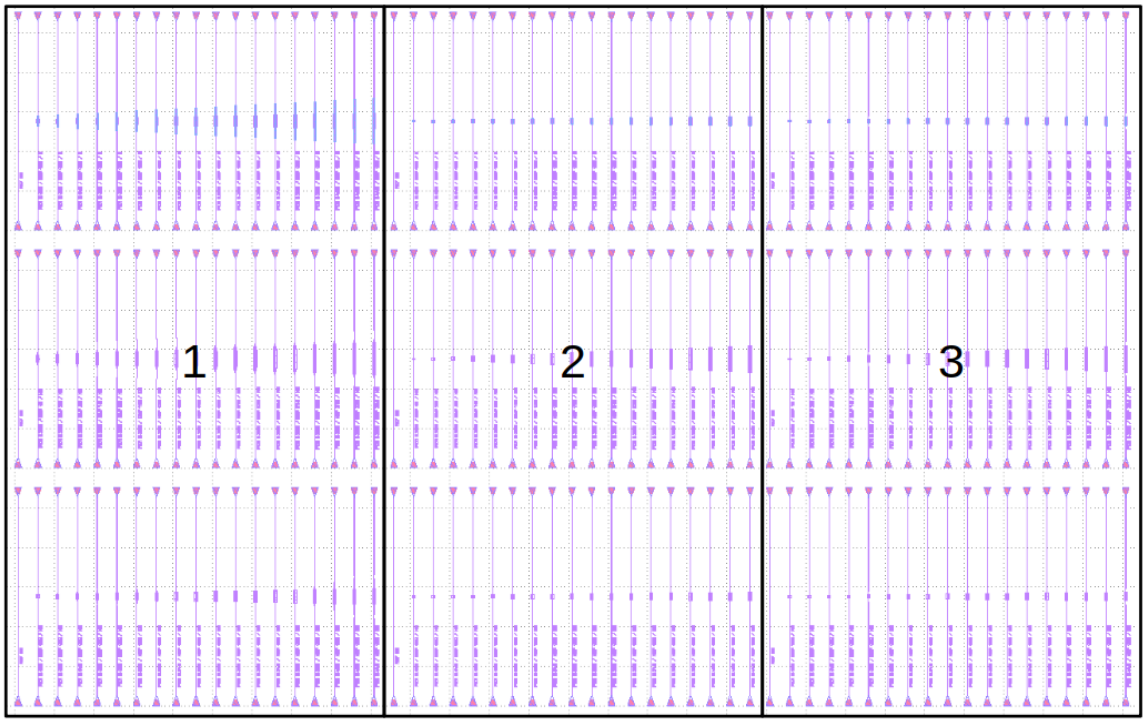

Figure C.2 – Subcell for SWG interdigitated combs straight waveguides.

SWG interdigitated combs waveguides within all-pass racetrack resonators

This subcell is presented on figure C.3. It is divided between:

1. SWG interdigitated combs waveguides within all-pass racetrack resonators.
2. Released SWG interdigitated combs waveguides within all-pass racetrack resonators.

The goal of this subcell is to demonstrate the integration of released and unreleased SWG interdigitated combs waveguides within all-pass (*i.e.* with a unique bus waveguide) racetrack resonators. Multiple waveguide lengths, gaps (between the bus waveguide and the racetrack resonator) and SWG pitches are explored.

This subcell is exploited for the measurements presented on section VII.2.3.

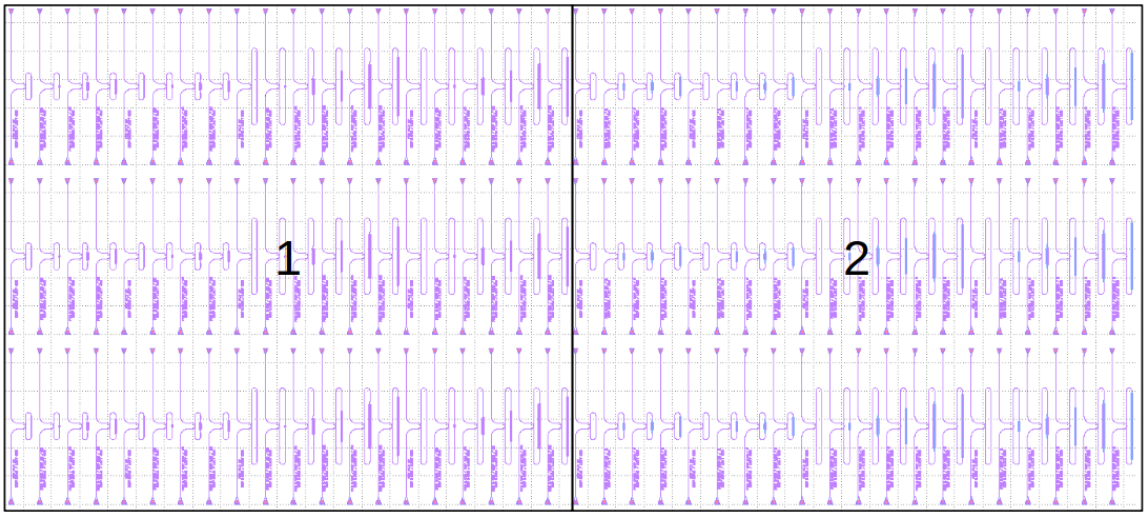

Figure C.3 – Subcell for SWG interdigitated combs within all-pass racetrack resonators.

SWG interdigitated combs waveguides within Mach-Zehnder interferometers

This subcell is presented on figure C.4. It is divided between:

1. SWG interdigitated combs waveguides within a Mach-Zehnder interferometer (MZI).
2. Released SWG interdigitated combs waveguides within a MZI.

More precisely, both arms of the MZI are constituted with SWG interdigitated combs waveguides. The left waveguide is kept constant, while the right waveguide presents a

variable overlap. Released and unreleased waveguides of various SWG pitches are explored.

The goal of this subcell was to measure the phase shift under mechanical motion. As the overlap is varied between each geometry, the effect of mechanical motion is statically reproduced. This way, the relation between the phase shift and the mechanical motion can be calibrated.

In practice, experimental results on these geometries were too noisy to be exploitable.

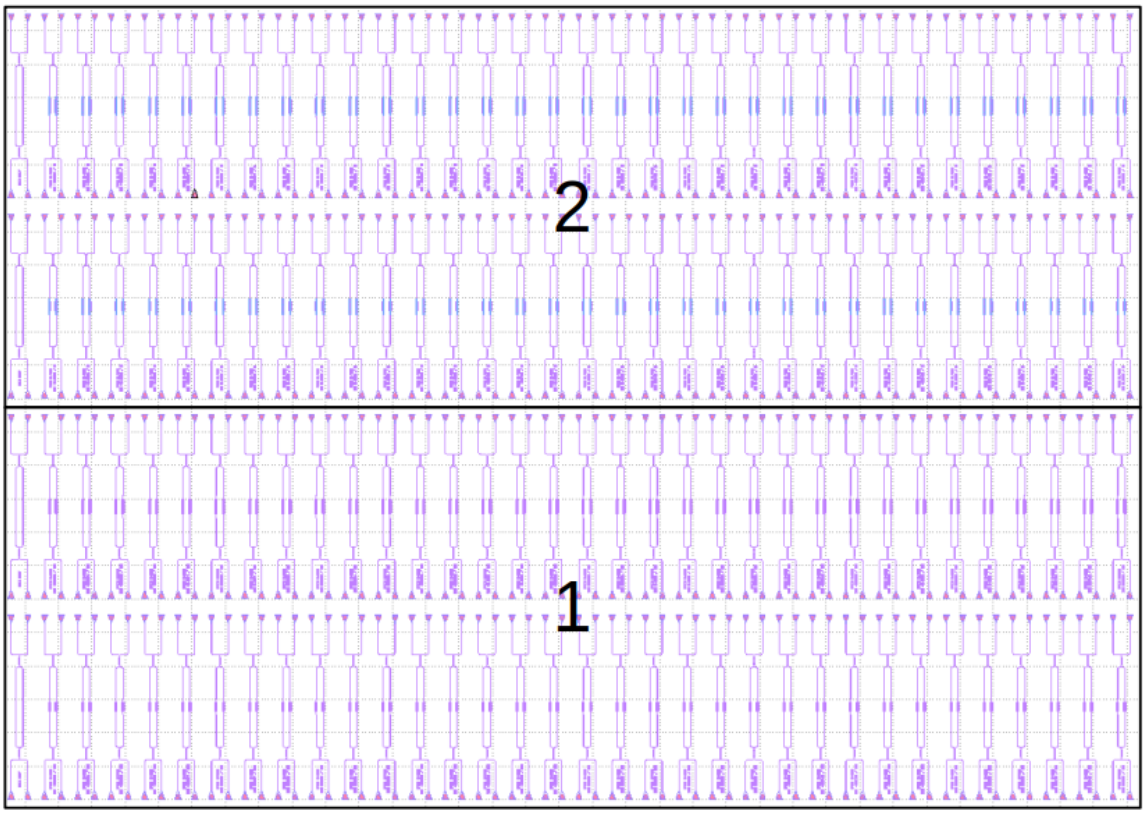

Figure C.4 – Subcell for SWG interdigitated combs waveguides within Mach-Zehnder interferometers.

Classical ring resonators

This subcell is presented on figure C.5. Multiple ring radii and gaps were explored. This subcell is exploited all along section V.2 when experimental results on classical ring resonators are presented.

Additionally, this subcell was a way to compare our different fabrication runs, based on the measured figures of merit of the ring resonators.

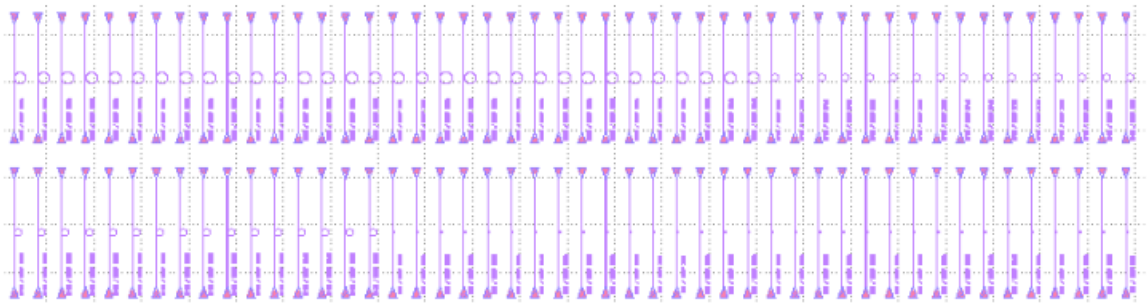

Figure C.5 – Subcell for classical ring resonators.

SWG interdigitated combs waveguides within add-drop racetrack resonators

This subcell is presented on figure C.6. It is divided between:

1. Released SWG interdigitated combs waveguides within add-drop racetrack resonators.
2. SWG interdigitated combs waveguides within add-drop racetrack resonators.

The goal of this subcell is to demonstrate the integration of released and unreleased SWG interdigitated combs waveguides within add-drop (*i.e.* with two bus waveguides) racetrack resonators. Multiple waveguide lengths, gaps (between the bus waveguides and the racetrack resonator) and SWG pitches are explored.

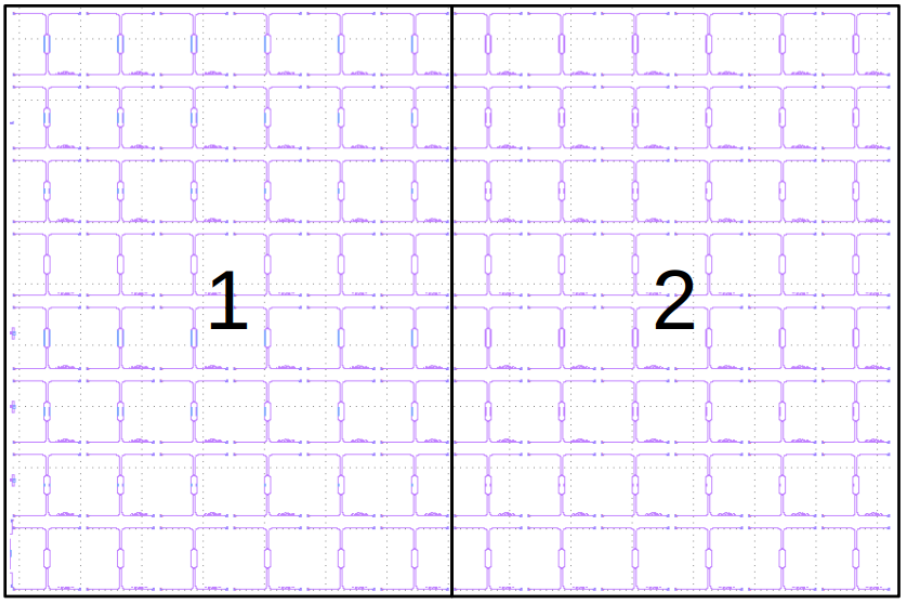

Figure C.6 – Subcell for SWG interdigitated combs waveguides within add-drop racetrack resonators.

SWG interdigitated combs waveguides within all-pass racetrack resonators, with electrical drive

This subcell is presented on figure C.7.

Figure C.7 – **Left:** Subcell for SWG interdigitated combs waveguides within all-pass racetrack resonators, with electrical drive. **Right:** Zoom on one structure

On this subcell, the SWG interdigitated comb structure is linked to a capacitive actuator with three metallic vias, and a holey suspended supporting structure. Released and unreleased SWG interdigitated combs waveguides are integrated within an all-pass racetrack resonator. Multiple waveguide lengths, gaps (between the bus waveguides and the racetrack resonator), SWG pitches and supporting structures are explored.

We did not have time to measure these structures, that were not present on the majority of our wafers, as we skipped the realization of the metal level (which includes lithographic, etching and doping steps) in order to accelerate the fabrication.

Spiral-shaped SWG interdigitated combs waveguides

This subcell is presented on figure C.8.

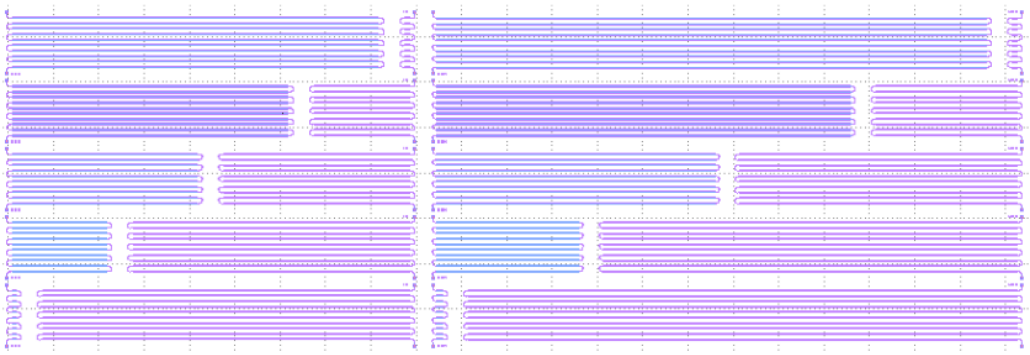

Figure C.8 – Subcell for Spiral-shaped SWG interdigitated combs waveguides.

The goal of this subcell is to measure propagation losses in released and encapsulated SWG interdigitated combs waveguides. Multiple SWG pitches are realized.

This subcell is exploited for the measurements presented on section VII.2.1.

SWG “ladder-like” waveguides

This subcell is presented on figure C.9. It is divided between:

1. SWG “ladder-like” waveguides integrated within directional couplers of multiple length and gap.
2. SWG “ladder-like” waveguides integrated within Fabry-Perot cavities of multiple length and number of DBR layers.
3. SWG “ladder-like” waveguides of variable pitch.
4. SWG “ladder-like” waveguides integrated within coupled Fabry-Perot cavities of multiple length, number of DBR layers and gap.

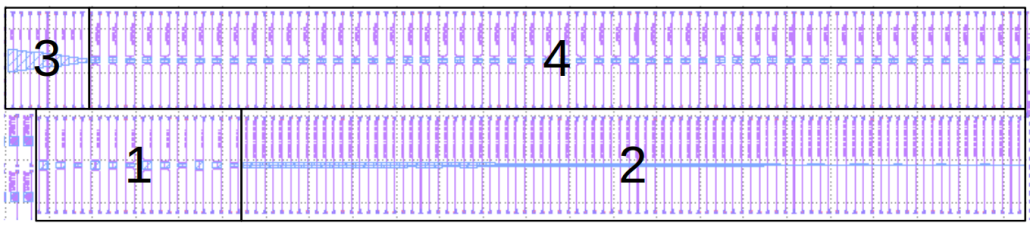

Figure C.9 – Subcell for SWG “ladder-like” waveguides.

This subcell is exploited for the measurements presented on section VII.3.

Suspended ring resonators

This subcell is presented on figure C.10. Multiple ring radii, gaps, number of arms and number of rings were explored. This subcell is exploited all along sections V.2 and V.3.

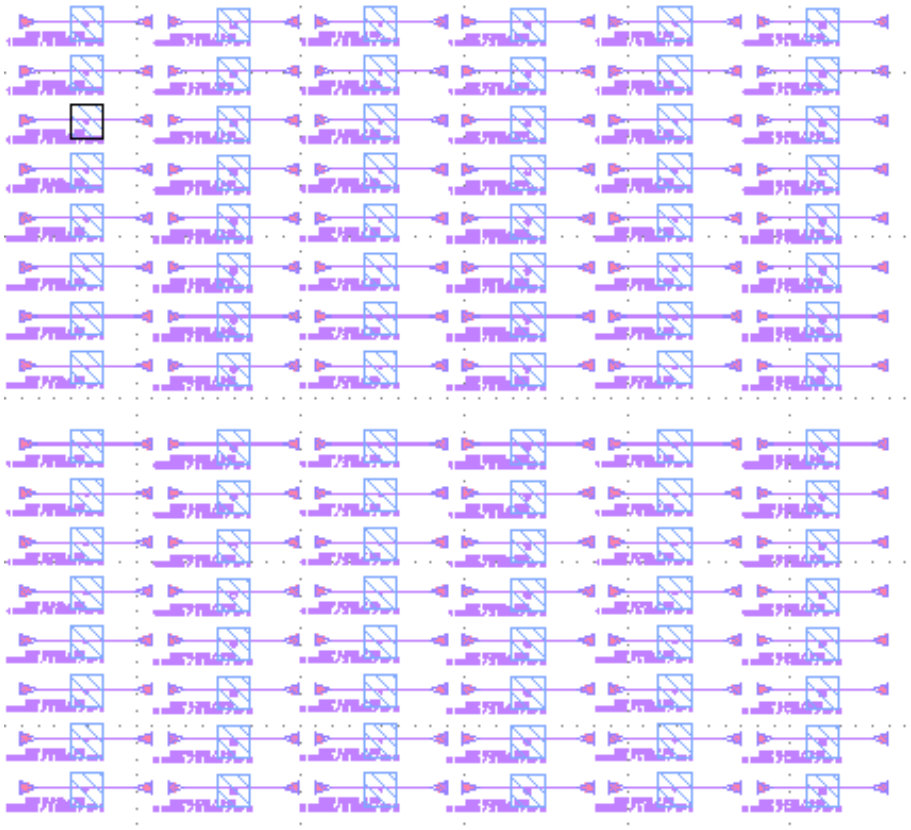

Figure C.10 – Subcell for suspended ring resonators.

Test cell for the asymmetric taper between strip and SWG interdigitated combs waveguides

This subcell is presented on figure C.11. Multiple SWG asymmetric tapers of variable length are cascaded. This subcell is exploited all along section VII.2.2.

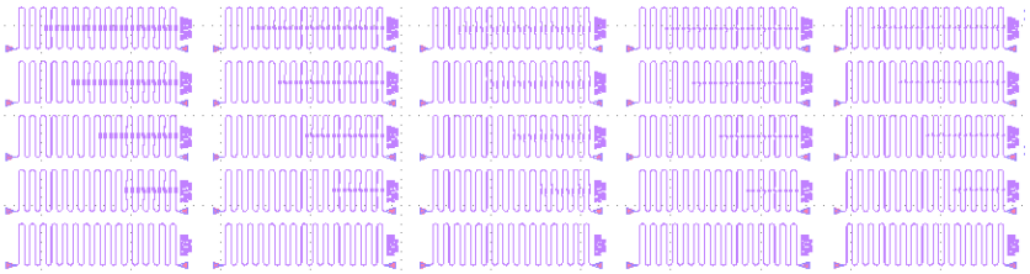

Figure C.11 – Subcell for the asymmetric taper between strip and SWG interdigitated combs waveguides.

Ring-shaped SWG interdigitated combs waveguides

This subcell is presented on figure C.12. It is divided between:

1. Encapsulated ring-shaped SWG interdigitated combs waveguides, without the mechanical supports.
2. Encapsulated ring-shaped SWG interdigitated combs waveguides, with the mechanical supports.
3. Released ring-shaped SWG interdigitated combs waveguides.

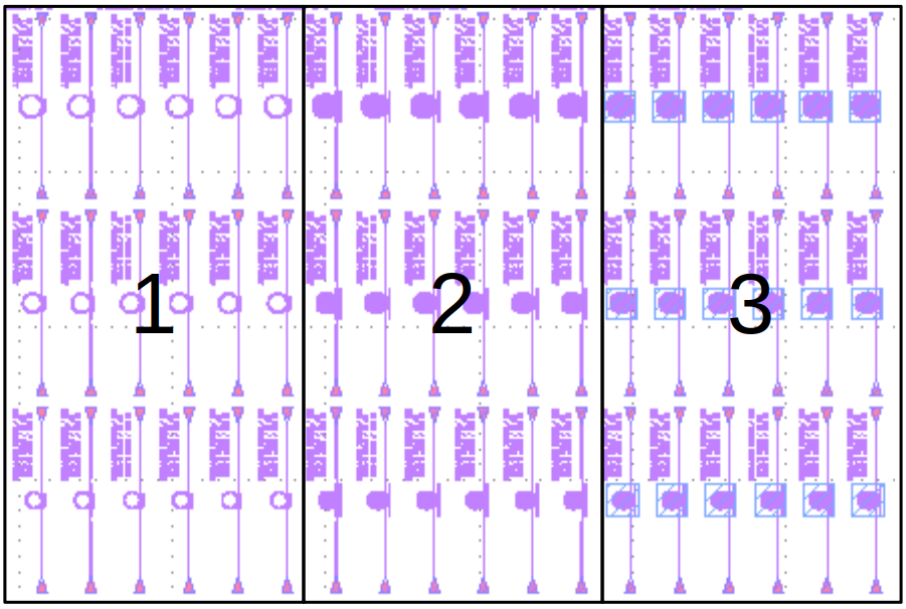

Figure C.12 – Subcell for Ring-shaped SWG interdigitated combs waveguides.

Multiple radii and gaps are explored. Experimental results based on this subcell are presented on section VII.2.3.

Test cell for photonic devices

This subcell is presented on figure C.13. It is divided between:

1. Bent waveguides of variable radii, for the measurement of bent losses.
2. Directional couplers of variable radii and gaps.
3. Suspended waveguides.
4. Spiral-shaped waveguides, for the measurement of propagation losses.
5. Used for technological verification.

6. Cascaded MMI.

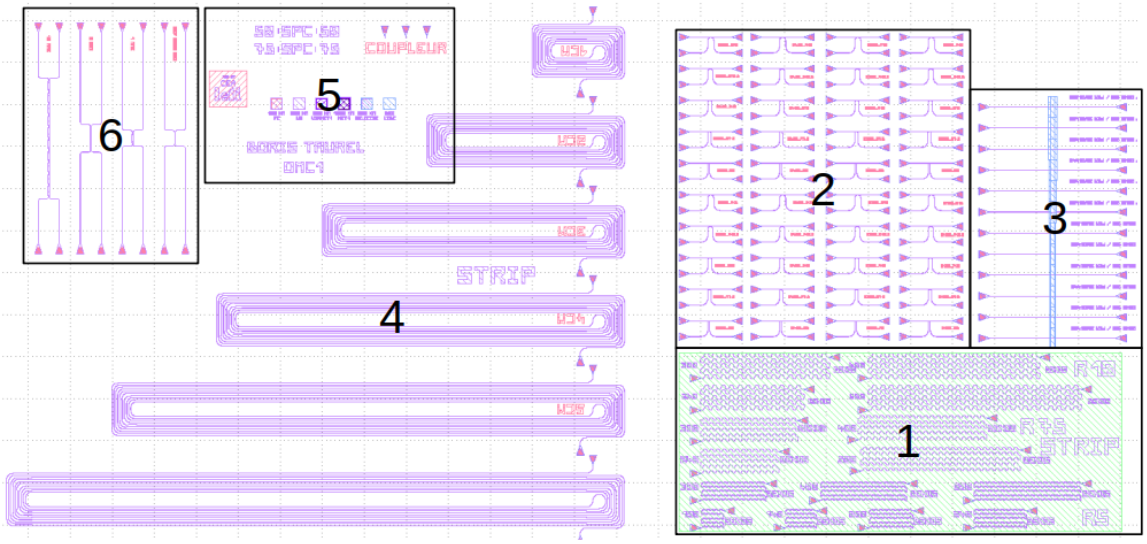

Figure C.13 – Test cell for photonic devices.

APPENDIX D

Silicon nitride suspended ring resonators

Introduction

All results presented along the thesis were obtained on silicon-based structures. In parallel to this work, we also briefly studied silicon nitride-based ring resonators as a way to realize suspended optomechanical cavities.

Silicon nitride is a good candidate for photonic integration. It exhibits a large transparency window at both visible and infra-red wavelengths, and displays negligible two-photons absorption at telecom wavelengths [137]. Propagation losses in fabricated waveguides are relatively low, and ring resonators with quality factors superior to 10^6 have already been demonstrated [213, 214].

Mechanically speaking, silicon nitride is a high tensile stress material, which allows to achieve unusually elevated mechanical quality factors [215, 216].

As a good candidate for photonics and nanomechanics, silicon nitride is hence a good candidate for cavity optomechanics. On the following, we present early results that we obtained on silicon nitride.

Fabrication

Briefly, the fabrication steps are the following:

1. Grating couplers and waveguides etching (figure D.1 ; steps 4 to 7):

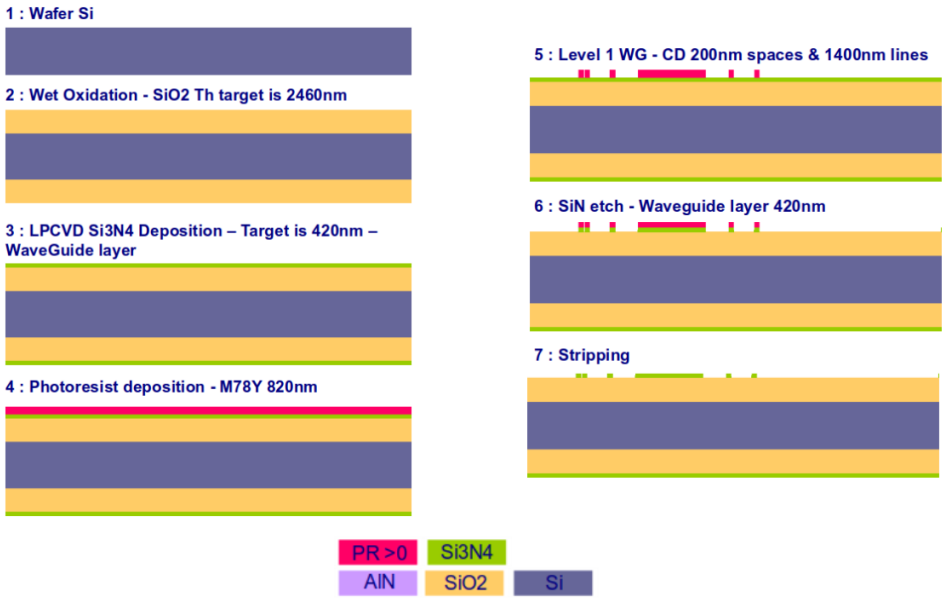

Figure D.1 – Grating couplers and waveguides etching. Contrary to Silicon wafers, the GC we use here are totally etched, such that both GC and photonic waveguides are patterned during the same single etching step.

   (a) Resist deposition, insulation & development.

   (b) Complete etching of the SiN layer.

   (c) Resist removal.

2. Waveguide encapsulation (figure D.2 ; steps 8 and 9):

   (a) Deposition of a 2600 nm thick SiO2 layer.

   (b) CMP of the SiO2 layer, down to 600 nm above the waveguide level.

3. Waveguide release (figures D.2 and D.3 ; steps 10 to 16):

   (a) Deposition of an AlN layer.

   (b) Resist deposition, insulation & development.

   (c) Etching of the AlN layer.

   (d) 1800 nm dry etching of the SiO2 layer, down to 200 nm above the waveguide level.

   (e) Resist removal.

   (f) Wet etching of the BOX and SiO2 layers.

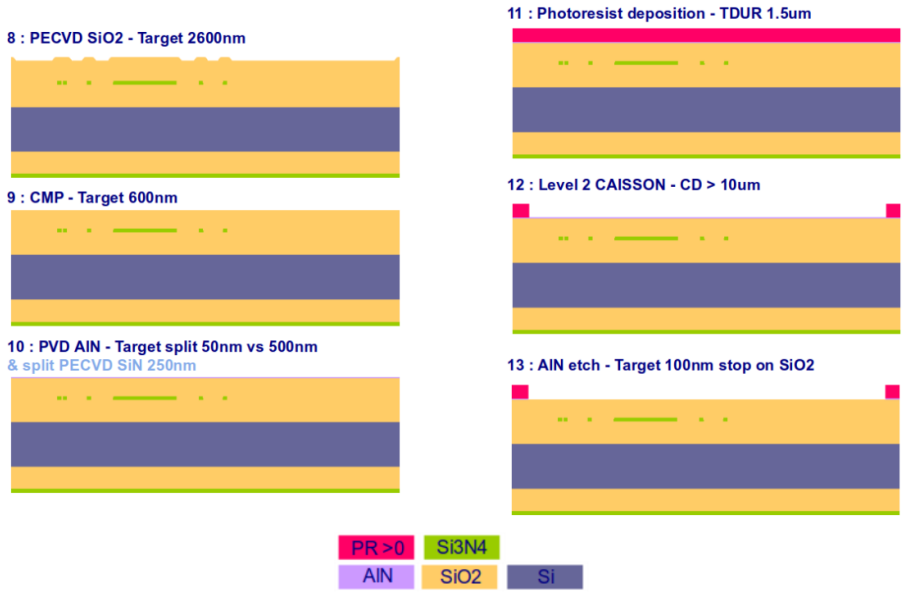

Figure D.2 – Waveguide encapsulation and patterning of a AlN hard mask.

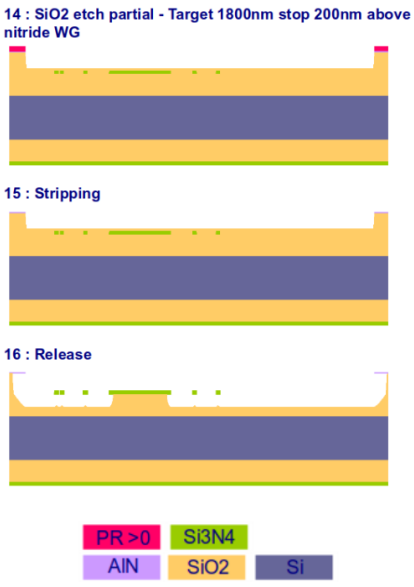

Figure D.3 – Waveguide release.

Optical experiments on SiN ring resonators.

Optical experiments are conducted on optical probers. The experimental setup and the measurement protocol are the same that in section V.2.

Preliminary measurements: grating couplers efficiency, linear losses and bending losses

We begin optical experiments by measuring the GC efficiency. The results are presented on table D.1

	Loses (dB)	$\lambda_{\text{Max.}}$ (nm)
Median	-11.25	1510.36
Average	-11.48	1513.70
Standard deviation	1.17	11.81
Best result	-9.71	

Table D.1 – GC losses

Next, we measure propagation losses. The optical transmission spectrum of spiral-shaped waveguides of various lengths (few centimeters) is realized. A linear regression between the lengths and the output powers directly gives access to the linear losses. The results are presented on table D.2.

Wavelength	1530 nm	1550 nm	1570 nm
Median (dB/cm)	-3.24	-1.91	-0.65
Average (dB/cm)	-3.41	-2.16	-0.90
Standard deviation (dB/cm)	0.84	0.97	0.77
Best result (dB/cm)	-2.05	-0.56	-0.02

Table D.2 – Propagation losses in 1400 nm × 420 nm silicon nitride waveguides, with a TE_0 polarization.

Bending loses are measured with numerous bent waveguides and a linear regression between the number of bends and the output powers. The results are presented on table D.3.

Discussion: The waveguide design was conducted with numerical FEM simulations. The silicon nitride height of 420 nm was imposed by available wafers, such that we chose

Radius (μm)	15	25	50
Median (dB/90^o)	-0.314	-0.173	-0.040
Average (dB/90^o)	-0.292	-0.139	-0.073
Std (dB/90^o)	0.077	-0.109	-0.105
Best result (dB/90^o)	-0.049	-0.146	-0.321

Table D.3 – Bending losses in 1400 nm × 420 nm silicon nitride waveguides, with a TE_0 polarization, at a 1550 nm wavelength.

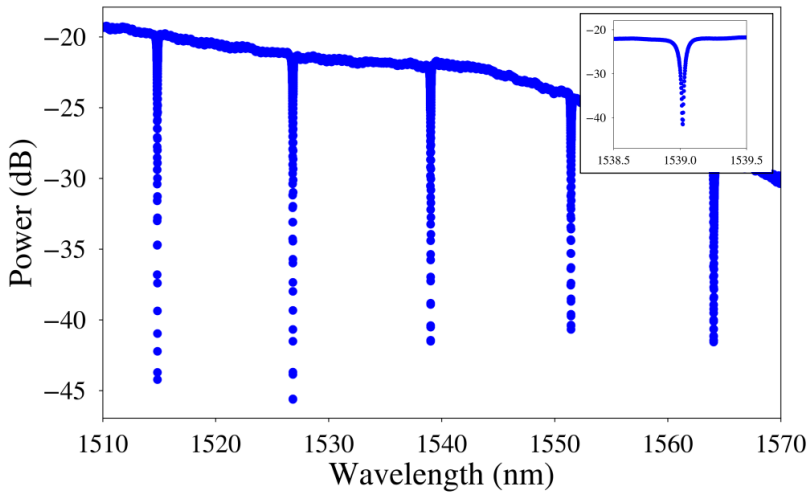

Figure D.4 – Typical experimental spectrum of an encapsulated SiN ring resonator of radius 15 μm and gap 500 nm.

a 1400 nm width, in order to ensure a single mode TE_0 behavior. The waveguide cross-section is hence 1400 nm × 420 nm.

Propagation losses and bending losses are at the state-of-the-art level [217]. Grating couplers are a little less efficient, but remain at a totally appropriate level.

Ring resonators

Encapsulated ring resonators of various gaps and radius were designed, fabricated, and measured. A typical experimental spectrum is presented on figure D.4.

For each spectrum, the position, contrast and quality factor of each peak are calculated. Statistical values over an entire wafer are summarized on figure D.5.

We globally observe an increase of the quality factor with the ring radius, as well as with the gap. These results are coherent with theory: when the gap is increased, the coupling between the bus waveguide and the cavity decreases, and so do the intra-cavity losses.

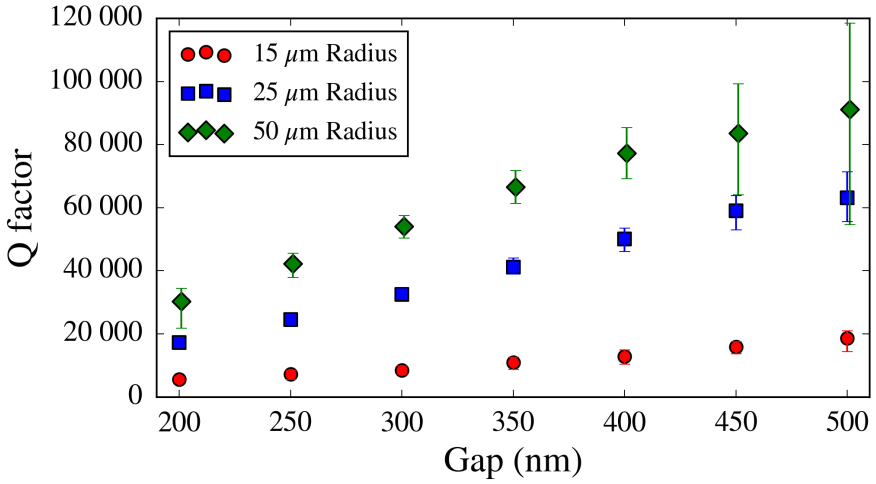

Figure D.5 – SiN ring resonators quality factors, for various radii and gaps. The dot (resp. errorbar) corresponds to the median (resp. lower and upper range) of the data.

Suspended ring resonators

Suspended ring resonators of various design were fabricated. At time of writing, we could not however observe resonance peaks on the optical spectrum. The reason is evidenced on figure D.6. On the right SEM image, we see that the bus waveguide and suspended ring are not aligned at the coupling region. Consequently, light is not coupled into the ring.

We believe the misalignment to be a consequence of pressure forces exerted during the fabrication. The mastery of this step is an on-going work.

Conclusion

In this appendix, we have presented preliminary results on silicon nitride suspended ring resonators and photonic waveguides in general. We measured promising photonic performances, with state-of-the-art propagation and bending losses, and attained optical quality factors above 100 000 on encapsulated ring resonators.

The next step is now to master the release of suspended ring resonator, from which cavity optomechanics experiments could be conducted.

Silicon nitride suspended ring resonators are appealing for cavity optomechanics applications, because they exhibit negligible TPA effects. In this regard, it is possible to use high optical powers (and hence benefit from more “practical signal”) without suffering from thermo-optic and non-linear effects, whose negative impact was evidenced on silicon

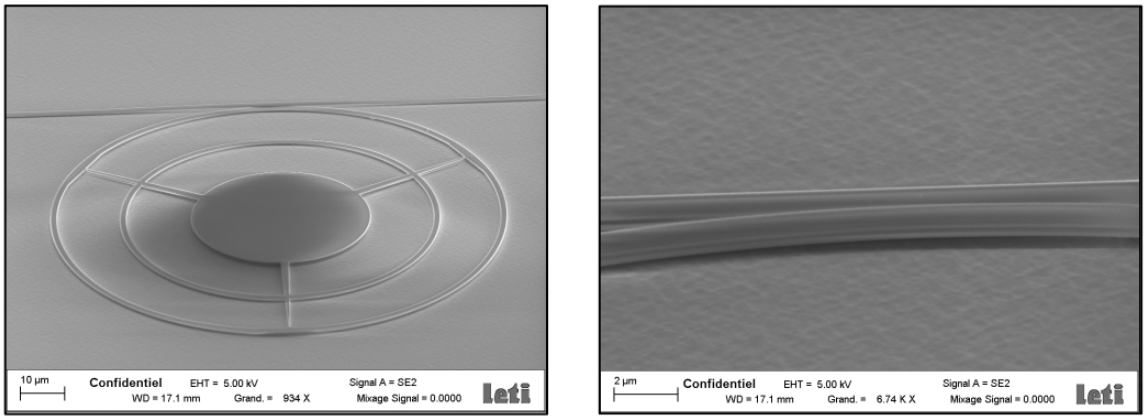

Figure D.6 – **Left:** SEM image of a SiN suspended ring resonator. **Right:** Zoom at the coupling region. The bus waveguide and ring are not aligned.

suspended ring resonators. Additionally, silicon nitride also offer interesting mechanical properties, as a high tensile stress material.

Bibliography

[1] Peter Lebedew. Untersuchungen Ãijber die druckkrÃdfte des lichtes. *Annalen der Physik*, 311(11):433–458, 1901.

[2] E. F. Nichols and G. F. Hull. A preliminary communication on the pressure of heat and light radiation. *Phys. Rev. (Series I)*, 13:307–320, Nov 1901.

[3] V. B. Braginsky and Anatolii Borisovich Manukin. Ponderomotive effects of electromagnetic radiation. *JETP*, 25(4):653, 1967.

[4] V. B. Braginsky and Anatolii Borisovich Manukin. *Measurement of weak forces in physics experiments / V. B. Braginsky and A. B. Manukin ; edited by David H. Douglass*. University of Chicago Press Chicago, 1977.

[5] Vladimir B. Braginsky, Farid Ya Khalili, and Kip S. Thorne. *Quantum Measurement*. Cambridge University Press, 1992.

[6] S. Mancini and P. Tombesi. Quantum noise reduction by radiation pressure. *Phys. Rev. A*, 49:4055–4065, May 1994.

[7] S. Bose, K. Jacobs, and P. L. Knight. Preparation of nonclassical states in cavities with a moving mirror. *Phys. Rev. A*, 56:4175–4186, Nov 1997.

[8] A. Ashkin. Acceleration and trapping of particles by radiation pressure. *Phys. Rev. Lett.*, 24:156–159, Jan 1970.

[9] A. Ashkin. Trapping of atoms by resonance radiation pressure. *Phys. Rev. Lett.*, 40:729–732, Mar 1978.

[10] Harold J. Metcalf and Peter van der Straten. *Laser Cooling and Trapping*. Springer, New York, NY, 1999.

[11] T. J. Kippenberg, H. Rokhsari, T. Carmon, A. Scherer, and K. J. Vahala. Analysis of radiation-pressure induced mechanical oscillation of an optical microcavity. *Phys. Rev. Lett.*, 95:033901, Jul 2005.

[12] H. Rokhsari, T. J. Kippenberg, T. Carmon, and K. J. Vahala. Radiation-pressure-driven micro-mechanical oscillator. *Opt. Express*, 13(14):5293–5301, Jul 2005.

[13] H. Rokhsari, T. J. Kippenberg, T. Carmon, and K. J. Vahala. Theoretical and experimental study of radiation pressure-induced mechanical oscillations (parametric instability) in optical microcavities. *IEEE Journal of Selected Topics in Quantum Electronics*, 12(1):96–107, Jan 2006.

[14] Olivier Arcizet, P-F Cohadon, Tristan Briant, Michel Pinard, and Antoine Heidmann. Radiation-pressure cooling and optomechanical instability of a micromirror. *Nature*, 444(7115):71, 2006.

[15] J. D. Thompson, B. M. Zwickl, A. M. Jayich, Florian Marquardt, S. M. Girvin, and J. G. E. Harris. Strong dispersive coupling of a high-finesse cavity to a micromechanical membrane. *Nature*, 452(7183):72–75, March 2008.

[16] Jordi Gomis-Bresco, Daniel Navarro-Urrios, Mourad Oudich, Saïd El-Jallal, Amadeu Griol, Daniel Puerto, E Chavez, Yan Pennec, Bahram Djafari-Rouhani, Francesc Alzina, et al. A one-dimensional optomechanical crystal with a complete phononic band gap. *Nature communications*, 5:4452, 2014.

[17] Charles Kittel et al. *Introduction to solid state physics*, volume 8. Wiley New York, 1976.

[18] Xiankai Sun, King Y. Fong, Chi Xiong, Wolfram H. P. Pernice, and Hong X. Tang. Ghz optomechanical resonators with high mechanical q factor in air. *Opt. Express*, 19(22):22316–22321, Oct 2011.

[19] Yuxiang Liu, Marcelo Davanço, Vladimir Aksyuk, and Kartik Srinivasan. Electromagnetically induced transparency and wideband wavelength conversion in silicon nitride microdisk optomechanical resonators. *Phys. Rev. Lett.*, 110:223603, May 2013.

[20] B. M. Zwickl, W. E. Shanks, A. M. Jayich, C. Yang, A. C. Bleszynski Jayich, J. D. Thompson, and J. G. E. Harris. High quality mechanical and optical properties of commercial silicon nitride membranes. *Applied Physics Letters*, 92(10):103125, 2008.

[21] Dac Trung Nguyen, Christophe Baker, William Hease, Selsabil Sejil, Pascale Senellart, Aristide Lemaitre, Sara Ducci, Giuseppe Leo, and Ivan Favero. Ultrahigh q-frequency product for optomechanical disk resonators with a mechanical shield. *Applied Physics Letters*, 103(24):241112, 2013.

[22] Markus Aspelmeyer, Tobias J. Kippenberg, and Florian Marquardt, editors. *Cavity Optomechanics*, pages 497–497. Springer Netherlands, Dordrecht, 2016.

[23] Garrett D. Cole, Simon GrÃűblacher, Katharina Gugler, Sylvain Gigan, and Markus Aspelmeyer. Monocrystalline algaas heterostructures for high-reflectivity high-q micromechanical resonators in the mhz regime. *Applied Physics Letters*, 92(26):261108, 2008.

[24] AG Kuhn, M Bahriz, O Ducloux, Claude Chartier, O Le Traon, T Briant, P-F Cohadon, A Heidmann, Christine Michel, L Pinard, et al. A micropillar for cavity optomechanics. *Applied Physics Letters*, 99(12):121103, 2011.

[25] Matthew J Weaver, Brian Pepper, Fernando Luna, Frank M Buters, Hedwig J Eerkens, Gesa Welker, Blaise Perock, Kier Heeck, Sven de Man, and Dirk Bouwmeester. Nested trampoline resonators for optomechanics. *Applied Physics Letters*, 108(3):033501, 2016.

[26] Constanze Höhberger Metzger and Khaled Karrai. Cavity cooling of a microlever. *Nature*, 432(7020):1002, 2004.

[27] Ivan Favero, Sebastian Stapfner, David Hunger, Philipp Paulitschke, Jakob Reichel, Heribert Lorenz, Eva M. Weig, and Khaled Karrai. Fluctuating nanomechanical system in a high finesse optical microcavity. *Opt. Express*, 17(15):12813–12820, Jul 2009.

[28] Lu Ding. High Frequency GaAs Nano-Optomechanical Disk Resonator. *Physical Review Letters*, 105(26), 2010.

[29] Xuefeng Jiang, Min Wang, Mark C. Kuzyk, Thein Oo, Gui-Lu Long, and Hailin Wang. Chip-based silica microspheres for cavity optomechanics. *Opt. Express*, 23(21):27260–27265, Oct 2015.

[30] Gustavo S Wiederhecker, Long Chen, Alexander Gondarenko, and Michal Lipson. Controlling photonic structures using optical forces. *Nature*, 462(7273):633, 2009.

[31] Gustavo O. Luiz, Rodrigo S. Benevides, Felipe G. S. Santos, Yovanny A. V. Espinel, Thiago P. Mayer Alegre, and Gustavo S. Wiederhecker. Efficient anchor loss suppression in coupled near-field optomechanical resonators. *Opt. Express*, 25(25):31347–31361, Dec 2017.

[32] Georg Anetsberger, Olivier Arcizet, Quirin P Unterreithmeier, Rémi Rivière, Albert Schliesser, Eva Maria Weig, Jörg P Kotthaus, and Tobias J Kippenberg. Near-field cavity optomechanics with nanomechanical oscillators. *Nature Physics*, 5(12):909, 2009.

[33] Jasper Chan, Amir H. Safavi-Naeini, Jeff T. Hill, SeÃąn Meenehan, and Oskar Painter. Optimized optomechanical crystal cavity with acoustic radiation shield. *Applied Physics Letters*, 101(8):081115, 2012.

[34] Florian Marquardt, Joe P. Chen, A. A. Clerk, and S. M. Girvin. Quantum theory of cavity-assisted sideband cooling of mechanical motion. *Phys. Rev. Lett.*, 99:093902, Aug 2007.

[35] I. Wilson-Rae, N. Nooshi, W. Zwerger, and T. J. Kippenberg. Theory of ground state cooling of a mechanical oscillator using dynamical backaction. *Phys. Rev. Lett.*, 99:093901, Aug 2007.

[36] A. Schliesser, P. Del'Haye, N. Nooshi, K. J. Vahala, and T. J. Kippenberg. Radiation pressure cooling of a micromechanical oscillator using dynamical backaction. *Phys. Rev. Lett.*, 97:243905, Dec 2006.

[37] Schwab Gigan, HR Böhm, Mauro Paternostro, Florian Blaser, G Langer, JB Hertzberg, Keith C Schwab, Dieter Bäuerle, Markus Aspelmeyer, and Anton Zeilinger. Self-cooling of a micromirror by radiation pressure. *Nature*, 444(7115):67, 2006.

[38] Stefano Mancini, David Vitali, and Paolo Tombesi. Optomechanical cooling of a macroscopic oscillator by homodyne feedback. *Phys. Rev. Lett.*, 80:688–691, Jan 1998.

[39] P. F. Cohadon, A. Heidmann, and M. Pinard. Cooling of a mirror by radiation pressure. *Phys. Rev. Lett.*, 83:3174–3177, Oct 1999.

[40] Dustin Kleckner and Dirk Bouwmeester. Sub-kelvin optical cooling of a micromechanical resonator. *Nature*, 444(7115):75, 2006.

[41] M. Poggio, C. L. Degen, H. J. Mamin, and D. Rugar. Feedback cooling of a cantilever's fundamental mode below 5 mk. *Phys. Rev. Lett.*, 99:017201, Jul 2007.

[42] C. Genes, D. Vitali, P. Tombesi, S. Gigan, and M. Aspelmeyer. Ground-state cooling of a micromechanical oscillator: Comparing cold damping and cavity-assisted cooling schemes. *Phys. Rev. A*, 77:033804, Mar 2008.

[43] V.B. Braginsky, S.E. Strigin, and S.P. Vyatchanin. Parametric oscillatory instability in fabryâĂŞperot interferometer. *Physics Letters A*, 287(5):331 – 338, 2001.

[44] K. E. Petersen. Silicon as a mechanical material. *Proceedings of the IEEE*, 70(5):420–457, May 1982.

[45] Mo Li, WHP Pernice, and HX Tang. Broadband all-photonic transduction of nanocantilevers. *Nature nanotechnology*, 4(6):377, 2009.

[46] Ioana Voiculescu and Mona Zaghloul, editors. *Nanocantilever beams: modeling, fabrication and applications*. Pan Stanford Publishing, Singapore, 2016. OCLC: 965509840.

[47] Chi Xiong, Xiankai Sun, King Y. Fong, and Hong X. Tang. Integrated high frequency aluminum nitride optomechanical resonators. *Applied Physics Letters*, 100(17):171111, 2012.

[48] Dustin W. Carr, S. Evoy, L. Sekaric, H. G. Craighead, and J. M. Parpia. Measurement of mechanical resonance and losses in nanometer scale silicon wires. *Applied Physics Letters*, 75(7):920–922, 1999.

[49] Olivier Arcizet, P-F Cohadon, T Briant, M Pinard, A Heidmann, J-M Mackowski, Christine Michel, L Pinard, O Français, and L Rousseau. High-sensitivity optical monitoring of a micromechanical resonator with a quantum-limited optomechanical sensor. *Physical review letters*, 97(13):133601, 2006.

[50] Kartik Srinivasan, Houxun Miao, Matthew T Rakher, Marcelo Davanco, and Vladimir Aksyuk. Optomechanical transduction of an integrated silicon cantilever probe using a microdisk resonator. *Nano letters*, 11(2):791–797, 2011.

[51] Fenfei Liu, Seyedhamidreza Alaie, Zayd C. Leseman, and Mani Hossein-Zadeh. Sub-pg mass sensing and measurement with an optomechanical oscillator. *Opt. Express*, 21(17):19555–19567, Aug 2013.

[52] T. O. Rocheleau, A. J. Grine, K. E. Grutter, R. A. Schneider, N. Quack, M. C. Wu, and C. T. C. Nguyen. Enhancement of mechanical Q for low phase noise optomechanical oscillators. In *2013 IEEE 26th International Conference on Micro Electro Mechanical Systems (MEMS)*, pages 118–121, January 2013.

[53] A Schliesser, G Anetsberger, R Rivière, O Arcizet, and T J Kippenberg. High-sensitivity monitoring of micromechanical vibration using optical whispering gallery mode resonators. *New Journal of Physics*, 10(9):095015, sep 2008.

[54] V. T. K. Sauer, Z. Diao, M. R. Freeman, and W. K. Hiebert. Nanophotonic detection of side-coupled nanomechanical cantilevers. *Applied Physics Letters*, 100(26):261102, 2012.

[55] Mani Hossein-Zadeh and Kerry J Vahala. An optomechanical oscillator on a silicon chip. *IEEE Journal of selected topics in Quantum Electronics*, 16(1):276–287, 2009.

[56] X. Steve Yao and Lute Maleki. Optoelectronic microwave oscillator. *J. Opt. Soc. Am. B*, 13(8):1725–1735, Aug 1996.

[57] Jeff T Hill, Amir H Safavi-Naeini, Jasper Chan, and Oskar Painter. Coherent optical wavelength conversion via cavity optomechanics. *Nature communications*, 3:1196, 2012.

[58] Amir H Safavi-Naeini and Oskar Painter. Proposal for an optomechanical traveling wave phonon–photon translator. *New Journal of Physics*, 13(1):013017, 2011.

[59] M. Hossein-Zadeh and K. J. Vahala. Photonic rf down-converter based on optomechanical oscillation. *IEEE Photonics Technology Letters*, 20(4):234–236, Feb 2008.

[60] Arkady Pikovsky, Jurgen Kurths, Michael Rosenblum, and Jürgen Kurths. *Synchronization: a universal concept in nonlinear sciences*, volume 12. Cambridge university press, 2003.

[61] C. A. Holmes, C. P. Meaney, and G. J. Milburn. Synchronization of many nanomechanical resonators coupled via a common cavity field. *Phys. Rev. E*, 85:066203, Jun 2012.

[62] Georg Heinrich, Max Ludwig, Jiang Qian, Björn Kubala, and Florian Marquardt. Collective dynamics in optomechanical arrays. *Phys. Rev. Lett.*, 107:043603, Jul 2011.

[63] Mian Zhang, Gustavo S. Wiederhecker, Sasikanth Manipatruni, Arthur Barnard, Paul McEuen, and Michal Lipson. Synchronization of micromechanical oscillators using light. *Phys. Rev. Lett.*, 109:233906, Dec 2012.

[64] Mahmood Bagheri, Menno Poot, Linran Fan, Florian Marquardt, and Hong X. Tang. Photonic cavity synchronization of nanomechanical oscillators. *Phys. Rev. Lett.*, 111:213902, Nov 2013.

[65] Mian Zhang, Shreyas Shah, Jaime Cardenas, and Michal Lipson. Synchronization and phase noise reduction in micromechanical oscillator arrays coupled through light. *Phys. Rev. Lett.*, 115:163902, Oct 2015.

[66] Matthew H. Matheny, Jeffrey Emenheiser, Warren Fon, Airlie Chapman, Anastasiya Salova, Martin Rohden, Jarvis Li, Mathias Hudoba de Badyn, Márton Pósfai, Leonardo Duenas-Osorio, Mehran Mesbahi, James P. Crutchfield, M. C. Cross, Raissa M. D'Souza, and Michael L. Roukes. Exotic states in a simple network of nanoelectromechanical oscillators. *Science*, 363(6431), 2019.

[67] Jonathan P Marangos. Electromagnetically induced transparency. *Journal of Modern Optics*, 45(3):471–503, 1998.

[68] G. S. Agarwal and Sumei Huang. Electromagnetically induced transparency in mechanical effects of light. *Phys. Rev. A*, 81:041803, Apr 2010.

[69] Stefan Weis, Rémi Rivière, Samuel Deléglise, Emanuel Gavartin, Olivier Arcizet, Albert Schliesser, and Tobias J. Kippenberg. Optomechanically induced transparency. *Science*, 330(6010):1520–1523, 2010.

[70] Hao Xiong and Ying Wu. Fundamentals and applications of optomechanically induced transparency. *Applied Physics Reviews*, 5(3):031305, 2018.

[71] Hermann A. Haus. *Waves and Fields in Optoelectronics*. Prentice-Hall, Englewood Cliffs, New Jersey, 1984.

[72] H. D. Conway. *Formulas for Natural Frequency and Mode Shape, by Robert D. Blevins*. Krieger Publishing Company, 1980.

[73] Peter T. Rakich, Miloš A. Popović, and Zheng Wang. General treatment of optical forces and potentials in mechanically variable photonic systems. *Opt. Express*, 17(20):18116–18135, Sep 2009.

[74] Mo Li, Wolfram H. P. Pernice, and Hong X. Tang. Reactive cavity optical force on microdisk-coupled nanomechanical beam waveguides. *Phys. Rev. Lett.*, 103:223901, Nov 2009.

[75] Florian Elste, S. M. Girvin, and A. A. Clerk. Quantum noise interference and backaction cooling in cavity nanomechanics. *Phys. Rev. Lett.*, 102:207209, May 2009.

[76] M. L. Gorodetksy, A. Schliesser, G. Anetsberger, S. Deleglise, and T. J. Kippenberg. Determination of the vacuum optomechanical coupling rate using frequency noise calibration. *Opt. Express*, 18(22):23236–23246, Oct 2010.

[77] A. Dorsel, J. D. McCullen, P. Meystre, E. Vignes, and H. Walther. Optical bistability and mirror confinement induced by radiation pressure. *Phys. Rev. Lett.*, 51:1550–1553, Oct 1983.

[78] Florian Marquardt, J. G. E. Harris, and S. M. Girvin. Dynamical multistability induced by radiation pressure in high-finesse micromechanical optical cavities. *Phys. Rev. Lett.*, 96:103901, Mar 2006.

[79] Tal Carmon, Hossein Rokhsari, Lan Yang, Tobias J. Kippenberg, and Kerry J. Vahala. Temporal behavior of radiation-pressure-induced vibrations of an optical microcavity phonon mode. *Phys. Rev. Lett.*, 94:223902, Jun 2005.

[80] Tal Carmon, M. C. Cross, and Kerry J. Vahala. Chaotic quivering of micron-scaled on-chip resonators excited by centrifugal optical pressure. *Phys. Rev. Lett.*, 98:167203, Apr 2007.

[81] Stewart E Miller. Integrated optics: An introduction. *The Bell System Technical Journal*, 48(7):2059–2069, 1969.

[82] Mool C Gupta and John Ballato. *The handbook of photonics*. CRC press, 2018.

[83] A.W. Snyder and J. Love. *Optical Waveguide Theory*. Science paperbacks. Springer US, 1983.

[84] Rohan D. Kekatpure, Aaron C. Hryciw, Edward S. Barnard, and Mark L. Brongersma. Solving dielectric and plasmonic waveguide dispersion relations on a pocket calculator. *Opt. Express*, 17(26):24112–24129, Dec 2009.

[85] Enrique AJ Marcatili. Dielectric rectangular waveguide and directional coupler for integrated optics. *Bell System Technical Journal*, 48(7):2071–2102, 1969.

[86] Wouter J Westerveld and H Paul Urbach. *Silicon Photonics*. 2053-2563. IOP Publishing, 2017.

[87] R Scarmozzino, Anand Gopinath, R Pregla, and S Helfert. Numerical techniques for modeling guided-wave photonic devices. *IEEE Journal of Selected Topics in Quantum Electronics*, 6(1):150–162, 2000.

[88] T. Kamalakis and T. Sphicopoulos. Frequency dependence of the coupling coefficients and resonant frequency detuning in a nanophotonic waveguide-cavity system. *IEEE Journal of Quantum Electronics*, 42(8):827–837, Aug 2006.

[89] Q. Lin, Oskar J. Painter, and Govind P. Agrawal. Nonlinear optical phenomena in silicon waveguides: Modeling and applications. *Opt. Express*, 15(25):16604–16644, Dec 2007.

[90] Ivan D. Rukhlenko, Malin Premaratne, and Govind P. Agrawal. Analytical study of optical bistability in silicon-waveguide resonators. *Opt. Express*, 17(24):22124–22137, Nov 2009.

[91] Yurii A. Vlasov and Sharee J. McNab. Losses in single-mode silicon-on-insulator strip waveguides and bends. *Opt. Express*, 12(8):1622–1631, Apr 2004.

[92] Francois Ladouceur and E Labeye. A new general approach to optical waveguide path design. *Journal of Lightwave Technology*, 13(3):481–492, 1995.

[93] Bellegarde Cyril, Pargon Erwine, Sciancalepore Corrado, Petit-Etienne Camille, Hughes Vincent, Hartmann Jean-Michel, and Lyan Philippe. Improvement of sidewall roughness of sub-micron silicon-on-insulator waveguides for low-loss on-chip links, 2017.

[94] Akihiro Yahata, Satoshi Urano, Tomoki Inoue, and Takashi Shinohe. Smoothing of si trench sidewall surface by chemical dry etching and sacrificial oxidation. *Japanese journal of applied physics*, 37(7R):3954, 1998.

[95] D. K. Sparacin, S. J. Spector, and L. C. Kimerling. Silicon waveguide sidewall smoothing by wet chemical oxidation. *Journal of Lightwave Technology*, 23(8):2455–2461, Aug 2005.

[96] Kevin K. Lee, Desmond R. Lim, Hsin-Chiao Luan, Anuradha Agarwal, James Foresi, and Lionel C. Kimerling. Effect of size and roughness on light transmission in a si/sio2 waveguide: Experiments and model. *Applied Physics Letters*, 77(11):1617–1619, 2000.

[97] PK v Tien. Light waves in thin films and integrated optics. *Applied optics*, 10(11):2395–2413, 1971.

[98] see commercial SMF28 fibers For example. Smf28 fiber.

[99] Inna Krasnokutska, Jean-Luc J. Tambasco, Xijun Li, and Alberto Peruzzo. Ultra-low loss photonic circuits in lithium niobate on insulator. *Opt. Express*, 26(2):897–904, Jan 2018.

[100] Minh Tran, Duanni Huang, Tin Komljenovic, Jonathan Peters, Aditya Malik, and John Bowers. Ultra-low-loss silicon waveguides for heterogeneously integrated silicon/iii-v photonics. *Applied Sciences*, 8(7):1139, 2018.

[101] N. Boynton, M. Gehl, C. Dallo, A. Pomerene, A. Starbuck, D. Hood, D. Trotter, A. Lentine, and C. T. DeRose. Characterization of low loss photonic waveguides using arrayed waveguide structure. In *2018 IEEE Optical Interconnects Conference (OI)*, pages 31–32, June 2018.

[102] C. G. H. Roeloffzen, M. Hoekman, E. J. Klein, L. S. Wevers, R. B. Timens, D. Marchenko, D. Geskus, R. Dekker, A. Alippi, R. Grootjans, A. van Rees, R. M. Oldenbeuving, J. P. Epping, R. G. Heideman, K. WÃűrhoff, A. Leinse, D. Geuzebroek, E. Schreuder, P. W. L. van Dijk, I. Visscher, C. Taddei, Y. Fan, C. Tabal-

lione, Y. Liu, D. Marpaung, L. Zhuang, M. Benelajla, and K. Boller. Low-loss si3n4 triplex optical waveguides: Technology and applications overview. *IEEE Journal of Selected Topics in Quantum Electronics*, 24(4):1–21, July 2018.

[103] Lin Chang, Andreas Boes, Paolo Pintus, Weiqiang Xie, Jon D. Peters, M. J. Kennedy, Warren Jin, Xiao-Wen Guo, Su-Peng Yu, Scott B. Papp, and John E. Bowers. Low loss (al)gaas on an insulator waveguide platform. *Opt. Lett.*, 44(16):4075–4078, Aug 2019.

[104] T. Goh, M. Yasu, K. Hattori, A. Himeno, M. Okuno, and Y. Ohmori. Low loss and high extinction ratio strictly nonblocking 16/spl times/16 thermooptic matrix switch on 6-in wafer using silica-based planar lightwave circuit technology. *Journal of Lightwave Technology*, 19(3):371–379, March 2001.

[105] Mo Li, WHP Pernice, and HX Tang. Tunable bipolar optical interactions between guided lightwaves. *Nature Photonics*, 3(8):464, 2009.

[106] Xiankai Sun, Xufeng Zhang, and Hong X. Tang. High-q silicon optomechanical microdisk resonators at gigahertz frequencies. *Applied Physics Letters*, 100(17):173116, 2012.

[107] Janderson R. Rodrigues and Vilson R. Almeida. Optical forces through the effective refractive index. *Opt. Lett.*, 42(21):4371–4374, Nov 2017.

[108] Peter T. Rakich, Paul Davids, and Zheng Wang. Tailoring optical forces in waveguides through radiation pressure and electrostrictive forces. *Opt. Express*, 18(14):14439–14453, Jul 2010.

[109] Robert E Newnham. *Properties of materials: anisotropy, symmetry, structure*. Oxford University Press on Demand, 2005.

[110] David K. Biegelsen. Photoelastic tensor of silicon and the volume dependence of the average gap. *Phys. Rev. Lett.*, 32:1196–1199, May 1974.

[111] Christopher Baker, William Hease, Dac-Trung Nguyen, Alessio Andronico, Sara Ducci, Giuseppe Leo, and Ivan Favero. Photoelastic coupling in gallium arsenide optomechanical disk resonators. *Opt. Express*, 22(12):14072–14086, Jun 2014.

[112] W.H.P. Pernice, Mo Li, and H.X. Tang. Theoretical investigation of the transverse optical force between a silicon nanowire waveguide and a substrate. *Opt. Express*, 17(3):1806–1816, Feb 2009.

[113] Michelle L Povinelli, Marko Lončar, Mihai Ibanescu, Elizabeth J Smythe, Steven G Johnson, Federico Capasso, and John D Joannopoulos. Evanescent-wave bonding between optical waveguides. *Optics letters*, 30(22):3042–3044, 2005.

[114] Steven G. Johnson, M. Ibanescu, M. A. Skorobogatiy, O. Weisberg, J. D. Joannopoulos, and Y. Fink. Perturbation theory for maxwell's equations with shifting material boundaries. *Phys. Rev. E*, 65:066611, Jun 2002.

[115] Kerry J Vahala. Optical microcavities. *nature*, 424(6950):839, 2003.

[116] D. K. Armani, T. J. Kippenberg, S. M. Spillane, and K. J. Vahala. Ultra-high-q toroid microcavity on a chip. *Nature*, 421(6926):925, Feb 2003.

[117] Maxime Hermouet, Louise Banniard, Marc Sansa, Alexandre Fafin, Marc Gely, Sebastien Pauliac, Pierre Brianceau, Jacques-Alexandre Dallery, Pierre Etienne Allain, Eduardo Gil Santos, Ivan Favero, Thomas Alava, Guillaume Jourdan, and Sebastien Hentz. 1 million-q optomechanical microdisk resonators with very large scale integration. *Proceedings*, 1(4), 2017.

[118] G. Anetsberger, R. RiviÃĺre, A. Schliesser, O. Arcizet, and T. J. Kippenberg. Ultralow-dissipation optomechanical resonators on a chip. *Nature Photonics*, 2:627–633, 2008.

[119] Hansuek Lee, Tong Chen, Jiang Li, Ki Youl Yang, Seokmin Jeon, Oskar Painter, and Kerry J. Vahala. Chemically etched ultrahigh-Q wedge-resonator on a silicon chip. *Nature Photonics*, 6(6):369–373, June 2012.

[120] Siddharth Tallur, Suresh Sridaran, and Sunil A. Bhave. A monolithic radiation-pressure driven, low phase noise silicon nitride opto-mechanical oscillator. *Optics Express*, 19(24):24522–24529, November 2011.

[121] Sheng-Shian Li, Yu-Wei Lin, Yuan Xie, Zeying Ren, and C.T.-C. Nguyen. Micromechanical "hollow-disk" ring resonators. In *17th IEEE International Conference on Micro Electro Mechanical Systems. Maastricht MEMS 2004 Technical Digest*, pages 821–824, Jan 2004.

[122] G. Piazza, P. J. Stephanou, J. M. Porter, M. B. J. Wijesundara, and A. P. Pisano. Low motional resistance ring-shaped contour-mode aluminum nitride piezoelectric micromechanical resonators for uhf applications. In *18th IEEE International Conference on Micro Electro Mechanical Systems, 2005. MEMS 2005.*, pages 20–23, Jan 2005.

[123] S. Pourkamali and F. Ayazi. High frequency capacitive micromechanical resonators with reduced motional resistance using the harpss technology. In *Digest of Papers. 2004 Topical Meeting on Silicon Monolithic Integrated Circuits in RF Systems, 2004.*, pages 147–150, Sep. 2004.

[124] Dominik G. Rabus. *Integrated Ring Resonators: The Compendium.* Springer Series in Optical Sciences. Springer-Verlag, Berlin Heidelberg, 2007.

[125] A. Yariv. Universal relations for coupling of optical power between microresonators and dielectric waveguides. *Electronics Letters*, 36(4):321–322, Feb 2000.

[126] Yangyang Liu and MiloÅą A. PopoviÄĞ. High-Q contacted ring microcavities with scatterer-avoiding âĂIJwigglerâĂİ Bloch wave supermode fields. *Applied Physics Letters*, 104(20):201102, May 2014.

[127] Tatsuhiko Fukazawa, Tomohisa Hirano, Fumiaki Ohno, and Toshihiko Baba. Low loss intersection of si photonic wire waveguides. *Japanese Journal of Applied Physics*, 43(2):646–647, feb 2004.

[128] L. Schwab, P. E. Allain, L. Banniard, A. Fafin, M. Gely, O. Lemonnier, P. Grosse, M. Hermouet, S. Hentz, I. Favero, B. Legrand, and G. Jourdan. Comprehensive optical losses investigation of VLSI Silicon optomechanical ring resonator sensors. In *2018 IEEE International Electron Devices Meeting (IEDM)*, pages 4.7.1–4.7.4, December 2018.

[129] Hiromichi Watanabe, Naofumi Yamada, and Masahiro Okaji. Linear thermal expansion coefficient of silicon from 293 to 1000 k. *International Journal of Thermophysics*, 25(1):221–236, Jan 2004.

[130] Kishore Padmaraju and Keren Bergman. Resolving the thermal challenges for silicon microring resonator devices. *Nanophotonics*, 3(4-5):269–281, 2013.

[131] M. Dinu, F. Quochi, and H. Garcia. Third-order nonlinearities in silicon at telecom wavelengths. *Applied Physics Letters*, 82(18):2954–2956, 2003.

[132] Christopher Baker. *Resonateurs nano-optomecaniques a mode de galerie sur puce.* PhD thesis, Universite Paris-Diderot, Paris VII, 2013.

[133] David Parrain. *Optomecanique fibree des disques GaAs : dissipation, amplification et non-linearites.* PhD thesis, Universite Paris-Diderot, Paris VII, 2014.

[134] Govind P. Agrawal. Nonlinear fiber optics. In P. L. Christiansen, M. P. Sørensen, and A. C. Scott, editors, *Nonlinear Science at the Dawn of the 21st Century*, pages 195–211, Berlin, Heidelberg, 2000. Springer Berlin Heidelberg.

[135] Christophe Baker, Sebastian Stapfner, David Parrain, Sara Ducci, Giuseppe Leo, Eva M. Weig, and Ivan Favero. Optical instability and self-pulsing in silicon nitride whispering gallery resonators. *Opt. Express*, 20(27):29076–29089, Dec 2012.

[136] H. Gao, Y. Jiang, Y. Cui, L. Zhang, J. Jia, and L. Jiang. Investigation on the thermo-optic coefficient of silica fiber within a wide temperature range. *Journal of Lightwave Technology*, 36(24):5881–5886, Dec 2018.

[137] Kazuhiro Ikeda, Robert E. Saperstein, Nikola Alic, and Yeshaiahu Fainman. Thermal and kerr nonlinear properties of plasma-deposited silicon nitride/silicon dioxide waveguides. *Opt. Express*, 16(17):12987–12994, Aug 2008.

[138] Ivan D. Rukhlenko, Malin Premaratne, and Govind P. Agrawal. Analytical study of optical bistability in silicon ring resonators. *Opt. Lett.*, 35(1):55–57, Jan 2010.

[139] Magdalena S. Nawrocka, Tao Liu, Xuan Wang, and Roberto R. Panepucci. Tunable silicon microring resonator with wide free spectral range. *Applied Physics Letters*, 89(7):071110, 2006.

[140] Vilson R. Almeida and Michal Lipson. Optical bistability on a silicon chip. *Opt. Lett.*, 29(20):2387–2389, Oct 2004.

[141] Frank P Incropera, Adrienne S Lavine, Theodore L Bergman, and David P DeWitt. *Fundamentals of heat and mass transfer.* Wiley, 2007.

[142] H.M. Gibbs. *Optical bistability: controlling light with light*. Academic Press, 1 1985.

[143] S. Timoshenko. *Vibration Problems In Engineering*. D.Van Nostrand Company INC., 1937.

[144] Augustus Edward Hough Love. *A treatise on the mathematical theory of elasticity*. Cambridge university press, 2013.

[145] T. Charnley, R. Perrin, V. Mohanan, and H. Banu. Vibrations of thin rings of rectangular cross-section. *Journal of Sound and Vibration*, 134(3):455 – 488, 1989.

[146] COMSOL Multiphysics ® v. 5.4. www.comsol.com. [Accessed 02-August-2019].

[147] Mian Zhang, Gustavo Luiz, Shreyas Shah, Gustavo Wiederhecker, and Michal Lipson. Eliminating anchor loss in optomechanical resonators using elastic wave interference. *Applied Physics Letters*, 105(5):051904, 2014.

[148] Kerry J. Vahala. Back-action limit of linewidth in an optomechanical oscillator. *Phys. Rev. A*, 78:023832, Aug 2008.

[149] K. L. Ekinci and M. L. Roukes. Nanoelectromechanical systems. *Review of Scientific Instruments*, 76(6):061101, 2005.

[150] A. N. Cleland and M. L. Roukes. Noise processes in nanomechanical resonators. *Journal of Applied Physics*, 92(5):2758–2769, 2002.

[151] Yeghishe Tsaturyan, Andreas Barg, Eugene S Polzik, and Albert Schliesser. Ultracoherent nanomechanical resonators via soft clamping and dissipation dilution. *Nature nanotechnology*, 12(8):776, 2017.

[152] M. Pandey, R. B. Reichenbach, A. T. Zehnder, A. Lal, and H. G. Craighead. Reducing anchor loss in mems resonators using mesa isolation. *Journal of Microelectromechanical Systems*, 18(4):836–844, Aug 2009.

[153] T. L. Naing, T. O. Rocheleau, Z. Ren, S. Li, and C. T. . Nguyen. High- q uhf spoke-supported ring resonators. *Journal of Microelectromechanical Systems*, 25(1):11–29, Feb 2016.

[154] Minhang Bao and Heng Yang. Squeeze film air damping in mems. *Sensors and Actuators A: Physical*, 136(1):3 – 27, 2007. 25th Anniversary of Sensors and Actuators A: Physical.

[155] K. Y. Yasumura, T. D. Stowe, E. M. Chow, T. Pfafman, T. W. Kenny, B. C. Stipe, and D. Rugar. Quality factors in micron- and submicron-thick cantilevers. *Journal of Microelectromechanical Systems*, 9(1):117–125, March 2000.

[156] Janna Rodriguez, Saurabh A Chandorkar, Christopher A Watson, Grant M Glaze, CH Ahn, Eldwin J Ng, Yushi Yang, and Thomas W Kenny. Direct detection of akhiezer damping in a silicon mems resonator. *Scientific reports*, 9(1):2244, 2019.

[157] Ron Lifshitz and M. L. Roukes. Thermoelastic damping in micro- and nanomechanical systems. *Phys. Rev. B*, 61:5600–5609, Feb 2000.

[158] S. A. Chandorkar, M. Agarwal, R. Melamud, R. N. Candler, K. E. Goodson, and T. W. Kenny. Limits of quality factor in bulk-mode micromechanical resonators. In *2008 IEEE 21st International Conference on Micro Electro Mechanical Systems*, pages 74–77, Jan 2008.

[159] Marcel W Pruessner, Doewon Park, Todd H Stievater, Dmitry A Kozak, and William S Rabinovich. An optomechanical transducer platform for evanescent field displacement sensing. *IEEE Sensors Journal*, 14(10):3473–3481, 2014.

[160] Grigorii B Malykin. The sagnac effect: correct and incorrect explanations. *Physics-Uspekhi*, 43(12):1229, 2000.

[161] G. A. Sanders, M. G. Prentiss, and S. Ezekiel. Passive ring resonator method for sensitive inertial rotation measurements in geophysics and relativity. *Opt. Lett.*, 6(11):569–571, Nov 1981.

[162] E. J. POST. Sagnac effect. *Rev. Mod. Phys.*, 39:475–493, Apr 1967.

[163] Guohong He and K. Najafi. A single-crystal silicon vibrating ring gyroscope. In *Technical Digest. MEMS 2002 IEEE International Conference. Fifteenth IEEE International Conference on Micro Electro Mechanical Systems (Cat. No.02CH37266)*, pages 718–721, Jan 2002.

[164] Huikai Xie and Gary K Fedder. Integrated microelectromechanical gyroscopes. *Journal of aerospace engineering*, 16(2):65–75, 2003.

[165] Jacob Scheuer and Amnon Yariv. Sagnac effect in coupled-resonator slow-light waveguide structures. *Phys. Rev. Lett.*, 96:053901, Feb 2006.

[166] F Dell'Olio, T Tatoli, C Ciminelli, and MN Armenise. Recent advances in miniaturized optical gyroscopes. *Journal of the European optical society-Rapid publications*, 9, 2014.

[167] National Instruments ®. https://www.ni.com/fr-fr/shop/labview.html. [Accessed 25-August-2019].

[168] W. Bogaerts, P. De Heyn, T. Van Vaerenbergh, K. De Vos, S. Kumar Selvaraja, T. Claes, P. Dumon, P. Bienstman, D. Van Thourhout, and R. Baets. Silicon microring resonators. *Laser & Photonics Reviews*, 6(1):47–73, 2012.

[169] Brent E. Little, Juha-Pekka Laine, and Sai T. Chu. Surface-roughness-induced contradirectional coupling in ring and disk resonators. *Opt. Lett.*, 22(1):4–6, Jan 1997.

[170] Jiří Čtyroký, Ivan Richter, and Milan Šiňor. Dual resonance in a waveguide-coupled ring microresonator. *Optical and Quantum Electronics*, 38(9):781–797, Jul 2006.

[171] Matthew Borselli, Thomas J. Johnson, and Oskar Painter. Beyond the rayleigh scattering limit in high-q silicon microdisks: theory and experiment. *Opt. Express*, 13(5):1515–1530, Mar 2005.

[172] Qing Li, Ali A. Eftekhar, Zhixuan Xia, and Ali Adibi. Azimuthal-order variations of surface-roughness-induced mode splitting and scattering loss in high-q microdisk resonators. *Opt. Lett.*, 37(9):1586–1588, May 2012.

[173] R. Paschotta. Noise of mode-locked lasers (part i): numerical model. *Applied Physics B*, 79(2):153–162, Jul 2004.

[174] Wei C. Jiang, Jidong Zhang, and Qiang Lin. Compact suspended silicon microring resonators with ultrahigh quality. *Opt. Express*, 22(1):1187–1192, Jan 2014.

[175] J. P. van der Ziel. PhaseâĹŠmatched harmonic generation in a laminar structure with wave propagation in the plane of the layers. *Applied Physics Letters*, 26(2):60–61, 1975.

[176] Stoyan Tanev, Valery Tuchin, Pavel Cheben, Przemek Bock, Jens Schmid, and James Pond. Advances in photonics design and modeling for nano- and bio-photonics applications. *Proc SPIE*, 7747, 10 2010.

[177] Przemek J. Bock, Pavel Cheben, Jens H. Schmid, Jean Lapointe, Andre DelÃćge, Siegfried Janz, Geof C. Aers, Dan-Xia Xu, Adam Densmore, and Trevor J. Hall. Subwavelength grating periodic structures in silicon-on-insulator: a new type of microphotonic waveguide. *Optics Express*, 18(19):20251–20262, September 2010.

[178] Pavel Cheben, Przemek J. Bock, Jens H. Schmid, Jean Lapointe, Siegfried Janz, Dan-Xia Xu, Adam Densmore, André Delâge, Boris Lamontagne, and Trevor J. Hall. Refractive index engineering with subwavelength gratings for efficient microphotonic couplers and planar waveguide multiplexers. *Opt. Lett.*, 35(15):2526–2528, Aug 2010.

[179] Junjia Wang, Ivan Glesk, and Lawrence R. Chen. Subwavelength grating filtering devices. *Opt. Express*, 22(13):15335–15345, Jun 2014.

[180] Przemek J. Bock, Pavel Cheben, Jens H. Schmid, Jean Lapointe, André Delâge, Dan-Xia Xu, Siegfried Janz, Adam Densmore, and Trevor J. Hall. Subwavelength grating crossings for silicon wire waveguides. *Opt. Express*, 18(15):16146–16155, Jul 2010.

[181] Junjia Wang, Reza Ashrafi, Rhys Adams, Ivan Glesk, Ivana Gasulla, Jose Capmany, and Lawrence R. Chen. Subwavelength grating enabled on-chip ultra-compact optical true time delay line. *Scientific Reports*, 6, Jul 2016.

[182] Robert Halir, P Cheben, JH Schmid, R Ma, D Bedard, S Janz, D-X Xu, A Densmore, J Lapointe, and I Molina-Fernández. Continuously apodized fiber-to-chip surface grating coupler with refractive index engineered subwavelength structure. *Optics letters*, 35(19):3243–3245, 2010.

[183] Zeinab Jafari and Abbas Zarifkar. Dispersion flattened single etch-step waveguide based on subwavelength grating. *Optics Communications*, 393:219 – 223, 2017.

[184] Daniel Benedikovic, Mathias Berciano, Carlos Alonso-Ramos, Xavier Le Roux, Eric Cassan, Delphine Marris-Morini, and Laurent Vivien. Dispersion control of silicon nanophotonic waveguides using sub-wavelength grating metamaterials in near- and mid-ir wavelengths. *Opt. Express*, 25(16):19468–19478, Aug 2017.

[185] J. Soler Penades, A. Ortega-Mo nux, M. Nedeljkovic, J. G. Wangüemert-Pérez, R. Halir, A. Z. Khokhar, C. Alonso-Ramos, Z. Qu, I. Molina-Fernández, P. Cheben, and G. Z. Mashanovich. Suspended silicon mid-infrared waveguide devices with subwavelength grating metamaterial cladding. *Opt. Express*, 24(20):22908–22916, Oct 2016.

[186] Richard Soref. Mid-infrared pohotonics in silicon and germanium. *Nature Photonics*, 4:495–497, August 2010.

[187] M. Nedeljkovic, A. Z. Khokhar, Y. Hu, X. Chen, J. Soler Penades, S. Stankovic, H. M. H. Chong, D. J. Thomson, F. Y. Gardes, G. T. Reed, and G. Z. Mashanovich. Silicon photonic devices and platforms for the mid-infrared. *Opt. Mater. Express*, 3(9):1205–1214, Sep 2013.

[188] Jonas Flueckiger, Shon Schmidt, Valentina Donzella, Ahmed Sherwali, Daniel M. Ratner, Lukas Chrostowski, and Karen C. Cheung. Sub-wavelength grating for enhanced ring resonator biosensor. *Opt. Express*, 24(14):15672–15686, Jul 2016.

[189] Serguei Mikhailovitch Rytov. Electromagnetic properties of a finely stratified medium. *Soviet Physics JETP*, 2(3):466–475, May 1956.

[190] Alejandro Ortega-Mo nux, Jiří Čtyroký, Pavel Cheben, Jens H. Schmid, Shurui Wang, Í nigo Molina-Fernández, and Robert Halir. Disorder effects in subwavelength grating metamaterial waveguides. *Opt. Express*, 25(11):12222–12236, May 2017.

[191] J. Darío Sarmiento-Merenguel, Alejandro Ortega-Mo nux, Jean-Marc Fédéli, J. Gonzalo Wangüemert-Pérez, Carlos Alonso-Ramos, Elena Durán-Valdeiglesias, Pavel Cheben, Í nigo Molina-Fernández, and Robert Halir. Controlling leakage losses in subwavelength grating silicon metamaterial waveguides. *Opt. Lett.*, 41(15):3443–3446, Aug 2016.

[192] Diego Perez Galacho, Robert Halir, Luis Zavargo Peche, Gonzalo WangÃijemert Perez, Alejandro Ortega MoÃśux, ÃĐÃśigo Molina FernÃąndez, and Pavel Cheben. Adiabatic transitions for sub-wavelength grating waveguides. In *16th European Conference on Integrated Optics*, 2012.

[193] P. Robert, V. Nguyen, S. Hentz, L. Duraffourg, G. Jourdan, J. Arcamone, and S. Harrisson. M nems: A new approach for ultra-low cost 3d inertial sensor. In *SENSORS, 2009 IEEE*, pages 963–966, Oct 2009.

[194] I Favero and K Karrai. Cavity cooling of a nanomechanical resonator by light scattering. *New Journal of Physics*, 10(9):095006, sep 2008.

[195] Luca Luschi and Francesco Pieri. An analytical model for the determination of resonance frequencies of perforated beams. *Journal of Micromechanics and Microengineering*, 24(5):055004, 2014.

[196] BD Hauer, C Doolin, KSD Beach, and JP Davis. A general procedure for thermomechanical calibration of nano/micro-mechanical resonators. *Annals of Physics*, 339:181–207, 2013.

[197] M. L. Povinelli, Steven G. Johnson, Marko Loncar, Mihai Ibanescu, Elizabeth J. Smythe, Federico Capasso, and J. D. Joannopoulos. High-Q enhancement of attractive and repulsive optical forces between coupled whispering-gallery-mode resonators. *Optics Express*, 13(20):8286, 2005.

[198] Dries Van Thourhout and Joris Roels. Optomechanical device actuation through the optical gradient force. *Nature Photonics*, 4(4):211, 2010.

[199] Peter T Rakich, Miloš A Popović, Marin Soljačić, and Erich P Ippen. Trapping, corralling and spectral bonding of optical resonances through optically induced potentials. *Nature Photonics*, 1(11):658, 2007.

[200] Andres Castellanos-Gomez, Nicolas Agraït, and Gabino Rubio-Bollinger. Dynamics of quartz tuning fork force sensors used in scanning probe microscopy. *Nanotechnology*, 20(21):215502, 2009.

[201] Xiankai Sun, Jiangjun Zheng, Menno Poot, Chee Wei Wong, and Hong X Tang. Femtogram doubly clamped nanomechanical resonators embedded in a high-q two-dimensional photonic crystal nanocavity. *Nano letters*, 12(5):2299–2305, 2012.

[202] Kevin K. Lee, Desmond R. Lim, Lionel C. Kimerling, Jangho Shin, and Franco Cerrina. Fabrication of ultralow-loss si/sio2 waveguides by roughness reduction. *Opt. Lett.*, 26(23):1888–1890, Dec 2001.

[203] F. Gao, Y. Wang, G. Cao, X. Jia, and F. Zhang. Reduction of sidewall roughness in silicon-on-insulator rib waveguides. *Applied Surface Science*, 252(14):5071 – 5075, 2006.

[204] Peng Wang, Aron Michael, and Chee Yee Kwok. Fabrication of sub-micro silicon waveguide with vertical sidewall and reduced roughness for low loss applications. *Procedia Engineering*, 87:979–982, 2014.

[205] Joyce KS Poon, Jacob Scheuer, Yong Xu, and Amnon Yariv. Designing coupled-resonator optical waveguide delay lines. *JOSA B*, 21(9):1665–1673, 2004.

[206] Temple H Fay and Sarah Duncan Graham. Coupled spring equations. *International Journal of Mathematical Education in Science and Technology*, 34(1):65–79, 2003.

[207] RWP Drever, John L Hall, FV Kowalski, J_ Hough, GM Ford, AJ Munley, and H Ward. Laser phase and frequency stabilization using an optical resonator. *Applied Physics B*, 31(2):97–105, 1983.

[208] Synopsys ®. https://www.synopsys.com/optical-solutions/rsoft/rsoft-products.html. [Accessed 06-Nov-2019].

[209] J. Buus. The effective index method and its application to semiconductor lasers. *IEEE Journal of Quantum Electronics*, 18(7):1083–1089, July 1982.

[210] Jean-Pierre Berenger. A perfectly matched layer for the absorption of electromagnetic waves. *Journal of computational physics*, 114(2):185–200, 1994.

[211] Richard Courant, Kurt Friedrichs, and Hans Lewy. On the partial difference equations of mathematical physics. *IBM journal of Research and Development*, 11(2):215–234, 1967.

[212] Mordehai Heiblum and Jay Harris. Analysis of curved optical waveguides by conformal transformation. *IEEE Journal of Quantum Electronics*, 11(2):75–83, 1975.

[213] Alexander Gondarenko, Jacob S. Levy, and Michal Lipson. High confinement micron-scale silicon nitride high q ring resonator. *Opt. Express*, 17(14):11366–11370, Jul 2009.

[214] Ming-Chun Tien, Jared F. Bauters, Martijn J. R. Heck, Daryl T. Spencer, Daniel J. Blumenthal, and John E. Bowers. Ultra-high quality factor planar si3n4 ring resonators on si substrates. *Opt. Express*, 19(14):13551–13556, Jul 2011.

[215] Scott S. Verbridge, Jeevak M. Parpia, Robert B. Reichenbach, Leon M. Bellan, and H. G. Craighead. High quality factor resonance at room temperature with nanostrings under high tensile stress. *Journal of Applied Physics*, 99(12):124304, 2006.

[216] Quirin P. Unterreithmeier, Thomas Faust, and Jörg P. Kotthaus. Damping of nanomechanical resonators. *Phys. Rev. Lett.*, 105:027205, Jul 2010.

[217] D. J. Blumenthal, R. Heideman, D. Geuzebroek, A. Leinse, and C. Roeloffzen. Silicon nitride in silicon photonics. *Proceedings of the IEEE*, 106(12):2209–2231, Dec 2018.

Abstract

In this work, we study ring shaped suspended optomechanical resonators, and Sub-Wavelength Grating (SWG) based optomechanical resonators.

The first approach presented - suspended ring resonators - serves as an introduction over general equations and experimental techniques.

On a second approach, we propose to co-integrate SWG waveguides inside of a Fabry-Perot cavity. The refractive index of a SWG waveguide is periodic with a pitch way smaller than the wavelength that results in a lossless propagation with no diffraction effects. The medium can be approximated as uniform, with an averaging effect over its refractive index. In particular, we evidence new optomechanical mechanisms arising from the SWG waveguide, and expect a strong optomechanical coupling strength.

All along the thesis, a systematic optical, mechanical, and optomechanical study of each structure is conducted, with both simplified analytical models and numerical simulations. The technological realization of the structures over 200 mm silicon wafers is presented, along with optical and optomechanical experimental characterizations.

Keywords: Cavity optomechanics – photonics – optical forces – sub-wavelength grating – suspended waveguide – ring resonator – silicon – analytical – experimental – fabrication.

Résumé

Dans ce travail, nous étudions les résonateurs optomécaniques en forme d'anneaux suspendus et les résonateurs optomécaniques à base de guide d'onde sub-longueur d'onde (SWG - pour Sub-Wavelength Grating).

La première approche présentée - les anneaux suspendus - sert d'introduction aux notions générales et aux techniques expérimentales.

Dans une deuxième approche, nous proposons de co-intégrer des guides d'ondes SWG à l'intérieur d'une cavité Fabry-Pérot. L'indice de réfraction d'un guide d'ondes SWG est périodique avec un pas beaucoup plus petit que la longueur d'onde, ce qui permet une propagation optique sans perte et sans effet de diffraction. Le milieu peut être considéré uniforme, avec un effet de moyennage sur son indice de réfraction. En particulier, nous mettons en évidence de nouveaux mécanismes optomécaniques issus du guide d'ondes SWG, et attendons un fort taux de couplage optomécanique.

Tout au long de la thèse, l'étude systématique des propriétés optiques, mécaniques et optomécaniques de chaque structure est menée, sur la base de modèles analytiques simplifiés et de simulations numériques. La réalisation technologique des structures sur wafers silicium de 200 mm est présentée, ainsi que des caractérisations expérimentales optiques et optomécaniques.

Mots clés : Optomécanique en cavité – photonique – forces optiques – sub-longueur d'onde – guide d'onde suspendu – anneau résonnant – silicium – analytique – expérimental – fabrication.